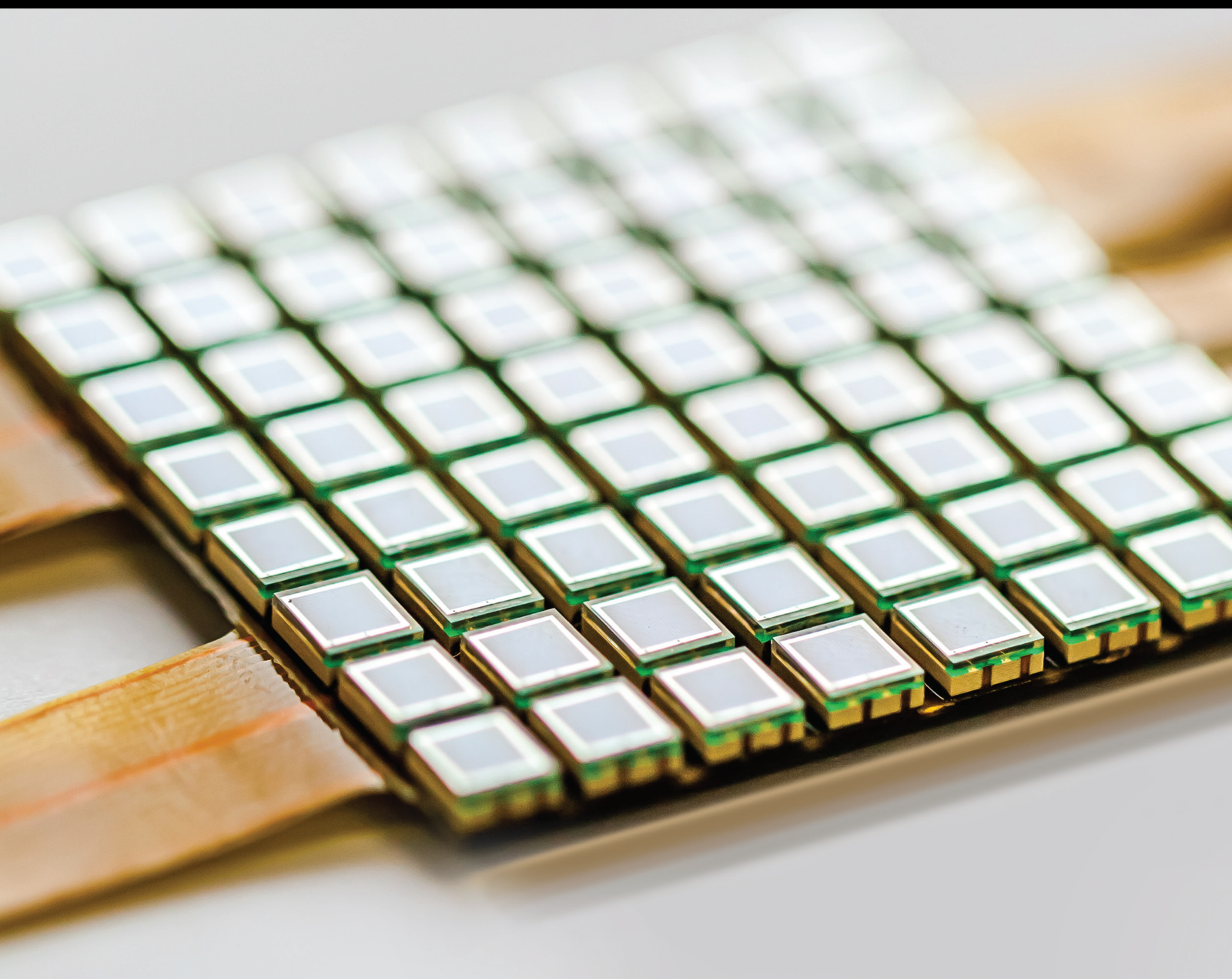


Multi-Sensor Integration Algorithms and Applications for Navigation

Lead Guest Editor: Qiuzhao Zhang

Guest Editors: Haiying Liu and Panagiotis Psimoulis





Multi-Sensor Integration Algorithms and Applications for Navigation

Journal of Sensors

Multi-Sensor Integration Algorithms and Applications for Navigation

Lead Guest Editor: Qiuzhao Zhang

Guest Editors: Haiying Liu and Panagiotis
Psimoulis






Copyright © 2022 Hindawi Limited. All rights reserved.

This is a special issue published in "Journal of Sensors." All articles are open access articles distributed under the Creative Commons Attribution License, which permits unrestricted use, distribution, and reproduction in any medium, provided the original work is properly cited.

Chief Editor

Harith Ahmad , Malaysia

Associate Editors

Duo Lin , China
Fanli Meng , China
Pietro Siciliano , Italy
Guiyun Tian, United Kingdom

Academic Editors

Ghufran Ahmed , Pakistan
Constantin Apetrei, Romania
Shonak Bansal , India
Fernando Benito-Lopez , Spain
Romeo Bernini , Italy
Shekhar Bhansali, USA
Matthew Brodie, Australia
Ravikumar CV, India
Belén Calvo, Spain
Stefania Campopiano , Italy
Binghua Cao , China
Domenico Caputo, Italy
Sara Casciati, Italy
Gabriele Cazzulani , Italy
Chi Chiu Chan, Singapore
Sushank Chaudhary , Thailand
Edmon Chehura , United Kingdom
Marvin H Cheng , USA
Lei Chu , USA
Mario Collotta , Italy
Marco Consales , Italy
Jesus Corres , Spain
Andrea Cusano, Italy
Egidio De Benedetto , Italy
Luca De Stefano , Italy
Manel Del Valle , Spain
Franz L. Dickert, Austria
Giovanni Diraco, Italy
Maria de Fátima Domingues , Portugal
Nicola Donato , Italy
Sheng Du , China
Amir Elzwawy, Egypt
Mauro Epifani , Italy
Congbin Fan , China
Lihang Feng, China
Vittorio Ferrari , Italy
Luca Francioso, Italy

Libo Gao , China
Carmine Granata , Italy
Pramod Kumar Gupta , USA
Mohammad Haider , USA
Agustin Herrera-May , Mexico
María del Carmen Horrillo, Spain
Evangelos Hristoforou , Greece
Grazia Iadarola , Italy
Syed K. Islam , USA
Stephen James , United Kingdom
Sana Ullah Jan, United Kingdom
Bruno C. Janegitz , Brazil
Hai-Feng Ji , USA
Shouyong Jiang, United Kingdom
Roshan Prakash Joseph, USA
Niravkumar Joshi, USA
Rajesh Kaluri , India
Sang Sub Kim , Republic of Korea
Dr. Rajkishor Kumar, India
Rahul Kumar , India
Nageswara Lalam , USA
Antonio Lazaro , Spain
Chengkuo Lee , Singapore
Chenzong Li , USA
Zhi Lian , Australia
Rosalba Liguori , Italy
Sangsoon Lim , Republic of Korea
Huan Liu , China
Jin Liu , China
Eduard Llobet , Spain
Jaime Lloret , Spain
Mohamed Louzazni, Morocco
Jesús Lozano , Spain
Oleg Lupan , Moldova
Leandro Maio , Italy
Pawel Malinowski , Poland
Carlos Marques , Portugal
Eugenio Martinelli , Italy
Antonio Martinez-Olmos , Spain
Giuseppe Maruccio , Italy
Yasuko Y. Maruo, Japan
Zahid Mehmood , Pakistan
Carlos Michel , Mexico
Stephen. J. Mihailov , Canada
Bikash Nakarmi, China

Ehsan Namaziandost , Iran
Heinz C. Neitzert , Italy
Sing Kiong Nguang , New Zealand
Calogero M. Oddo , Italy
Tinghui Ouyang, Japan
SANDEEP KUMAR PALANISWAMY ,
India
Alberto J. Palma , Spain
Davide Palumbo , Italy
Abinash Panda , India
Roberto Paolesse , Italy
Akhilesh Pathak , Thailand
Giovanni Pau , Italy
Giorgio Pennazza , Italy
Michele Penza , Italy
Sivakumar Poruran, India
Stelios Potirakis , Greece
Biswajeet Pradhan , Malaysia
Giuseppe Quero , Italy
Linesh Raja , India
Maheswar Rajagopal , India
Valerie Renaudin , France
Armando Ricciardi , Italy
Christos Riziotis , Greece
Ruthber Rodriguez Serrezuela , Colombia
Maria Luz Rodriguez-Mendez , Spain
Jerome Rossignol , France
Maheswaran S, India
Ylias Sabri , Australia
Sourabh Sahu , India
José P. Santos , Spain
Sina Sareh, United Kingdom
Isabel Sayago , Spain
Andreas Schütze , Germany
Praveen K. Sekhar , USA
Sandra Sendra, Spain
Sandeep Sharma, India
Sunil Kumar Singh Singh , India
Yadvendra Singh , USA
Afaque Manzoor Soomro , Pakistan
Vincenzo Spagnolo, Italy
Kathiravan Srinivasan , India
Sachin K. Srivastava , India
Stefano Stassi , Italy

Danfeng Sun, China
Ashok Sundramoorthy, India
Salvatore Surdo , Italy
Roshan Thotagamuge , Sri Lanka
Guiyun Tian , United Kingdom
Sri Ramulu Torati , USA
Abdellah Touhafi , Belgium
Hoang Vinh Tran , Vietnam
Aitor Urrutia , Spain
Hana Vaisocherova - Lislalova , Czech
Republic
Everardo Vargas-Rodriguez , Mexico
Xavier Vilanova , Spain
Stanislav Vitek , Czech Republic
Luca Vollero , Italy
Tomasz Wandowski , Poland
Bohui Wang, China
Qihao Weng, USA
Penghai Wu , China
Qiang Wu, United Kingdom
Yuedong Xie , China
Chen Yang , China
Jiachen Yang , China
Nitesh Yelve , India
Aijun Yin, China
Chouki Zerrouki , France

Contents

Modified Adaptive Fusion Scheme for Kalman Filter Based on the Hypothesis Test

Chen Jiang , Wenkai Liu , Hui Li , and Haijun Xu 





Research Article (12 pages), Article ID 4064339, Volume 2022 (2022)

Automatic Calibration Method for Airborne LiDAR Systems Based on Approximate Corresponding Points Model

Yu Tian, Yibo Zhao, Shaogang Lei , Chuning Ji, Lei Duan, and Vladimír Sedlák





Research Article (13 pages), Article ID 4853419, Volume 2022 (2022)

A Robust Visual-Aided Inertial Navigation Algorithm for Pedestrians

Langping An , Xianfei Pan , Tingting Li , and Mang Wang 




Research Article (12 pages), Article ID 1311221, Volume 2022 (2022)

A New Triple Filtering Algorithm and Its Application for Aerial GNSS/INS-Integrated Direct Georeferencing System

Qusen Chen , Leilei Li , Keyi Xu, Xiangdong An , and Yu Wu 

Research Article (13 pages), Article ID 6527356, Volume 2021 (2021)

Orthorectification of WorldView-3 Satellite Image Using Airborne Laser Scanning Data

Biswajeet Pradhan , Ahmed A. Ahmed, Subrata Chakraborty , Abdullah Alamri, and Chang-Wook Lee 



Research Article (12 pages), Article ID 5273549, Volume 2021 (2021)

A State-Domain Robust Chi-Square Test Method for GNSS/INS Integrated Navigation

Zhangjun Yu , Qiuzhao Zhang , Ke Yu , and Nanshan Zheng 


Research Article (8 pages), Article ID 1745383, Volume 2021 (2021)

Improved Mitigation Method for the Multipath Delays of BDS-3 Code Observations with the Aid of a Sparse Modeling Algorithm

Chao Hu , Qianxin Wang , and Alberto Hernandez Moraleda

Research Article (19 pages), Article ID 9947704, Volume 2021 (2021)

A New GPT2w Model Improved by PSO-LSSVM for GNSS High-Precision Positioning

Xuanxuan Zhang, Yamin Dang, and Changhui Xu 

Research Article (15 pages), Article ID 9990831, Volume 2021 (2021)

Research Article

Modified Adaptive Fusion Scheme for Kalman Filter Based on the Hypothesis Test

Chen Jiang , Wenkai Liu , Hui Li , and Haijun Xu 

College of Surveying and Geo-Informatics, North China University of Water Resources and Electric Power, Zhengzhou 450045, China

Correspondence should be addressed to Haijun Xu; xuhaijun@ncwu.edu.cn

Received 4 June 2021; Accepted 5 January 2022; Published 29 January 2022

Academic Editor: Qiu-Zhao Zhang

Copyright © 2022 Chen Jiang et al. This is an open access article distributed under the Creative Commons Attribution License, which permits unrestricted use, distribution, and reproduction in any medium, provided the original work is properly cited.

In the literature, the fading factor was constructed to overcome the shortage of model uncertainties in the Kalman filter. However, the a priori covariance matrix might be inflated abnormally by the fading factor once the measurement is unreliable. Thus, the fading factor may become invalid, and this problem is rarely discussed and tested. In this paper, squares of the Mahalanobis distance are introduced as the judging index, and the fading factor or the covariance inflation factor is adopted conditionally according to the hypothesis testing result. Therefore, an adaptive filtering scheme based on the Mahalanobis distance is put forward for the systems with model uncertainties. The proposed algorithm is implemented with the actual data collected by the integration of the global navigation satellite system (GNSS) and the inertial navigation system and INS (inertial navigation system) integrated systems (INS). For the systems with model uncertainties, experimental results demonstrate that the influences of both the outlying measurements and model errors are controlled effectively with the proposed scheme.

1. Introduction

As the linear estimator of the mean and covariance, the Kalman filter has become the classic fusion algorithm in many fields [1, 2], and it is implemented as the basic fusion method in the data processing with multiple sensors [3, 4]. It has been proved that the Kalman filter is optimal only when the assumptions of Gaussian-distributed process or measurement noise hold [5]. Unfortunately, the Kalman filter is susceptible to outlying measurements, and it performs inadequately with the model errors and uncertain statistical information. Aiming at the outlying measurements, many robust Kalman filtering algorithms were proposed. Outlier detection for all measurements is the most straightforward strategy, and the measurements with relatively large residuals will be rejected [6]. Nevertheless, all measurements should be tested, and this strategy may be inefficient and complex. The filters based on the median may be highly robust; however, many measurements are ignored, and the low efficiency limits its practical applications [7]. The H_{∞} filter was put forward aiming at the uncertain noises of mea-

surement with the minimized estimation error for all possible disturbances [5]. However, the performance would be degraded significantly by the outliers [8]. As the generalized Kalman filter, the Bayesian estimator was derived robustly based on the M-estimation [9]. DIA (detection, identification, and adaptation) methods were developed to resist the influences of outliers, but the identification is valid only when the measurement is reliable [10]. Influences of the model errors can be weakened with many types of adaptive filters [11–13]. In terms of adaptive filter, the MMAE (multiple-model-based adaptive estimation) and IAE (innovation-based adaptive estimation) [14] are two basic strategies. For the data fusion of GNSS/INS integrated systems, the IAE strategy performs better than the MMAE strategy [11]. Besides, another type of adaptive-robust filter where both the adaptation and robustness were considered simultaneously was developed using the adaptive factors and the M-estimation, including four adaptive factors and four detective statistics [15]. Based on this adaptive-robust filter, the influences on the adaptive factor from the outlying measurements were discussed [16], and an alternative strategy

was constructed to control the influences of both model uncertainties and outliers. However, the covariance of the measurement noises remains constant at the normal epochs, and the relatively smaller outliers are more likely to be neglected which should be improved further.

In theory, the fading filter is another kind of adaptive filter, and it can control the influences of the dynamic model errors [17]. The most important problem for the fading filter is to construct a suitable factor S_k . Then, the fading matrix was proposed to adjust the covariance matrix $P_{k/k-1}$ in different data channels [18, 19], and the fading matrix has been adopted in the data processing of GNSS/INS integrated systems [20]. The main superiority to the conventional Kalman filter lies on inflating the covariance matrix of the a priori state, namely, $P_{k/k-1}$, and this indicates that the state estimation $\hat{X}_{k/k}$ relies more on the current observation information. However, both the single factor and the fading matrix are constructed based on the residual vector. Therefore, the fading filter performs well only when the measurement is reliable, and the filter divergence may happen in the presence of outlying measurements, but this problem is seldom discussed. Consequently, aiming at the influences of outlying measurements, the robustness of the conventional fading filter should be improved further.

In this paper, a modified adaptive filtering scheme using the fading factors is proposed for the system with model uncertainty, and the Mahalanobis distance from the measurement to its prediction is applied to construct the judging index for the hypothesis test. Whether the fading filter or the robust estimation method is performed at each epoch depends on the result of hypothesis test. The proposed algorithm is tested using the actual data obtained through the self-developed GNSS/INS integrated systems in actual environment. Both the conventional fading filter and the proposed algorithm are implemented in the testing section of this paper. Results demonstrate that the proposed scheme is superior among all the other tested algorithms of this paper with or without the outlying measurements, and the filter divergence is restrained with the proposed algorithm.

Remaining of this paper is arranged as follows. The related theory of the fading filter is introduced in Section 2. In Section 3, a modified adaptive data fusion scheme is constructed based on the hypothesis test and the conventional fading filter. In Section 4, the dynamic model and measurement model for the GNSS/INS integrated systems are provided; then, a flowchart of the proposed algorithm is demonstrated. In Section 5, experiments with actual data are implemented, and performance the comparative algorithms together with the proposed scheme is tested. Section 6 provides the conclusions of this paper.

2. The Fading Filter

2.1. Basic Models of the Fading Filter. Kalman filter performs well when the assumptions of Gaussian distribution hold. However, the filter divergence may happen, resulting from big model errors. Aiming at this problem, the fading filter was proposed to limit the “memory length” of the Kalman filter [21]. Assume that x_k and x_{k-1} are the state vector at

epoch k and $k-1$, respectively, $\Phi_{k/k-1}$ denotes the state transition matrix, and w_k is the state noise matrix; then, the dynamic equation is obtained

$$x_k = \Phi_{k/k-1}x_{k-1} + w_k, \quad (1)$$

and the a priori state is given by

$$x_{k/k-1} = \Phi_{k/k-1}x_{k-1}. \quad (2)$$

Assume that H_k and z_k are the measurement matrix and measurement vector, respectively, v_k is the measurement noise, and S_k is the fading factor (in general, $S_k \geq 1$). Then, the optimality criterion is defined by [21]:

$$V_k^T R_k^{-1} V_k + \frac{1}{S_k} (x_{k/k} - x_{k/k-1})^T P_{k/k-1}^{-1} (x_{k/k} - x_{k/k-1}) + (x_{k/k} - x_{k/k-1})^T Q_k^{-1} (x_{k/k} - x_{k/k-1}) = \min. \quad (3)$$

Then, the iterative solution is listed below:

$$x_{k/k} = x_{k/k-1} + \bar{K}_k (z_k - H_k x_{k/k-1}), \quad (4)$$

$$\bar{K}_k = \bar{P}_{k/k-1} H_k^T (H_k \bar{P}_{k/k-1} H_k^T + R_k)^{-1}, \quad (5)$$

$$\bar{P}_{k/k-1} = S_k \Phi_{k/k-1} P_{k-1} \Phi_{k/k-1}^T + Q_k, \quad (6)$$

where \bar{K}_k denotes the equivalent gain matrix, $\bar{P}_{k/k-1}$ denotes the equivalent covariance matrix of $x_{k/k-1}$, P_{k-1} denotes the covariance matrix of $x_{k-1/k-1}$, and R_k and Q_k are the covariance matrices of measurement and state noises, respectively.

In the fading filter, the covariance matrix of $x_{k/k-1}$ is inflated for S_k times when compared with that of the conventional Kalman filter, and this indicates that the current measurement information is treated with bigger weight [21]. Consequently, the model errors brought from the previous state are weakened with the fading factor.

2.2. Construction of the Fading Factor or Matrix. In the fading filter, the main work concentrates on the construction of the reasonable factor. In theory, the factor S_k should be inflated if errors of \hat{x}_{k-1} is abnormal. A fading filter with the optimal fading factor was developed, and the simplified and applicable fading factor is given by [22]

$$S_k = \max \left\{ 1, \frac{\text{tr}(N_k)}{\text{tr}(M_k)} \right\}, \quad (7)$$

and $N_k = P_{V_k} - H_k Q_k H_k^T - R_k$, $M_k = H_k \Phi_{k/k-1} P_{k-1} \Phi_{k/k-1}^T H_k^T$, $P_{V_k} = E(V_k V_k^T)$, and $V_k = H_k x_{k/k-1} - z_k$, where $\text{tr}(\cdot)$ means the trace of a matrix, V_k is the residual vector, P_{V_k} is the covariance matrix of V_k , and $\hat{P}_{V_k} = (1/k) \sum_{i=1}^k V_i V_i^T$.

Apart from the fading filter with a single factor, the fading matrix for the fading filter was developed [18]. Different from the single factor, the fading filter with the fading matrix is adjusted in multiple data channels according to the

observabilities of the state vector elements. The fading matrix S_k' is derived by

$$S_k' = \text{diag}(s_1, s_2, \dots, s_i \dots, s_t, 1, \dots, 1, \dots, 1), \quad (8)$$

$$s_i = \max \left(1, \sqrt{\frac{[v_i(k)]^2}{\lambda_i^2 j_{ii}(k) \varepsilon_i} - \frac{b_{ii}(k)}{j_{ii}(k)}} \right), \quad (i = 1, 2, \dots, t), \quad (9)$$

where t is the dimension of measurement equation, v_i is the i th element of V_k , λ_i is the i th observable element of H_k , j_{ii} is the i th diagonal element of J_k and $J_k = \Phi_k P_{k-1} \Phi_k^T$, b_{ii} is the i th diagonal element of B_k , $B_k = H_k Q_{k-1} H_k^T + R_k$, and ε_i is the threshold determined by the Chi-square distribution under the predetermined significance level. In Equation (9), s_1, s_2, \dots, s_t are estimated adaptively, and the other elements in S_k' should be 1.

3. Modified Adaptive Data Fusion Scheme

As depicted in Section 2, the current measurement information is treated with bigger weight in the fading filter, and the current measurement information must be reliable to achieve an ideal filtering performance. In the fading filter however, the circumstance, when the current measurement information is unreliable, is rarely discussed and tested with actual data. In fact, both a single fading factor and the fading matrix in the fading filter are constructed by the predicted residual vector obtained from the measurements. Therefore, the performance of the fading factor would be affected easily by unreliable measurements, and a mistaken adjustment towards the a priori covariance matrix may result in inferior performance or even the filter divergence. Thus, the fading factor or matrix should be implemented in a timely and more reasonable way, and the strategy on processing the unreliable measurements should be discussed further.

With the Gaussian distribution process and measurement noise, the discrete linear stochastic state space model is given by [5]

$$\begin{cases} x_k = \Phi_{k/k-1} x_{k-1} + w_k, \\ z_k = H_k x_k + v_k. \end{cases} \quad (10)$$

An optimal solution is obtained if the assumptions of Gaussian distribution process and measurement noise hold with the mean \bar{z}_k and covariance $P_{\bar{z}_k}$. Probability density function $\rho(z_k)$ of the m -dimensional measurement is [1]

$$\begin{aligned} \rho(z_k) &= N(z_k; \bar{z}_k, P_{\bar{z}_k}) \\ &= \frac{\exp \left(-(1/2)(z_k - \bar{z}_k)^T (P_{\bar{z}_k})^{-1} (z_k - \bar{z}_k) \right)}{\sqrt{(2\pi)^m |P_{\bar{z}_k}|}}. \end{aligned} \quad (11)$$

Nevertheless, $\rho(z_k)$ would no longer hold once the outlying measurements exist or the measurement noises disobey the Gaussian distribution. Therefore, if $\rho(z_k)$ does not hold, and this in turn indicates that an outlier exists at some epoch

or the Gaussian distribution of measurement noise is contaminated. Accordingly, the hypothesis test is performed with the null hypothesis that the measurement corresponds to the assumptions. In fact, the square of the Mahalanobis distance M_k^2 from the measurement z_k to its mean \bar{z}_k , namely, $M_k^2 = (z_k - \bar{z}_k)^T (P_{\bar{z}_k})^{-1} (z_k - \bar{z}_k)$, is applied as the test statistic [23], and this test statistic has been adopted as to construct the robust Kalman filter [1]. According to the inertial assumptions, the test statistic should obey the Chi-square distinction with the degree of freedom m . Then, the α -quantile χ_α is obtained with the provided significance level α . Obviously, the null hypothesis should be accepted if M_k^2 is less than χ_α ; under this circumstance, no outliers exist, and the key problem is to weaken the influences of the model errors. Otherwise, the null hypothesis should be rejected, and the outliers should be processed carefully.

In order to weaken the influences of unreliable measurements, R_k is estimated and updated in an adaptive way. In general, components in the vector of the a priori state are correlated; the covariance matrix of the measurement noise is updated with the covariance inflation factor λ_{ij} , namely,

$$\lambda_{ij} = \sqrt{\lambda_{ii} \cdot \lambda_{jj}}, \quad (12)$$

$$\lambda_{ii} = \begin{cases} 1 & \left| \bar{V}_{\bar{x}_{ki}} \right| \leq c \\ \frac{\left| \bar{V}_{\bar{x}_{ki}} \right|}{c} & \left| \bar{V}_{\bar{x}_{ki}} \right| > c \end{cases}, \quad (13)$$

where $\left| \bar{V}_{\bar{x}_{ki}} \right|$ denotes the standardized predicted residual and c is fixed within 1.0 ~ 1.5. Consequently, R_k is rewritten as

$$\bar{R}_k = \lambda_{ij} R_k. \quad (14)$$

In practice, the complex observation environment determines that R_k is usually not a constant matrix, and the filter may perform better with adaptively updated R_k . Therefore, at the epochs with normal measurements, R_k is updated adaptively in a sequential way based on the Sage-Husa filter [24]; in this paper and the influences of the outlying measurements will be weakened further, namely,

$$R_k = (1 - d_{k-1}) R_{k-1} + d_{k-1} (V_k V_k^T + H_k P_{k/k-1} H_k^T), \quad (15)$$

where $d_k = (1 - b)/(1 - b^k)$ and b is the forgetting factor.

With the hypothesis test based on the Mahalanobis distance, the outlying measurement is identified. Meanwhile, the covariances of the outlying measurement noises and the normal measurements noises will be updated through the Equations (14) and (15), respectively. Both the judging index M_k^2 and R_k are computed using the current measurements, and this indicates a strong sensitivity towards the abnormal measurements and a relatively light computational burden. Accordingly, a modified adaptive data fusion scheme is constructed. In this proposed scheme, the hypothesis test based on the Mahalanobis distance is implemented

at every epoch. For each epoch, if the null hypothesis is accepted, both the fading filter and the sequential updating of R_k are implemented. Otherwise, only the equivalent covariance matrix \bar{R}_k is performed, and this strategy is conducted adaptively. Therefore, a modified scheme is developed concerning the circumstance when the current measurement information is unreliable.

4. Models for GNSS/INS Integrated Systems

The GNSS/INS integrated systems have become a well applied technique in the field of dynamic navigation and positioning [25, 26]. GNSS and INS are integrated mainly in three types, and the loosely coupled type is applied in this paper. For the GNSS/INS and various other integrated systems, the nonlinear filter should be implemented aiming at the nonlinear problem. The cubature Kalman filter (CKF) was proposed to address the high-dimensional state estimation [27]. With a fifteen-dimension state vector \hat{X} , including the position error ΔR^e , the velocity error ΔV^e , the attitude error φ^e of the carrier and the bias of the gyroscope ∇^b , and the accelerometer ε^b , the CKF is adopted in this paper, where e means the earth frame and b means the body frame. Elements of \hat{X} are listed below.

$$\hat{X} = \begin{bmatrix} \Delta R^e & \Delta V^e & \varphi^e & \nabla^b & \varepsilon^b \end{bmatrix}^T, \quad (16)$$

For the nonlinear discrete system

$$\begin{cases} x_k = f(x_{k-1}) + w_{k-1}, \\ z_k = h(x_k) + v_k, \end{cases} \quad (17)$$

where $f(\cdot)$ and $h(\cdot)$ are the nonlinear functions. In the CKF, the time updating process is derived by [27, 28]:

$$X_{i/k-1} = s_{k-1/k-1} \xi + x_{k-1/k-1}, \quad (18)$$

$$P_{k-1/k-1} = s_{k-1/k-1} s_{k-1/k-1}^T, \quad (19)$$

$$X_{i,k-1}^* = f(X_{i,k-1}, w_k), \quad (20)$$

$$x_{k/k-1} = \frac{1}{m} \sum_{i=1}^m w_i X_{i,k/k-1}^*, \quad (21)$$

$$P_{k/k-1} = \frac{1}{m} \sum_{i=1}^m w_i X_{i,k/k-1}^* X_{i,k/k-1}^{*T} - x_{k/k-1} x_{k/k-1}^T + Q_k. \quad (22)$$

And the measurement updating process is derived by

$$x_{k/k} = x_{k/k-1} + K_k (z_k - z_{k/k-1}), \quad (23)$$

$$K_k = P_{xz,k/k-1} P_{zz,k/k-1}^{-1}, \quad (24)$$

$$P_{k/k} = P_{k/k-1} - K_k P_{zz,k/k-1} K_k^T, \quad (25)$$

$$\begin{cases} X_{k/k-1} = s_{k/k-1} \xi + x_{k/k-1}, \\ P_{k/k-1} = s_{k/k-1} s_{k/k-1}^T, \\ Z_{i,k/k-1} = h(X_{i,k/k-1}), \\ z_{k/k-1} = \frac{1}{m} \sum_{i=1}^m w_i Z_{i,k/k-1}, \\ P_{xz,k/k-1} = \frac{1}{m} \sum_{i=1}^m w_i X_{i,k/k-1} Z_{i,k/k-1}^T - x_{k/k-1} z_{k/k-1}^T, \\ P_{zz,k/k-1} = \frac{1}{m} \sum_{i=1}^m w_i Z_{i,k/k-1} Z_{i,k/k-1}^T - z_{k/k-1} z_{k/k-1}^T + R_k, \end{cases} \quad (26)$$

where X denotes the m cubature points generated from states and $m = 2n$, n denotes dimension of the state vector, $s_{k/k-1}$ denotes the square root of $P_{k/k-1}$, $\xi = \sqrt{(m/2)}[1]_i$, and $X_{i,k/k-1}^*$ and $Z_{i,k/k-1}$ denote the propagated cubature points from states and measurements, respectively. Differences of the carrier position and velocity between GNSS and INS, namely, $\Delta r = r_{\text{INS}} - r_{\text{GNSS}}$ and $\Delta v = v_{\text{INS}} - v_{\text{GNSS}}$, are adopted in the process of measurement update. Therefore, the vector of the measurement z_k is constructed below.

$$z_k = \begin{bmatrix} \Delta r \\ \Delta v \end{bmatrix}, \quad (27)$$

Actually, the measurement equation is linear, and the measurement updating process should be modified as follows.

$$x_{k/k} = x_{k/k-1} + K_k (z_k - H_k x_{k/k-1}), \quad (28)$$

$$K_k = P_{k/k-1} H_k^T (H_k P_{k/k-1} H_k^T + R_k)^{-1}, \quad (29)$$

$$P_{k/k} = P_{k/k-1} - K_k H_k P_{k/k-1}. \quad (30)$$

Obviously, the precision of the estimates relies largely on the quality of the measurements, and unreliable measurements may result in inestimable influences. In practice, however, unreliable measurements are inevitable. Therefore, the abnormal measurements must be deliberately processed. Both the fading factor or matrix and the covariance inflation factor have been adopted in the data processing of the GNSS/INS integrated systems. Aiming at the influences on the fading factor, the judging index constructed based on the Mahalanobis distance and the covariance inflation factor is implemented to improve the performance of the filtering process.

5. Performance Evaluation and Analysis

Data processing experiments using different filtering algorithms were designed and implemented. Equipped with the GNSS receiver (Trimble R8) and the inertial measurement unit (IMU, SPAN-CPT), the land vehicle was used as the testing carrier, and a three-axis open-loop gyroscope and three-axis MEMS accelerometers are included in the IMU.

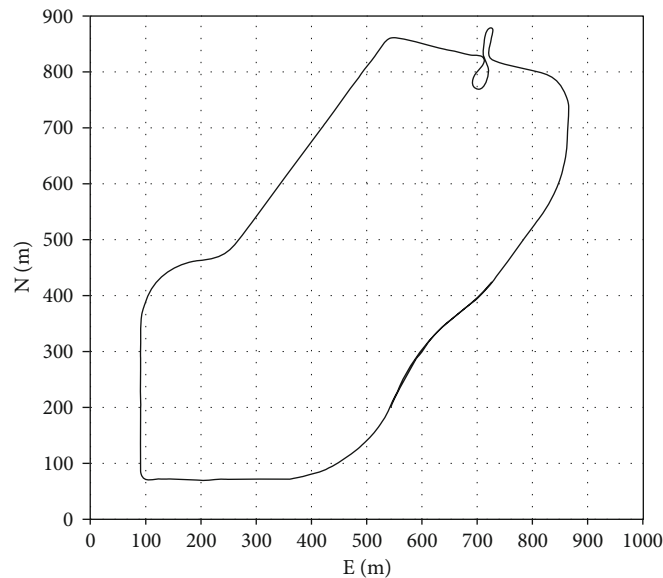


FIGURE 1: Motion trajectory of the land vehicle.

TABLE 1: Main technical parameters from the suppliers.

Sensors	Constant bias	Bias instability	Bias repeatability	Random walk	Scale factor instability
Gyroscope	$20^\circ/h$	$1^\circ/h (1\sigma)$	$3^\circ/h$	$0.0667^\circ/h^{1/2}$	1500 ppm
Accelerometer	50 mg	0.25 mg (1σ)	0.75 mg	$50 \mu g/h^{1/2}$	4000 ppm

The average speed of the land vehicle was about 3.5 m/s. Meanwhile, another GNSS receiver called the base station was set on top of the building. Motion trajectory of the land vehicle (in the North and East directions) is demonstrated in Figure 1. The main technical parameters provided by the suppliers were listed in Table 1. Then, the data was collected with the land vehicle under real conditions. Position and velocity from GNSS were computed using double-difference pseudo-range measurement, and the position and velocity deviations were 0.25 m^2 and $(0.05 \text{ m/s})^2$, respectively. In the testing systems, the cut-off angle was set by 10° , and the sampling frequency was 1 Hz for GNSS and 100 Hz for INS. In this paper, the tightly coupled results provided by the commercial software IE using double-difference carrier phase measurements were regarded as the references.

As to data fusion of the GNSS/INS integrated systems of the paper, the CKF was adopted as the basic filter, and time interval of the data fusion was one second. In the experiments, both the initial data and the data with artificially added outliers were adopted to test the performances of different algorithms more clearly. Consequently, two cases were designed and performed. Each case consists of four algorithms, and the differences between the references and the results of each algorithm are thought to be errors. Comparing the fading filters with a fading factor and fading matrix, the fading matrix performs better by adjusting the covariance matrix in multiple data channels simultaneously, and the ability to resist the model mismatch is enhanced. Therefore, the fading matrix was adopted in this paper. For all algorithms of this paper, the initial value of the covari-

ance are fixed by experience. Thus, the statistical deviations of the models exist, and it is suitable to test the proposed estimation algorithm. Four different algorithms of each case are designed below.

Algorithm 1. The conventional CKF.

Algorithm 2. The fading filter with fading matrix (MF-CKF).

Algorithm 3. The fading filter with fading matrix is implemented at the epochs when the null hypothesis is accepted (Partial-MF-CKF).

Algorithm 4. The fading filter with fading matrix is implemented while the null hypothesis is accepted; otherwise, the covariance inflation factor is adopted for outlying measurements and sequential updating for normal measurements (RMF-CKF).

Case 5. In this case, the initial data collected through the self-developed GNSS/INS integrated navigation systems is processed with the above four algorithms, respectively. Positioning errors of the land vehicle of each algorithm are demonstrated in Figures 2–5.

As mentioned above, each algorithm was implemented based on the initial measurements collected under ideal observation conditions, and little outliers exist in the measurements. Accordingly, positioning errors were mainly brought by the model errors. Comparing Figures 2–5, apparently, error amplitudes in X, Y, and Z directions of the CKF

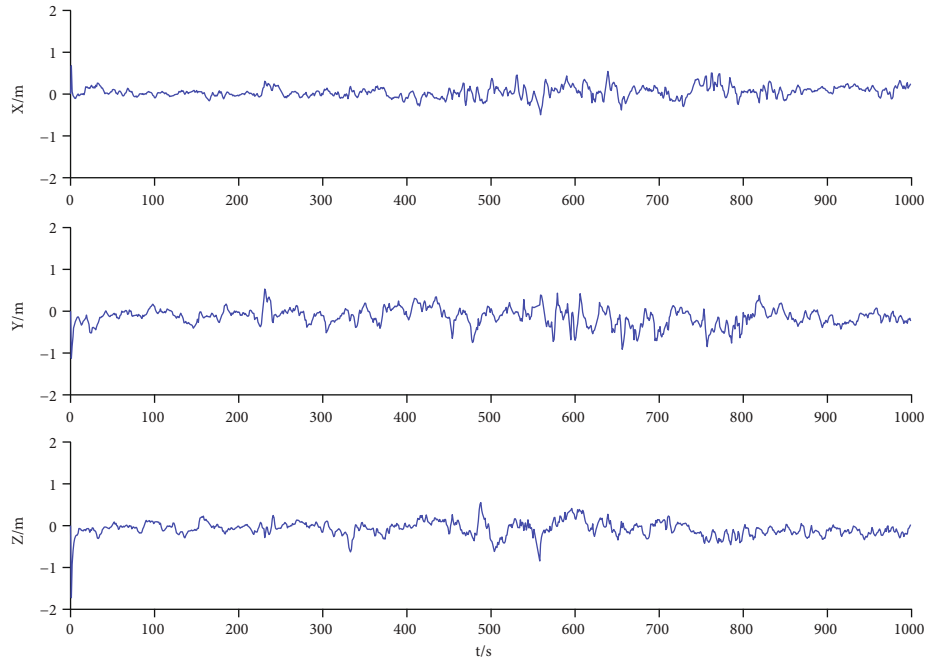


FIGURE 2: Position errors of the CKF algorithm.

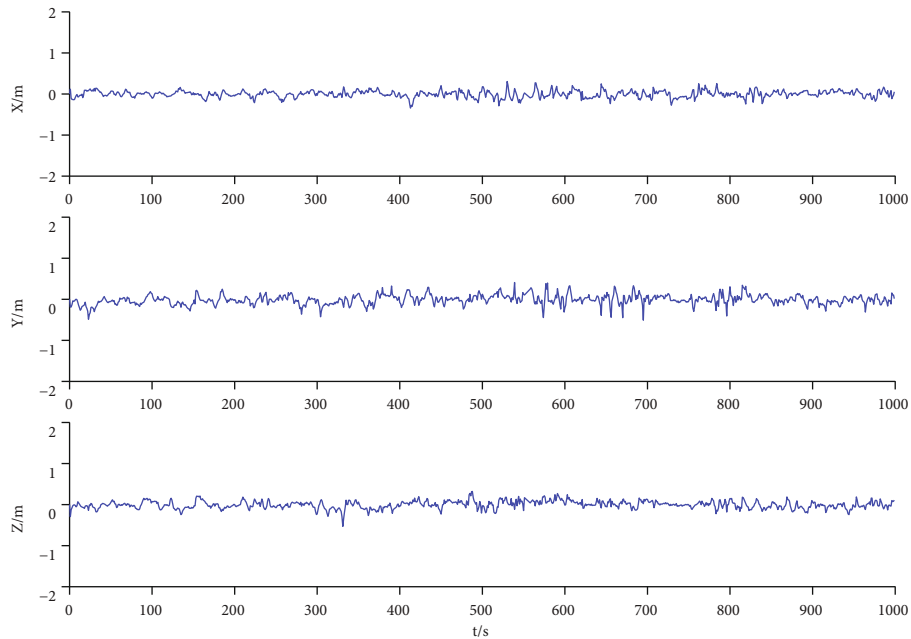


FIGURE 3: Position errors of the MF algorithm.

algorithm are much bigger than the other algorithms, and this indicates that the performance of the conventional CKF algorithm is improved significantly. Moreover, stability of the filter was improved, and the filter divergence resulted from the model uncertainties was restrained effectively with the last three algorithms. In theory, main differences between the Algorithms 2 and 3 lie on the circumstance when the fading matrix is adopted. With the initial measurements, the null hypothesis was accepted at most epochs; thus, the results of the Algorithms 2 and 3 are similar. In

the MF-CKF algorithm, the fading matrix was implemented at all epochs, and the model errors were well-considered. Except for the epochs when the null hypothesis was accepted, the covariance inflation factor in the RMF algorithm was adopted at other epochs, and the influences of abnormal measurements were weakened. Consequently, error amplitudes of the processed algorithm displayed in Figure 4 are smaller than those of other three algorithms.

The root mean square error (RMSE) of these positioning errors was computed to examine the performances of each

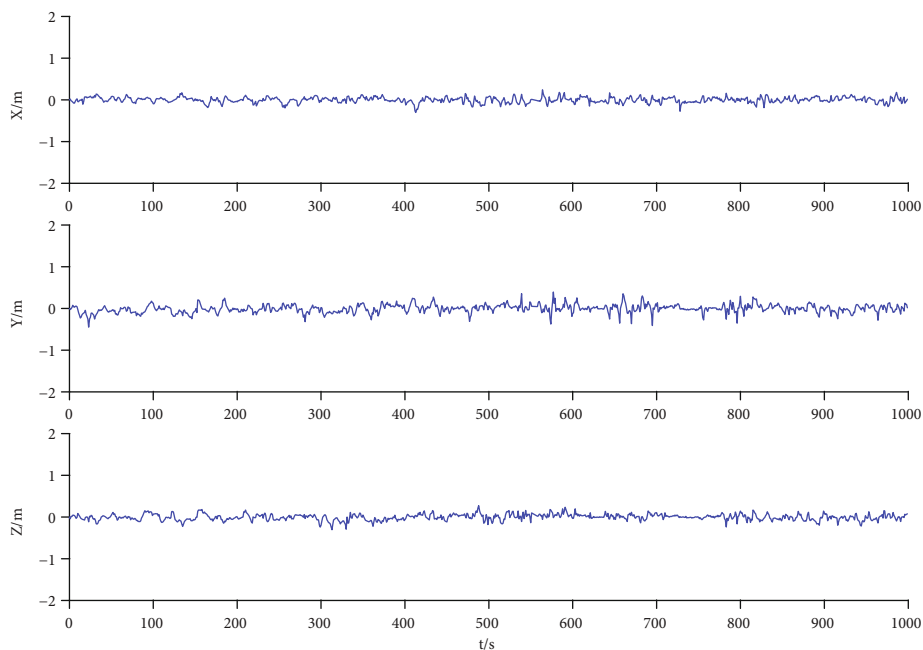


FIGURE 4: Position errors of the Partial-MF-CKF algorithm.

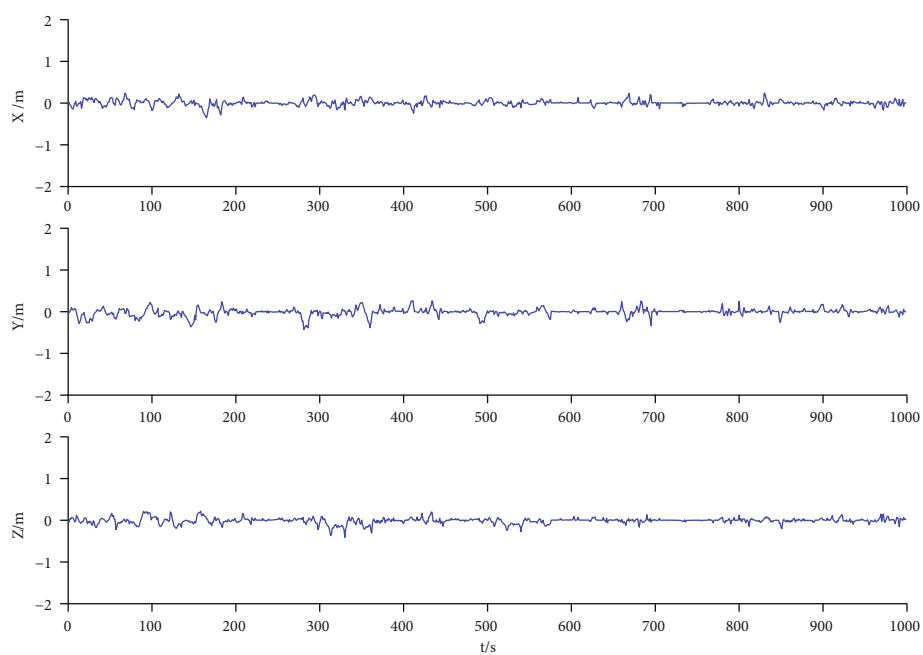


FIGURE 5: Position errors of the RMF-CKF algorithm.

algorithm quantificationally. Figure 6 displays RMSEs in X , Y , and Z directions of each algorithm. Meanwhile, the detailed RMSEs (position (P_X, P_Y), velocity (V_X, V_Y), and attitude (Yaw) are taken as examples) of these four algorithms are listed in Table 2.

In terms of RMSE values in Figure 6 and Table 2, CKF is much bigger than other three algorithms, and this indicates that the robustness and stability of the conventional CKF should be enhanced further. Comparing the RMSE values

of MF-CKF and Partial-MF-CKF algorithms, the former performed better since the influences of model errors were more significant than those of abnormal measurements. Based on the Partial-MF-CKF, the covariance inflation factor was implemented at the epochs when the null hypothesis was rejected. Thus, superiorities of the Mahalanobis distance, the fading filter, and the robust estimation are combined in the proposed algorithm. Meanwhile, RMSE values of the other schemes are all bigger than those of the RMF-

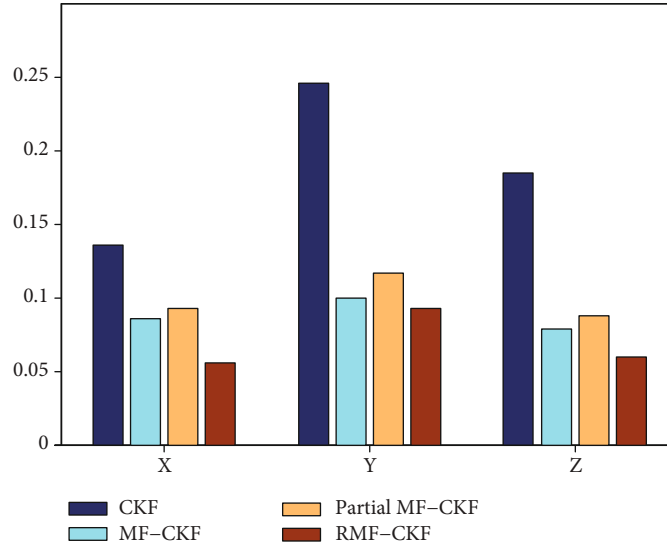


FIGURE 6: Positioning error RMSEs of different algorithms (m). In X, Y, and Z directions, RMSEs of the Algorithms 1, 2, 3, and 4 are depicted in order from the left to the right, respectively.

TABLE 2: Error RMSEs of different algorithms.

Algorithm	P_X (m)	P_Y (m)	V_X (m/s)	V_Y (m/s)	Yaw ($^\circ$)
CKF	0.147	0.270	0.186	0.160	6.242
MF-CKF	0.079	0.100	0.099	0.096	4.169
Partial-MF-CKF	0.093	0.117	0.104	0.098	4.318
RMF-CKF	0.065	0.087	0.056	0.061	3.620

CKF algorithm, and this indicates that better performance is achieved with the processed algorithm. In Table 2, obviously, RMSEs of all the fading filtering algorithms are smaller than the CKF algorithm since effects of the model errors are weakened, and the RMF-CKF algorithm outperforms the other algorithms in terms of accuracy. Compared with the conventional MF algorithm, the accuracy of positioning is improved for 17.7% and 13.0% in X and Y directions, respectively, using the RMF-CKF algorithm.

Case 6. In this case, the continuously changing and the separated positioning outliers were introduced artificially into the measurements to test the robustness and stability of each algorithm. Thus, the perturbation data based on the initial data was constructed. All the above four algorithms were implemented based on the perturbation data, and positioning errors of each algorithm are illustrated in Figures 7–10.

Since positioning outliers were introduced into the measurements, the outliers, instead of the model errors, became the principal factor in affecting the filtering performance. It is demonstrated in Figures 7–10 that amplitudes of all algorithms were much bigger than those of Case 1, and this denotes that all algorithms were affected significantly by the outlying measurements. Meanwhile, as to error amplitudes, all the algorithms with fading matrix are better than the CKF algorithm. Since the outlying measurements were not addressed effectively in the CKF and Partial-MF-CKF

algorithms, Figures 7 and 9 illustrate that effects of the outlying measurements are more apparent. As shown in Figures 7 and 9, the fading matrix was implemented when the null hypothesis was accepted and the model errors were well controlled; thus, the Partial-MF-CKF algorithm performed superior than the CKF. In the MF-CKF algorithm, the fading matrix is implemented at all epochs; the fading matrix performs better when the null hypothesis is accepted. However, the fading filter becomes instable when the null hypothesis is rejected. Therefore, once the fading matrix is applied mistakenly, the MF-CKF algorithm may become inferior to the CKF algorithm. Comparing Figures 7 and 8, it is illustrated that amplitudes at some epochs of the MF-CKF algorithm are even bigger than those of the CKF algorithm, and this is the influences brought from the outlying measurements. In other words, implementing the fading matrix mistakenly may affect the filtering performance at the current together with the future epochs. In the RMF-CKF algorithm, both the model errors and the outlying measurements were considered. Meanwhile, the fading matrix was implemented at the relatively reasonable epochs. In Figure 10, amplitudes in three directions are much smaller than the other algorithms, and a better performance is achieved with the RMF-CKF algorithm. However, as to the constantly changing outliers, the values may small enough to go through the hypothesis test, and the fading matrix will be implemented mistakenly. Therefore, at some epochs in Figure 10, performance of the RMF-CKF algorithm was still apparently affected by the constantly changing outliers.

Figure 11 depicts RMSEs of each algorithm, and the detailed RMSEs of these four algorithms are provided in Table 3.

Comparing the RMSEs in Figures 6 and 11, it is concluded that all algorithms were affected by the outlying measurements. Under the effects of outlying measurements, the model errors were weakened effectively; thus, the MF-CKF algorithm performed better than the CKF algorithm.

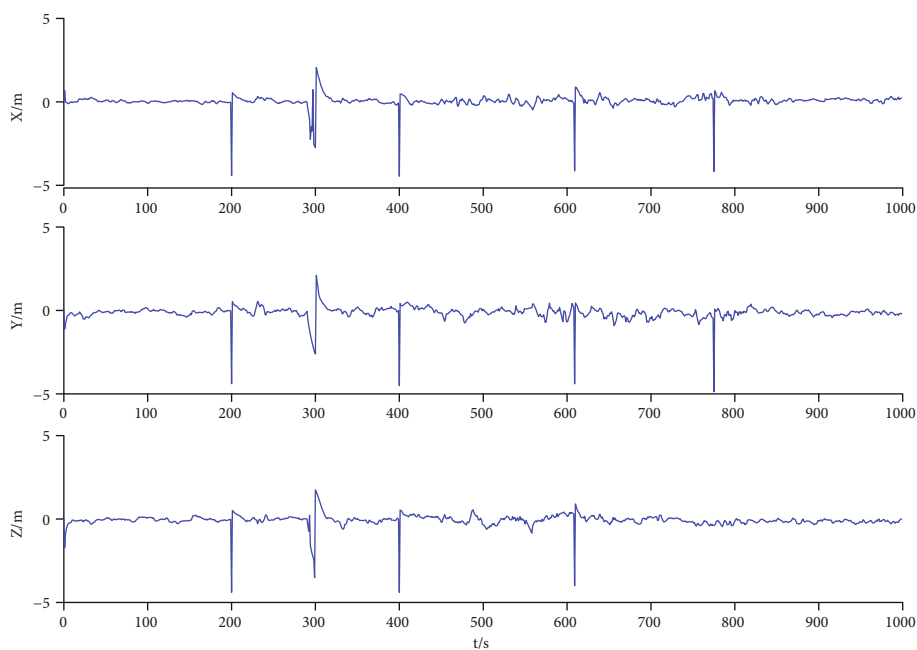


FIGURE 7: Position errors of the CKF algorithm.

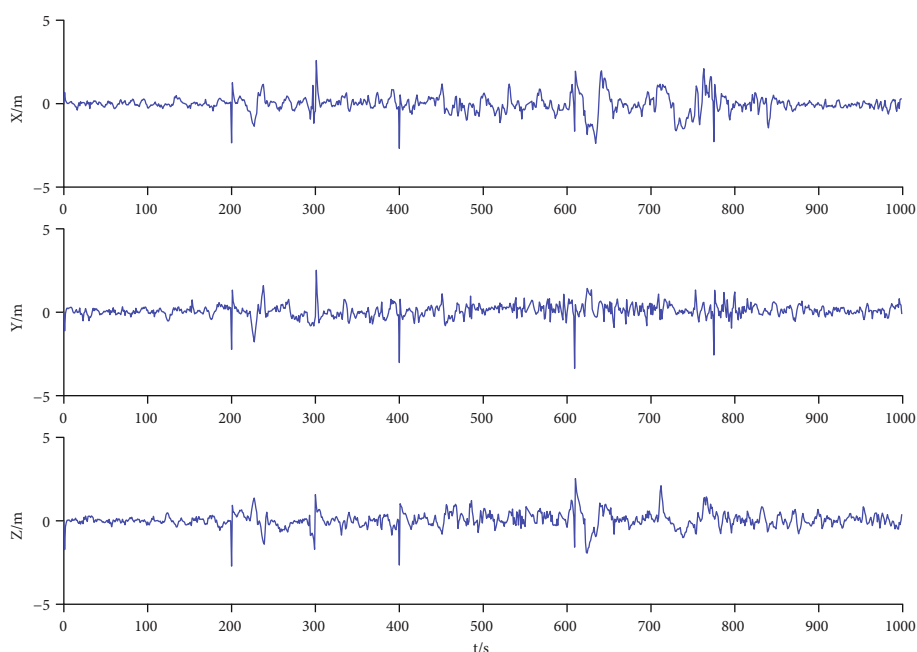


FIGURE 8: Position errors of the MF-CKF algorithm.

Although both the MF and Partial-MF algorithms were affected significantly by the outlying measurements, the fading matrix was implemented only when the null hypothesis was accepted, and the negative effects from mistakenly used fading matrix were avoided in the Partial-MF-CKF algorithm. Therefore, the Partial-MF-CKF algorithm performed better than the MF-CKF algorithm. Corresponding to the qualitative conclusions, RMSEs of the RMF-CKF algorithm are much smaller than the other algorithms; apparently, better performance is achieved with the proposed algorithm.

Comparing Tables 2 and 3, it is demonstrated that the performances of all algorithms were degraded by the outlying measurements, and the filters with fading matrix are more stable and robust than CKF algorithm. By integrating the superiorities of the multiple fading filter and the robust estimation method, the smaller RMSE values and a relatively stable performance were obtained with the proposed algorithm. In this circumstance, the accuracy of positioning are improved for 60.1% and 58.5% in X and Y directions, respectively, using the RMF-CKF algorithm, and this in turn

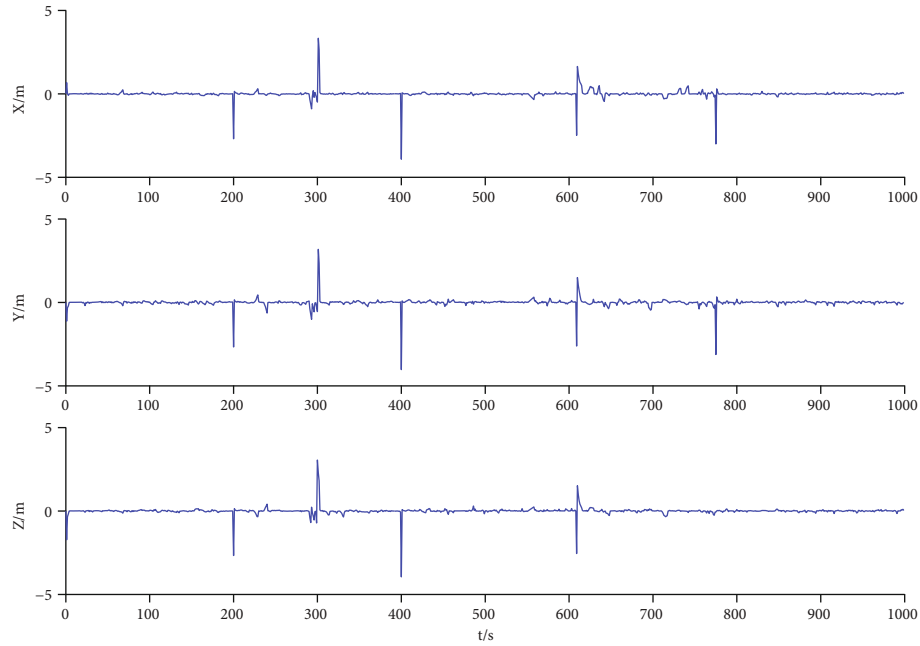


FIGURE 9: Position errors of the Partial-MF-CKF algorithm.

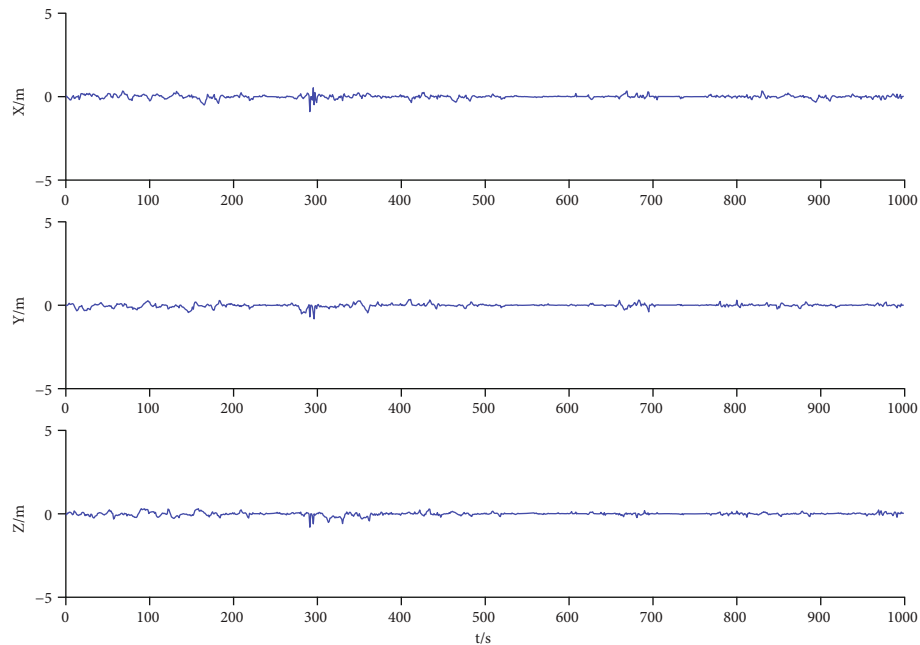


FIGURE 10: Position errors of the RMF-CKF algorithm.

demonstrates that the MF algorithm is affected by the outlying measurements seriously.

6. Conclusions

In this paper, a rarely discussed problem about how to apply the fading factor or matrix with unreliable measurements adaptively is researched, and a modified adaptive filter and an alternative scheme are developed. In the proposed scheme, the hypothesis test was performed using the statistics derived from the Mahalanobis distance, and the actual

measurements were collected with self-developed GNSS/INS integrated systems; then, the contrastive experiments and analysis were implemented to test the performance of the proposed algorithm. Detailed conclusions of this paper are summarized below:

- (1) Compared with the conventional CKF, the adaptive filter with the fading matrix can control the negative effects of model uncertainties; however, the performance may be degraded significantly when there exist outlying measurements

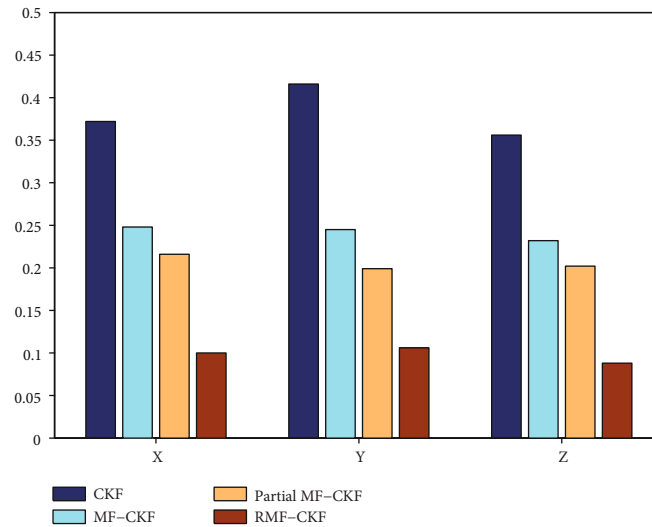


FIGURE 11: Error RMSE of different algorithms (m). In X, Y, and Z directions, RMSEs of the Algorithms 1, 2, 3, and 4 are depicted in order from the left to the right, respectively.

TABLE 3: Error RMSEs of different algorithms.

Algorithm	P_X (m)	P_Y (m)	V_X (m/s)	V_Y (m/s)	Yaw ($^{\circ}$)
CKF	0.392	0.436	0.189	0.162	6.403
MF-CKF	0.263	0.265	0.120	0.104	5.615
Partial-MF-CKF	0.231	0.209	0.108	0.095	5.127
RMF-CKF	0.105	0.110	0.069	0.078	4.351

- (2) In the fading filter, unreliable measurements will construct unreliable fading matrix, and performance of the filter may be even inferior to the conventional Kalman filter if the fading matrix is applied mistakenly. Therefore, it is suggested that the fading matrix be applied in a timely and more reasonable way
- (3) Statistics derived from the Mahalanobis distance can be adopted to test the quality of measurements, and stability of the fading filter is improved with the hypothesis test. By integrating the advantages of the fading matrix and the covariance inflation factor, effects of both the model errors and the outlying measurements are controlled using the proposed scheme for the systems with model uncertainties. Also, the proposed adaptive fusion scheme is more suitable when there exist outliers in the measurements

Data Availability

Some or all data, models, or code that support the findings of this study are available from the corresponding author upon reasonable request (email: xuhaijun@ncwu.edu.cn).

Conflicts of Interest

The authors declare no conflict of interest.

Acknowledgments

This research project was supported by the Natural Science Foundation of Henan Province (212300410198), the Nation Key Research Program of China (2017YFE0131400), and the State Key Laboratory of Geodesy and Earth's Dynamics (SKLGED 2020-3-1-E).

References

- [1] G. B. Chang, "Robust Kalman filtering based on Mahalanobis distance as outlier judging criterion," *Journal of Geodesy*, vol. 88, no. 4, pp. 391–401, 2014.
- [2] R. E. Kalman, "A new approach to linear filtering and prediction problems," *Journal of Basic Engineering*, vol. 82, no. 1, pp. 35–45, 1960.
- [3] M. Aslinezhad, A. Malekijavan, and P. Abbasi, "ANN-assisted robust GPS/INS information fusion to bridge GPS outage," *EURASIP Journal on Wireless Communications and Networking*, vol. 1, 18 pages, 2020.
- [4] F. A. L. Costa and E. A. Mitishita, "An approach to improve direct sensor orientation using the integration of photogrammetric and lidar datasets," *International Journal of Remote Sensing*, vol. 40, no. 14, pp. 5651–5672, 2019.
- [5] D. Simon, *Optimal State Estimation: Kalman, H Infinity, and Nonlinear Approaches*, John Wiley & Sons, 2006.
- [6] X. Xu, Y. Sun, Y. Yao, and T. Zhang, "A robust in-motion optimization-based alignment for SINS/GPS integration," *IEEE Transactions on Intelligent Transportation Systems*, vol. 99, pp. 1–11, 2021.
- [7] R. Ihsan, S. Almufti, and R. Marqas, "A median filter with evaluating of temporal ultrasound image for impulse noise removal for kidney diagnosis," *Journal of Applied Science and Technology Trends*, vol. 1, no. 2, pp. 71–77, 2020.
- [8] G. Rigatos, P. Siano, P. Wira, K. Busawon, and R. Binns, "A nonlinear H-infinity control approach for autonomous truck and trailer systems," *Unmanned Systems*, vol. 8, no. 1, pp. 49–69, 2020.

- [9] Y. X. Yang, "Robust Bayesian estimation," *Journal of Geodesy*, vol. 65, no. 3, pp. 145–150, 1991.
- [10] Y. X. Yang, H. B. He, and G. Xu, "Adaptively robust filtering for kinematic geodetic positioning," *Journal of Geodesy*, vol. 75, no. 2-3, pp. 109–116, 2001.
- [11] A. H. Mohamed and K. P. Schwarz, "Adaptive Kalman filtering for INS/GPS," *Journal of Geodesy*, vol. 73, no. 4, pp. 193–203, 1999.
- [12] C. Sadhukhan, S. Mitra, M. Naskar, and M. Sharifpur, "Fault diagnosis of a nonlinear hybrid system using adaptive unscented Kalman filter bank," *Engineering with Computers*, vol. 2, pp. 1–12, 2021.
- [13] R. P. Tripathi, A. K. Singh, and P. Gangwar, "Innovation-based fractional order adaptive Kalman filter," *Journal of Electrical Engineering*, vol. 71, no. 1, pp. 60–64, 2020.
- [14] R. Mehra, "On the identification of variances and adaptive Kalman filtering," *IEEE Transactions on Automatic Control*, vol. 15, no. 2, pp. 175–184, 1970.
- [15] Y. X. Yang, X. Ren, and Y. Xu, "Main progress of adaptively robust filter with applications in navigation," *Journal of Navigation and Positioning*, vol. 1, no. 1, pp. 9–15, 2013.
- [16] C. Jiang and S. B. Zhang, "A novel adaptively-robust strategy based on the Mahalanobis distance for GPS/INS integrated navigation systems," *Sensors*, vol. 18, no. 3, p. 695, 2018.
- [17] E. Zerdali, R. Yildiz, R. Inan, R. Demir, and M. Barut, "Improved speed and load torque estimations with adaptive fading extended Kalman filter," *International Transactions on Electrical Energy Systems*, vol. 31, no. 10, p. 12684, 2021.
- [18] Y. R. Geng and J. Wang, "Adaptive estimation of multiple fading factors in Kalman filter for navigation applications," *GPS Solutions*, vol. 12, no. 4, pp. 273–279, 2008.
- [19] H. M. Qian, G. E. Lei, and P. Yu, "Multiple fading factors Kalman filter and its application in SINS initial alignment," *Journal of Chinese Inertial Technology*, vol. 20, pp. 287–291, 2012.
- [20] Y. R. Chen and J. P. Yuan, "An improved robust H_∞ multiple fading fault-tolerant filtering algorithm for INS/GPS integrated navigation," *Journal of Astronautics*, vol. 30, no. 3, pp. 930–936, 2009.
- [21] Y. X. Yang, *Adaptive Navigation and Kinematic Positioning (the Second Version)*, Surveying and Mapping Press, Beijing, China, 2017.
- [22] Q. J. Xia, Y. X. Sun, and C. H. Zhou, "An optimal adaptive algorithm for fading Kalman filter and its application," *Acta Automatica Sinica*, vol. 16, no. 3, pp. 210–216, 1990.
- [23] A. J. Izenman, *Modern Multivariate Statistical Techniques: Regression, Classification, and Manifold Learning*, Springer, Berlin, 2008.
- [24] Y. Wang, J. Liu, J. Wang, Q. Zeng, X. Shen, and Y. Zhang, "Micro aerial vehicle navigation with visual-inertial integration aided by structured light," *The Journal of Navigation*, vol. 73, no. 1, pp. 16–36, 2020.
- [25] K. W. Chiang, G. J. Tsai, H. W. Chang, C. Joly, and N. El-Sheimy, "Seamless navigation and mapping using an INS/GNSS/grid-based SLAM semi-tightly coupled integration scheme," *Information Fusion*, vol. 50, pp. 181–196, 2019.
- [26] S. Hasheminasab, T. Zhou, and A. Habib, "GNSS/INS-assisted structure from motion strategies for UAV-based imagery over mechanized agricultural fields," *Remote Sensing*, vol. 12, no. 3, p. 351, 2020.
- [27] I. Arasaratnam and S. Haykin, "Cubature Kalman filters," *IEEE Transactions on Automatic Control*, vol. 54, no. 6, pp. 1254–1269, 2009.
- [28] G. Reina, A. Leanza, and A. Messina, "Terrain estimation via vehicle vibration measurement and cubature Kalman filtering," *Journal of Vibration and Control*, vol. 26, no. 11-12, pp. 885–898, 2020.

Research Article

Automatic Calibration Method for Airborne LiDAR Systems Based on Approximate Corresponding Points Model

Yu Tian,¹ Yibo Zhao,² Shaogang Lei ,¹ Chuning Ji,¹ Lei Duan,² and Vladimír Sedlák³

¹School of Environment Science and Spatial Informatics, China University of Mining and Technology, Xuzhou 221116, China

²Engineering Research Center for Coal Mining Subsided Land and Goaf Treatment of Shandong, Jining 272100, China

³Institute of Geography, Faculty of Science, Pavol Jozef Šafárik University in Košice, Jesenná 5, 040 01 Košice, Slovakia

Correspondence should be addressed to Shaogang Lei; lsgang@126.com

Received 29 June 2021; Revised 25 November 2021; Accepted 13 December 2021; Published 25 January 2022

Academic Editor: Bin Gao

Copyright © 2022 Yu Tian et al. This is an open access article distributed under the Creative Commons Attribution License, which permits unrestricted use, distribution, and reproduction in any medium, provided the original work is properly cited.

The calibration of the light detection and ranging (LiDAR) system is critical to ensure the accuracy of point data. In this paper, the lever-arm measurement of airborne LiDAR system (ALS) was realized by photogrammetry. An automatic iterative boresight calibration method based on approximate corresponding points (CPs) matching was proposed to correct the boresight misalignment. It was based on iterative closest point (ICP) registration algorithm with a normal space sampling strategy, and approximate CPs were obtained by establishing filter rules. The experimental results showed that the absolute accuracy of the calibrated ALS reached 7.13 cm when the flight altitude was 100 m, meeting the accuracy requirements.

1. Introduction

ALS is widely used in topographic mapping, digital city, power line inspection, and other fields. A laser scanner, a global position system (GPS), and an inertial navigation system (INS) were integrated into ALS. It calculates the distance between the scanner and the target by the time interval from transmitting laser pulse to receiving echo signal. Then, the 3D spatial coordinates of the target are calculated by combining the position and attitude of the laser scanner observed by the GPS and the inertial measurement unit (IMU) [1]. As a multisensor integrated system, the accuracy of laser point cloud data acquired by ALS is affected by various factors such as GPS positioning error, IMU angle measurement error, system integration error, and laser ranging error [2]. Although the manufacturer calibrates ALS equipment before leaving the factory, the transportation, disassembly, and installation processes will inevitably impact the different components of the airborne LiDAR system. Bore-sight (angular misalignment between the mounting axes of the laser scanner and IMU) and lever-arm (physical offset from the

laser scanner to GNSS antenna) can occur in the system [3]. Bore-sight misalignment and lever-arm offsets are the primary error sources that bias the LiDAR point cloud positioning [4]. Their presence causes noncoincidence and misalignment between LiDAR point cloud strips, which seriously affects the overall accuracy and precision of the data [5, 6]. Given the above, high-precision geospatial applications of UAVs especially require calibration of the boresight misalignment and lever-arm offsets [7].

In the local coordinate system of IMU, the lever-arm offset is constant, usually measured by a straightedge or obtained from the design drawings. The boresight angles cannot be measured directly, so they should be calibrated by manual calibration (MC) or least-squares adjustment with the collected point cloud [8]. Manual calibration is performed by laying out suitable routes to obtain laser point clouds of characteristic features such as flat roads and gable-roofed buildings and then gradually computing the three error angles according to the empirical formula. The boresight angles are computed iteratively until the point clouds obtained from different strips

overlap well [9]. Due to the limited number of point clouds selected for each profile, this method is susceptible to factors such as flight quality and characteristic ground conditions. Therefore, MC is time-consuming and challenging to ensure calibration accuracy.

The least-squares adjustment-based calibration methods can be divided into data-driven methods and strict model-driven methods, depending on whether the boresight angles are directly represented by the geometric reference equation (8). The methods described in Mass (2000) [10] and Ayman et al. (2010) [11] are data-driven approaches that use only the position information of georeferenced LiDAR points to reduce the interstrip variance. This approach does not require raw data, such as GNSS/INS measurements, which are not always available to the user. However, these methods are considered less rigorous because arbitrary transformations cannot compensate for all the biases associated with point cloud georegistration. The rigorous model-driven approach expresses the apparent axis angle explicitly in the georeferenced equations. The boresight angles are estimated by constraining the set of feature points (such as connection points/control points and plane points) obtained from multiple overlapped strips or other reference data to fit the corresponding geometric model and minimizing the weighted sum of squares of residuals [12]. To quantify the discrepancies between strips, conjugate tie points, planar patches, and/or modelled surfaces is typically matched in overlapping point clouds from the strips. These differences are then used to determine unaligned criteria that are typically defined as distances [13]. Compared with the image data obtained from aerial photogrammetry, ALS point cloud data do not have real CPs due to the irregularity and dispersion of spatial distribution, making it challenging to adjust directly by the “connection point” constraint [9]. The parity model based on conjugate plane matching is the most used in boresight correction. Filin and Sagi (2003) [14] first recovered the boresight in an ALS system using natural and artificial surfaces. They used the least-squares adjustment (LAS) to estimate the boresight angles from surfaces with known parameters in different directions. Sklode and Lichti (2007) [4] improved the boresight calibration based on plane features by estimating the plane parameters and the boresight angles simultaneously instead of using fixed, known plane parameters. The improved method significantly enhanced the calibration performance. Identifying and selecting conjugate surfaces require rigorous preprocessing steps (e.g., region growing, principal component analysis, or RANSAC) and suitable sites, such as urban environments [15]. Point-to-patch matching methods [16, 17] advantageously present direct and automated communication. Once the correspondence is established, the boresight angles are represented as a parameter of the optimized target. LSA was then performed to estimate the correction parameters. Glira et al. (2016) [17] proposed a LiDAR strip adjustment method. Their method was able to correct for deviations in the LiDAR-GNSS/INS calibration parameters and other system errors such as laser ranging deviations or scale factors and biases in GNSS/INS observations. Their approach minimized the discrepancy between robustly selected point-to-plane correspondences from overlapping LiDAR strips by LSA. Recently, Keyetieu and Seube

(2019) [18] discussed the optimal selection of strip-adjusted LiDAR observations. The authors relied on model measurement uncertainty of georeferenced LiDAR points to achieve the smallest LSA problem size.

Generally speaking, the current calibration method using line/plane features has specific requirements for the normal direction and distribution of line/plane features. In order to achieve higher calibration accuracy, the plane should be perpendicular to three coordinate axes as much as possible, and the distribution of corresponding features should be uniform as much as possible [19]. These conditions are only applicable to areas with rich geometric features in urban areas. It is tough to automatically extract precise lines and planes in complex environments, limiting these algorithms’ applicability.

Compared with the extraction and matching of line/plane features, point features are more readily available in natural scenes and easier to realize automation. The adjustment method based on point features has potential advantages. It will help improve the practicality and automation of the calibration method if the CPs can be utilized for correction parameters calculation. However, due to the nature of LiDAR data, automatic identification of CPs is unreliable, restricting the development of a strict adjustment model with CPs. The ICP algorithm [20, 21] provides a way to accurately align the source point cloud and target point cloud due to the small boresight angles in ALS.

In view of the above, a strict adjustment model for boresight based on ICP and approximate CPs was presented to solve the challenge of automatic selection and matching CPs between LiDAR strips. The proposed method eliminates the dependence on pre-laid calibration markers or targets. It can operate automatically even in natural scenes without important geometric features, such as planes in multiple directions. Further, benefitting from the rigorous screening process for CPs, the proposal method can effectively reduce the probability of incorrect convergence.

2. Materials and Methods

2.1. Data Acquisition. We carried out three flight experiments at the China University of Mining and Technology (Figure 1). In the three experiments, the flight heights were 150 m, 100 m, and 80 m, respectively, and the flight speeds were 8 m/s, 6 m/s, and 6 m/s, respectively. Two of the four flight belts were parallel, and the other two were perpendicular to them. Ten ground control points were set up in the two experimental areas before the flight, and a GPS receiver was used to measure them. GNSS/IMU data was processed by PosPac (v8.5) software to obtain attitude and position of the aircraft and time matched with the ranging data of the laser scanner. After rotation and translation, the final multistrip initial LiDAR point cloud was obtained.

2.2. Sensor Payload. All sensors were integrated into a mature industrial-grade UAV, a WIND 4 (DJI Technology Co., Ltd., Shenzhen, China). The integrated sensors include a RoboSense RS-LiDAR-32, a coupled GNSS/IMU sensor with a multifrequency, multiconstellation GNSS receiver (Applanix APX-15), and an onboard computer. We fixed the GNSS/IMU sensor

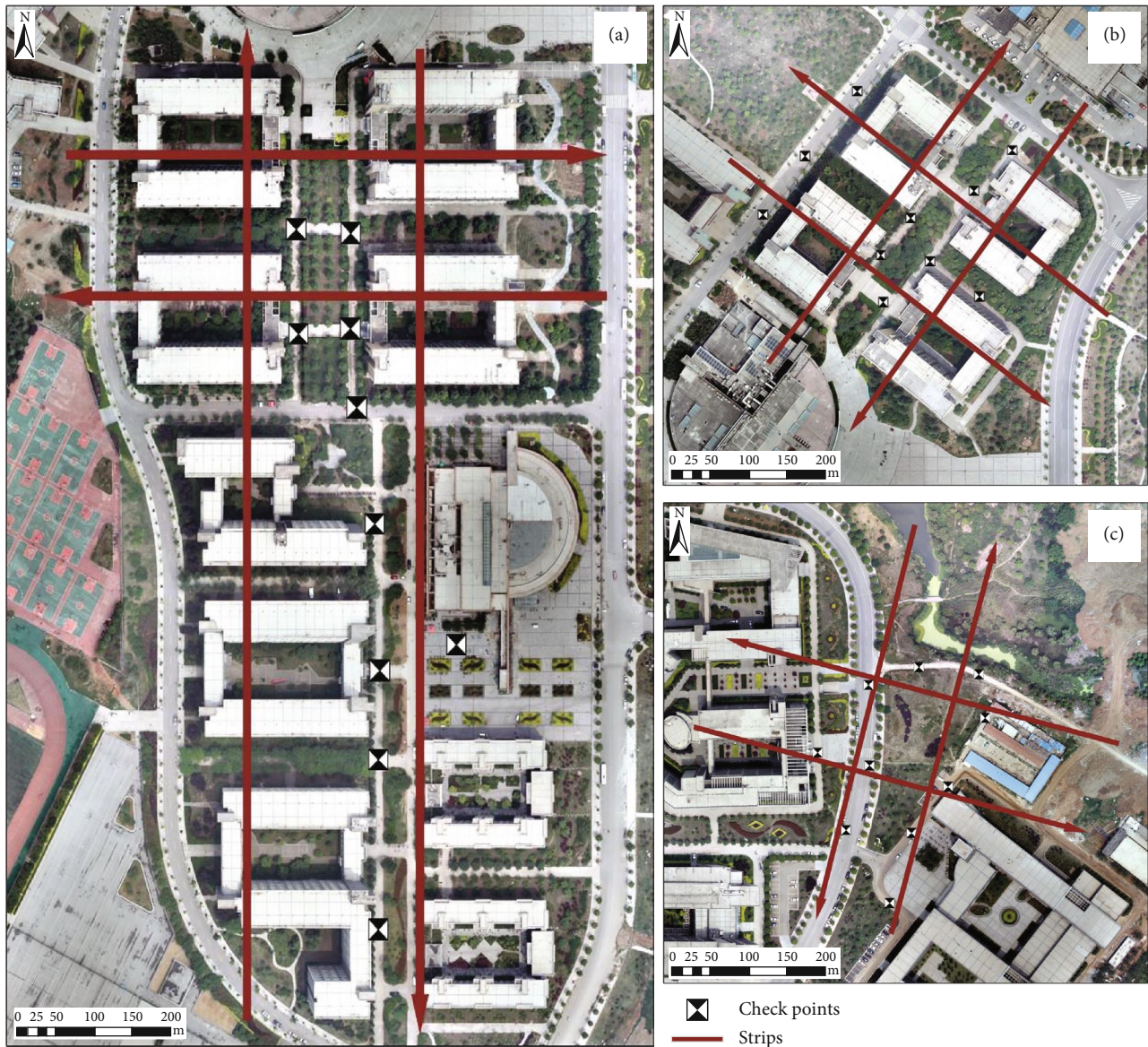


FIGURE 1: Experimental data acquisition scenarios: (a) experiment 1; (b) experiment 2; (b) experiment 3.

and the on-board computer in a protective shield and attached the laser scanner to the protection by screws. The antenna was fixed on the side of the UAV and was 10 cm above the propeller to ensure the uninterrupted reception of satellite signals (Figure 2). Our installation ensured that the three axes of the UAV coordinate system, the IMU coordinate system, and the laser scanner coordinate system were nearly parallel, reducing the difficulty and error of postprocessing.

2.3. Antenna to Laser Scanner Lever-Arm Offsets. Measuring the lever-arm offsets from GNSS antenna to laser scanner is a necessary step for ALS self-calibration. Kersting et al. (2012) [16] claimed that the vertical lever-arm component could not be estimated by looking at the strip-to-strip correspondence alone since errors in the vertical lever-arm parameters have the same effect regardless of the flight direction or flight altitude. The vertical lever-arm offset can only

be computed when at least one vertical ground control point (GCP) is employed. This limitation was again emphasized by Ravi et al. (2018) [22]. An accurate measurement of the offset vector from the GNSS antenna to the laser scanner center is required to eliminate lever-arm errors. However, it is not easy to ensure the exact alignment of the measurement direction with the coordinate system using manual measurements. Therefore, we took 293 highly overlapping photos of the UAV from different angles and heights using a cell phone. The ALS was finely modelled with the help of the structure-from-motion (SfM) method. It can be rotated randomly in space to correct misalignment to achieve accurate measurements of the lever-arm offsets [3]. Due to the smooth and reflective nature of the UAV and sensor housing, the texture was not sufficiently clear at specific angles. To ensure 3D reconstruction accuracy, we set up a total of 23 high-contrast marker points on the UAV and ground.

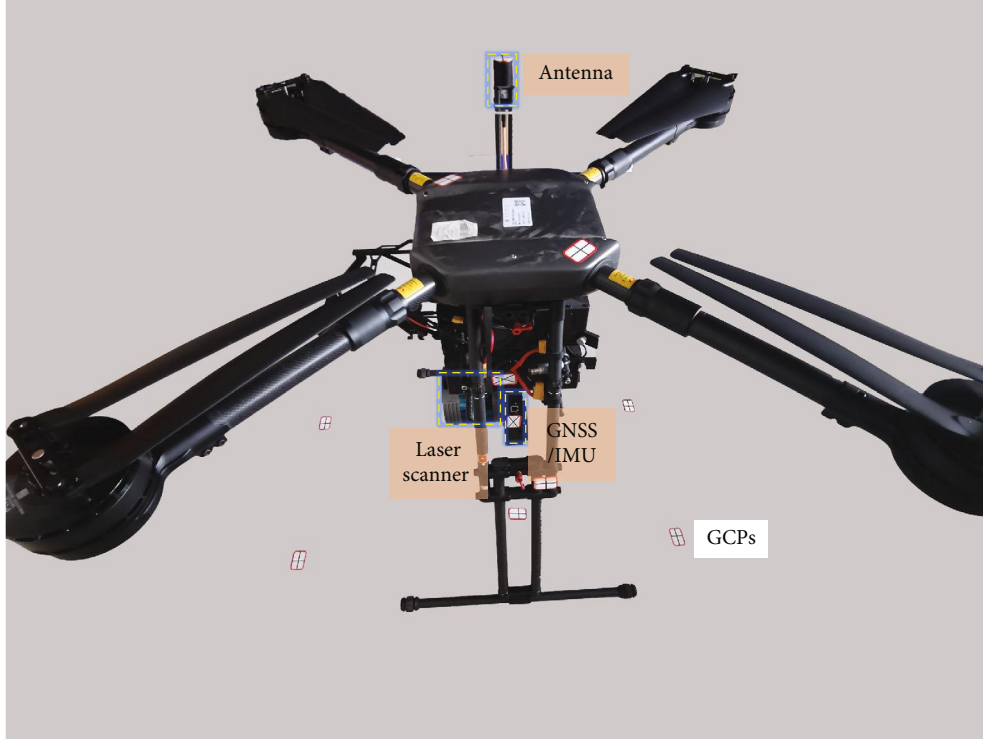


FIGURE 2: Airborne LiDAR systems.

Ten of them were measured with steel ruler at different heights as control points to assist aerial triangulation. The overlapping images were then processed using Agisoft's Photoscan (v1.2.6) (<http://www.agisoft.com/>) to obtain a dense ALS 3D point cloud (Figure 3). High-quality and gentle filtering patterns were set to create dense point clouds. The dense point cloud was scaled with the measured GCPs to produce an absolute size ALS model. This scaled point cloud was then imported into Cloudcompare (v2.11.3) (<http://www.cloudcompare.org/>) to measure the lever-arm offsets.

2.4. Boresight Self-Calibration. We proposed a strict boresight calibration method based on approximate CPs matching. This method consists of two parts: approximate CPs matching and estimation of boresight angles using LSA. Taking the point clouds scanned by two strips as an example, the calculation process of boresight angles is shown in Figure 4.

2.4.1. General Formulation. The calibration of the ALS parameters is based on the laser point positioning equation. First, the target coordinates in the laser scanner coordinate system are converted into IMU coordinate system by using the lever-arm offsets and boresight angles between the laser scanner and GNSS/IMU. Then, the IMU coordinate system coordinates are converted to a local horizontal coordinate system using the traverse roll, pitch, and heading angle provided by GNSS/IMU. Finally, the local coordinates are converted to WGS84-ECEF using the latitude, longitude, and ellipsoidal altitude supplied by GNSS/IMU. The georeferenced equation describing the conversion of the scan point

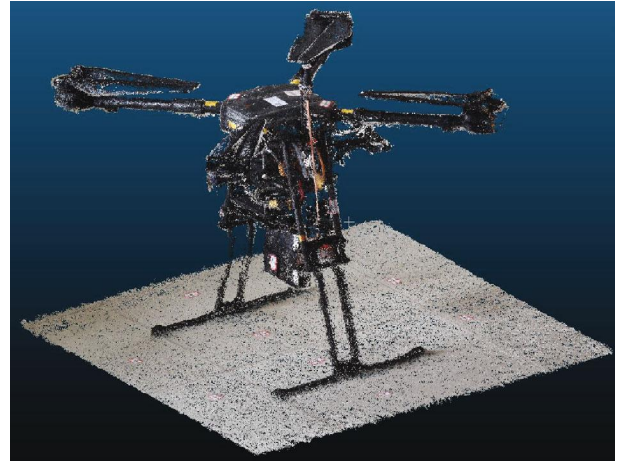


FIGURE 3: Scaled point cloud of ALS.

from the laser scan frame to the WGS84 ECEF frame is given.

$$X_W = R_n^w(B, L)R_i^n(r, p, h)(R_i^i(\alpha, \beta, \gamma)x_i + P) + g_w(B, L, H), \quad (1)$$

where X_W is the positioning vector of the point in the WGS84 ECEF frame; x_i is the positioning vector of the point in the laser scanner frame; R_i^i is the rotation matrix from the laser scanner frame to the IMU frame; P is the position of the laser scanner in the IMU frame; α, β, γ are the boresight angles

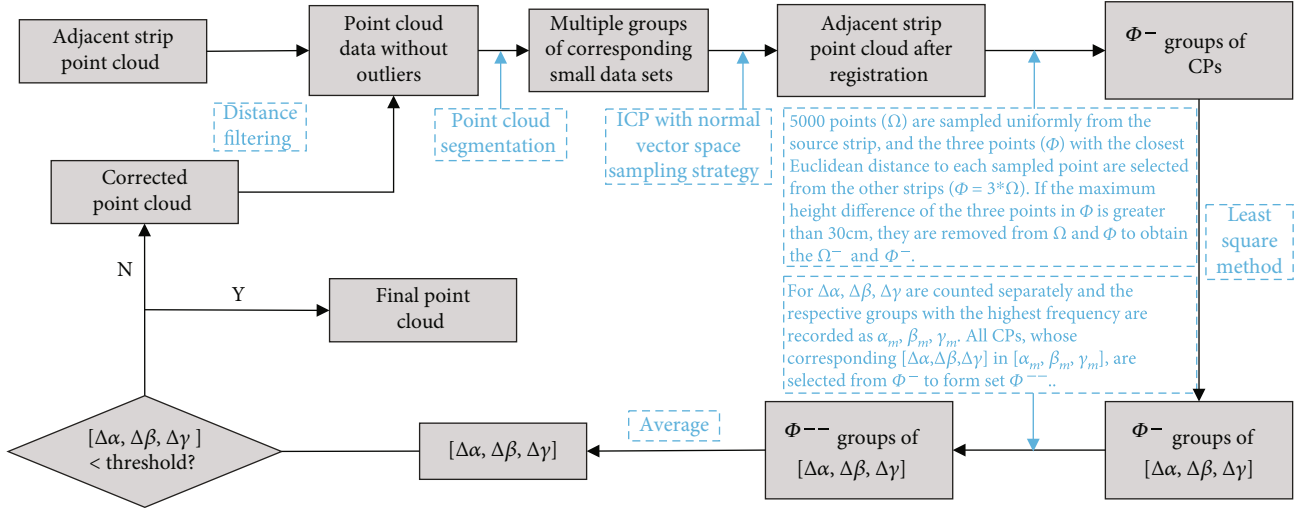


FIGURE 4: Algorithm flowchart.

between the laser scanner and the GNSS/MU system; P is the lever-arm offsets vector between the laser scanner and the GNSS/IMU system; R_i^n is the rotation matrix between the IMU frame and the navigation coordinate system; R_n^w is the rotation matrix between the navigation coordinate system and the WGS84 ECEF frame; $g_w(B, L, H)$ is the position of the UAV in the WGS84 ECEF frame; B, L, H are the latitude, longitude, and ellipsoidal height provided by the GNSS/IMU; r, p, h are the roll, pitch, and heading provided by the GNSS/IMU.

The lever-arm offsets can be measured directly from the scaled model with sufficient accuracy so that the error caused by the lever arm offset error is negligible. Under good GNSS conditions, the positioning error and IMU attitude error have little effect on the positioning accuracy, while the boresight angles mainly determine the total error of the point cloud. $\Delta\alpha, \Delta\beta,$ and $\Delta\gamma$ are the boresight angles in the roll, pitch, and heading directions, respectively. Since the boresight angles are small, generally in the range of -3° to 3° , the geolocation equation can be described as follows.

$$X_w = R_n^w(B, L)R_i^n(r, p, h)(\Delta R_i^i(\Delta\alpha, \Delta\beta, \Delta\gamma)R_i^i(\alpha, \beta, \gamma)x_i + P) + g_w(B, L, H), \quad (2)$$

where

$$R_i^i(\alpha, \beta, \gamma) = \begin{bmatrix} \cos \gamma & -\sin \gamma & 0 \\ \sin \gamma & \cos \gamma & 0 \\ 0 & 0 & 1 \end{bmatrix} \begin{bmatrix} \cos \beta & 0 & \sin \beta \\ 0 & 1 & 0 \\ -\sin \beta & 0 & \cos \beta \end{bmatrix} \begin{bmatrix} 1 & 0 & 0 \\ 0 & \cos \alpha & -\sin \alpha \\ 0 & \sin \alpha & \cos \alpha \end{bmatrix}, \quad (3)$$

$$\Delta R_i^i(\Delta\alpha, \Delta\beta, \Delta\gamma) = \begin{bmatrix} 1 & -\Delta\gamma & \Delta\beta \\ \Delta\gamma & 1 & -\Delta\alpha \\ -\Delta\beta & \Delta\alpha & 1 \end{bmatrix}. \quad (4)$$

If the point X_w^m is scanned from the m -th strip and its corresponding point in the n -th strip is X_w^n , the deviation

between the points X_w^m and X_w^n can be calculated by the error equation (5).

$$V_w^{mn} = X_w^m - X_w^n. \quad (5)$$

Suppose N corresponding points are found from different scan directions or different strips. In that case, the boresight correction parameters can be derived by minimizing the total deviation of the N corresponding points as follows.

$$\text{sum} = \sum_{i=1}^N V_i^T V_i. \quad (6)$$

2.4.2. Approximate CP Strategy. Unlike grayscale images, there are no true CPs in the point clouds of different strips due to the randomness and discreteness of LiDAR points. This property of LiDAR points is the most critical reason limiting strip adjustment models based on CPs matching. Of course, some scholars have proposed the intersection of the feature line with the surface as the feature point at this stage. However, such methods require filtering and fitting the points, which is challenging to implement in complex LiDAR points.

ICP algorithm is the mainstream algorithm in the fine alignment stage of point clouds. For two sets of point clouds with good initial positions, the ICP algorithm can achieve the ideal alignment effect. Since the boresight angles of ALS is generally minor, the different strip point clouds collected in a short time can be obtained by rigid transformation when the UAV flight altitude is low. Therefore, in this paper, the following matching strategies for different strip approximation CPs are proposed based on the ICP algorithm.

- (1) Removal of points in the point cloud that are too far from the overall point cloud using distance filtering, which is a prerequisite for fine alignment using ICP

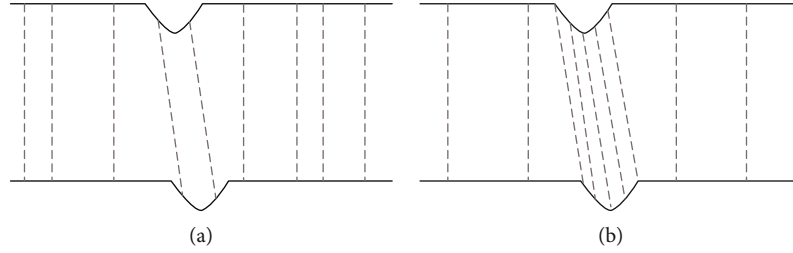


FIGURE 5: Corresponding point pairs selected by the (a) “random sampling” and (b) “normal-space sampling” strategies for an incised mesh.

- (2) The point cloud on each strip is split into small pieces using timestamps at 5 s intervals. The time interval is chosen according to the flight speed and should not be too large so that the large-scale point clouds can be better processed and the corresponding point clouds can be better aligned accurately by ICP
- (3) After partitioning the point cloud of each strip into small sections, the 3D bounding boxes of all sections are calculated. Then, they are used to detect the overlapping regions to construct the overlapping relationship between the parts of the point cloud. The alignment is performed between the sections that overlap each other
- (4) A large amount of data in a dense point cloud makes effective alignment of overlapping regions difficult. The normal vector is an essential geometric feature of the surface, and the angle of the normal vector can be used to determine the surface change at that place. To improve the matching efficiency, we adopt the normal vector space sampling strategy [23] in the ICP variant algorithm for point cloud refinement (Figure 5) and then use the ICP algorithm to align the overlapping sections
- (5) After alignment, 5000 points (Ω) are sampled uniformly from the source strip, and the three points (Φ) with the closest Euclidean distance to each sampled point are selected from the other strips ($\Phi = 3 * \Omega$)
- (6) If the maximum height difference of the three points in Φ is greater than 30 cm, they are removed from Ω and Φ to obtain the Ω^- and Φ^-

Two north-south flight strips in each experiment were taken as an example. First, the initial point cloud of each strip was filtered by distance to eliminate the outliers. Then, the point cloud was divided into small pieces to calculate the overlapping area of the strip point cloud (Figure 6). The normal vector space of the point cloud was computed, and the streamlined point cloud was obtained by uniform sampling in the normal vector space. The ICP alignment was performed on the streamlined point cloud to get the aligned point clouds of the two strips. Five thousand points were randomly selected from the overlapping area of the source point cloud (Figures 5 (a), 5(c), and 5(e)). The sampling points selected in experiments 1-3 were filtered according to the strategy proposed in

Section 2.4.2 to obtain Ω_1^- , Ω_2^- , and Ω_3^- , where $\Omega_1^- = 2345$, $\Omega_2^- = 3294$, and $\Omega_3^- = 3622$ (Figures 5(b), 5(d), and 5(e)). The three points closest to each point in Ω were extracted from the target strip to form Φ . Therefore, Φ_1^- , Φ_2^- , and Φ_3^- in experiments 1-3 are 7035, 9882, and 10866, respectively.

It is worth noting that the convergence of ICP alignment is crucial to obtain reliable alignment results. We adopted three steps to improve the accuracy of ICP alignment: first, after removing the outliers, the point cloud was divided into small blocks to ensure the consistency between the source point cloud and the target point cloud through a rigid transformation; second, the feature points were selected by uniform sampling in normal vector space. This sampling strategy can preserve the local features of the point cloud surface while extracting the thin point cloud, which is more favorable for accurate matching; third, all boresight angles were prealigned. The prealignment makes the initial value of the placement angle error close to zero, allowing the algorithm to converge efficiently.

In addition, several parameters in the approximate CPs filtering process need to be set reasonably according to the actual scenario. For example, we sampled 5000 points uniformly from the source point cloud, and each point took the three points with the closest Euclidean distance in the target point cloud to constitute a set of approximate CPs. To get more CPs, the readers can increase “5000” or “3” appropriately. However, we recommend selecting at least three nearest points because the positioning accuracy of the points is greatly affected by the random error generated by the scanning angle and measuring distance of the laser scanner. The selection of only one nearest neighbor point will introduce many mistakes to the settlement of the boresight error. As for the elevation difference threshold, it needs to be adjusted according to the point cloud density. We suggest that when the point cloud density is lower than $150/m^2$, the elevation difference threshold should be increased appropriately.

2.4.3. Boresight Angle Correction Parameter Estimation. Because of the boresight error, the CPs in the overlapping strips are not coincident. Therefore, the calibration procedure uses the CPs position consistency as a constraint to recover the Boresight angles correction parameters. When the systematic error is eliminated, all point clouds are restored to their true positions.

Assuming that the CPs of the two strips are X_w^1 and X_w^2 , respectively, the observation equation can be expressed as

$$X_w^1 = X_w^2 + \Delta. \quad (7)$$

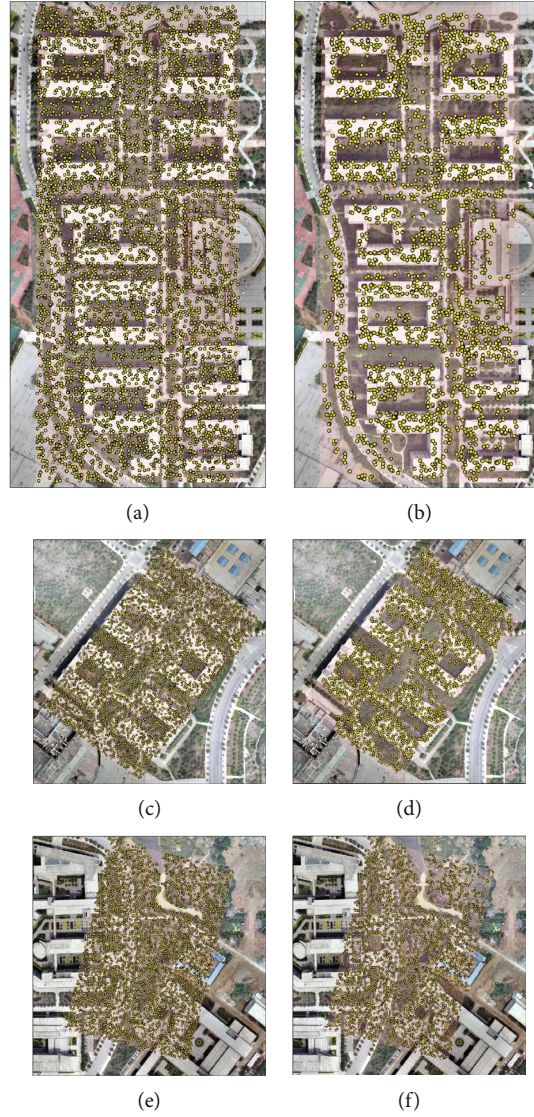


FIGURE 6: Distribution of sampling points in the source point cloud. (a) and (c) are the sampling points before the first filtering of experiments 1 and 2, respectively; (b) and (d) are the sampling points after the first filtering of experiments 1 and 2, respectively. The red areas are the strip overlap areas, and the yellow points are the sampling points of the source point cloud.

TABLE 1: The lever-arm offset measured from a scaled point cloud of the ALS.

Lever-arm	Offset (cm)
GNSS antenna to IMU	[3.36, 10.34, -51.44]
IMU to laser scanner	[7.58, -3.8, -0.5]

According to equation (2), the laser point coordinates are expressed as a function of the system parameters to be solved. After linearizing the equation, the error equation (8) can be listed by setting the coordinate residuals as V and solved according to the least-squares principle.

$$V = BX + L, \quad (8)$$

where B is the coefficient matrix of the unknown, $B =$

$$\begin{bmatrix} \partial X/\partial \Delta\alpha & \partial X/\partial \Delta\beta & \partial X/\partial \Delta\gamma \\ \partial Y/\partial \Delta\alpha & \partial Y/\partial \Delta\beta & \partial Y/\partial \Delta\gamma \\ \partial Z/\partial \Delta\alpha & \partial Z/\partial \Delta\beta & \partial Z/\partial \Delta\gamma \end{bmatrix}; X \text{ is the matrix of bore-sight angles, } X = [\Delta\alpha, \Delta\beta, \Delta\gamma]^T; L \text{ is a constant matrix, } L = (R_n^w R_i^n P)^1 + g_w^1 - (R_n^w R_i^n P)^2 + g_w^2.$$

When the value of the expression $V^T P V$ is the most minor, the correction parameters of the boresight angles can be obtained according to equation (9).

$$X = -(B^T P B)^{-1} B^T P L. \quad (9)$$

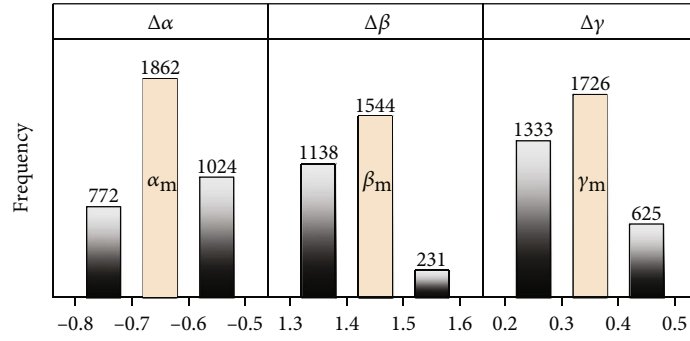


FIGURE 7: Frequency statistics of boresight angles calculated from the approximate CPs after the first filtering.

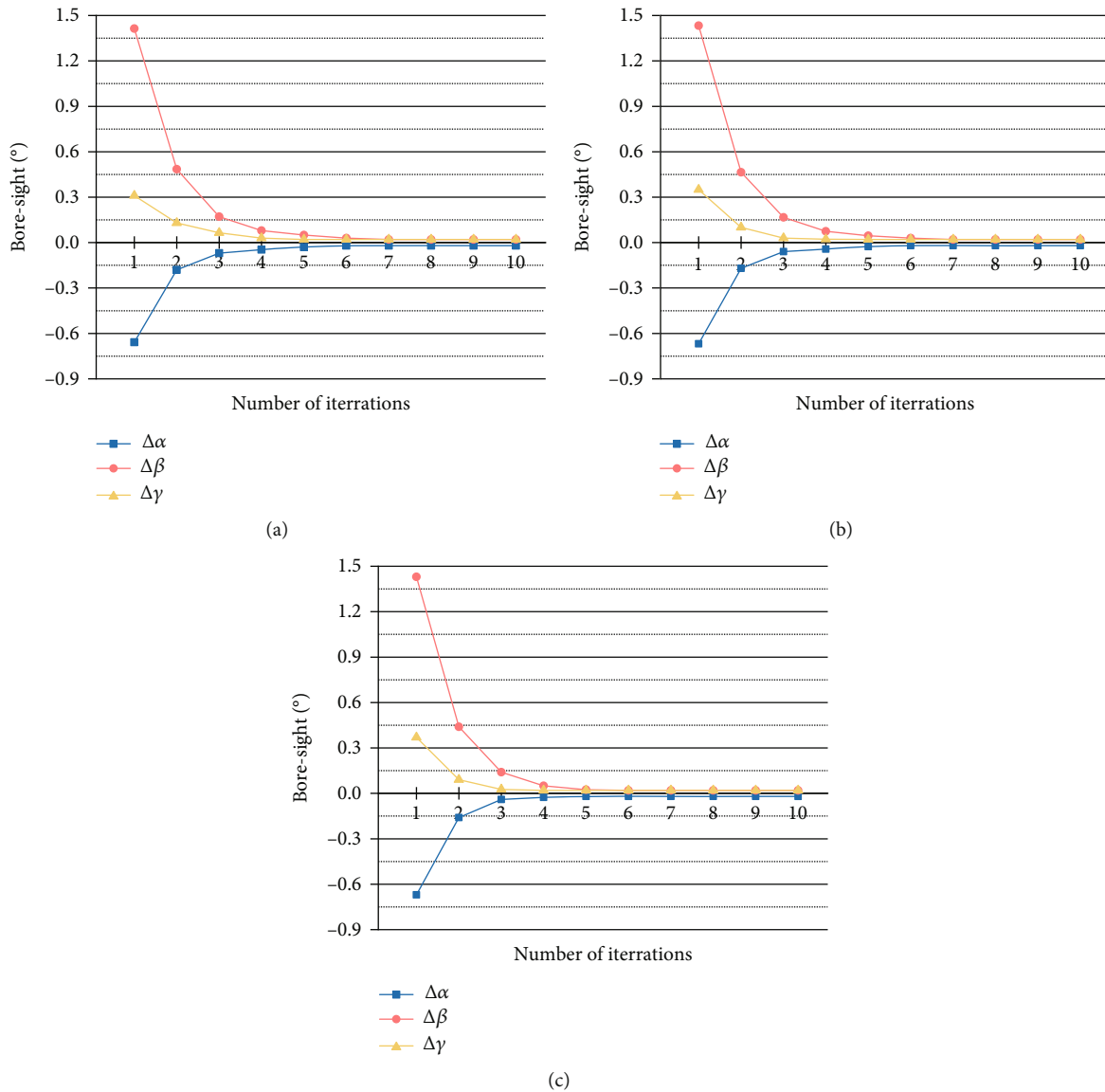


FIGURE 8: Variation of the boresight angles with the number of iterations. (a) Experiment 1; (b) experiment 2; (b) experiment 3.

In order to solve the boresight angles correction parameter, it is only necessary to determine the corresponding laser points on different strips to estimate the system param-

eters according to the least-squares principle. The number of unknowns to be solved in Eq. (9) is three, and three equations can be listed for each pair of CPs, so at least one pair

TABLE 2: Result of boresight calibration (°).

	Experiment 1			Experiment 2			Experiment 3		
	$\Delta\alpha$	$\Delta\beta$	$\Delta\gamma$	$\Delta\alpha$	$\Delta\beta$	$\Delta\gamma$	$\Delta\alpha$	$\Delta\beta$	$\Delta\gamma$
Our method	[-1.001, 2.224, 0.533]			[-0.997, 2.234, 0.521]			[-1.003, 2.238, 0.528]		
VTPM	[-0.999, 2.231, 0.534]			[-0.998, 2.236, 0.514]			[-1.001, 2.232, 0.531]		
MC	[-1.003, 2.217, 0.543]			[-1.009, 2.248, 0.509]			[-1.003, 2.235, 0.518]		

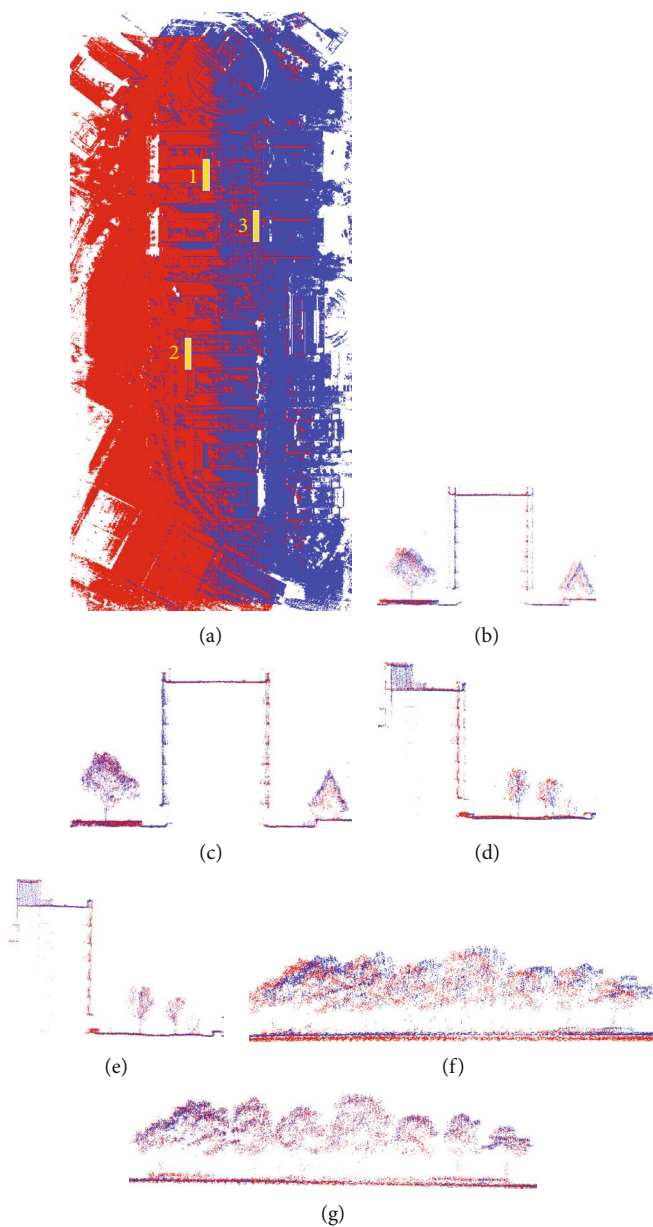


FIGURE 9: Multiple point clouds before and after boresight calibration in experiment 1. (a) Original point cloud; ((b), (d), and (f)) point clouds of cross-section 1, cross-section 2, and cross-section 3 before boresight calibration; ((c), (e), and (g)) point cloud of cross-section 1, cross-section 2, and cross-section 3 after boresight calibration. Points derived from different strips have different colors.

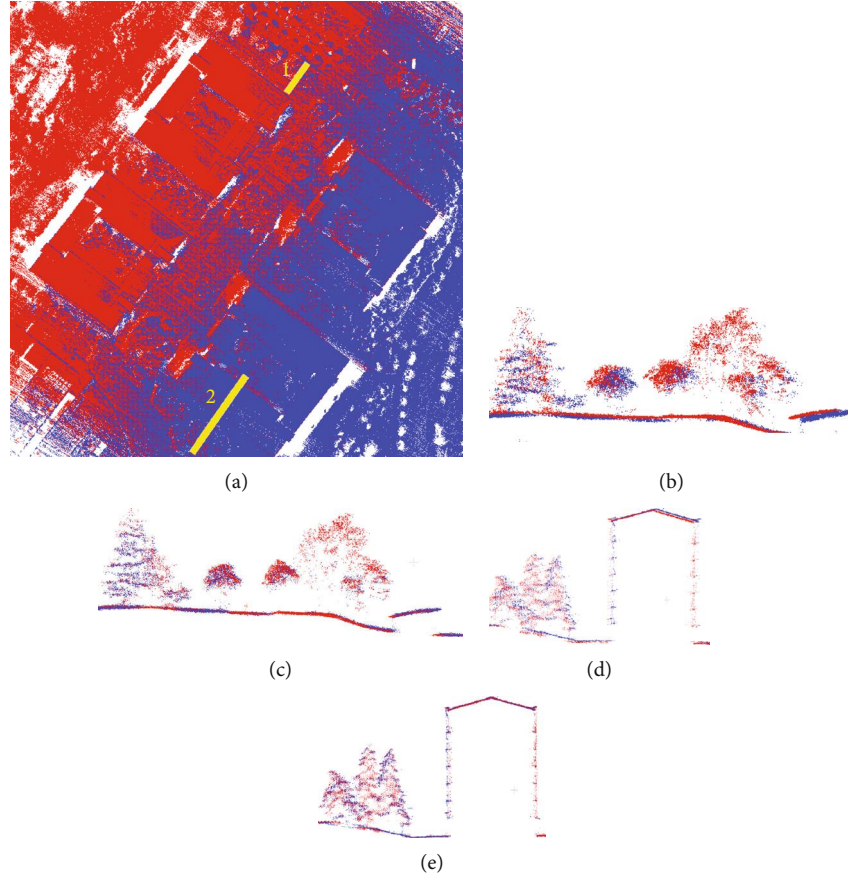


FIGURE 10: Multiple point clouds before and after boresight calibration in experiment 2. (a) Original point cloud; ((b) and (d)) point clouds of cross-section 1 and cross-section 2 before boresight calibration; ((c) and (e)) point cloud of cross-section 1 and cross-section 2 after boresight calibration. Points derived from different strips have different colors.

of CPs is needed for the solution. Multiple sets of boresight angle correction parameters can be derived by applying the above LSA model using the approximate CPs filtered by Section 2.4.2. However, because some points are located at the edge of the scanned area, vegetation area, or are too much affected by random errors, the accuracy of the obtained correction parameters is not enough or even completely wrong.

Therefore, we counted the frequency of the calculated $\Delta\alpha$, $\Delta\beta$, and $\Delta\gamma$ according to the gradient of 0.1° , respectively, and recorded the most frequent group of each as α_m , β_m , and γ_m . All CPs, whose corresponding $[\Delta\alpha, \Delta\beta, \Delta\gamma]$ in $[\alpha_m, \beta_m, \gamma_m]$, were selected from Φ^- to form set Φ^{--} . The boresight angles in Φ^{--} were averaged to obtain the final correction parameters. The calibration parameter solution is not performed only once but repeated iteratively until the resulting boresight error is below the set accuracy threshold.

2.5. ALS Alignment Evaluation. We laid some checkpoints on the ground in the experimental area. Taking each checkpoint as the center, the corrected point cloud in the sphere with a radius of 20 cm was intercepted. The point cloud intercepted at each checkpoint is plane-fitted, and D_i is defined as the orthogonal distance from the i -th checkpoint to the corresponding fit plane. If the ALS error correction accuracy is high enough, then D_i should be close to zero. Two metrics D_L and σ_L are introduced to evaluate the ALS

error correction accuracy [24]. D_L is defined as the average of all D_i calculated for each checkpoint. σ_L is the average of all σ_j , where σ_j is the standard deviation of the distribution of the set of points around the plane fitted to the point cloud intercepted by each checkpoint. D_L evaluates the absolute accuracy of the alignment, but σ_L evaluates its relative accuracy.

3. Results and Discussion

3.1. Lever-Arm Correction. The lever-arm offsets between sensors were measured in a scaled LAS point cloud, as shown in Table 1. The accuracy of the lever-arm offsets estimation depends on the accuracy of the GCPs measurement, the inherent error of the SfM modelling, and the estimation accuracy of the sensor reference points within the point cloud. The GCPs were measured with a rigid ruler and a lead hammer. The uncertainty of the rigid ruler measurement was within ± 0.1 cm, while the accuracy of the lead hammer measurement was somewhat worse, around ± 0.2 cm. Therefore, the maximum uncertainty of the GCP measurement was considered to be ± 0.3 cm. The uncertainty of GPCs combined with the uncertainty in the intrinsic modelling of the SfM was translated into uncertainty in the 3D model. Since the images were taken at a very short distance of less than 1.5 m, the SfM inherent uncertainty was considered

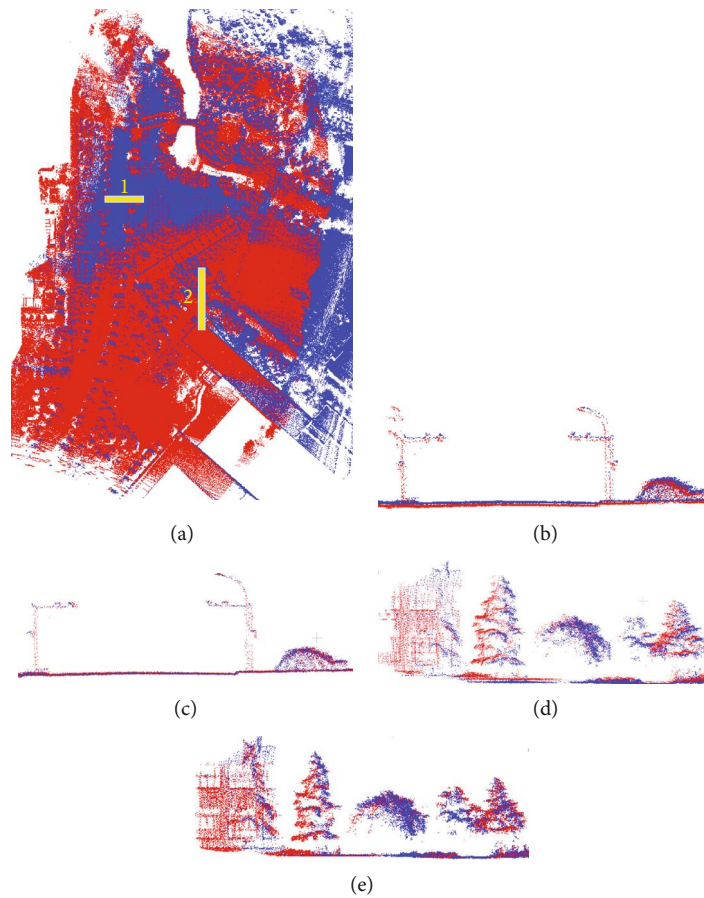


FIGURE 11: Multiple point clouds before and after boresight calibration in experiment 3. (a) Original point cloud; ((b) and (d)) point clouds of cross-section 1 and cross-section 2 before boresight calibration; ((c) and (e)) point cloud of cross-section 1 and cross-section 2 after boresight calibration. Points derived from different strips have different colors.

within the measurement accuracy of the GCPs. Thus, the uncertainty in the ALS 3D model was considered to be within ± 0.5 cm. When the uncertainty of the selected points on the ALS model point cloud was added, the final calculated total uncertainty associated with the lever-arm offsets estimate was ± 0.6 cm. Manual measurement is difficult to ensure that the measurement direction of the straightedge is in the same direction as the axis of the IMU coordinate system, so the SfM-based lever arm measurement method is more accurate than the manual measurement method.

3.2. Boresight Angle Correction Parameter Estimation. The least-squares adjustment model was applied to the first filtering results of experiment 1-3 to obtain 7035, 9882, and 10866 boresight angle correction parameter matrices, respectively. Taking experiment 2 as an example, $\Delta\alpha$, $\Delta\beta$, and $\Delta\gamma$ were counted as frequencies according to a gradient of 0.1° (Figure 7). The sampling points corresponding to $[\Delta\alpha, \Delta\beta, \Delta\gamma]$ in $[\alpha_m, \beta_m, \gamma_m]$ were picked in Φ_2^- to get Φ_2^- ($= 1326$). Similarly, we got $\Phi_1^- = 987$ and $\Phi_3^- = 1541$. The boresight angle correction parameters for the first iteration of experiments 1-3 were derived by averaging $\Delta\alpha$, $\Delta\beta$, and $\Delta\gamma$ obtained from the approximately CPs in Φ_1^- , Φ_2^- , and Φ_3^- , respectively.

The above process was iterated until the boresight angles obtained are less than the set threshold value (Figure 8). All

three groups of experiments reached a steady state after 6-7 iterations. The convergence speed of experiment 3 was the fastest among the three groups. This is due to the fact that experiment 3 has more approximate CPs involved in the calculation. It is also related to the low flight altitude and small deformation between strip point clouds in experiment 3. The final cumulative boresight angle errors were shown in Table 2.

We corrected the point cloud using the final boresight angles (Figures 9–11). The points scanned from different strips had different colors, and there were obvious deviations between the original point clouds of different strips before calibration. To more intuitively and qualitatively evaluate the correction effect, seven point cloud profiles before and after boresight calibration were visualized (Figures 9–11). As seen from the figure, the point clouds of different strips after calibration by our method had achieved complete overlap, and the accuracy of the point clouds had been greatly improved.

Finally, we quantified and evaluated the corrected point clouds using the ground checkpoints arranged in advance and conducted comparison tests with the virtual tie point model-based method (VTPM) proposed by Jing et al. (2013) [25] and the MC. The results were listed in Tables 2 and 3. Table 2 showed that the final boresight angles of three experiments calculated by the three methods were close. Table 3 showed that the point cloud corrected by the two

TABLE 3: Performance comparison of three methods.

	Experiment 1		Experiment 2		Experiment 3	
	Accuracy (cm)	Running time (s)	Accuracy (cm)	Running time (s)	Accuracy (cm)	Running time (s)
Our method	D_L :9.32 σ_L :10.41	175	D_L :7.13 σ_L :6.83	268	D_L :5.94 σ_L :5.31	291
VTPM	D_L :9.27 σ_L :10.38	942	D_L :7.26 σ_L :6.88	423	D_L :6.01 σ_L :5.54	463
MC	D_L :10.14 σ_L :11.72	/	D_L :7.34 σ_L :6.92	/	D_L :6.13 σ_L :5.77	/

automatic methods was more accurate than MC. Considering the random errors of the laser rangefinder range, GPS positioning, and attitude, we therefore believed that the boresight angle calculation results met the expectation of error correction. Among the three sets of experiments, the worst point cloud accuracy in experiment 1 was mainly due to the high flight altitude. The higher flight amplified the attitude and ranging random errors, resulting in a more discrete point cloud. It was also illustrated by the fact that σ_L is larger than D_L . In experiment 1, the point cloud accuracy obtained by the VTPM method was better than our method. This was due to the fact that a large percentage of the 5000 sampling points uniformly generated by our method in experiment 1 were located in the plant areas and the edge areas of buildings. Few CPs remained after sampling point filtering (<1000). For this scene, the number of sampling points can be increased appropriately to improve the accuracy of our method. In experiments 2 and 3, the accuracy of our proposed method was much less time consuming and better than that of VTPM, mainly because our CP filtering process removed most of the pseudocorresponding points that were incorrectly matched due to random errors, speeding up the iterative process and avoiding incorrect convergence.

4. Conclusions

The calibration of ALS is a critical step before performing data postprocessing and directly affects the quality of the point cloud. We used a cell phone to measure the lever-arm. In addition, we proposed an automated, fast iterative boresight correction algorithm based on approximate corresponding point matching. It overcomes the difficulty of accurately extracting corresponding points from LiDAR point cloud. It enables the potential point matching adjustment model to be successfully applied to the boresight angles correction. Our research results showed that the accuracy of the proposed algorithm was ideal, and we believed it could be better promoted in the future.

Data Availability

The data used to support the findings of this study are included within the article.

Conflicts of Interest

The authors declare no conflict of interest.

Acknowledgments

The research was supported by the projects funded by National Key R&D Program of China, grant number 2017YFE0119600; the Fundamental Research Funds for the Central Universities, grant number 2019BSCX26; and the Slovak Research and Development Agency, grant number APVV-SK-CN-RD-18-0015.

References

- [1] E. P. Baltsavias, "Airborne laser scanning: basic relations and formulas," *ISPRS Journal of Photogrammetry and Remote Sensing*, vol. 54, no. 2–3, pp. 199–214, 1999.
- [2] X. Zhang, *Airborne Technology Theory and Methods*, Wuhan University Press, 2007.
- [3] D. Gautam, A. Lucieer, C. Watson, and C. Mccoull, "Lever-arm and boresight correction, and field of view determination of a spectroradiometer mounted on an unmanned aircraft system," *ISPRS Journal of Photogrammetry and Remote Sensing*, vol. 155, pp. 25–36, 2019.
- [4] J. Skaloud and D. Lichti, "Rigorous approach to bore-sight self-calibration in airborne laser scanning," *ISPRS Journal of Photogrammetry and Remote Sensing*, vol. 61, no. 1, pp. 47–59, 2006.
- [5] S. Jin and A. Komjathy, "GNSS reflectometry and remote sensing: new objectives and results," *Advances in Space Research*, vol. 46, no. 2, pp. 111–117, 2010.
- [6] P. D. Groves, R. J. Handley, and A. R. Runnalls, "Optimising the integration of terrain referenced navigation with INS and GPS," *Journal of Navigation*, vol. 59, no. 1, pp. 71–89, 2006.
- [7] D. Gautam, A. Lucieer, Z. Malenovsky, and C. Watson, "Comparison of MEMS-based and FOG-based IMUs to determine sensor pose on an unmanned aircraft system," *Journal of Surveying Engineering*, vol. 143, no. 4, p. 4017009, 2017.
- [8] Z. Li, J. Tan, and H. Liu, "Rigorous boresight self-calibration of Mobile and UAV LiDAR scanning systems by strip adjustment," *Remote Sensing*, vol. 11, no. 4, p. 442, 2019.
- [9] L. Dong, C. Wang, X. Xi, Z. Zuo, and J. Zhu, "An automatic bore-sight calibration method for airborne LiDAR based on co-planar constrains," *Science Survey Mapping*, vol. 42, no. 9, pp. 98–103, 2017.

- [10] H. G. Maas, "Least-squares matching with airborne laserscanning data in a TIN structure," *International Archives of the Photogrammetry, Remote Sensing*, vol. 33, pp. 548–555, 2000.
- [11] H. Ayman, K. I. Bang, K. A. Paula, and C. Jacky, "Alternative methodologies for LiDAR system calibration," *Remote Sensing*, vol. 2, no. 3, pp. 874–907, 2010.
- [12] T. O. Chan, D. D. Lichti, and C. L. Glennie, "Multi-feature based boresight self-calibration of a terrestrial mobile mapping system," *ISPRS Journal of Photogrammetry and Remote Sensing*, vol. 82, pp. 112–124, 2013.
- [13] K. I. Bang, A. Habib, and A. Kersting, "Estimation of biases in lidar system calibration parameters using overlapping strips," *Canadian Journal of Remote Sensing*, vol. 36, no. sup2, pp. S335–S354, 2010.
- [14] Filin and Sagi, "Recovery of systematic biases in laser altimetry data using natural surfaces," *Photogrammetric Engineering and Remote Sensing*, vol. 69, no. 11, pp. 1235–1242, 2003.
- [15] M. Hebel and U. Stilla, "Simultaneous calibration of ALS systems and alignment of multiview LiDAR scans of urban areas," *IEEE Transactions on Geoscience and Remote Sensing*, vol. 50, no. 6, pp. 2364–2379, 2012.
- [16] A. P. Kersting, A. Habib, K. I. Bang, and J. Skaloud, "Automated approach for rigorous light detection and ranging system calibration without preprocessing and strict terrain coverage requirements," *Optical Engineering*, vol. 51, no. 7, pp. 076201–076219, 2012.
- [17] P. Glira, N. Pfeifer, and G. Mandlbürger, "Rigorous strip adjustment of UAV-based laserscanning data including time-dependent correction of trajectory errors," *Photogrammetric Engineering and Remote Sensing*, vol. 82, no. 12, pp. 945–954, 2016.
- [18] R. Keyetieu and N. Seube, "Automatic data selection and boresight adjustment of LiDAR systems," *Remote Sensing*, vol. 11, no. 9, p. 1087, 2019.
- [19] A. Pothou, C. Toth, S. Karamitsos, and A. Georgopoulos, *An Approach to Optimize Reference Ground Control Requirements for Estimating LIDAR/IMU Bore-sight Misalignment*, vol. -XXXVII, pp. 301–308, The international archives of the photogrammetry, remote sensing and spatial information sciences, 2008.
- [20] P. J. Besl and H. D. McKay, "A method for registration of 3-D shapes," *IEEE Transactions on Pattern Analysis and Machine Intelligence*, vol. 14, no. 2, pp. 239–256, 1992.
- [21] Y. Chen and G. Medioni, "Object modelling by registration of multiple range images," *Image and Vision Computing*, vol. 10, no. 3, pp. 145–155, 1992.
- [22] R. Ravi, Y. J. Lin, M. Elbahnasawy, T. Shamseldin, and A. Habib, "Simultaneous system calibration of a multi-LiDAR multicamera mobile mapping platform," *IEEE Journal of Selected Topics in Applied Earth Observations and Remote Sensing*, vol. 11, no. 5, pp. 1694–1714, 2018.
- [23] S. Rusinkiewicz and M. Levoy, "Efficient variants of the ICP algorithm," in *Proceedings third international conference on 3-D digital imaging and modeling*, pp. 145–152, Quebec City, QC, Canada, May 2001.
- [24] Q. Pentek, P. Kennel, T. Allouis, C. Fiorio, and O. Strauss, "A flexible targetless LiDAR-GNSS/INS-camera calibration method for UAV platforms," *ISPRS Journal of Photogrammetry and Remote Sensing*, vol. 166, pp. 294–307, 2020.
- [25] Z. Jing, J. I. Mo-Shou, and J. San, "Automated airborne LIDAR system calibration using virtual tie point model," *Acta Geodetica Et Cartographica Sinica*, vol. 42, no. 3, pp. 389–396, 2013.

Research Article

A Robust Visual-Aided Inertial Navigation Algorithm for Pedestrians

Langping An , Xianfei Pan , Tingting Li , and Mang Wang 

College of Intelligence Science and Technology, National University of Defence Technology, Changsha 410073, China

Correspondence should be addressed to Xianfei Pan; 3312395807@qq.com

Received 10 August 2021; Revised 8 October 2021; Accepted 10 November 2021; Published 6 January 2022

Academic Editor: Qiu-Zhao Zhang

Copyright © 2022 Langping An et al. This is an open access article distributed under the Creative Commons Attribution License, which permits unrestricted use, distribution, and reproduction in any medium, provided the original work is properly cited.

Real-time and robust state estimation for pedestrians is a challenging problem under the satellite denial environment. The zero-velocity-aided foot-mounted inertial navigation system, with the shortcomings of unobservable heading, error accumulation, and poorly adaptable parameters, is a conventional method to estimate the pose relative to a known origin. Visual and inertial fusion is a popular technology for state estimation over the past decades, but it cannot make full use of the movement characteristics of pedestrians. In this paper, we propose a novel visual-aided inertial navigation algorithm for pedestrians, which improves the robustness in the dynamic environment and for multi-motion pedestrians. The algorithm proposed combines the zero-velocity-aided INS with visual odometry to obtain more accurate pose estimation in various environments. And then, the parameters of INS have adjusted adaptively via taking errors between fusion estimation and INS outputs as observers in the factor graphs. We evaluate the performance of our system with real-world experiments. Results are compared with other algorithms to show that the absolute trajectory accuracy in the algorithm proposed has been greatly improved, especially in the dynamic scene and multi-motions trials.

1. Introduction

Pedestrian navigation has been extensively investigated over the last decades, because independent positioning is necessary and challenging under satellite denial environments, such as indoor navigation, mine rescue, and individual combat. Due to the autonomy and continuity of both cameras and inertial measurement units (IMU), visual odometry and inertial navigation system (INS) are the main methods to estimate the pose relative to a known starting point for pedestrians [1]. Besides, visual-inertial odometry (VIO) has become popular in recent years because of the complementary properties of cameras and IMU [2, 3]. Some advanced pedestrian navigation algorithms have already attained satisfactory performance, such as the solution algorithm of the strap-down inertial navigation system (SINS) [1, 4], visual-based methods [5–7], and visual-inertial algorithms [2, 3, 8]. However, several drawbacks, especially poor robustness in the dynamic environment and for multi-motion pedestrians, are limiting the usage of these algorithms in practice.

The error of INS accumulates with time, and it is hard to meet the long-term navigation precision of MIMU for pedestrians. On the one hand, the heading error of pedestrian inertial navigation is not observable, which cannot effectively restrain the heading drift, then the heading error will accumulate over time [4]. On the other hand, the parameters are poor adaptability for different pedestrians under various motion conditions, so that the performance of pedestrian inertial navigation is related to the movement characteristics of pedestrians [9]. Thus, it is the key to adjust parameters adaptively for a robust pedestrian navigation system.

The robustness of the visual navigation in dynamic environments is also challenge for pedestrians. Complex scenes bring unpredictable abnormal observations to the system, which would probably corrupt the quality of the state estimation and even lead to system failure [10]. In addition, the motion characteristics of pedestrians also affects the performance of the system.

The conventional visual-inertial navigation algorithms do not make full use of the human motion characteristics.

Lupton and Sukkah first proposed the theory of inertial integral increment without initial value to solve the problem of inertial vision integrated navigation under high dynamic conditions [11]. The fusion algorithm based on the pre-integration theory only gives scale information through inertial data [3, 8]. We can apply the gait characteristics heading of pedestrians for errors correction.

In this paper, we proposed a robust visual-inertial navigation algorithm to improve the robustness under the condition of limited vision and pedestrian movement, which fuses the cameras with foot-mounted MIMU and adjust parameters of INS adaptively. The conceptual diagram of the algorithm is shown in Figure 1. In the system, the pedestrian state, coming from VO and SINS, is optimized in a batch to obtain a more accurate and robust pose correction. Additionally, we establish the model between zero-velocity interval offset and navigation result error in one step. And taking the optimized result as observation, we estimate the parameters of zero-velocity interval detection to obtain a more accurate pose estimation. In short, our main contributions are as follows:

- (i) A novel pose graph optimization algorithm to fusion foot-mounted IMU with visual odometry
- (ii) An algorithm to adaptively adjust parameters of the zero-velocity detector, which is driven by the navigation result error
- (iii) The general framework to fuse foot-mounted IMU with various sensors, which combines optimization framework and filtering framework to achieves robust localization
- (iv) We demonstrate the performance and robustness of our method with extensive experiments. Challenges included dynamic scenarios and multi-motions pedestrians

The remainder of the article is structured as follows. In Sect. II, we discuss relevant literature about ZUPT-aided inertial navigation and the visual-inertial navigation. We give an overview of the algorithm proposed in Sect. III. A pose fusion algorithm between foot-mounted IMU and camera is presented in Sect. IV. Sect. V discusses the result-driven method for adaptive parameter adjustment. The experimental results and their discussion are shown in Sect. VI. Final, Sect. VII concludes the article.

2. Related Work

2.1. ZUPT-Aided Inertial Navigation. Traditional inertial navigation system integrates IMU measurements to estimate the pedestrian pose relative to a known origin. Typically, pedestrian navigation applies filter approaches [2] or optimized approaches [12–15] to fuse measurements other available sensors with the IMU. Combined with the topic of this paper, we summarize the related research on ZUPT-aided INS, multi-sensors navigation based on optimization framework for pedestrians.

The zero-velocity-aided INS, based on facts that the velocity is zero while the foot touches the ground for pedestrians, fuses the pseudo-measurement of the velocity state with Extended Kalman Filter (EKF) to reduce the accumulated error originating from the integration of noisy IMU measurement. The performance of the navigation system highly relies on the accuracy of the zero-velocity interval detection. Skog *et al.* presented a typical detector named the stance hypothesis optimal detection (SHOE), which achieve good performance for specific pedestrian and movement [16]. However, the parameters of ZUPT are quite different either under various motion states or from person to person. Thus, it is the key to adjust parameters adaptively for a robust pedestrian navigation system [4, 9]. Research work for solving the issue can be classified into two aspects. One is to improve the adaptability of the model-based algorithm by optimizing the parameters in real-time [1, 9, 15, 17–19]. The other is to replace the model-based architecture with a learned algorithm [4]. The adaptive algorithm, driven by the measurement of IMU, analyses the characteristics of parameters. The first is a threshold adjustment method based on speed or movement pattern classification [9, 16, 20]. For example, Brandon *et al.* train two separate support vector machine (SVM) classifiers for adaptive thresholds [4]. One to classify a user's motion type, and another to identify stationary periods given the current motion type. In addition, the model is constructed for zero-velocity detection based on the data characteristics [9]. Seong *et al.* propose a zero-velocity detection algorithm that does not require thresholds, by processing the gyro and accelerometer outputs based on an appropriate algorithm [19]. Different from the above, we present a result-derived algorithm to adjust the zero-velocity detection interval self-adaptively.

Unlike recursive estimation in filter-based frameworks, factor graph optimization estimates the states in a batch to achieve higher accuracy. The theory of inertial pre-integration makes it possible to provide scale information for other pose estimations for the IMU readings.

However, the pre-integration theory cannot be extended to pedestrians. At present, the pedestrian navigation framework based on optimization is based on the PDR algorithm to fuse other information sources. In terms of the use of information sources, posterity has done a lot of research. Researchers fusion GNSS [12, 21], WIFI-fingerprint [22], UWB [20], and other sensor [14, 20] information to optimize the pose of PDR. Compared with the SINS, the multi-sensors navigation based on PDR has drawbacks in accuracy and robustness. We analyse the error characteristics and propose a parameter adaptive adjustment method, which not only is useful for parameter adjustment but also provides support to combine optimization framework and filtering framework in theory.

2.2. Visual-Inertial Navigation. Due to the complementary nature of the IMU and vision, Motion estimation fusing cameras with IMUs has been an extensive research topic for many years. Noticeable approaches include MSCKF [2], VINS-Mono [3], SVO [6], DSO [7], and ORB-SLAM [5]. In this section, we will give a summary of visual-inertial

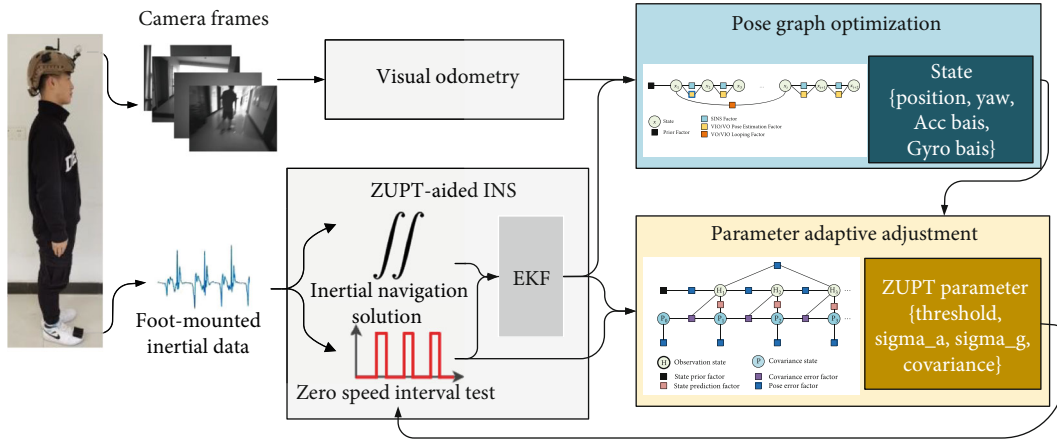


FIGURE 1: The conceptual diagram of the algorithm illustrating the full pipelines. MIMU and cameras are attached on the pedestrian. Pose graph optimization updates the 4-DOF pose and biases of IMU and parameter adaptive adjustment optimizes the parameters of zero-velocity detection with factor graphs.

odometry methods. We also focus the discussion on the application of visual inertia in pedestrians.

MCKF [2], a tightly-coupled VIO algorithm based on EKF, uses visual measurements of the same feature across multiple camera views to form a multi-constraint update, in which there is not necessary to include the spatial position of feature points in the observation model. But the problem of inconsistent filter estimation also produces. Different from filtering-based algorithms, the energy minimization-based approaches overall optimize the posture. Lupton presented the theory of pre-integration to realize inertial vision integrated navigation in high dynamic conditions, with which the algorithm based on optimization can be realized. VINS-Mono [3] is a very accurate and robust monocular inertial odometry system, with loop-closing using DBoW2 and 4-DoF pose-graph optimization, and map-merging. Feature tracking is performed with Lucas-Kanade tracker, being slightly more robust than descriptor matching. ORB-SLAM [5] can close loops and reuse the map, which takes advantage of Bag-of-World. A 7-DOF pose graph optimization is followed by loop detection.

As mentioned earlier, visual-inertial fusion is an effective method to improve the accuracy of the navigation system for pedestrians. However, the installation position of the foot-mounted IMU limits the widespread research on visual-inertial fusion for pedestrians. Considering the pedestrian movement patterns and characteristics of sensors, we study a new method to fusion foot-mounted IMU and cameras [23].

2.3. Algorithm Framework. The block diagram of the proposed algorithm for pedestrian navigation is shown in Figure 2. The proposed approach mainly includes four main modules: zero-velocity-aided INS, odometry tracking, pose graph optimization, parameter adaptive adjustment. The first two, the basis of navigation system, provide initial pose estimation, respectively. The latter two are the core of the algorithm proposed. One is for pose fusion odometry with foot-mounted MIMU, and the other is for optimizing zero-velocity intervals derived by navigation results.

The algorithm starts with pose estimation. In the zero-velocity-aided INS module, IMU measurement is integrated to estimate the 6D pose in SINS. And zero-velocity measurements are fused with SINS in EKF to reduce error growth over time. Odometry tracking, based on VINS-Mono, estimates the pedestrian's pose incrementally evolves from the starting point. Unlike a fixed coordinate transformation relation between sensors, the module of pose graph optimization continuously optimizes the coordinate transformation matrix based on both VO/VIO pose estimate and SINS position output. And then parameters are adjusted adaptively according to the fuse position estimates in the parameter optimization module. Specifically, we quantify the influence of inertial navigation parameters on inertial navigation results with the analysis of errors in EKF, which lays a foundation for finding the most accurate zero-velocity intervals.

3. Pose Graph Optimization

3.1. Measurement Pre-Processing. For sensors fusion between cameras and foot-mounted IMU, we assume that there are similar position increments among sensors mounted on pedestrians at the same time. Considering the characteristics of movement for pedestrians, we update the pose according to the frequency of gaits with the moving average filtering of acceleration. As is shown in as in Figure 3, each negative peak is the starting point of each step, and the interval between the two negative peaks is a step.

The input data consist of camera images and IMU measurements. Both are not assumed to be synchronized. The pedestrian is a flexible body but has a similar position estimation in diverse parts of the body. Thus, sensors, different from sensor rigid connection, are attached to the pedestrian and have similar position and yaw at the same time. As is shown in Figure 4, we correct the synchronization by aligning visual keyframes with IMU measurements and the camera keyframes in accordance with the distance. And we think the keyframe has the same pose with the to the closest IMU measurement.

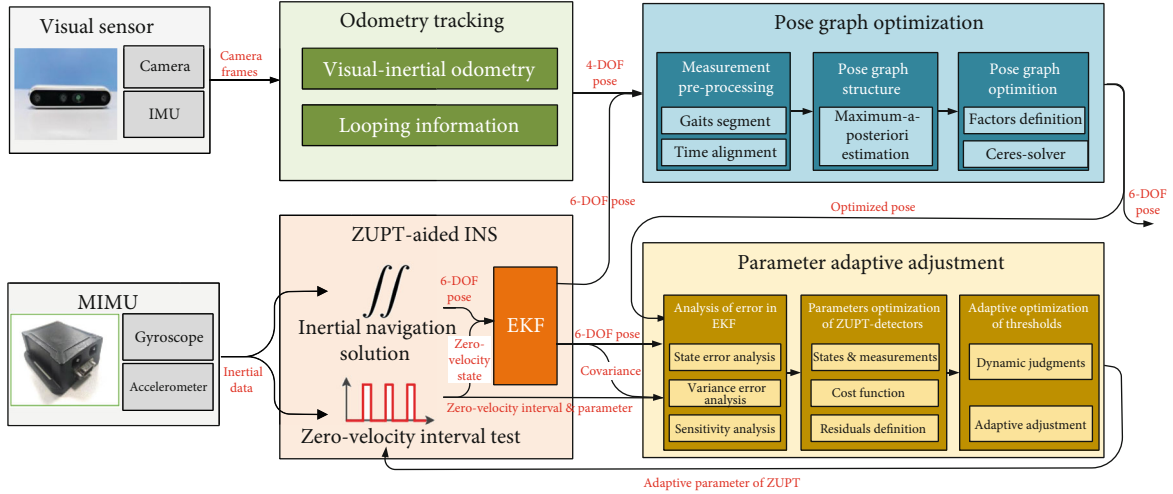


FIGURE 2: Algorithm framework illustrating the full pipelines. Odometry tracking outputs the odometry navigation results and looping information. In ZUPT-aided INS, zero-velocity measurements are fused with SINS in an Extended Kalman Filter to reduce error growth. Pose graph optimization continuously optimizes the pose graph based on both VO/VIO pose estimate and SINS position output. Parameter adaptive adjustment module first analyses the error between truth values and navigation results and construct optimization problem to solve accurate zero-velocity detection thresholds.

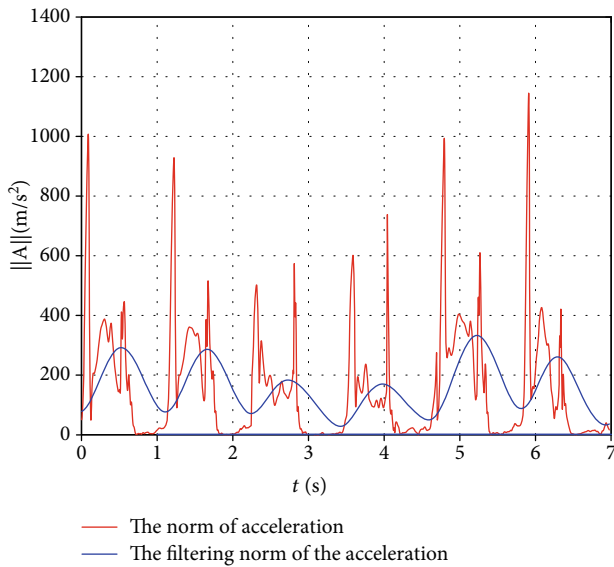


FIGURE 3: The norm and filtering norm of the accelerated velocity vector of IMU during various motions. Each negative peak is the starting of each step, and the interval between the two negative peaks is a step.

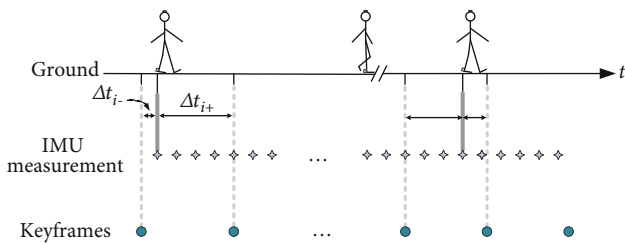


FIGURE 4: Time alignment. We consider camera/IMU time alignment to solve the problems of time mismatch.

3.2. *Pose Graph Structure.* Assuming that $k_g \in \mathbb{R}$ is the gait indices up to time t_g and there are a number of keyframes C_j between the adjacent foot tribal time t_i and t_{i-1} (i is the gait index, and $i \leq k_g$), where $j \in \mathbf{m}_i$, \mathbf{m}_i on behalf of the number of keyframes. We then define the objective of the estimation problem as the history of pedestrian states \mathbf{x}_i and keyframes detected up to t_g .

$$\chi_f \triangleq \bigcup_{i=0}^{k_g} \left[\{\mathbf{x}_i\}, \bigcup_{\forall j \in \mathbf{m}_i} \{C_j\} \right] \quad (1)$$

The factor graph framework aims to find the most likely posterior state χ_f when given the history of measurements \mathbf{z}_i . As is shown in Figure 5, the nature of positioning problem is a Maximum A Posteriori (MAP) problem.

$$\chi_f^* = \arg \max_{\chi_f} \prod_{t=0}^{k_g} \prod_{\tau \in \mathbf{F}} P(\mathbf{z}_i^{\tau} | \chi) \quad (2)$$

$$\mathbf{F} = \{\text{imu, vio, prior state, landmarks}\}$$

\mathbf{F} is the set of measurements, which includes VO/VIO measurements, MIMU measurements, prior state and landmarks, τ is the measurement's type. If the measurements are conditionally independent and corrupted by zero-mean Gaussian noise, the MAP estimate corresponds to the minimum of the negative log-posterior, and (2) is equivalent to a least squares problem of the form.

$$\chi_f^* = \arg \max_{\chi_f} \sum_{i=0}^{k_g} \sum_{\tau \in \mathbf{F}} \mathbf{r}_{\tau_i}^2 \quad (3)$$

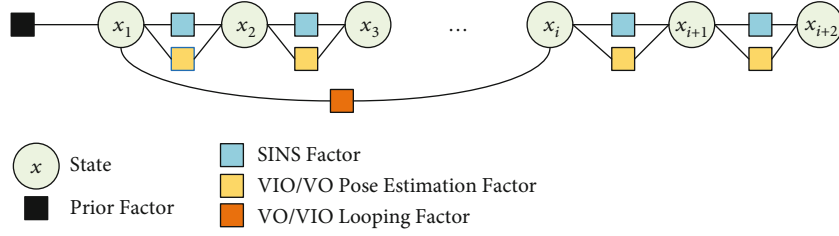


FIGURE 5: An illustration of the pose fusion graph structure. Every node represents the pedestrian's state in the world frame, which contains position yaw and IMU measurement bias. The edges between two consecutive nodes are constrained by both VO/VIO estimation and the INS pose increment. Others is looping constraint.

where \mathbf{r}_{τ_i} is the residual of the error between the predicted and measured value of at step index i , the quadratic cost of each residual is weighted by the corresponding covariance Σ_{τ_i} .

The following equation minimizes the energy of the system as a whole:

$$\chi_f^* = \arg \min_{\chi_f} \left\{ r_{0\Sigma_0}^2 + \sum_{(l_0, j) \in C} \mathbf{r}_{C_{j,0}}^2 + \sum_{i=0}^{k_g} \mathbf{r}_{\tau_i}^2 + \sum_{(l_j) \in C} \mathbf{r}_{C_j}^2 \sum_l \# \right\} \quad (4)$$

Where l is the landmark, l_0 is the prior landmark, and the residuals Σ_0 , $\Sigma_{C_{j,0}}$, Σ_{τ_i} , $\sum_l \#$ are from: state prior, landmark prior, IMU factors, odometry factors.

3.3. Factors Definition

- (1) State Prior Factors: In the proposed system, prior factors are used to anchor the pose to a fixed reference frame. The residual is defined as the error between the estimated state \mathbf{x}_0 and the prior \mathbf{z}_{p0}

$$\mathbf{r}_0(\mathbf{x}_0, \mathbf{z}_{p0}) = \begin{bmatrix} \mathbf{p}_0 - \mathbf{p}_{p0} \\ y_0 - y_{p0} \\ \mathbf{b}_0^w - \mathbf{b}_{p0}^w \\ \mathbf{b}_0^a - \mathbf{b}_{p0}^a \end{bmatrix} \quad (5)$$

where \mathbf{p}_i and y_i (with $i \in \{0, \dots, p, 0\}$) are position and yaw. \mathbf{b}_i^w and \mathbf{b}_i^a express the bias of gyro and accelerometer, respectively, at i . The prior state of the system is determined by IMU initialization.

- (2) Landmark Prior Factors: The landmark prior residual $\mathbf{r}_{C_{j,0}}$ is the error between the prior on the landmark location $C_{j,0}$ and the estimated landmark location C_j

$$\mathbf{r}_{C_{j,0}}(\mathbf{x}_{C_{j,0}}, \mathbf{z}_{C_j}) = \mathbf{P}_{C_{j,0}} - \mathbf{P}_{C_j} \quad (6)$$

The landmark prior is generated online through an initial triangulation procedure in visual inertia odometer. The covariance $\Sigma_{C_{j,0}}$ is determined by the triangulation accuracy.

- (3) VIO Factors: Since focusing on the relative increment between step g_{t-1} and step g_t , we define the residual of VO/VIO factor \mathbf{r}_{C_j} as:

$$\mathbf{r}_{C_j} = \mathbf{z}_t^c - \mathbf{h}_t^c(\chi) = \mathbf{z}_t^c - \mathbf{h}_t^c(\mathbf{x}_{t-1}, \mathbf{x}_t) = \begin{bmatrix} \mathbf{p}_t^c - \mathbf{p}_t^w \\ y_t^c - y_t^w \end{bmatrix} \quad (7)$$

where \mathbf{p}_i^r and y_i^r (with $r \in \{c, w\}$) is position at time i (with i as $t, t-1$) in the odometer or the global pose estimator. The covariance for VO/VIO measurements, is determined by the estimation accuracy, which is influenced by environmental conditions, pedestrian dynamics, etc. In our case, we adjust if according to the experimental conditions.

- (4) SINS Factors: Raw measurements of SINS are position increment and quaternion in the Inertial Coordinate System. In order to fusion the pose with the VIO, we set the positions and yaw as the optimized state, and considering the roll and pitch as the global posture. Generally, knowing the longitude and latitude at the origin point, we can convert them into the Earth Coordinate System. The IMU measurement is obtained according to the SINS. The IMU factor is derived as:

$$\mathbf{r}_{I_i} = \mathbf{z}_i^I - \mathbf{h}_i^I(\chi) = \mathbf{z}_i^I - \mathbf{h}_i^I(\mathbf{x}_{i-1}, \mathbf{x}_i) = \begin{bmatrix} \mathbf{p}_i^I - \mathbf{p}_i^w \\ y_i^I - y_i^w \\ \mathbf{b}_i^a - \mathbf{b}_{i-1}^a \\ \mathbf{b}_i^w - \mathbf{b}_{i-1}^w \end{bmatrix} \quad (8)$$

where the couple (\mathbf{q}_i^I, y_i^I) is position and orientation at time i in the SINS based on ZUPT. And the couple (\mathbf{q}_i^w, y_i^w) represent the pose of the system. The covariance is determined by performance of IMU devices and accuracy of zero speed detection.

4. Adaptive Parameter Adjustment in INS

ZUPT-aided INS contains two parts: one obtains increment of the pose with inertial integral, the other correct navigation error and measurement bias based on the zero-velocity interval detection and EKF. If correctly identified, zero-velocity updates can significantly improve localization estimates. However, either false-positive or false-negative detections bring observation error to EKF, thus lead to rapid and unbounded error growth. In fact, the error.

between truth values and navigation results is available to analyse the performance of EKF. In practice, we assume navigation errors attribute to inaccurate observations and estimate the length offset of the zero-velocity interval with the navigation error. In addition, variance error analysis is a very important method to measure the estimation of state error. Although there is indeed a consistency deviation between the estimated variance error and the true error. However, we can continuously enhance the consistency because the inconsistency of variance error will be fed back to the state error, and the algorithm is driven by state error. In other words, the difference the estimated variance error and the true error can be measured indirectly and gradually decreases with the correction of the state error.

As is identified following Figure 6, this section presents an optimization algorithm based on error analysis to update parameters of INS. We derive the recurrence formula of state error between two adjacent steps. Then the offset of interval length is translated to the change of observation. Additionally, observations, lengths of the zero-velocity interval, are optimized with a factors graph. Finally, the threshold is updated adaptively in a sliding window.

4.1. Error Analysis in EKF. Under the case of knowing the truth system, the covariance matrix can be propagated based on the system state error in EKF-aid INS, whether the model parameters or the mean square error are inaccurate. For pedestrian navigation, we assume that navigation offset is caused by inexact observation, that is, the zero-velocity interval error $\Delta\mathbf{H}_k$ at the k -th gate.

Knowing the truth value \mathbf{X}_k^r and the system output $\hat{\mathbf{X}}_k$, the state error $\tilde{\mathbf{X}}_k^e$ is defined as follows:

$$\tilde{\mathbf{X}}_k^e \triangleq \mathbf{X}_k^r - \hat{\mathbf{X}}_k \quad (9)$$

As is our concerned, the offsets of the zero-velocity interval are the only source of a navigation error. Therefore, $\tilde{\mathbf{X}}_k^e$ can be abbreviated as,

$$\begin{aligned} \hat{\mathbf{X}}_k^e &= (\mathbf{I} - \mathbf{K}_k \mathbf{H}_k) \tilde{\mathbf{X}}_{k|k-1}^p - \mathbf{K}_k \Delta\mathbf{H}_k \mathbf{X}_k^r - \mathbf{K}_k \mathbf{V}_k^r \\ \tilde{\mathbf{X}}_{k|k-1}^p &= \Phi_{k,k-1} \tilde{\mathbf{X}}_{k-1}^p + \Gamma_{k-1}^r \mathbf{W}_{k-1}^r \hat{\mathbf{X}}_{k-1} \end{aligned} \quad (10)$$

where $\tilde{\mathbf{X}}_{k|k-1}^p$ is the prediction mean square error, $\mathbf{K}_k \mathbf{H}_k$ is behalf of filter gain and measurements. \mathbf{W}_{k-1}^r represents the noise sequence. Besides, $\Phi_{g|g-1}$ and $\Gamma_{g|g-1}$ are the state transition matrix in EKF at time t_g . According to the definition of

variance, the variance error is formulated as,

$$\begin{aligned} \mathbf{P}_k^p &= (\mathbf{I} - \mathbf{K}_k \mathbf{H}_k) \mathbf{P}_{k|k-1}^p (\mathbf{I} - \mathbf{K}_k \mathbf{H}_k)^T + \mathbf{K}_k \Delta\mathbf{H}_k \mathbf{A}_k \Delta\mathbf{H}_k^T \mathbf{K}_k^T \\ &\quad + \mathbf{K}_k \mathbf{R}_k^r \mathbf{K}_k^T - (\mathbf{I} - \mathbf{K}_k \mathbf{H}_k) \mathbf{C}_{k,k-1}^T \Delta\mathbf{H}_k^T \mathbf{K}_k^T \\ &\quad - \mathbf{K}_k \Delta\mathbf{H}_k \mathbf{C}_{k|k-1} (\mathbf{I} - \mathbf{K}_k \mathbf{H}_k)^T \\ \mathbf{P}_{k|k-1}^p &= \Phi_{k,k-1} \mathbf{P}_{k-1}^p \Phi_{k,k-1}^T + \Gamma_{k-1}^r \mathbf{Q}_{k-1}^r \Gamma_{k-1}^r \end{aligned} \quad (11)$$

Where \mathbf{R}_g is the state matrix in EKF and

$$\begin{aligned} \mathbf{A}_k &= E[\mathbf{X}_k^r \mathbf{X}_k^{rT}] \\ \mathbf{C}_k &= E[\mathbf{X}_k^r \tilde{\mathbf{X}}_k^p] \\ \mathbf{C}_{k|k-1} &= E[\mathbf{X}_k^r \tilde{\mathbf{X}}_{k|k-1}^p] \end{aligned} \quad (12)$$

In our system, we take the last state as the Initial-values. And initial values of the mean square error are as followed.

$$\begin{aligned} \mathbf{P}_0^p &= E[(\mathbf{X}_{k-1}^r - \hat{\mathbf{X}}_{k-1})(\mathbf{X}_{k-1}^r - \mathbf{X}_{k-1})^T] \\ \mathbf{A}_0 &= E[\mathbf{X}_{k-1}^r \mathbf{X}_{k-1}^{rT}] \\ \mathbf{C}_0 &= E[\mathbf{X}_{k-1}^r (\mathbf{X}_{k-1}^r - \mathbf{X}_{k-1})^T] \end{aligned} \quad (13)$$

We assume that the pedestrian is equipped with a set of multi-rate sensors, with IMU sensors typically producing measurements at high rate and sensors such as monocular or stereo cameras generating measurements at lower rates. Some sensors may become inactive from time to time (e.g. GPS), while others may be active only for short periods of time (e.g. signal of opportunity).

4.2. Parameters Optimization of Zero-Velocity Detectors via Factor Graphs. In ZUPT-aided INS, navigation error is suppressed with both state covariance matrix and the zero-velocity observation. We assume that the truth value is known from another available information sources and set the state quantity of the previous time as the initial value of each step approximately. Our goal is to calculate the best INS parameter by fusing all the navigation error.

(1) State Definition: The state the state of the ZUPT-aided system at gate t_g as:

$$\begin{aligned} \mathbf{x}_g^e &= [\mathbf{P}_g^e, \mathbf{H}_g^e] \\ \mathbf{P}_g^e &= [P_{g,x}^e, P_{g,y}^e, P_{g,z}^e, P_{g,h}^e] \\ \mathbf{H}_g^e &= [\Delta v_{g,x}^e, \Delta v_{g,y}^e, \Delta v_{g,z}^e] \end{aligned} \quad (14)$$

where the couple $[\mathbf{P}_g^e, \mathbf{H}_g^e]$ represents covariance error and measurement offset at the g -th step (with time t_g), respectively.

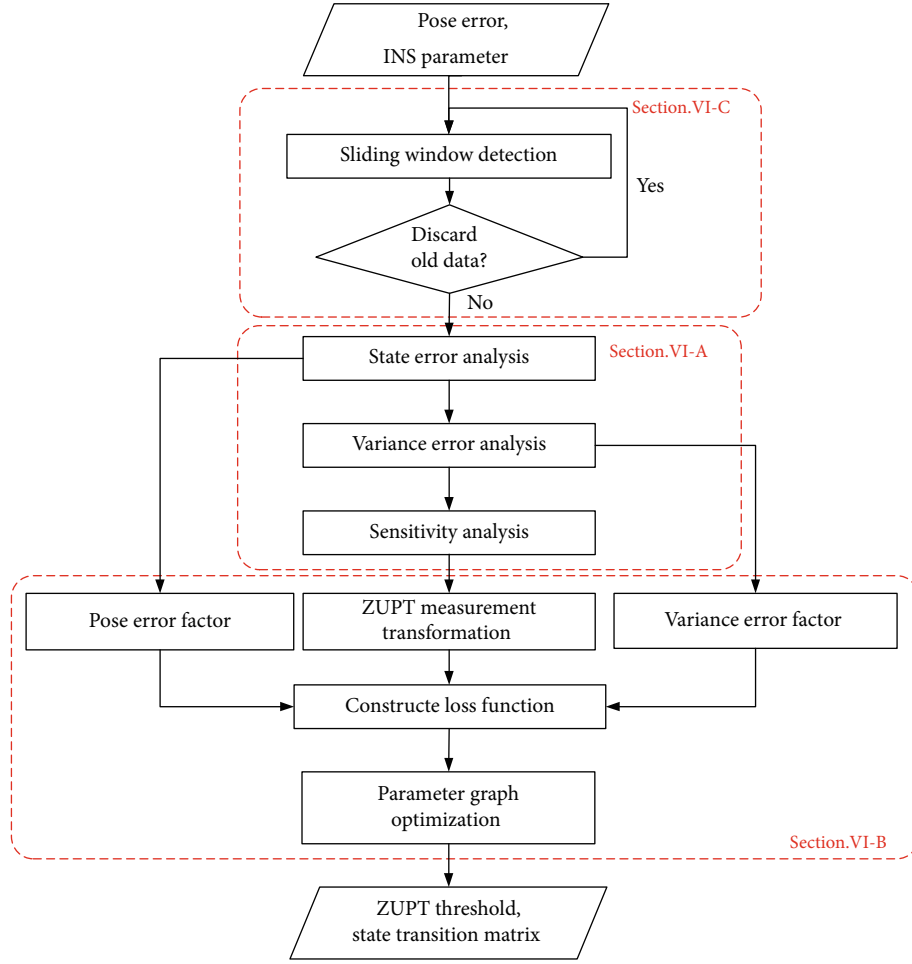


FIGURE 6: The program flow chart of parameter adaptive optimization.

$P_{g,i}^e$ is the state i ($i \in \{x, y, z, h, e, a, d, i, n, g\}$) variance at the g -th step. Let $\Delta v_{g,j}^e$ be the error of velocity measurement in orientation j .

With the help of we transform the disturbance of zero velocity interval into the change of the observable measurement in one step.

$$\mathbf{H}_g^e = \Delta \mathbf{l}_g \mathbf{r}_g \mathbf{T}_g^v \quad (15)$$

Where \mathbf{T}_g^v is the Observation transformation matrix and $\Delta \mathbf{l}_g$ is the disturbance of zero-velocity interval length in gait g -th, we then define the objective of our estimation problem \mathbf{X}_k as the history of robot states and landmarks detected up to t_g :

$$\mathbf{X}_k \triangleq \bigcup_{t=0}^{t_g} \mathbf{X}_g^e \quad (16)$$

- (2) Measurements: The input measurements consist of the pose error \mathbf{X}_k^e and covariance prediction \mathbf{P}_k^e , both of which are from truth values of system. k is the time index

$$\begin{aligned} \mathbf{X}_k^e &= \mathbf{X}_k^e - \widehat{\mathbf{X}}_e \\ \mathbf{P}_k^e &= \mathbf{P}_k^e - \widehat{\mathbf{P}}_e \end{aligned} \quad (17)$$

The pose input is the error between navigation results and truth values, and covariance prediction comes from propagation of the pose error in EKF.

- (3) Maximum-A-Posteriori Estimation: We assume the uncertainty of measurements is Gaussian distribution with mean and covariance. As is shown in Figure 7, the following equation minimizes the sum of prior and the Mahalanobis norm of all measurement residuals to obtain a maximum posterior estimation in a whole

$$\begin{aligned} \chi_p^* &= \arg \max_{\chi_p} \prod_{t=0}^{K_g} \prod_{k \in S} P(\mathbf{z}_t^k | \chi) = \arg \min_{\chi_p} \sum_{\tau} \sum_{i \in K_g} \mathbf{r}_{\tau i}^2 \sum_{\tau_i} \\ &= \arg \min_{\chi} \left\{ \mathbf{r}_p - \mathbf{H}_p \chi^2 + \sum_{k \in \mathcal{S}} \mathbf{r}_{\mathcal{S}} \left(\widehat{\mathbf{z}}_{b_{k+1}}^{b_k}, \chi \right)_{\mathbf{P}_{b_{k+1}}^{b_k}}^2 + \sum_{k \in \mathcal{B}} \mathbf{r}_{\mathcal{B}} \left(\widehat{\mathbf{z}}_{b_{k+1}}^{b_k}, \chi \right)_{\mathbf{P}_{b_{k+1}}^{b_k}}^2 \right\} \end{aligned} \quad (18)$$

Where \mathbf{r}_p , $\mathbf{r}_{\mathcal{B}}$ represent the residual of pose estimation and

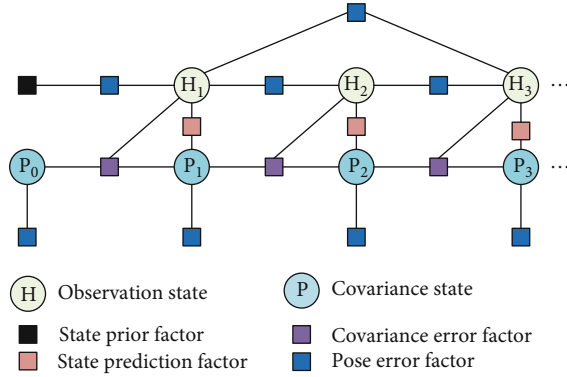


FIGURE 7: An illustration of the parameter graph structure. Every node represents one gait's parameter of pose filtering in ZUPT-aided INS. The node contains the length of zero-velocity interval and states covariances.

state variance, respectively. Detailed definition of the residual terms will be presented later in VI-D. Once the graph is built, optimizing it equals to finding the configuration of nodes that match all edges as much as possible.

We used Ceres Solver to carry out the nonlinear optimization. We run pose graph optimization at the frequency of gait update for a pedestrian. After every optimization, we obtain more accurate estimations fusing the SINS pose with VO/VIO.

- (4) State Variance Residual: In contrast to the stepwise recursion of the state covariance matrix, we define the state variance residual with a state covariance error, which is constrained only by two adjacent observations

Consider the EKF state within two consecutive time t_g and t_{g+1} , according to analysis of variance error in Sect. V-A, the residual for can be defined as:

$$\mathbf{r}_{\mathcal{V}}(\hat{\mathbf{z}}_{t_{g+1}}^g, \chi_p) = \mathbf{P}_g^e \quad (19)$$

- (5) Pose Error Residual: We establish a model to describe the influence of zero velocity interval disturbance on pose estimation in a gait. Based on the model, the relative pose constraint is produced

$$\mathbf{r}_{\mathcal{V}}(\hat{\mathbf{z}}_{t_{g+1}}^g, \chi_p) = \begin{bmatrix} \delta x_{p_{g+1}}^g \\ \delta y_{p_{g+1}}^g \\ \delta z_{p_{g+1}}^g \\ \delta \omega_{p_{g+1}}^g \end{bmatrix} = \mathbf{z}_g^{\mathcal{P}} - \mathbf{h}_g^{\mathcal{P}}(\chi_p) \quad (20)$$

$$\mathbf{h}_g^{\mathcal{P}}(\chi_p) = \tilde{\mathbf{X}}_k^e$$

where $\mathbf{h}_g^{\mathcal{P}}(\chi_p)$ extracts the pose offset at the state χ_p .

4.3. Adaptive Optimization of Zero-Velocity Thresholds. We keep a sliding window for graph optimization to get drift-free pose estimation and avoid wrong adjustments when the movement pattern changes. The size of the window is adjusted in real-time with the computation complexity. Additionally, old poses and measurements will be thrown when the motion pattern changed.

We judge whether the movement pattern changes according to positive peaks Within two adjacent steps. The movement pattern is considered to have changed if the ratio of peak values above is beyond the threshold adaptive adjustment rang.

5. Experiment Results

We perform real-world experiments to evaluate the proposed VA-INS system from two aspects in accuracy and robustness. In the indoor environment, which has a dynamic and small viewing field, we test the performance of the algorithm in dynamic environment. We then carry out an outdoor experiment with multi-motions pattern to test the performance of the real-time optimized INS. Additionally, A large-scale experiment is carried out to illustrate the long-time practicability of our system.

The performance of sensors is described in detail in Table 1. The sensor suite contains a foot-mounted MIMU (with gyroscope and accelerometer) operating at 400 Hz, a stereo camera (Intel Realsense D455) with 30 Hz, and the u-blox GNSS modules. As is shown in Figure 8, sensors are connected to the pedestrian but do not have a fixed coordinate relationship.

We get the ground truth with different methods between indoor and outdoor experimental conditions. In indoor experiments, ground truth mark points, either obvious turning points or the end of each step, are used to evaluate the experimental effect. Specifically, the subject pressed a hand-held trigger that recorded a timestamp to facilitate temporal alignment with ground truth when he arrived at the mark points. In outdoor experiments, the ground truth, which is calculated by the Differential GPS on the u-blox-NEO-M8N. The position accuracy of Differential GPS is about 0.1 m. Also, google maps are used for error judgment in large-scale experiments. The performance is evaluated by the horizontal position error (HPE) of trajectories. Sensors are connected to the pedestrian but do not have a fixed coordinate relationship.

We get the ground truth with different methods between indoor and outdoor experimental conditions. In indoor experiments, ground truth mark points, either obvious turning points or the end of each step, are used to evaluate the experimental effect. Specifically, the subject pressed a hand-held trigger that recorded a timestamp to facilitate temporal alignment with ground truth when he arrived at the mark points. In outdoor experiments, the ground truth, which is calculated by the Differential GPS on the u-blox-NEO-M8N. The position accuracy of Differential GPS is about 0.1 m. Also, google maps are used for error judgment in large-scale experiments. The performance is evaluated by the horizontal position error (HPE) of trajectories.

TABLE 1: Results in the multi-motion experiment outdoor.

Sensor	Parameter	Index
Gyroscope	Bias stability	$<8^\circ/\text{h}$
	Angle random walk	$0.36^\circ/\text{h}$
	Sampling frequency	400 Hz
Accelerometer	Bias stability	0.03 mg
	Random walk	$0.045 \text{ m/s/h}^{0.5}$
	Sampling frequency	400 Hz
Camera	Image resolution ratio	1280*720
	Baseline	36.2625 mm
U-blox	Navigation sensitivity	-167 dBm
	Sampling frequency	10 Hz

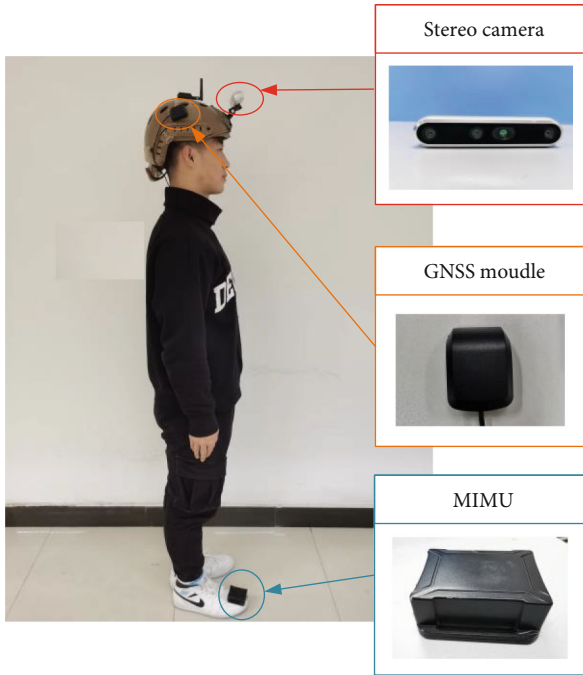


FIGURE 8: The sensor suite we used for the experiment, which contains a foot-mounted MIMU and a stereo camera (Intel RealSense D455).

In these experiments, we compare the algorithm proposed with both VINS-Mono and ZUPT-aided INS. VINS-Mono is a robust and versatile monocular visual-inertial state estimator. ZUPT-aided INS uses the SHOE detector to discover the zero-velocity interval and takes zero velocity as the virtual observation of the filtering algorithm to modify the INS results with the Extended Kalman Filter.

6. The Hallway Experiment Indoor

In the hallway experiment indoor, we choose our laboratory environment as the experiment area. The test subject suits sensors and walks at a normal pace in the hallway of the lab-

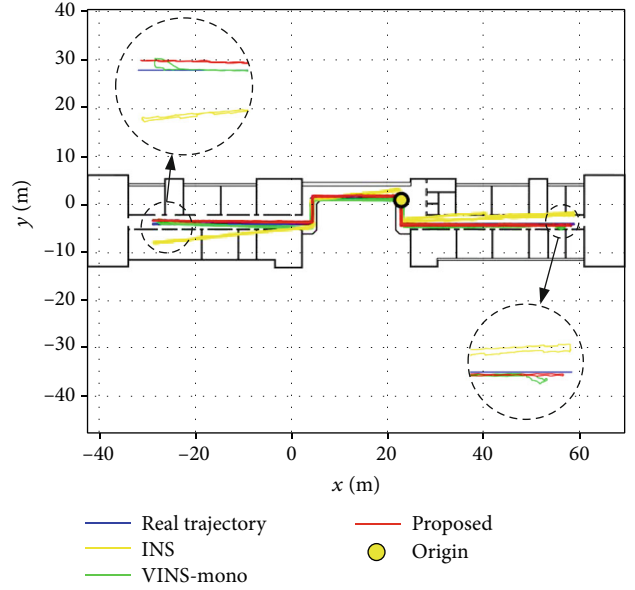


FIGURE 9: The trajectories of our indoor hallway experiment recovered from real trajectory, ZUPT-aided INS, VINS-Mono and the proposed algorithm, respectively.

TABLE 2: Results in the mu Hallway Experiment Indoor.

Algorithm	VINS-mono	SHOE	VA-INS
MEAN[m]	0.60	2.01	0.36
RMSE[m]	0.69	2.61	0.39

oratory. During the trial, the subject went along hallways and rooms with the same stride, and returned to the origin along the same path.

From Figure 9, we can see that heading error of INS accumulates over time and the visual odometer has less pose drift than zero-velocity INS in the environment of unrestricted vision. Most notably, VA-INS proposed continuously improves the accuracy of navigation. Table 2 shows the RMSE (Root Mean Square Errors) and MEAN (Mean Errors) of HPE. In the indoor environment with good visual conditions, the performance of a visual-inertial odometer is better than that of pure inertia. Especially, VINS-Mono with loop detection suppresses the drift of course. It is worth noting that VA-INS combines the advantages of the two and achieves the best performance.

7. The Visual-Restricted Experiment

In the mixed experiment of stairs and corridors, the trial walk along the corridors and walk up the stairs from the second floor to the fifth floor, where he encounters pedestrians, low light condition, texture-less area, glass, and reflection. Then, the trial climb down the stairs and walk back to the origin. Key-frames of typical scenes are shown in Figure 10.

As shown in Figure 11, we compare our results with VINS-Mono and fixed-threshold INS. Noticeable VIO drifts

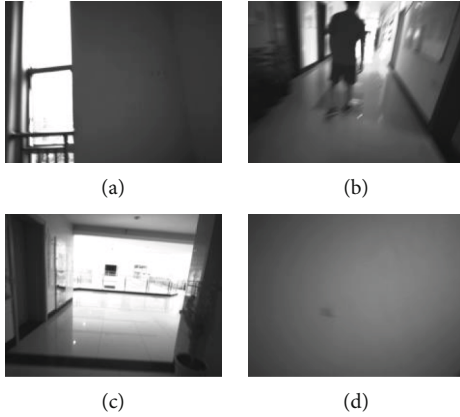


FIGURE 10: B Experimental key-frames of the camera for pose estimation in VIO, which consist of glass/reflection(a), pedestrian(b), high light condition(c), texture-less area (d).

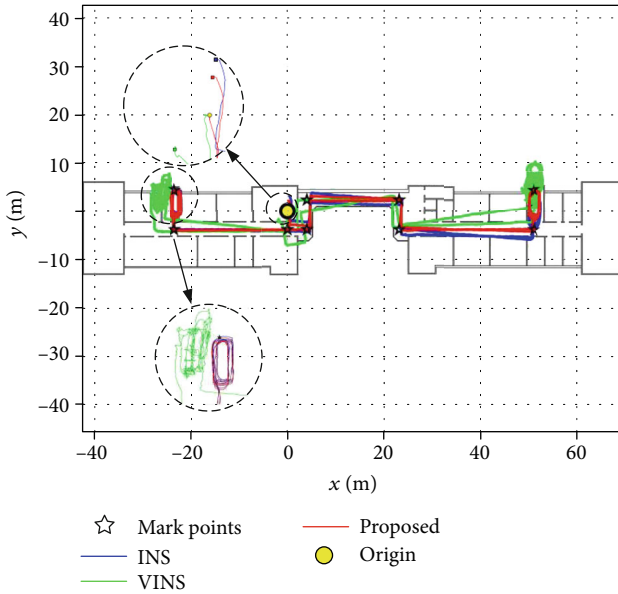


FIGURE 11: The trajectories of our indoor visual-restricted experiment recovered from real trajectory, ZUPT-aided INS, VINS-Mono and the proposed algorithm, respectively.

TABLE 3: Results in visual-restricted Experiment indoor.

Algorithm	VINS-mono	SHOE	VA-INS
MEAN[m]	7.62	3.51	2.38
RMSE[m]	7.89	3.74	2.57

occurred when the experimenter encounters the dynamic objects, and the system is even unavailable when the experimenter climbed up and down the stairs, where texture-less area is in all places. In sharp contrast, although ZUPT-aided INS has the cumulative error with time, it is more robust to changes in experimental scenes. In contrast to them, the fusion foot-mounted IMU with cameras suppresses the error accumulation and improves the robustness by exerting their respective advantages.

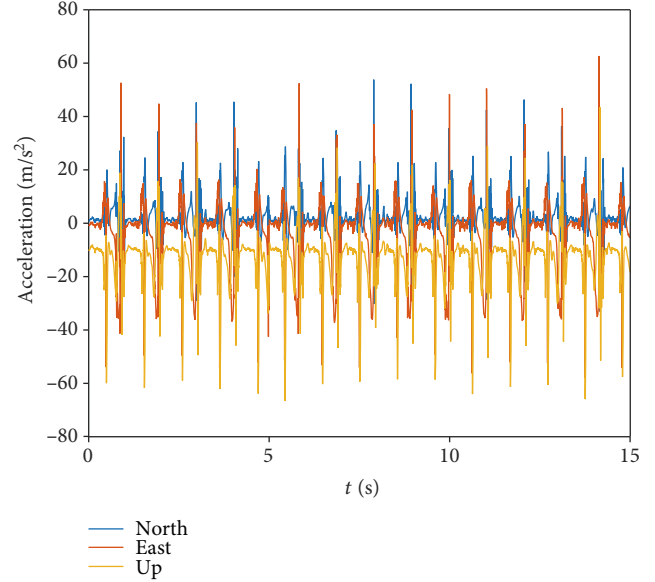


FIGURE 12: Partial acceleration measurements of foot-mounted MIMU in multi-motion experiment outdoor. For MIMU, there is different characteristics in various motion states.

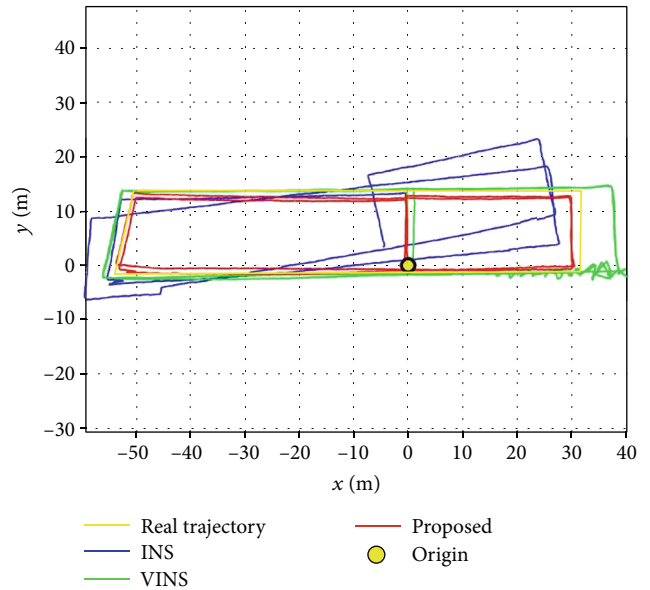


FIGURE 13: The trajectories of our multi-motion experiment recovered from real trajectory, ZUPT-aided INS, VINS-Mono and the proposed algorithm, respectively.

Table 3 shows the RMSE (Root Mean Square Errors) and MEAN (Mean Errors) of HPE. The robustness of the visual odometer is poor in the indoor environment with limited visual conditions, where the error of INS accumulates with time but is limited. VA-INS uses the pose estimation of VINS-Mono in a good environment to correct the error of INS. Combining the trials above, we can see that the visual odometer is poor robust in the dynamic environment and our algorithm outperforms VINS-Mono and ZUPT-aided INS, which demonstrates the algorithm proposed effectively

TABLE 4: Results in the multi-motion experiment outdoor.

Algorithm	VINS-mono	SHOE	Proposed
MEAN[m]	5.56	2.54	0.89
RMSE[m]	6.12	3.16	0.91

TABLE 5: Results in the large-scale experiment.

Algorithm	VINS-mono	SHOE	Proposed
MEAN[m]	13.36	18.75	5.58
RMSE[m]	21.73	26.04	7.53

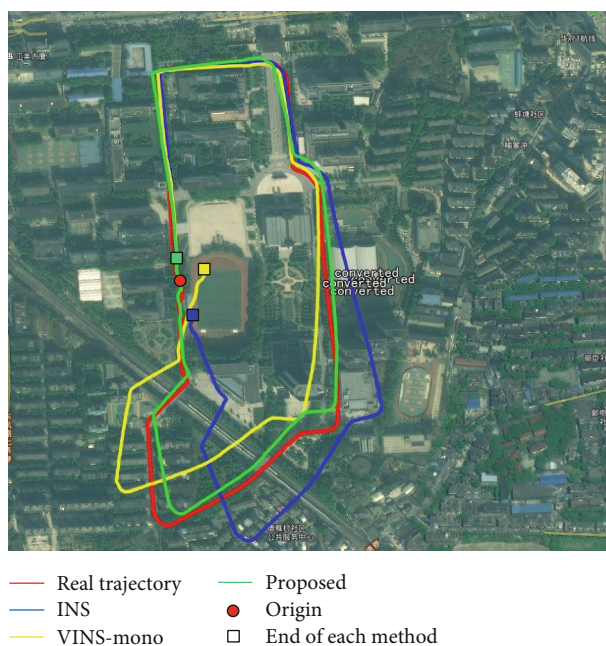


FIGURE 14: The trajectories of the large-scale experiment outdoor recovered from ZUPT-aided INS, VINS-Mono, and the proposed algorithm, respectively.

reduces the influence of experimental scene on vision and improve navigation accuracy.

7.1. The Multi-Motion Experiment Outdoor. We evaluated our proposed detector over longer trajectories by carrying out a multi-motions trial in an outdoor setting. The trial subject started and ended at the same position on the test course. The experimenter started from the doorway of the building and walked along the building. Then the trial instructed to alternate between jogging, walking, and fast running. Finally, we went back to the building and returned to the origin. The whole trajectory is more than 450 meters and lasts approximately eight minutes. The IMU measurement of multi-motion states can be seen in Figure 12.

Figure 13 shows trajectory comparison is shown. The RMSE (Root Mean Square Errors).

and MEAN (Mean Errors) of HPE is shown in Table 4. Due to the low adaptability of the threshold for various states, we can see obvious translation drift in the estimated trajectory of INS. What's more, VINS-Mono is almost no

heading deviation but there are offsets in position estimation when the trial jogs or runs. From the trajectory comparison, we can see that the proposed system improved the accuracy of INS a lot with the real-time adaptive parameters. The algorithm proposed achieved the best performance.

7.2. A Large-Scale Experiment. We have chosen a campus environment as the experimental scene to verify the improvement in the long-range positioning performance. In this large-scale scene test, the trial distance is 2.2 km with about 164028 min.

As is shown in Table 5. The RMSE of HPE in the proposed algorithm is 7.53 m. Under the same test conditions, results by the fixed-threshold INS and VINS-Mono are 26.04 m and 21.73 m. Similarly, the mean error of our algorithm is significantly lower than the others. It is obvious that the algorithm proposed provides accurate positioning even in the large-scale scene.

The estimated trajectory is aligned with Google Map in Figure 14. It can be seen from the figure that the visual loop can correct the navigation error. However, the overall optimization of the trajectory may also affect the overall pose estimation accuracy. Compared with Google Map, we can see our results are almost drift-free in this very long-duration test.

8. Conclusions

In this work, we have proposed a novel visual-aid inertial navigation system for pedestrians with a detailed description of its building blocks and an exhaustive evaluation. The approach could increase the accuracy of pose estimation with flexible-connection sensors fusion and optimize the parameter of INS. We establish the functional relationship between the zero-speed interval disturbance and the navigation results, which is the basis of our work. Using the factor graph, the visual odometer is fused with the foot-mounted MIMU to overcome the error drift in inertial navigation results. Then the fusion-optimized pose is taken as the observation to optimize the zero-velocity interval of each step, which further updates the zero-velocity detection threshold of the pedestrian in the current motion state. We show superior performance by comparing against both the pedestrian inertial navigation algorithm based on fixed threshold and the typical visual-inertial fusion algorithm. Future work will extend the method to fusion other sensors for more accurate pose estimation, such as GPS, WIFI-fingerprint, UWB, and Magnetometer. The goal is to not only further improve the accuracy of pose estimation but also realize the plug-and-play of sensor fusion for pedestrian navigation.

Data Availability

The visual inertia raw data used to support the findings of this study are available from the corresponding author upon request.

Conflicts of Interest

The author(s) declare(s) that they have no conflicts of interest.

Funding

This work is supported in part by National Natural Science Foundation (NNSF) of China under Grant 61773394 and 62073331.

References

- [1] Z. Wang, H. Zhao, S. Qiu, and Q. Gao, "Stance-phase detection for ZUPT-aided foot-mounted pedestrian navigation system," *IEEE/ASME Transactions on Mechatronics*, vol. 20, no. 6, pp. 3170–3181, 2015.
- [2] A. I. Mourikis and S. I. Roumeliotis, "A Multi-State Constraint Kalman Filter for Vision-aided Inertial Navigation," in *Proceedings 2007 IEEE International Conference on Robotics and Automation*, pp. 3565–3572, Rome, Italy, 2007.
- [3] T. Qin, P. Li, and S. Shen, "VINS-Mono: A Robust and Versatile Monocular Visual-Inertial State Estimator," *IEEE Transactions on Robotics*, vol. 34, no. 4, pp. 1004–1020, 2018.
- [4] B. Wagstaff, V. Peretroukhin, and J. Kelly, "Robust data-driven zero-velocity detection for foot-mounted inertial navigation," *IEEE Sensors Journal*, vol. 20, no. 2, pp. 957–967, 2020.
- [5] R. Mur-Artal, J. M. M. Montiel, and J. D. Tardós, "ORB-SLAM: a versatile and accurate monocular SLAM system," *IEEE Transactions on Robotics*, vol. 31, no. 5, pp. 1147–1163, 2015.
- [6] C. Forster, Z. Zhang, M. Gassner, M. Werlberger, and D. Scaramuzza, "SVO: Semidirect visual Odometry for monocular and multicamera systems," *IEEE Transactions on Robotics*, vol. 33, no. 2, pp. 249–265, 2017.
- [7] J. Engel, V. Koltun, and D. Cremers, "Direct sparse Odometry," *IEEE Transactions on Pattern Analysis and Machine Intelligence*, vol. 40, no. 3, pp. 611–625, 2018.
- [8] R. Mur-Artal and J. D. Tardós, "ORB-SLAM2: An open-source SLAM system for monocular, stereo, and RGB-D cameras," *IEEE Transactions on Robotics*, vol. 33, no. 5, pp. 1255–1262, 2017.
- [9] R. Zhang, H. Yang, F. Hoflinger, and L. M. Reindl, "Adaptive zero velocity update based on velocity classification for pedestrian tracking," *IEEE Sensors Journal*, vol. 17, no. 7, pp. 2137–2145, 2017.
- [10] C. Yu, Z. Liu, X. J. Liu et al., "DS-SLAM: a semantic visual SLAM towards dynamic environments," in *IEEE/RSJ International Conference on Intelligent Robots and Systems (IROS)*, pp. 1168–1174, Madrid, Spain, 2018.
- [11] T. Lupton and S. Sukkarieh, "Visual-inertial-aided navigation for high-dynamic motion in built environments without initial conditions," *IEEE Transactions on Robotics*, vol. 28, no. 1, pp. 61–76, 2012.
- [12] W. Li, X. Cui, and M. Lu, "A robust graph optimization realization of tightly coupled GNSS/INS integrated navigation system for urban vehicles," *Tsinghua Science and Technology*, vol. 23, no. 6, pp. 724–732, 2018.
- [13] V. Indelman, S. Williams, M. Kaess, and F. Dellaert, "Factor graph based incremental smoothing in inertial navigation systems," in *2012 15th International Conference on Information Fusion*, pp. 2154–2161, 2012.
- [14] J. Tan, X. Fan, S. Wang, and Y. Ren, "Optimization-Based Wi-Fi Radio Map Construction for Indoor Positioning Using Only Smart Phones," *Sensors*, vol. 18, no. 9, p. 3095, 2018.
- [15] V. Indelman, S. Williams, M. Kaess, and F. Dellaert, "Information fusion in navigation systems via factor graph based incremental smoothing," *Robotics and Autonomous Systems*, vol. 61, no. 8, pp. 721–738, 2013.
- [16] I. Skog, J. Nilsson, and P. Händel, "Evaluation of zero-velocity detectors for foot-mounted inertial navigation systems," in *2010 International Conference on Indoor Positioning and Indoor Navigation*, pp. 1–6, Zurich, Switzerland, 2010.
- [17] J. Wahlström, I. Skog, F. Gustafsson, A. Markham, and N. Trigoni, "Zero-velocity detection—a Bayesian approach to adaptive thresholding," *IEEE Sensors Letters*, vol. 3, no. 6, pp. 1–4, 2019.
- [18] M. Ma, Q. Song, Y. Li, and Z. Zhou, "A zero velocity intervals detection algorithm based on sensor fusion for indoor pedestrian navigation," in *2017 IEEE 2nd information technology, networking, Electronic and Automation Control Conference (ITNEC)*, pp. 418–423, Chengdu, China, 2017.
- [19] S. Y. Cho and C. G. Park, "Threshold-less zero-velocity detection algorithm for pedestrian dead reckoning," in *2019 European Navigation Conference (ENC)*, pp. 1–5, Warsaw, Poland, 2019.
- [20] F. Liu, J. Wang, J. Zhang, and H. Han, "An Indoor Localization Method for Pedestrians Base on Combined UWB/PDR/Floor Map," *Sensors*, vol. 19, no. 11, p. 2578, 2019.
- [21] K. Pan, M. Ren, P. Wang, and Y. Liu, "A federated filtering personal navigation algorithm based on MEMS-INS/GPS integrated," in *2016 Chinese Control and Decision Conference (CCDC)*, pp. 5237–5241, Yinchuan, China, 2016.
- [22] M. Nowicki and P. Skrzypczynski, "Indoor Navigation with a Smartphone Fusing Inertial and WiFi Data via Factor Graph Optimization," in *Mobile Computing, Applications, and Services*, S. Sigg, P. Nurmi, and F. Salim, Eds., vol. 162 of Lecture Notes of the Institute for Computer Sciences, Social Informatics, and Telecommunications Engineering, pp. 280–298, Springer, 2015.
- [23] L. An, X. Pan, Z. Chen, M. Wang, Z. Tu, and C. Chu, "A multi-sensor fusion algorithm for pedestrian navigation using factor graphs," in *2021 40th Chinese Control Conference (CCC)*, pp. 3727–3732, Shanghai, China, 2021.

Research Article

A New Triple Filtering Algorithm and Its Application for Aerial GNSS/INS-Integrated Direct Georeferencing System

Qusen Chen ¹, Leilei Li ², Keyi Xu,² Xiangdong An ³ and Yu Wu ²

¹GNSS Research Center, Wuhan University, No. 129 Luoyu Road, Wuhan 430000, China

²College of Aerospace Engineering, Chongqing University, Chongqing 400000, China

³Institute of Communications and Navigation Nautical Systems, German Aerospace Center, No. 53 Kalkhorstweg, Neustrelitz 17235, Germany

Correspondence should be addressed to Leilei Li; lill@cqu.edu.cn

Received 3 September 2021; Accepted 15 September 2021; Published 18 October 2021

Academic Editor: Qiu-Zhao Zhang

Copyright © 2021 Qusen Chen et al. This is an open access article distributed under the Creative Commons Attribution License, which permits unrestricted use, distribution, and reproduction in any medium, provided the original work is properly cited.

A global navigation satellite system and inertial navigation system- (GNSS/INS-) integrated system is employed to provide direct georeferencing (DG) in aerial photogrammetry. However, GNSS/INS suffers from stochastic error, strong nonlinearity, and weak observability problems in high dynamic or less maneuver scenarios. In this paper, we proposed a new triple filtering algorithm for aerial GNSS/INS integration. The new algorithm implements filtering in the sequence of forward, backward, and forward directions. Each filter is initialized by a previous filter to get a quick convergence, and the final result is combination of the last two filtering to smooth error. The proposed triple filtering strategy avoids inaccuracy in the 1st forward filtering when the system has not reached convergence. Moreover, it facilitates engineering implementation because backward filtering can employ the same equations with forward filtering. To assess stochastic error of the inertial measurement unit, the Allan variance method is used and abbreviated stochastic model is built. A real aerial testing is conducted, and the result indicates that DG can achieve horizontal accuracy of 5 cm by the proposed algorithm, which has 63% improvement compared to standard extended Kalman filter.

1. Introduction

Aerial photogrammetry performs surveying and mapping by taking images of ground from an elevated position. The images could be collected by sensors like digital cameras, Lidar, and multispectral or hyperspectral scanners, to make digital orthophoto map (DOM), digital elevation model (DEM), digital line graphic (DLG), and other mapping products. Before mapping, the exterior orientation elements (positions and attitude) of every image need to be known when taking images. Normally, these elements are resolved by ground control points and aerial triangulation (AT) algorithm. With the aid of a GNSS/INS-integrated system, which works as direct georeferencing (DG), the exterior orientation elements could be directly measured [1, 2]. Thus, the ground control points can be considerably reduced or even entirely eliminated.

Generally, differential GNSS is used to get 3-dimensional coordinates with centimeter-level precision [3, 4], while

inertial measurement unit (IMU) in aerial photogrammetry application is commonly of tactical grade, consisting of three close loop fiber optic gyros (FOG) with $0.1 \sim 10^\circ/\text{h}$ bias and three quartz accelerometers with $0.1 \sim 1 \text{ mg}$ bias. The primary error sources of GNSS/INS integration in aerial application are sensor stochastic error, strong nonlinearity, and weak observability, among which sensors' stochastic errors are very intractable as many types of stochastic processes are involved. They cause accumulative positioning and orientation error with time. Thus, the implementation of GNSS/INS-integrated system requires careful and accurate error modeling. On the other hand, it is unreasonable to model all the stochastic processes since their observability will significantly decrease in GNSS denied environment and deficient maneuver scenarios, which consequently results in system instability. In most cases, abbreviated stochastic processes are accounted to approximate real situation in the integration model, while others are ignored or merged to existing

error [5]. These approximate models would make the system performance worse, especially in high kinematic scenarios.

Inertial navigation is a typical nonlinear system, and the nonlinearity of INS will be strengthened when vehicle makes rapid maneuver such as turning, acceleration, and deceleration. Classical extended Kalman filter (EKF) takes linearization to the nonlinear model and implements the linear KF algorithm for estimation of the state vector; thus, it has been extensively used in many engineering applications. However, it suffers from strong nonlinearity, such as large maneuver or environment influence. For these cases, some other nonlinear filters are carried out to solve the nonlinearity problem, such as iterated EKF [6, 7], unscented Kalman filter (UKF) [8, 9], particle filter (PF) [10–12], and neural network method [13, 14], among which iterated EKF and UKF are effective for a nonlinear model, but they are on the assumption of Gaussian stochastic process. PF and neural network can deal well with both nonlinearity and inaccurate model problem. However, these nonlinear filters are not valid to improve observability.

Weak observability is another problem in aerial GNSS/INS integration, which often happens when GNSS signal is challenged or the vehicle is lack of maneuver. The former is mainly caused by signal interference, ionosphere scintillation, or signal blockage by inclined airframe when making U-turn, while the latter is due to the rarely changed flight state in aerial photogrammetry. The plane requires to fly with straight and parallel air routes to capture images of ground and make a U-turn while switching to the adjacent air route. Long straight and steady flying lead to decrease of heading observability, so that heading accuracy is degraded in each straight air route. The theoretical scheme to solve this heading observability reduction is to shorten the straight routes and make more turning, but it will clearly decrease the mapping efficiency. In practical processing, a back propagation model is always applied to estimate system states since aerial photography does not require real-time processing in most cases. Different from the standard forward model, the back propagation model has good observability at the end of straight route or GNSS outage, but weak observability at the beginning. The combination of the forward and backward propagation model leads to the smoothing EKF. Several smoothers can be found in the literature [15], in which the most used are forward-backward (FB) smoother [16, 17], Rauch–Tung–Striebel (RTS) smoother [18, 19], and their modifications. FB smoother needs to define new variable to avoid matrix inversion and provide a valid boundary initialization. It employs the information form of EKF instead of the standard EKF for backward filtering. By comparison, RTS does not require full backward EKF that results in good computational efficiency. However, the computation is not of first priority in posttask. Meanwhile, RTS also requires a different form of EKF for backward filtering. Moreover, the attitude is not accurate at the beginning of forward filtering for both FB smoother and RTS, because the initial attitude is obtained by coarse alignment, which will deteriorate the combined result in spite of being averaged by backward filtering.

In this research, we present a new triple filtering algorithm for aerial GNSS/INS-integrated DG. Firstly, stochastic

processes are investigated by the Allan variance method. The state equation of EKF is built including the navigation error propagation model and abbreviated stochastic model of IMU. Secondly, a forward-backward-forward EKF (FBF-EKF) is proposed to address the inaccurate model, strong nonlinearity, and weak observability problems. Specifically, this algorithm implements triple filtering in the sequence of forward, backward, and forward filtering. The 1st forward EKF mainly works for convergence of the filter, and the last two EKFs are initialized by foregoing EKF. Our final result is combination of the backward EKF and the 2nd forward EKF. The scheme of FBF-EKF leads to two principal benefits compared with commonly used smoothers: (1) eliminations of inaccuracy before EKF convergence and (2) easy implementation on the base of standard EKF.

The content of this paper is organized as follows. Section 2 introduces the identification and modeling of IMU stochastic process. Section 3 describes the error model of Kalman Filter, including the navigation propagation model and stochastic processing model. Section 4 presents the FBF-EKF algorithm, and the experiment is outlined in Section 5. Conclusion is presented in Section 6.

2. Identification for IMU Stochastic Process

The error of IMU sensor consists of deterministic and stochastic errors. According to IEEE Standard 647 and Standard 528 [20, 21], stochastic errors include white noise, rate random walk, Markov process, quantization noise, flicker noise, sinusoidal noise, and rate ramp. The bias is different every time when the IMU sensor is powered on, and it is not correlated to the angle rate or acceleration; thus, the bias can be modeled as a random constant. The rate white noise, also called angle random walk, is a result of wide band noise being added on the rate data. Integrating rate white noise on angular acceleration and jerk results in rate random walk. Flicker noise is the low-frequency bias fluctuations on the measured rate data, which represents the best instability of sensor. Flicker noise can be modeled by the combination of several Markov processes, while rate ramp can be modeled by a second-order differential equation driven by white noise. Sinusoidal noise can be usually characterized by a number of distinct frequencies, and quantization noise is caused by sampling a continuous signal with finite byte length. Models of each stochastic error are shown in Equation (1), taking a gyro as an example.

$$\left\{ \begin{array}{l} \dot{b}_\omega = 0, \\ s\dot{f}_\omega = 0, \\ w_\omega = N \cdot v, \\ \delta\dot{\omega}_K = K \cdot v, \\ \delta\dot{\omega}_B = -\beta_B \delta\omega_B + \beta_B B \cdot v, \\ \delta\ddot{\omega}_R = R \cdot v, \\ \delta\dot{\omega}_M = -\beta_M \delta\omega_M + \beta_M M \cdot v, \end{array} \right. \quad (1)$$

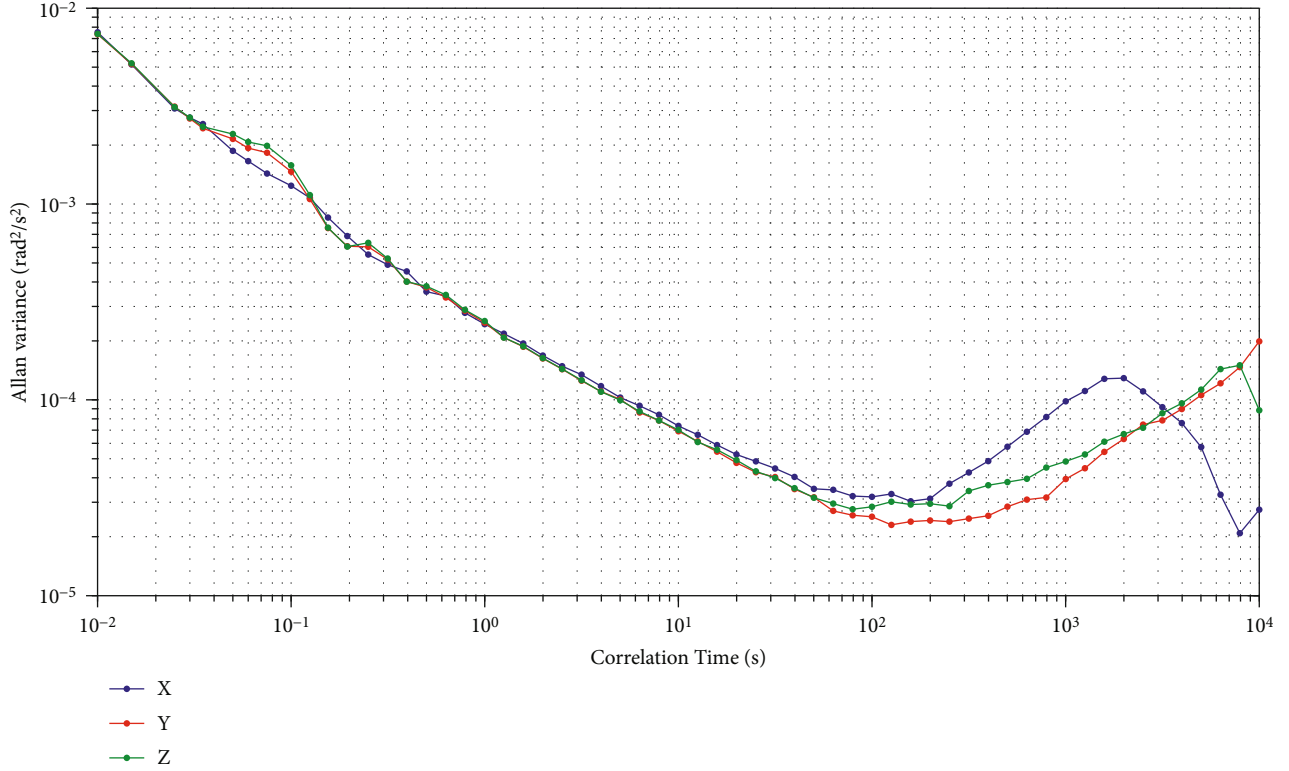


FIGURE 1: Allan variance of gyros.

where b_ω is the gyro's bias, sf_ω denotes the scale factor error, w_ω is the white noise, $\delta\omega_K$ represents the rate random walk, $\delta\omega_B$ denotes the flicker noise, $\delta\omega_R$ shows the rate ramp, and $\delta\omega_M$ is Markov process. N , K , B , R , and M are the power spectral density (PSD) coefficients of rate white noise, rate random walk, flicker noise, rate ramp, and Markov process, respectively, while v is a unit Gaussian white noise.

Assuming all of the above stochastic processes are independent, the total stochastic error is the sum of each noise type, which is shown in Equation (2), including both gyro and accelerometer.

$$\begin{cases} \delta a = sf_a \cdot a + b_a + \delta a_K + \delta a_B + \delta a_R + \delta a_M + w_a, \\ \delta \omega = sf_\omega \cdot \omega + b_\omega + \delta \omega_K + \delta \omega_B + \delta \omega_R + \delta \omega_M + w_\omega, \end{cases} \quad (2)$$

where $b_a, sf_a, w_a, \delta a_K, \delta a_B, \delta a_R$, and δa_M are the accelerometer's bias, scale factor error, white noise, rate random walk, flicker noise, rate ramp, and Markov process, respectively. ω and a are the angle rate and specific force.

Allan variance is a standard approach to characterize stochastic errors of inertial sensors. To identify and evaluate the stochastic process of IMU, the Allan variance method was used due to its recognized simplicity and efficiency in our previous work [5]. The relationship between Allan variance and PSD is expressed as follows:

$$\sigma^2(\tau) = 4 \int_0^\infty S_\omega(f) \frac{\sin^4(\pi f \tau)}{\pi f \tau^2} df, \quad (3)$$

where τ is the correlation time, $\sigma^2(\tau)$ denotes the Allan variance, f presents the frequency, and $S_\omega(f)$ is the PSD of inertial sensor's output.

Equation (3) can be considered a band-pass filter, and its bandwidth depends on correlation time τ . The resulted Allan variance is proportional to the energy of signal within the bandwidth. In general, different stochastic processes have different correlation times. They present different piecewise linearity with associated slope and intercept after passing through the filter, which can be used for identification of stochastic processes. A detailed relationship between the slope, stochastic process, and coefficient can be found in reference [21].

Assuming that the angular rate ω is sampled with rate f_s for a collection of N data points, The data can be divided into $K = N/M$ clusters, where M is the number of points in each cluster. The corresponding correlation time is $\tau = M/f_s$. Then, the average of each cluster is

$$\bar{\omega} = \frac{1}{M} \sum_{i=1}^M \omega_{(k-1)M+i}, \quad k = 1, \dots, K. \quad (4)$$

Allan Variance can be computed by the following averaging operation:

$$\sigma_A^2(\tau_M) = \frac{1}{2(K-1)} \sum_{k=1}^{K-1} [\bar{\omega}_{k+1}(M) - \bar{\omega}_k(M)]^2. \quad (5)$$

In this work, eight hours' static IMU data was sampled

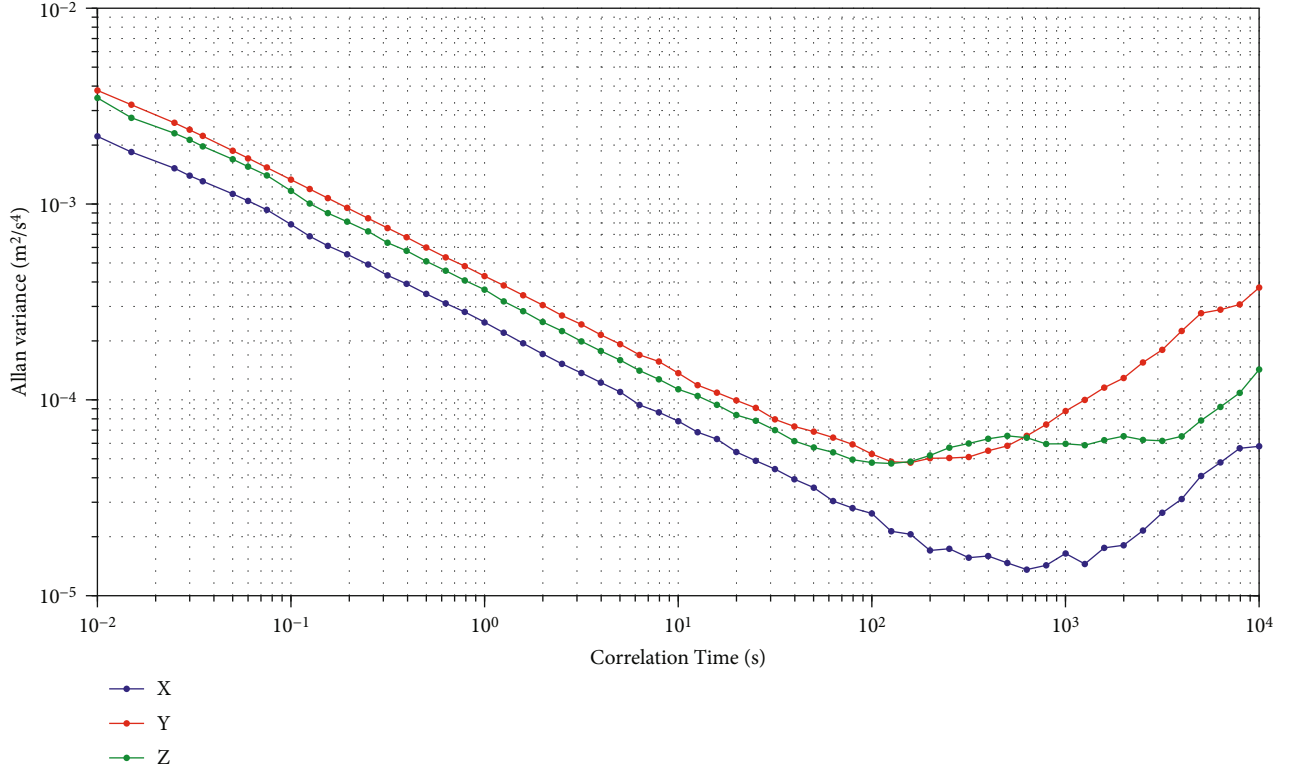


FIGURE 2: Allan variance of accelerometers.

with a rate of 200 Hz. The Allan variance results are shown in Figures 1 and 2. The dominant stochastic processes are rate white noise and rate random walk for both FOG and accelerometers. The PSD coefficients of these two stochastic processes are listed in Table 1, in which the largest values among three axes are used for the following Kalman filter. Flicker noise is also found in Figures 1 and 2. However, it is highly unlikely to model all of the stochastic processes and to make estimation because of poor observability. This effort may even lead to the instability of the filter. Therefore, only selected and principal stochastic processes are considered in practical applications. Here, four stochastic components are considered for the aerial referencing system, which are bias, white noise, rate random walk, and scale factor error. Both bias and scale factor error are modeled as random constant. Then, Equation (2) can be rewritten as follows:

$$\begin{cases} \delta\omega = sf_{\omega} \cdot \omega + b_{\omega} + \delta\omega_K + w_{\omega}, \\ \delta a = sf_a \cdot a + b_a + \delta a_K + w_a, \end{cases} \quad (6)$$

3. Error Models in Kalman Filter

The data fusion schemes for GNSS/INS are generally divided into loosely coupling and tightly coupling modes based on combination information, among which the Kalman filter in loosely coupling has a lower order and is more reliable compared to tightly coupling. The main reason is that GNSS and INS work independently in the loosely coupling and integrate on navigation result. However, loosely coupling has to depend on pure INS when three or less GNSS satel-

TABLE 1: Stochastic process coefficient.

	N (rad/s ^{1/2})	K (m/s ^{3/2})
Gyro	2.53×10^{-3}	9.82×10^{-5}
Accelerometer	4.30×10^{-4}	8.81×10^{-5}

ites are observed. In free inertial mode, the accuracy will be quickly degraded because of sensor stochastic errors. By comparison, tightly coupling does not have limitation on the satellite number. The integration can work even when the GNSS satellite number is inadequate for positioning. Therefore, tightly coupling has a higher accuracy than the loosely coupling in GNSS-challenged scenario. Aerial application has an open view of satellites, and the satellite number normally can be more than 20 with gradual establishment of multiconstellation GNSS. Therefore, loosely coupling is used in the GNSS/INS-integrated DG with consideration of system reliability and GNSS quality control.

The INS equation must be linearized before filtering because of its strong nonlinearity [18]. The linearized state equation of continuous system and discrete observation equation are expressed as follows:

$$\begin{cases} \dot{x}(t) = F(t)x(t) + G(t)W(t), \\ y_k = H_k x_k + V_k, \end{cases} \quad (7)$$

where x_k is the error states vector of the Kalman filter, y_k

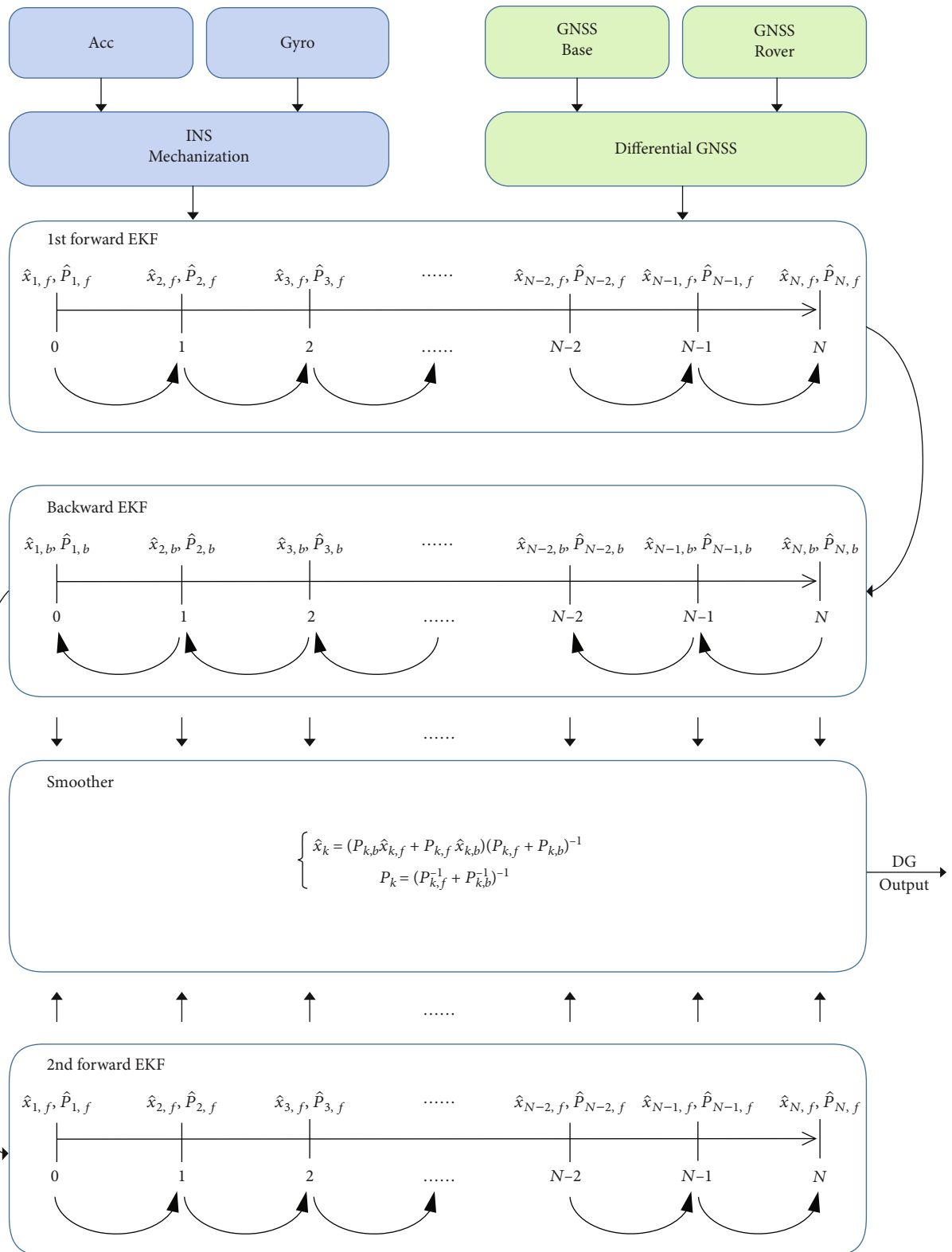


FIGURE 3: FBF-EKF Algorithm.

denotes the observation vector, and $F(t)$ and $G(t)$ are the dynamics matrix and coefficient matrix of process noise, respectively. H_k is the observation coefficient matrix, while

$W(t)$ and V_k are process noise and observation noise, respectively. Please note that the continuous state equation needs to be discretized before use.

According to the sensor stochastic error models in Equation (6) with considering navigation errors, the state equation of the Kalman filter can be concluded as

$$\begin{bmatrix} \dot{x}_{rve} \\ \dot{x}_a \\ \dot{x}_\omega \end{bmatrix} = \begin{bmatrix} F_{11} & F_{12} & F_{13} \\ F_{21} & F_{22} & F_{23} \\ F_{31} & F_{32} & F_{33} \end{bmatrix} \begin{bmatrix} x_{rve} \\ x_a \\ x_\omega \end{bmatrix} + \begin{bmatrix} G_{11} & G_{12} \\ G_{21} & G_{22} \\ G_{31} & G_{32} \end{bmatrix} \begin{bmatrix} W_a \\ W_\omega \end{bmatrix}, \quad (8)$$

where x_{rve} is the 9-order navigation error including position, velocity, and attitude. x_a and x_ω are the stochastic error of gyro and accelerometer, respectively. As depicted in Equation (6), they are composed by bias, rate random walk, and scale factor stochastic errors, which are shown in Equations (9) and (10), respectively.

$$x_a = [b_a \ \delta a_K \ sf_a]^T, \quad (9)$$

$$x_\omega = [b_\omega \ \delta \omega_K \ sf_\omega]^T. \quad (10)$$

The white noise in Equation (6) is not included in x_a and x_ω , as it is the component of the system-driven noises W_a and W_ω :

$$W_a = \begin{bmatrix} N_a \\ K_a \end{bmatrix} v, \quad (11)$$

$$W_\omega = \begin{bmatrix} N_\omega \\ K_\omega \end{bmatrix} v, \quad (12)$$

where N_a and K_a are accelerometer's PSD coefficients of rate white noise and rate random walk, respectively. N_ω and K_ω are gyro's PSD coefficients of rate white noise and rate random walk, respectively.

For dynamics matrix, F_{11} is the navigation coefficient matrix and can be found in many literatures, e.g., [22, 23]. F_{21} , F_{22} , F_{23} , F_{31} , F_{32} , and F_{33} are 9-order zero square matrices. F_{12} and F_{13} are presented as follows:

$$F_{12} = \begin{bmatrix} 0_{3 \times 3} & 0_{3 \times 3} & 0_{3 \times 3} \\ C_b^e & C_b^e & C_b^e \text{diag}(a) \\ 0_{3 \times 3} & 0_{3 \times 3} & 0_{3 \times 3} \end{bmatrix}, \quad (13)$$

$$F_{13} = \begin{bmatrix} 0_{3 \times 3} & 0_{3 \times 3} & 0_{3 \times 3} \\ 0_{3 \times 3} & 0_{3 \times 3} & 0_{3 \times 3} \\ C_b^e & C_b^e & C_b^e \text{diag}(\omega) \end{bmatrix}, \quad (14)$$

where C_b^e is the rotation matrix from body frame to reference frame, and ECEF is used in this paper. $\text{diag}()$ is a diagonal matrix of the elements.

According to the definition of system-driven noises W_a and W_ω in Equations (11) and (12), the coefficient matrix of process noise $G(t)$ is easily derived as



FIGURE 4: The assembly of sensors.



FIGURE 5: Aerial trajectory on Google Earth.

$$G_{11} = \begin{bmatrix} 0_{3 \times 3} & 0_{3 \times 3} \\ C_b^e & 0_{3 \times 3} \\ 0_{3 \times 3} & 0_{3 \times 3} \end{bmatrix}, \quad (15)$$

$$G_{12} = \begin{bmatrix} 0_{3 \times 3} & 0_{3 \times 3} \\ 0_{3 \times 3} & 0_{3 \times 3} \\ C_b^e & 0_{3 \times 3} \end{bmatrix}, \quad (16)$$

$$G_{21} = \begin{bmatrix} 0_{3 \times 3} & 0_{3 \times 3} \\ 0_{3 \times 3} & I_{3 \times 3} \\ 0_{3 \times 3} & 0_{3 \times 3} \end{bmatrix}, \quad (17)$$

$$G_{32} = \begin{bmatrix} 0_{3 \times 3} & 0_{3 \times 3} \\ 0_{3 \times 3} & 0_{3 \times 3} \\ 0_{3 \times 3} & I_{3 \times 3} \end{bmatrix}, \quad (18)$$

where $I_{3 \times 3}$ is a 3-order identity matrix. G_{22} and G_{31} are 9 by 6 zero matrices.

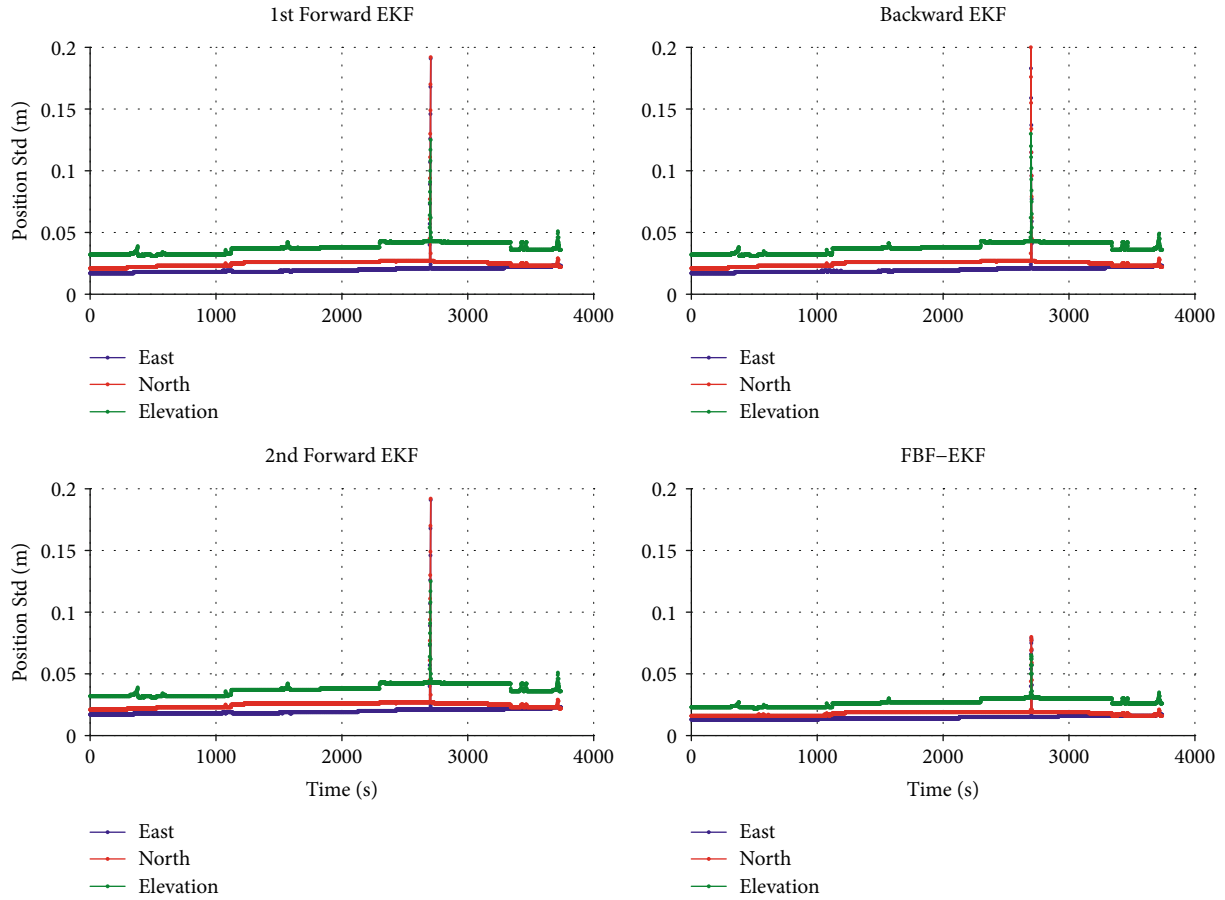


FIGURE 6: Position Std of FBF-EKF.

In loosely coupling, the observation is the difference between INS and GPS:

$$y = \begin{bmatrix} r_{\text{INS}} - r_{\text{GPS}} \\ v_{\text{INS}} - v_{\text{GPS}} \end{bmatrix}, \quad (19)$$

among which r_{INS} and v_{INS} are the 3-dimension position and velocity vectors by INS, r_{GPS} and v_{GPS} are the 3-dimension position and velocity vectors by GPS. The observation coefficient matrix can be written as

$$H = [I_6 \quad 0_{6 \times 21}]. \quad (20)$$

4. Forward-Backward-Forward EKF

The advantage of postprocessing is that all observations can be used for the state estimation at any epoch. Smoothing Kalman filter is very suitable for processing errors caused by an inaccurate system model and environment influence, such as inaccuracy of stochastic process model, linearization error of the extended Kalman filter, and GNSS interruption.

In this paper, a forward-backward-forward EKF (FBF-EKF) is proposed to smooth the navigation result. After filtering, for all epochs by the 1st forward, EKF runs in a reversed direction, which means the state equation evolves

in backward time sequence. Following that, forward filtering will be run for the second time. The final result is a combination of backward and the 2nd forward estimation. The main task of the 1st forward EKF is to provide initializations for the backward and 2nd forward EKFs, such as navigation states, sensor's error, and their covariance. These initializations are more accurate compared to the initial alignment. This triple filtering strategy avoids inaccuracy in the 1st forward EKF when the filter has not reached convergence. Another bonus is the backward filtering can employ standard EKF equations like forward EKF as it starts with a finite covariance. These characteristics are very attractive in the view of engineering implementation.

The algorithm of FBF-EKF is presented in Figure 3:

- (i) Perform forward EKF with Equation (7) as the system model
- (ii) Initialize the backward EKF with

$$\begin{cases} \hat{x}_{N,b}^- = \hat{x}_{N,f}^+ \\ P_{N,b}^- = P_{N,f}^+ \end{cases} \quad (21)$$

where $\hat{x}_{N,b}^-$ and $P_{N,b}^-$ are the prior estimation and covariance of backward EKF at the last epoch N ,

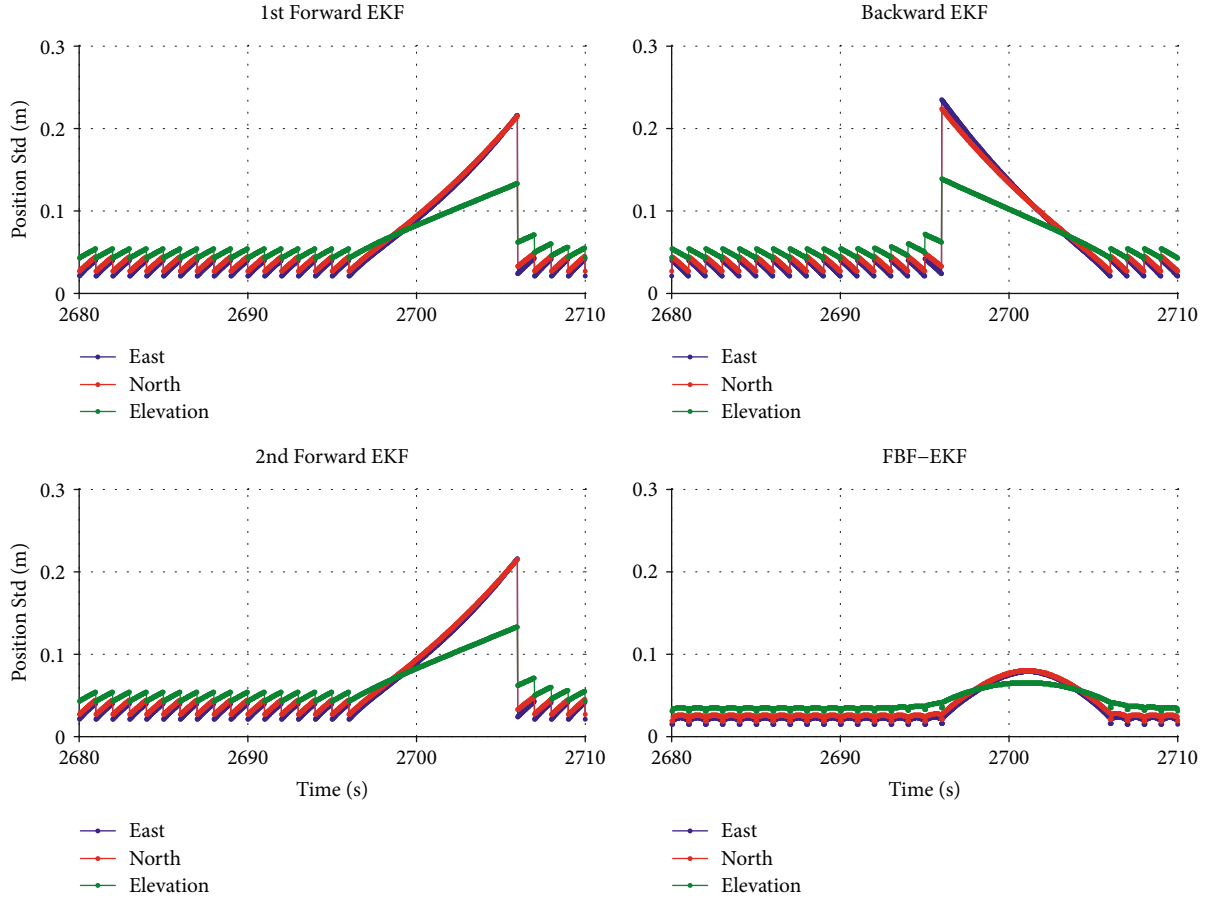


FIGURE 7: Partial details of position Std.

respectively. $\hat{x}_{N,f}^+$ and $P_{N,f}^+$ are posterior estimation and covariance of 1st forward EKF at the last epoch N , respectively

(iii) Perform backward EKF with the system model as

$$\begin{cases} \dot{x}(-t) = F(-t)x(-t) + G(-t)W(-t), \\ y_k = H_k x_k + V_k \end{cases} \quad (22)$$

(iv) Initialize the 2nd forward EKF with Equation (23),

$$\begin{cases} \hat{x}_{1,f}^- = \hat{x}_{1,b}^+, \\ P_{1,f}^- = P_{1,b}^+, \end{cases} \quad (23)$$

where $\hat{x}_{1,f}^-$ and $P_{1,f}^-$ are the prior estimation and covariance of 2nd forward EKF at the first epoch, respectively. $\hat{x}_{1,b}^+$ and $P_{1,b}^+$ are posterior estimation and covariance of backward EKF at the first epoch, respectively.

(v) Perform 2nd forward EKF with Equation (7) as the system model

(vi) Combine the 2nd forward estimation and backward estimation as

$$\begin{cases} \hat{x}_k = (P_{k,b}\hat{x}_{k,f} + P_{k,f}\hat{x}_{k,b})(P_{k,f} + P_{k,b})^{-1}, \\ P_k = (P_{k,f}^{-1} + P_{k,b}^{-1})^{-1}, \end{cases} \quad (24)$$

where \hat{x}_k and P_k are the combination estimation and covariance, respectively. $\hat{x}_{k,f}$ and $P_{k,f}$ denote the 2nd forward estimation and covariance, respectively, while $\hat{x}_{k,b}$ and $P_{k,b}$ present the backward estimation and covariance.

It should be noticed that the backward state propagation in Equation (22) is in the negative of time interval. It avoids the matrix inversion like other EKF smoothers. Similarly, the backward INS equations are also implemented in the negative of time interval. Therefore, only the time interval is changed for both backward EKF and backward INS compared to the standard algorithm. This makes the forward and backward algorithm possible to share the same coding

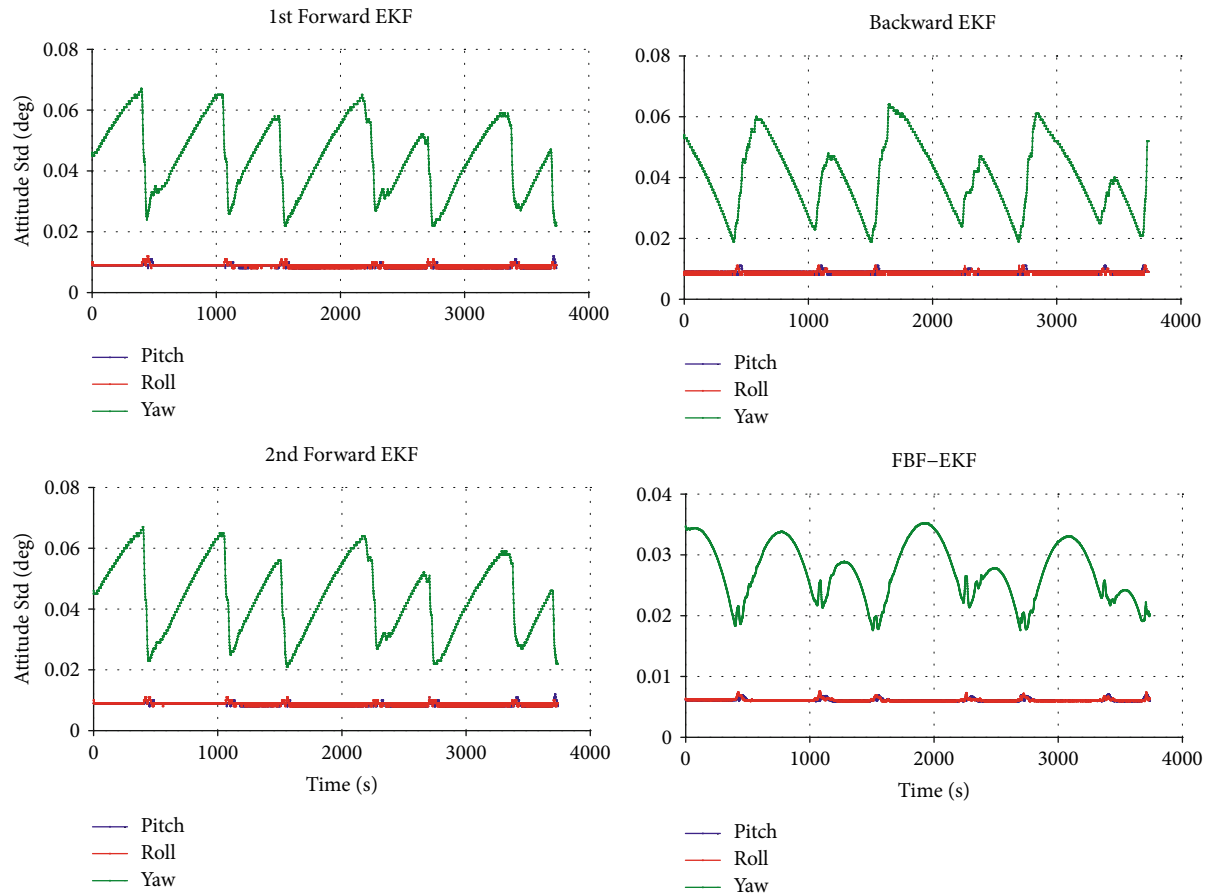


FIGURE 8: Attitude Std of FBF-EKF.

function and facilitates the FBF-EKF being extended from the EKF algorithm.

5. Aerial Test and Performance Assessment

To evaluate the performance of the proposed FBF-EKF algorithm, an aerial surveying task was performed in Huanghua, Hebei Province, China. Dual-frequency GPS/GLOANSS/BDS data of both base and rover receivers were collected with a sampling rate of 1 Hz. The flying time in surveying area was about 1 hour, and the longest baseline was about 50 km. An FOG based IMU with 200 Hz sampling rate was rigidly mounted with camera sensor to provide its exterior orientation elements. Figure 4 shows the assembly of all sensors, and the trajectory in surveying area is shown in Figure 5. The surveying area was 22 km long and 5.3 km wide, covered by 7 straight routes.

The position standard deviation (Std) of FBF-EKF on surveying routes was displayed in Figure 6, including the 1st forward, backward, 2nd forward, and the smoothing EKF. We observe that the Std of three single-directional EKF have similar values. Both horizontal and elevation Std are less than 5 cm for most epochs, while the smoothing EKF has smaller Std compared to single-directional EKF. All the four processing have a peak at the time of 45 min due to 10 seconds GNSS interruption.

To investigate the performance of FBF-EKF, partial details around GNSS interruption are presented in Figure 7. We find that the error presents periodicity according to GNSS observation. In each GNSS interval, the error of forward EKF grows up with increased time and reaches the largest value at end of the interval. However, the error of backward EKF rises with decreasing time and reaches the largest value at beginning of the interval. For the smoothing EKF, the error exhibits archy appearance. It rises and drops in each GNSS interval. The maximum error happens at middle of the GNSS observation. The maximum Stds of 2nd forward EKF in GNSS interruption are 21.6 cm, 21.5 cm, and 13.3 cm in the east, north, and elevation directions, respectively. By contrast, their values are 7.9 cm, 8.0 cm, and 6.5 cm, respectively, by smoothing EKF. In this way, the positioning error was reduced to approximate 37% in horizontal and 49% in elevation after utilizing smoothing EKF. On the other hand, it is reasonable to assume that positioning error grows quadratically with time, since the specific force is integrated twice to calculate position. After a combination of forward and backward EKF, the largest error happens at the middle time of each GNSS interval, where the error is approximately a quarter of the largest in theory, which is close to the performance obtained by processing results.

Figure 8 presents the attitude Std by single-directional EKF and smoothing EKF. It has the same characteristics with position Std when single-directional EKF and smoothing EKF

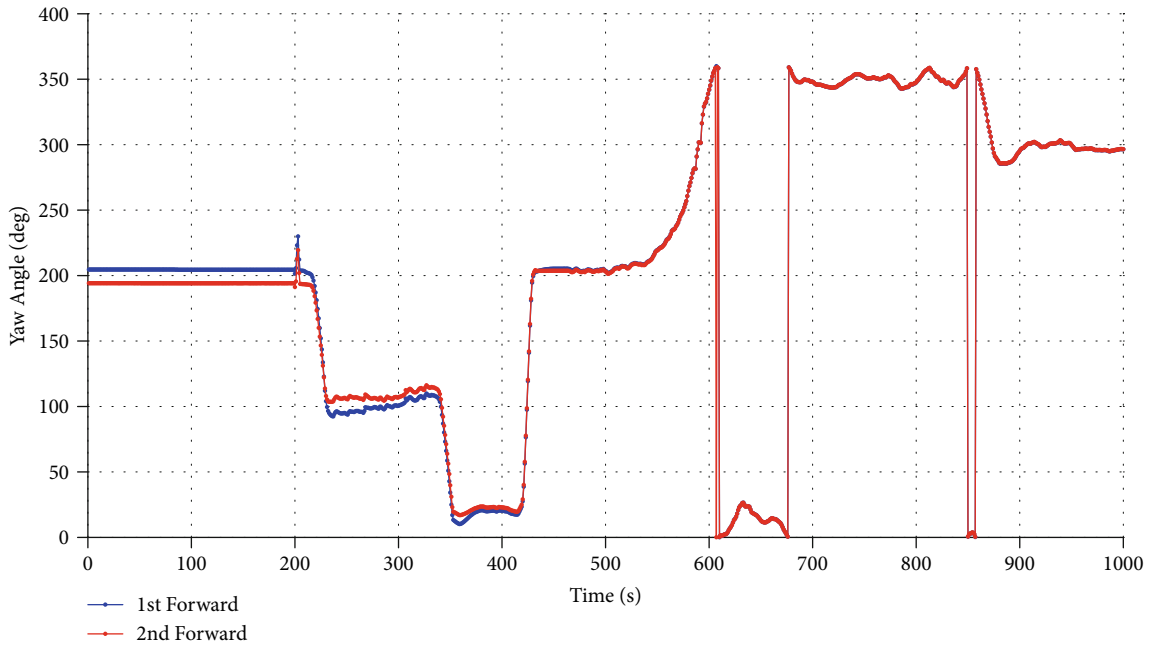


FIGURE 9: Initial yaw angle of the 1st and 2nd forward EKF.

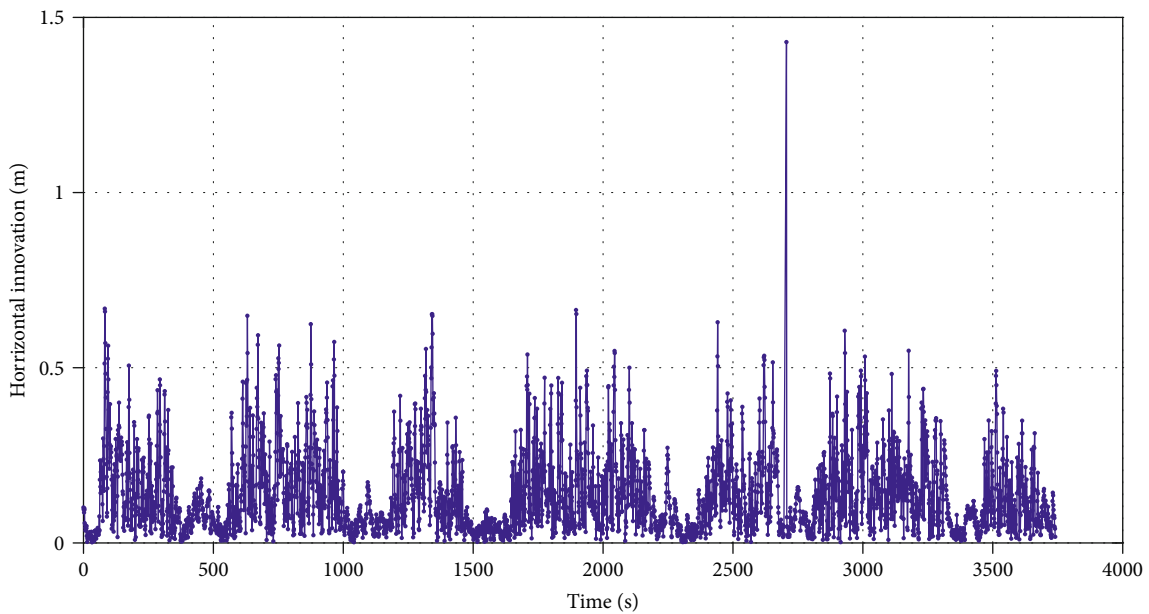


FIGURE 10: Horizontal innovation of the 2nd forward EKF.

are considered. The pitch and roll standard deviation are less than 0.01° , and the yaw is within 0.07° for single-directional EKF. By comparison, the smoothing EKF has better accuracy. The pitch and roll standard deviation are less than 0.008° , and the yaw is within 0.04° . However, the periodicity of attitude Std are different from position Std. Yaw Std presents obvious periodicity according to flight route, and it is contrary to position Std that possesses periodicity coincident with GNSS observation. Specifically, yaw Std grows up with increasing time by forward EKF and rises with decreasing time by backward EKF. For smoothed EKF, the yaw Std rises in the first half of

a straight route and decreases in the second half. This is because yaw has weak observability when the plane is in a straight movement. When the plane makes maneuvering like a U-turn, it can help calibrate the yaw angle. Another reason is the smoothing algorithm. Forward filtering yields a good estimation at beginning of the straight route but deteriorates at the end, while backward filtering has the opposite function. As a consequence, smoothing EKF presents an archy error in one straight route, compared to monotone increasing error by single-directional EKF. The value of attitude error is also reduced by the smoother.

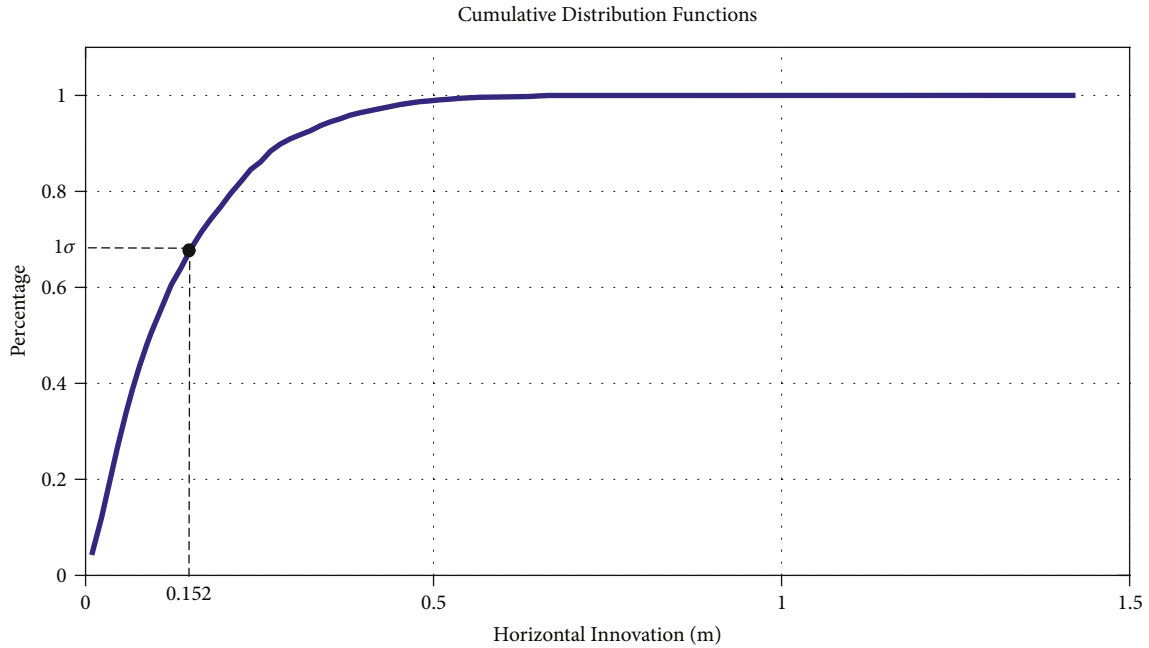


FIGURE 11: Cumulative distribution of horizontal Innovation in the 2nd forward EKF.

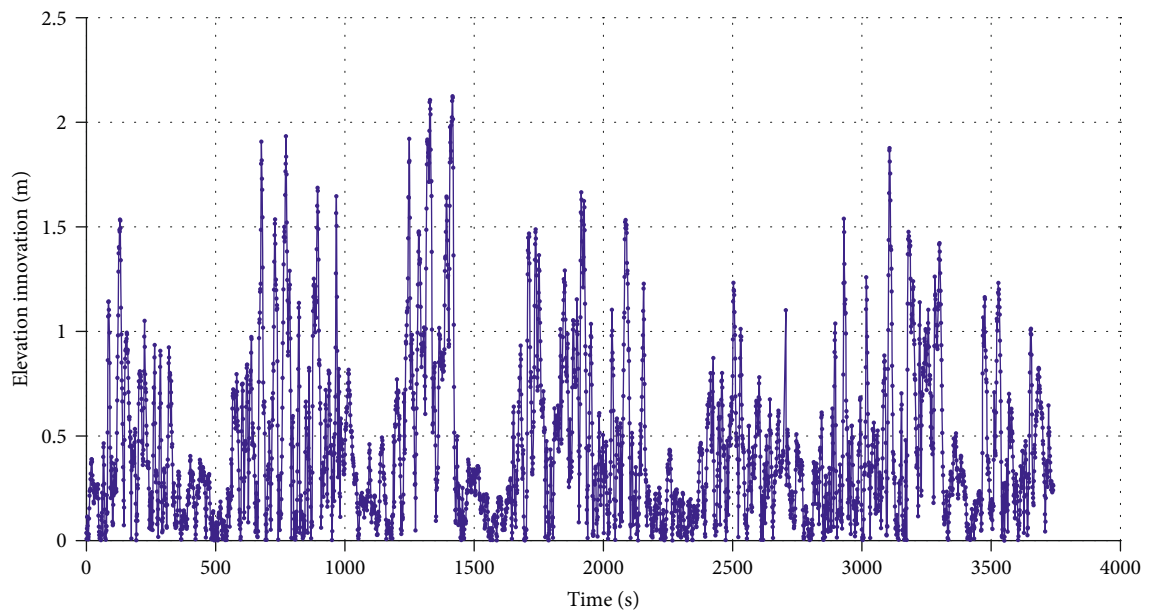


FIGURE 12: Elevation innovation of the 2nd forward EKF.

Figure 9 demonstrates the yaw angle of the 1st and 2nd forward filtering at beginning time of the test. We observe that there is about a 10.2-degree difference between two forward EKF at the beginning, and the difference decreases after the airplane starts at 200 s. After 5-minute maneuvering, the yaw angles between two forward EKF are basically identical. This is because the attitude is not convergent after coarse and fine alignment in the 1st forward EKF. It will deteriorate the smoother if 1st forward EKF and backward EKF are combined. In the FBF-EKF, the 2nd forward EKF is initialized by backward EKF, which makes better estima-

tion of attitude at the beginning time. Therefore, the 2nd forward EKF is essential to situations with deficient maneuver, during when the system cannot get convergent before entering surveying route.

Figure 10 presents horizontal positioning innovation of the 2nd forward EKF, while Figure 11 displays the cumulative distribution of positioning innovation. Elevation innovation of the 2nd forward EKF and its cumulative distribution are shown in Figures 12 and 13, respectively. Due to similar results as the 2nd forward EKF, innovation of the 1st forward EKF and backward EKF is not displayed

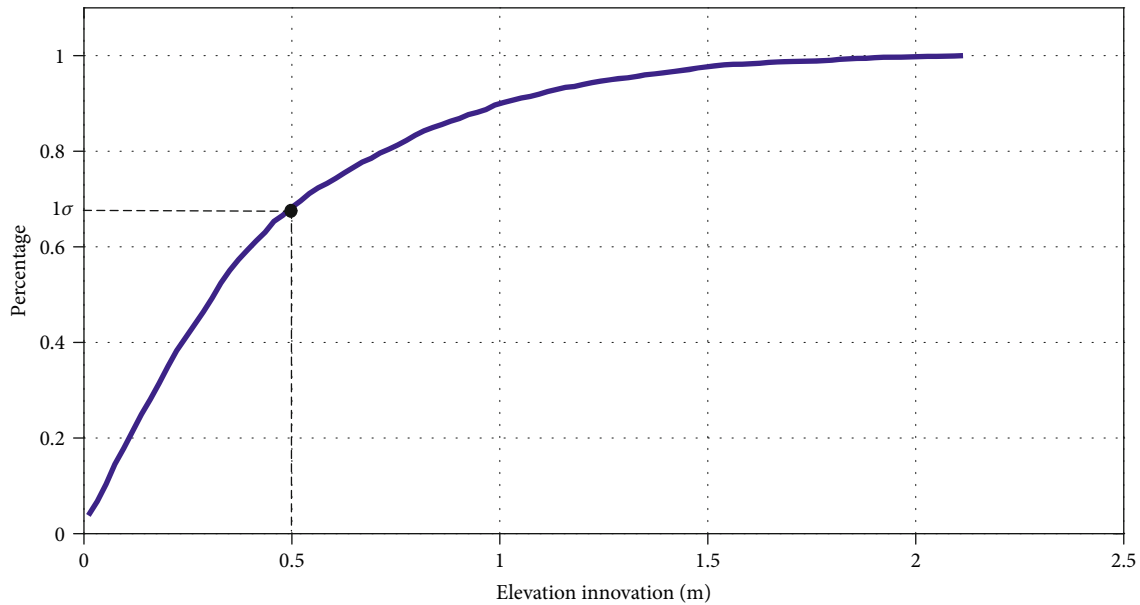


FIGURE 13: Cumulative distribution of elevation innovation in the 2nd forward EKF.

here. Considering differential GNSS result as a reference, innovation, that is, the observation in Equation (19), is used as evaluation of the INS error. We find that the forward EKF has horizontal positioning accuracy of 15.2 cm (1σ) and elevation positioning accuracy of 49.9 cm (1σ). According to Figures 6 and 7, the horizontal and elevation error can be reduced to 37% and 49% of single-directional EKF after the smoothing algorithm has been implemented. Therefore, the horizontal and elevation positioning accuracy of FBF-EKF are about 5.6 cm (1σ) and 24.4 cm (1σ), respectively. The largest error also happens at the middle time of each GNSS observation interval.

6. Conclusions

This paper studies the stochastic process modelling and smoothing method of GNSS/INS-integrated direct georeferencing system. To identify and evaluate the error types and values, Allan variance is applied for IMU static data of eight hours. Four types of stochastic errors are considered, that is, bias, rate random walk, scale factor, and white noise. A 27-order error state vector is established, including navigation errors and stochastic errors of IMU. In order to solve the problem of inaccuracy model, strong nonlinearity, and weak observability, which are commonly occurred in aerial photogrammetry applications, a new FBF-EKF is proposed to make optimal estimation. It carries out triple EKF, in which the 1st EKF converges the system and the last two smooth the error. This new scheme avoids inaccuracy of the 1st forward EKF and makes it possible to implement the same EKF equations and codes for all the three filtering process. Our testing result indicates that the horizontal and elevation accuracy can be improved by 63% and 51%, respectively, by utilizing the proposed algorithm. Finally, it leads to positioning accuracy of centimeter level (5.6 cm) in horizontal and decimeter level (24.4 cm) in elevation.

Data Availability

Raw data were generated at Chongqing University. Derived data supporting the findings of this study are available from the corresponding author lill@cqu.edu.cn.

Conflicts of Interest

The authors declare no conflict of interest.

Acknowledgments

This research was funded by the National Natural Science Foundation of China (Grant No. 42004017), National Dam Safety Research Center (Grant No. CX2019B05), and Open Research Fund of State Key Laboratory of Information Engineering in Surveying, Mapping and Remote Sensing, Wuhan University (Grant No. 20P02).

References

- [1] J.-C. Padró, F. J. Muñoz, J. Planas, and X. Pons, "Comparison of four UAV georeferencing methods for environmental monitoring purposes focusing on the combined use with airborne and satellite remote sensing platforms," *International Journal of Applied Earth Observation and Geoinformation*, vol. 75, pp. 130–140, 2019.
- [2] H. Sun, L. Li, X. Ding, and B. Guo, "The precise multimode GNSS positioning for UAV and its application in large scale photogrammetry," *Geo-spatial Information Science*, vol. 19, no. 3, pp. 188–194, 2016.
- [3] F. Benassi, E. Dall'Asta, F. Diotri et al., "Testing accuracy and repeatability of UAV blocks oriented with GNSS-supported aerial triangulation," *Remote Sensing*, vol. 9, no. 2, p. 172, 2017.
- [4] K. G. Nikolakopoulos, K. Soura, I. K. Koukouvelas, and N. G. Argyropoulos, "UAV vs classical aerial photogrammetry for

- archaeological studies,” *Journal of Archaeological Science: Reports*, vol. 14, pp. 758–773, 2017.
- [5] L. Li, D. A. G.-B. Pan, C. K. Toth, and H. Sun, “Allan variance analysis of the H764G stochastic sensor model and its application in land vehicle navigation,” in *Proceedings of the 2010 International Technical Meeting of the Institute of Navigation*, pp. 22–30, San Diego, CA, 2010.
- [6] B. Cui, X. Chen, Y. Xu, H. Huang, and X. Liu, “Performance analysis of improved iterated cubature Kalman filter and its application to GNSS/INS,” *ISA Transactions*, vol. 66, pp. 460–468, 2017.
- [7] X. Chen, X. Wang, and Y. Xu, “Performance enhancement for a GPS vector-tracking loop utilizing an adaptive iterated extended Kalman filter,” *Sensors*, vol. 14, no. 12, pp. 23630–23649, 2014.
- [8] Y. Meng, S. Gao, Y. Zhong, G. Hu, and A. Subic, “Covariance matching based adaptive unscented Kalman filter for direct filtering in INS/GNSS integration,” *Acta Astronautica*, vol. 120, pp. 171–181, 2016.
- [9] S. J. Julier and J. K. Uhlmann, “Unscented filtering and nonlinear estimation,” *Proceedings of the IEEE*, vol. 92, no. 3, pp. 401–422, 2004.
- [10] F. Gustafsson, “Particle filter theory and practice with positioning applications,” *IEEE Aerospace and Electronic Systems Magazine*, vol. 25, no. 7, pp. 53–82, 2010.
- [11] M. Moradi, S. Talaei, and S. Nasrollahi, “Comparison of particle filter performance with extended and hybrid extended Kalman filter in INS/GPS data fusion,” *Journal of Aeronautical Engineering*, vol. 22, no. 2, pp. 41–55, 2020.
- [12] J. Georgy, A. Noureldin, M. J. Korenberg, and M. M. Bayoumi, “Low-cost three-dimensional navigation solution for RISS/GPS integration using mixture particle filter,” *IEEE Transactions on Vehicular Technology*, vol. 59, no. 2, pp. 599–615, 2010.
- [13] C. Shen, Y. Zhang, X. Guo et al., “Seamless GPS/inertial navigation system based on self-learning square-root cubature Kalman filter,” *IEEE Transactions on Industrial Electronics*, vol. 68, no. 1, pp. 499–508, 2021.
- [14] S. Du, S. Zhang, and X. Gan, “A hybrid fusion strategy for the land vehicle navigation using MEMS INS, odometer and GNSS,” *IEEE Access*, vol. 8, pp. 152512–152522, 2020.
- [15] D. Simon, *Optimal State Estimation: Kalman, H ∞ , and Non-linear Approaches*, John Wiley and Sons, Hoboken, NJ, 2006.
- [16] M. Elbahnasawy, T. Shamseldin, and A. Habib, “Image-assisted GNSS/INS navigation for UAV-based mobile mapping systems during GNSS outages,” in *2018 IEEE/ION Position, Location and Navigation Symposium (PLANS)*, pp. 417–425, Monterey, CA, 2018.
- [17] H. Liu, S. Nassar, and N. El-Sheimy, “Two-filter smoothing for accurate INS/GPS land-vehicle navigation in urban centers,” *IEEE Transactions on Vehicular Technology*, vol. 59, no. 9, pp. 4256–4267, 2010.
- [18] S. Sarkka and J. Hartikainen, “On Gaussian optimal smoothing of non-linear state space models,” *IEEE Transactions on Automatic Control*, vol. 55, no. 8, pp. 1938–1941, 2010.
- [19] Z. Liu and S.-C. Chan, “Adaptive fading Bayesian unscented Kalman filter and smoother for state estimation of unmanned aircraft systems,” *IEEE Access*, vol. 8, pp. 119470–119486, 2020.
- [20] IEEE, “IEEE standard for inertial sensor terminology,” in *IEEE Std 528-2001*, The Institute of Electrical and Electronics Engineers, Inc., New York, NY, 2001.
- [21] IEEE, “IEEE standard specification format guide and test procedure for single-axis laser gyros,” in *IEEE Std 647-2006 (Revision of IEEE Std 647-1995)*, The Institute of Electrical and Electronics Engineers, Inc., New York, NY, 2006.
- [22] C. Jekeli, *Inertial Navigation Systems with Geodetic Applications*, Walter de Gruyter, Berlin, Germany, 2001.
- [23] D. H. Titterton and J. L. Weston, *Strapdown Inertial Navigation Technology*, The American Institute of Aeronautics, Reston, Virginia, USA, 2d ed. edition, 2004.

Research Article

Orthorectification of WorldView-3 Satellite Image Using Airborne Laser Scanning Data

Biswajeet Pradhan ^{1,2}, Ahmed A. Ahmed,¹ Subrata Chakraborty ¹, Abdullah Alamri,³ and Chang-Wook Lee ⁴

¹Centre for Advanced Modelling and Geospatial Information System (CAMGIS), Faculty of Engineering and IT, University of Technology, Sydney, NSW 2007, Australia

²Earth Observation Center, Institute of Climate Change, Universiti Kebangsaan Malaysia, 43600 UKM, Bangi, Selangor, Malaysia

³Department of Geology and Geophysics, College of Science, King Saud University, P.O. Box 2455, Riyadh 11451, Saudi Arabia

⁴Division of Science Education, Kangwon National University, Kangwondaehak-gil, Chuncheon-si, Gangwon-do 24341, Republic of Korea

Correspondence should be addressed to Biswajeet Pradhan; biswajeet24@gmail.com

Received 30 July 2021; Revised 13 September 2021; Accepted 1 October 2021; Published 16 October 2021

Academic Editor: Qiu-Zhao Zhang

Copyright © 2021 Biswajeet Pradhan et al. This is an open access article distributed under the Creative Commons Attribution License, which permits unrestricted use, distribution, and reproduction in any medium, provided the original work is properly cited.

Satellite images have been widely used to produce land use and land cover maps and to generate other thematic layers through image processing. However, images acquired by sensors onboard various satellite platforms are affected by a systematic sensor and platform-induced geometry errors, which introduce terrain distortions, especially when the sensor does not point directly at the nadir location of the sensor. To this extent, an automated processing chain of WorldView-3 image orthorectification is presented using rational polynomial coefficient (RPC) model and laser scanning data. The research is aimed at analyzing the effects of varying resolution of the digital surface model (DSM) derived from high-resolution laser scanning data, with a novel orthorectification model. The proposed method is validated on actual data in an urban environment with complex structures. This research suggests that a DSM of 0.31 m spatial resolution is optimum to achieve practical results (root-mean-square error = 0.69 m) and decreasing the spatial resolution to 20 m leads to poor results (root-mean-square error = 7.17). Moreover, orthorectifying WorldView-3 images with freely available digital elevation models from Shuttle Radar Topography Mission (SRTM) (30 m) can result in an RMSE of 7.94 m without correcting the distortions in the building. This research can improve the understanding of appropriate image processing and improve the classification for feature extraction in urban areas.

1. Introduction

Increased availability of high-resolution satellite images is driving the rapid expansion in remote sensing applications, including commercial, industrial, governmental, and research domains [1–10]. High-resolution satellite images are also commonly used in urban remote sensing applications, such as change detection, urban sprawl, land use/land cover mapping, environmental studies, and transportation [5–7].

Terrain distortions in satellite imagery off-nadir angle data acquisition require sophisticated data preprocessing algorithms to obtain useful data for these applications. The

effect of relief displacement on off-nadir satellite images causes difficulty in accurately extracting features in urban areas surrounded by high-rise buildings. Joshi et al. [2] and Peng et al. [6] suggested that using elevation data or multiple images acquired from different angles in remote sensing applications, such as image classification, building detection, and city modeling, is preferable. These problems originated from the reduced pixel dimensions and off-nadir viewing. One approach to correct such geometric errors in satellite images is called orthorectification, which is the adjustment of a perspective image geometrically to an orthogonal image by transforming the coordinates from an image to the ground spaces and removing relief displacements and tilt.

Different from other terrain correction methods, which depend on the horizontal position of image pixels [11], orthorectification considers the pixel positional shift caused by the earth's curvature and provides actual ground coordinates (X , Y , and Z values) for all pixels. Orthorectification requires a digital elevation model (DEM) and ground control points (GCPs). The DEM can be obtained from a variety of sources with various resolutions, such as Radarsat-1 and Light Detection and Ranging (LiDAR) data [12].

Several techniques and algorithms have been developed to improve the orthorectification processes and decrease the distortions resulting from these processes. Belfiore and Parente [13] compared different methods, including polynomial functions and rational functions, for correcting deformations of WorldView-2 satellite images with a variable number of GCPs. The rational functions were more suitable than the other techniques for correcting deformations in WorldView-2 images. Prakash et al. [14] proposed an inverse orthorectification method, which utilizes road data and DEM to correct geometric deformations in satellite images. These methods showed acceptable accuracy and improved the road feature extraction from satellite images. Alrajhi et al. [15] developed an automatic procedure that can orthorectify high-resolution satellite images with no GCPs and can respond to real-time geospatial data updates. Furthermore, Whiteside and Bartolo [16] investigated orthorectified images with the aid of the sensor's rational polynomial coefficients (RPCs) and GCPs using differential global positioning system (DGPS) with an accuracy of 10 cm. Zhang et al. [1] proposed a new method for integrated PCI-RPC and ArcGIS-Spline tools for orthorectification in satellite images. The integrated approach improved the RMSE accuracy from 2.94 m to 1.10 m. Henrico et al. [15] developed an orthorectification process based on high-quality 2 m DEM and applied two different GCP collection methods. First, field survey method with the aid of DGPS was adopted. In the second method, TerraSAR-X-based GCPs were acquired from Airbus Defense and Space. The manual GCPs yielded better positional orthoimages than the TerraSAR-X-based GCPs [17, 18].

The above literature review shows the various orthorectification processing methods. However, many researches confined correction the image geometry based on DEM and DSM data, not on the correcting the buildings distortions of high-resolution satellite images. As a result, the following sections present and discuss a novel orthorectification method designed for WorldView-3 data with a high off-nadir angle. The following important questions are answered: (1) the required resolution of DSM data to obtain practical results and (2) whether or not using high-resolution DSM data instead of the freely available digital elevation models is beneficial or is the latter sufficient for correcting terrain distortions in WorldView-3 imageries.

2. Materials and Methods

2.1. Study Area. The experiment was conducted in an area located in Selangor, Malaysia, that is geographically bounded between (101°30'–102°0') E and (3°00'–3°30') N. The study

area was carefully selected to successfully achieve our objectives. Various land uses, such as residential, commercial, industrial, public, sport, educational, and religious facilities, and land covers related to human activities are available in the study area, as shown in Figure 1.

2.2. Datasets. Laser cloud points: point clouds are defined as a set of vertices in a three-dimensional coordinate system, and these clouds add a new type of geometry to the system. Point clouds, as the output of 3D scanning processes, have many purposes, such as creating 3D models for multitude visualization, rendering, animation, and mass customization applications. In this research, airborne LiDAR point clouds were used to create an extremely high-resolution DEM and digital surface model (DSM), as shown in Figure 2. The LiDAR data were gathered by using an airborne system (Optech Airborne Laser Terrain Mapper 3100) on November 2, 2015. The camera had a spatial resolution of 10 cm; the laser scanner had a scanning angle of 60° with a camera angle of $\pm 30^\circ$ and the flying height of 1510 m with clear skies. The posting density of the LiDAR data was 3–4 pts/m² (average point spacing = 0.30 m) with a 25,000 Hz pulse rate frequency. The number of points is 1,300,000 points for the study area.

WorldView-3: the WorldView-3 satellite image showed eight bands of panchromatic spatial resolution, multispectral, short-wave infrared, and Clouds, Aerosols, Vapours, Ice, and Snow (CAVIS) resolution at 0.31, 1.24, 3.7, and 30 m, respectively. The four standard VNIR colours were blue, green, red, and near-infrared, and the additional VNIR colours were coastal, yellow, red edge, and near-IR2. Twelve (12) CAVIS bands (atmospheric sensor) were used, and the off-nadir angle was 14°. The data were gathered on April 25, 2015.

2.3. Methodology. Figure 3 shows the methodology adopted in this research using orthorectification and involves an indirect method. The indirect method requires building the RPC model to derive at least four GCPs from DEM 30 cm. A total of 55 GCPs, which were derived from DEM of 30 cm, were used. Orthorectification was applied through ArcGIS application to process the oblique images of tall buildings. Moreover, global mapper software was used to process the LiDAR data, whereas ENVI was used to build the RPCs, radiometric calibration, geometric calculations, and filtering. Pan-sharpening was responsible for merging high-resolution panchromatic and low-resolution multispectral images of the WorldView-3 to produce a high-resolution colour image.

Data preparation: two distinct datasets are prepared for this study.

- (1) LiDAR data processing: it consists of multiple steps, beginning with LiDAR georeferencing. It is defined by transforming the LiDAR data coordinate system to the Universal Transverse Mercator projection and the world geodetic system 1984 datum by using Global Mapper. The LiDAR data are classified based on the multiscale curvature classification (MCC)

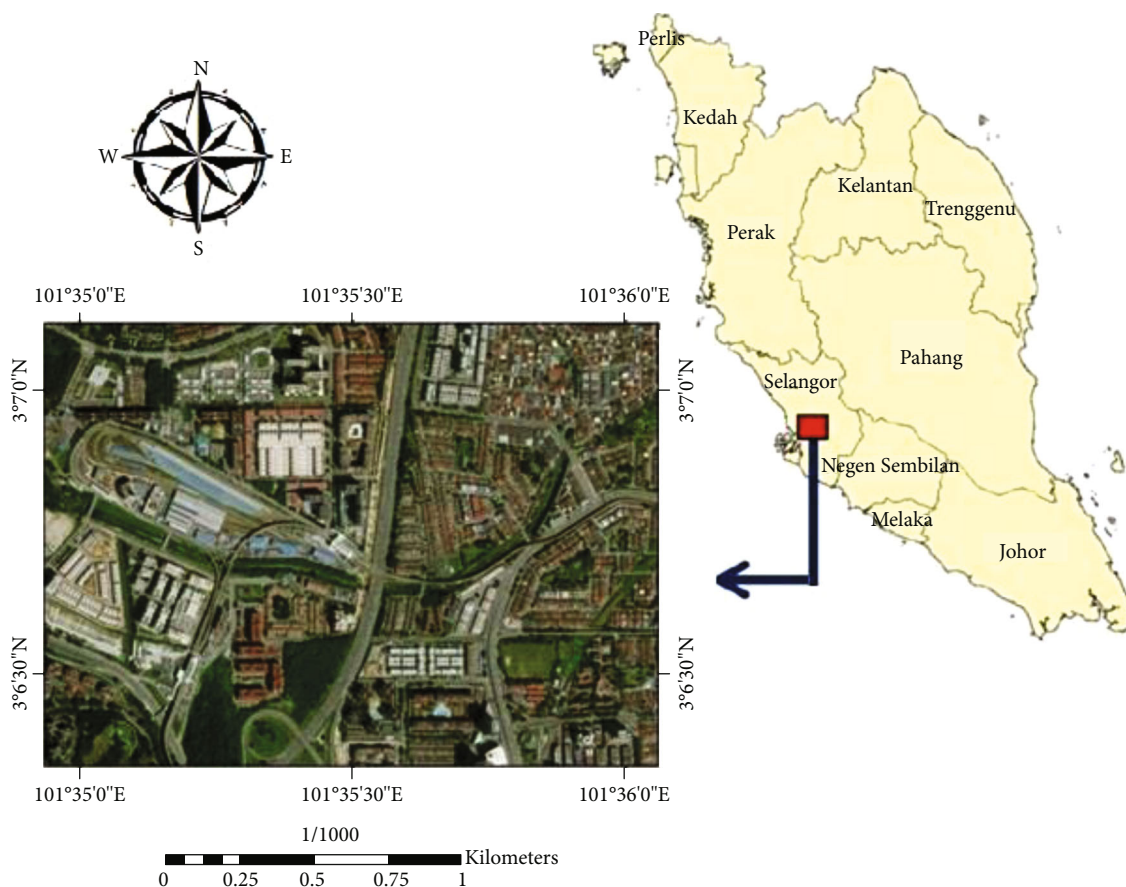


FIGURE 1: Study area map.

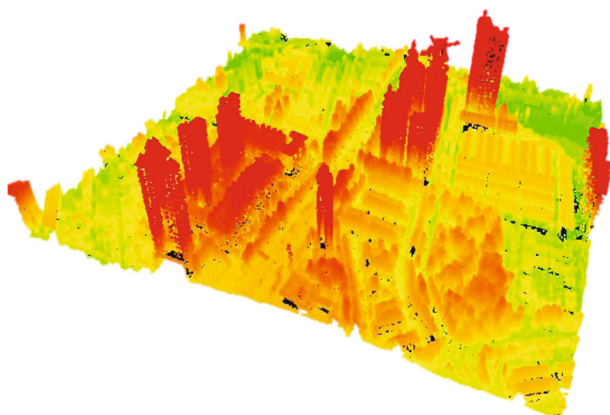


FIGURE 2: LiDAR point clouds representing the study area.

method [11] to classify the data into ground points and nonground points. Filtering is then applied to remove existing noise from the cloud points. However, the LiDAR data derived from DEM and DSM were created based on the point clouds with extension LAS by using the ArcGIS application. The multiscale curvature classification (MCC) algorithm was applied to classify the LiDAR returns to the ground and nonground points. The algorithm incorporated

curvature filtering with a scale component and variable curvature tolerance. A surface was interpolated at different resolutions using the thin-plate spline method [19], and the points were classified based on a progressive curvature threshold parameter. The curvature tolerance parameter increased as resolution coarsened to compensate for the slope effect because the data were generalized. Moreover, the DEM applied was 0.31 m, and the DSM values were 0.31, 0.5, 1, 3, 5, 10, 15, and 20 m

- (2) WorldView-3 image processing: this requires calibration because the spectral data acquired by the satellite sensors are influenced by several factors, such as sensor calibration, atmospheric absorption and scattering, sensor-target-illumination geometry, and image calibration, and these factors tend to change overtime. Therefore, radiometric correction must be performed by detecting actual landscape changes, as revealed by the changes in surface reflectance from multirate satellite images. After image calibration, we used and applied the pan-sharpening tool to merge the WorldView-3 panchromatic image (31 cm) with WorldView-3 multispectral image (1.24 m) to produce a high resolution of 31 cm with eight bands. This process involves producing a single high-resolution colour image by merging high-

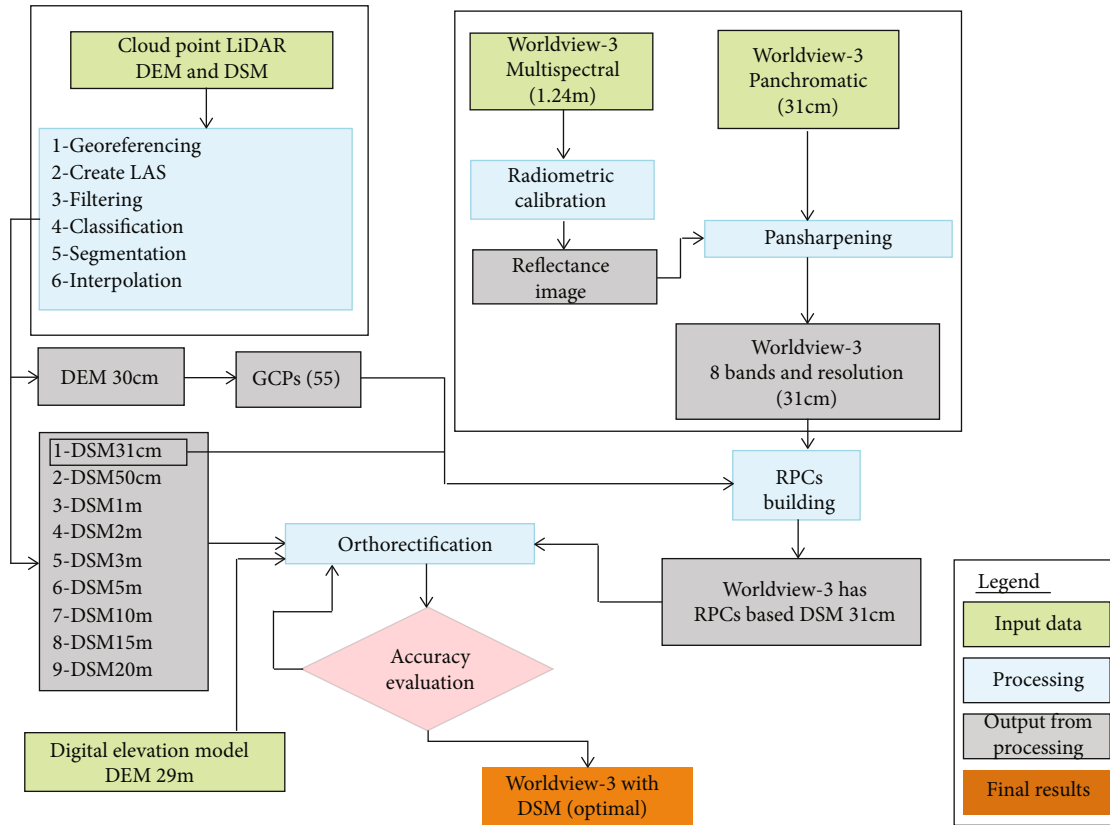


FIGURE 3: Methodology used in this study.

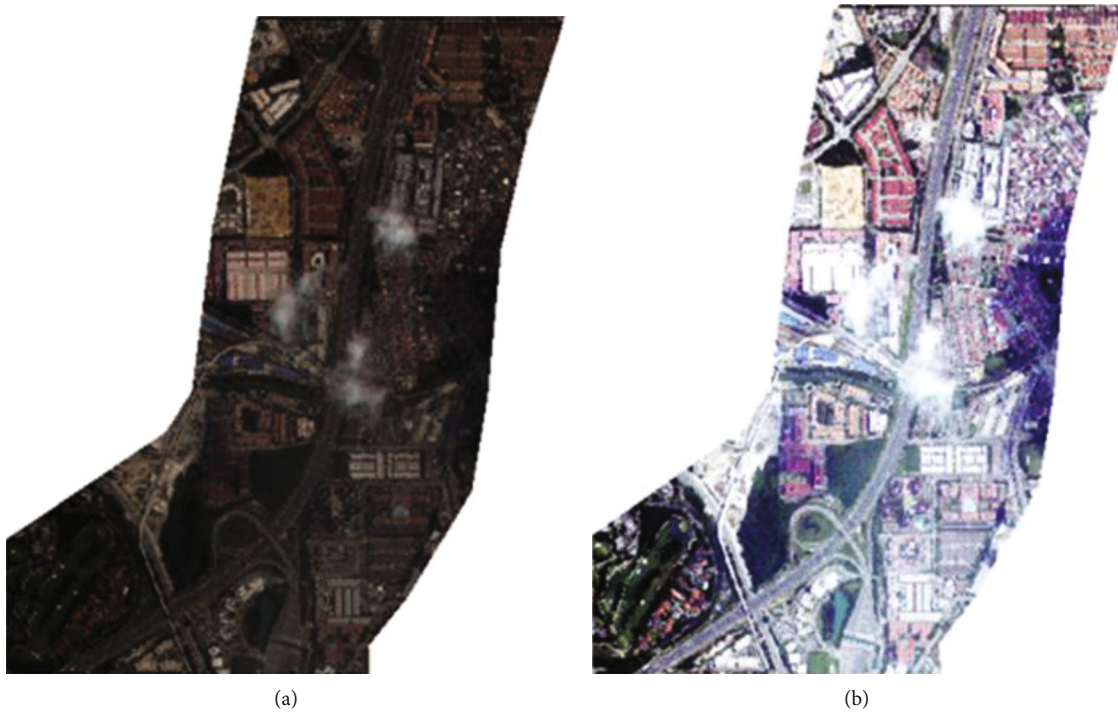


FIGURE 4: WorldView-3 after calibration and pan-sharpened process (a) before and (b) after.



FIGURE 5: GCP distribution on DEM raster.

resolution panchromatic and lower-resolution multispectral images. The benefit of this process is to obtain multispectral resolution with high-spatial resolution. Figure 4 shows the WorldView-3 image, before and after results of the processing

Orthorectification model: the modeling involves three stages.

- (1) GCP collection: GCP collection is required for orthorectification. In this study, the GCP data were acquired through a very high-resolution DEM (31 cm) based on LiDAR [12]. During orthorectification, 55 points were used in the area under consideration. Each GCP was situated on easily identifiable objects in the image that can be obtained in the field. It is positioned in the angle of the identified objects displayed in high contrast; the objects are usually artificial, such as bridges, street corner, and buildings. But in this study, we focused on the distortion building which the number of the distortion building is 43 in this study, so we added the GCP on these buildings as shown in Figure 5
- (2) Rectification model with RPC: Grodecki and Dial [20] reported that the RPC model is developed based on GCPs and DEM data to orthorectify images. This model is superior to the sensor model used to acquire lines and rows of images by using the ratio of two polynomial functions, which are functions of the ground coordinates. Nichol et al. [21] inferred that the RPC model is developed to generalize the polynomial and linear transform model, which is appropriate for different sensor types. In the RPC rectification model, the image coordinates are the

ratios of two polynomials, in which the three-dimensional coordinates of GCPs are set as independent variables, as shown in

$$\left(r_n = \frac{P_1(X_n, Y_n, Z_n)}{P_2(X_n, Y_n, Z_n)} \right), \quad (1)$$

$$\left(c_n = \frac{P_3(X_n, Y_n, Z_n)}{P_4(X_n, Y_n, Z_n)} \right), \quad (2)$$

where (r_n, c_n) and (X_n, Y_n, Z_n) are the normalized image coordinates (r, c) and ground coordinates (X, Y, Z) , respectively, derived from translating and scaling the RPC model.

$$\begin{aligned} \left(X_n = \frac{X - X_0}{X_s} \right), \\ \left(Y_n = \frac{Y - Y_0}{Y_s} \right), \\ \left(Z_n = \frac{Z - Z_0}{Z_s} \right), \\ \left(r_n = \frac{r - r_0}{r_s} \right), \\ \left(c_n = \frac{c - c_0}{c_s} \right), \end{aligned} \quad (3)$$

where $X_0, Y_0, Z_0, r_0,$ and C_0 represent the translating parameters for standardization, and these parameters are the coordinates of the origin of the RPC model in the mapping coordinate system. $X_s, Y_s, Z_s, r_s,$ and c_s are the proportionality parameters of standardization. In the polynomial, $P_i(X, Y, Z)$ ($i = 1, 2, 3, 4$) is the maximum, and the sum power of each coordinate component is not greater than three.

$$\begin{aligned} P(X, Y, Z) = & a_0 + a_1X + a_2Y + a_3Z + a_4XY + a_5XZ + a_6YZ \\ & + a_7X_2 + a_8Y_2 + a_9Z_2 + a_{10}XYZ + a_{11}X_2Y \\ & + a_{12}X_2Z + a_{13}Y_2X + a_{14}Y_2Z + a_{15}XZ_2 \\ & + a_{16}YZ_2 + a_{17}X_3 + a_{18}Y_3 + a_{19}Z_3, \end{aligned} \quad (4)$$

where the polynomial coefficients a_0, a_1, \dots, a_{19} are designated as the coefficients of the rational polynomial function. (2) Orthorectification principle of the RPC model:

$$\begin{aligned} \left(r = r_s \frac{P_1(X_n, Y_n, Z_n)}{P_2(X_n, Y_n, Z_n)} + r_0 \right), \\ \left(c = c_s \frac{P_3(X_n, Y_n, Z_n)}{P_4(X_n, Y_n, Z_n)} + c_0 \right), \\ r = r_s F(X_n, Y_n, Z_n) + r_0, \\ c = c_s G(X_n, Y_n, Z_n) + c_0. \end{aligned} \quad (5)$$



FIGURE 6: Image prior to orthorectification.

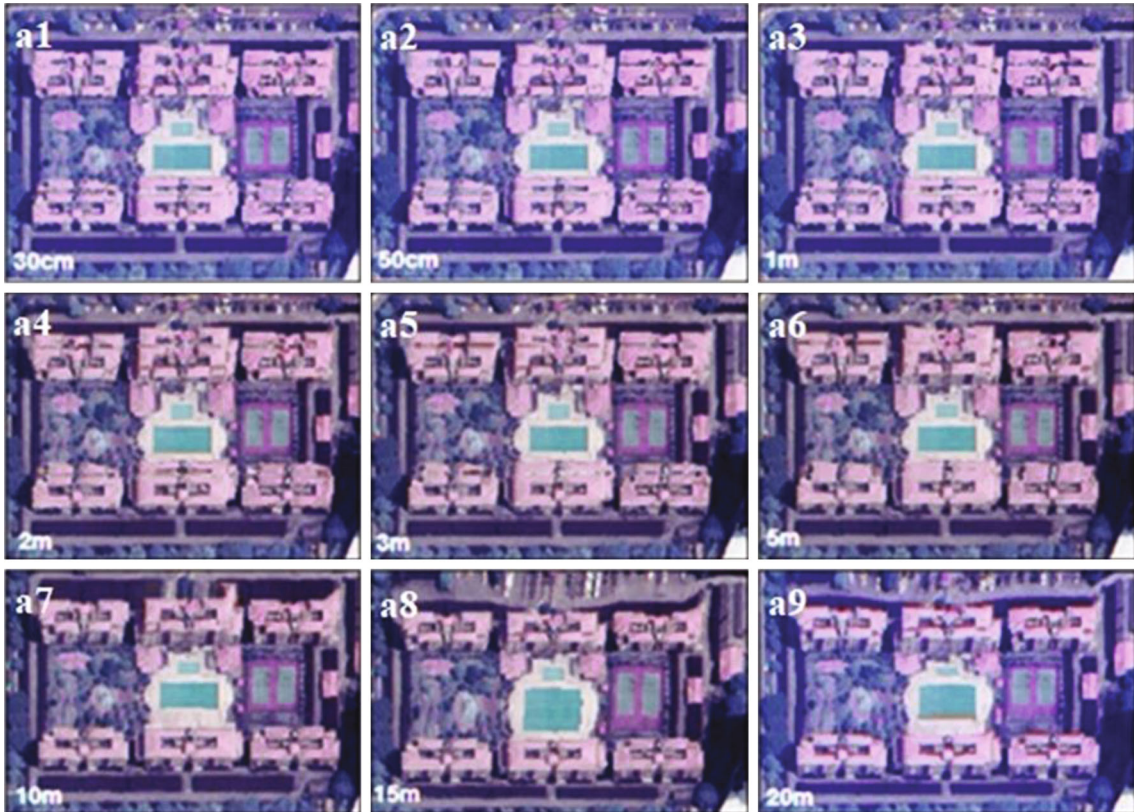


FIGURE 7: Image after orthorectification process based on different spatial resolution DSM.

Let $F(X_n, Y_n, Z_n) = (P_1(X_n, Y_n, Z_n)) / (P_2(X_n, Y_n, Z_n))$ and $G(X_n, Y_n, Z_n) = (P_1(X_n, Y_n, Z_n)) / (P_2(X_n, Y_n, Z_n))$; then, Equation (6) can be rewritten as follows:

$$\begin{cases} r = r + \frac{\partial_r}{\partial_x} \Delta X + \frac{\partial_r}{\partial_y} \Delta Y + \frac{\partial_r}{\partial_z} \Delta Z + r_0, \\ r = c + \frac{\partial_c}{\partial_x} \Delta X + \frac{\partial_c}{\partial_y} \Delta Y + \frac{\partial_c}{\partial_z} \Delta Z + c_0. \end{cases} \quad (6)$$

Equation (7) can be represented in Taylor formula format as follows:

$$\begin{cases} \vartheta_r = \begin{bmatrix} \frac{\partial_r}{\partial_x} & \frac{\partial_r}{\partial_y} & \frac{\partial_r}{\partial_z} \end{bmatrix} \begin{bmatrix} \Delta X \\ \Delta Y \\ \Delta Z \end{bmatrix} + (r - \hat{r}), \\ \vartheta_c = \begin{bmatrix} \frac{\partial_c}{\partial_x} & \frac{\partial_c}{\partial_y} & \frac{\partial_c}{\partial_z} \end{bmatrix} \begin{bmatrix} \Delta X \\ \Delta Y \\ \Delta Z \end{bmatrix} + (c - \hat{c}), \end{cases} \quad (7)$$

$$\begin{aligned}
V &= \begin{bmatrix} \vartheta_r \\ \vartheta_c \end{bmatrix}, \\
A &= \begin{bmatrix} \frac{\partial r}{\partial x} & \frac{\partial r}{\partial y} & \frac{\partial r}{\partial z} \\ \frac{\partial c}{\partial x} & \frac{\partial c}{\partial y} & \frac{\partial c}{\partial z} \end{bmatrix}, \\
\Delta &= \begin{bmatrix} \Delta X \\ \Delta Y \\ \Delta Z \end{bmatrix}, \\
l &= \begin{bmatrix} +(r - \hat{r}) \\ +(c - \hat{c}) \end{bmatrix}. \tag{8}
\end{aligned}$$

Lastly, the equation can be modified in a matrix and vector form, as follows:

$$V = A\Delta + l, \tag{9}$$

where $A\Delta$ is a matrix of $\Delta X, \Delta Y, \Delta Z$ representing the ground coordinates (X, Y, Z) and l is the normalized image coordinates.

Tao et al. suggested that the least squares solution of coordinate corrections can be derived from Equation (10), as follows:

$$\Delta = [\Delta X \quad \Delta Y \quad \Delta Z]^T = A^{-1}(V - l) = (A^T A)^{-1} A^T (V - l). \tag{10}$$

- (3) Orthorectification on GIS: orthorectification was applied using GIS tools to produce different orthorectified images that were derived from the integration of very high-resolution image (WorldView-3) and DSM with different accuracies, such as 0.31, 1, 2, 3, 5, 10, 15, and 20 m. The results were compared with one source (WorldView-3) to investigate the optimal image with DSM. Images can be orthorectified by pixel tying to an actual location in 3-dimensional (XYZ) space; orthorectification can be achieved with a mathematical model with RPCs or with a geometric model, which is more or less an internal sensor model; these techniques are called RPC orthorectification and rigorous orthorectification, respectively. Recently, several sensors, including RPCs, with image delivery systems have been used in this regard. Developing a system for images that are not associated with such RPCs is possible if the main properties of internal camera orientation and external environment are known. DEM, automated tie point generation, and a couple of ground control points can facilitate RPC orthorectification accurately

TABLE 1: Summary of residual errors of GCPs for orthoimages (unit: meter).

Warp image and DSM	Orthorectified image	RMSE
WorldView-3 and DSM 31 cm	a_1	0.638
WorldView-3 and DSM 50 cm	a_2	0.764
WorldView-3 and DSM 1 m	a_3	1.302
WorldView-3 and DSM 2 m	a_4	1.718
WorldView-3 and DSM 3 m	a_5	2.106
WorldView-3 and DSM 5 m	a_6	3.26
WorldView-3 and DSM 10 m	a_7	5.529
WorldView-3 and DSM 15 m	a_8	6.501
WorldView-3 and DSM 20 m	a_9	7.175
WorldView-3 and free DEM 30 m	a_{10}	7.947

3. Results and Discussion

3.1. WorldView-3 Image Orthorectification-Based GCPs and LiDAR DSM. WorldView-3 was orthorectified to the final orthoimage using the above-referenced method in Figure 6. The results are presented as nine images with different accuracies based on varying DSM resolutions (i.e., 31 cm, 50 cm, 1 m, 2 m, 3 m, 5 m, 10 m, 15 m, and 20 m) and GCPs, as shown in Figure 7.

3.2. Accuracy Assessment. Table 1 presents the results of the minimum, maximum, and the root-mean-square error (RMSE) of orthorectified images based on different DSM resolutions with respect to the GCPs. The horizontal accuracy of the orthorectified images is evaluated based on RMSE error value obtained by computing changes in the coordinate object at a very high-resolution DEM of 31 cm to the coordinate object in the orthoimage result. Equations (1), (2), and (3) [22] are used to determine the RMSE for X and Y coordinates and RMSE horizontal (X, Y), respectively.

$$RMSE = \sqrt{\frac{\sum_{i=1}^n (|x \text{ input} - x \text{ control}|)^2 + (|y \text{ input} - y \text{ control}|)^2}{n}}. \tag{11}$$

X and Y inputs represent the coordinates of the orthoimage WorldView-3 and X control; Y control represents the coordinates of the intensity of the DEM at 31 cm reference points. The parameters n and i represent the checkpoints tested for an integer between 1 to n , respectively. Table 1 indicates that the RMSE was 0.638 at DSM value of 31 cm. This value increased to 0.764 when the DSM resolution increased to 50 cm. A consistent increase in RMSE values was observed between DSM 1 m and 20 m resolution, yielding RMSE values from 1.302 to 7.175. Similarly, Figure 7 shows the image after orthorectification process based on different spatial resolution DSM such as a_1 with 31 cm and

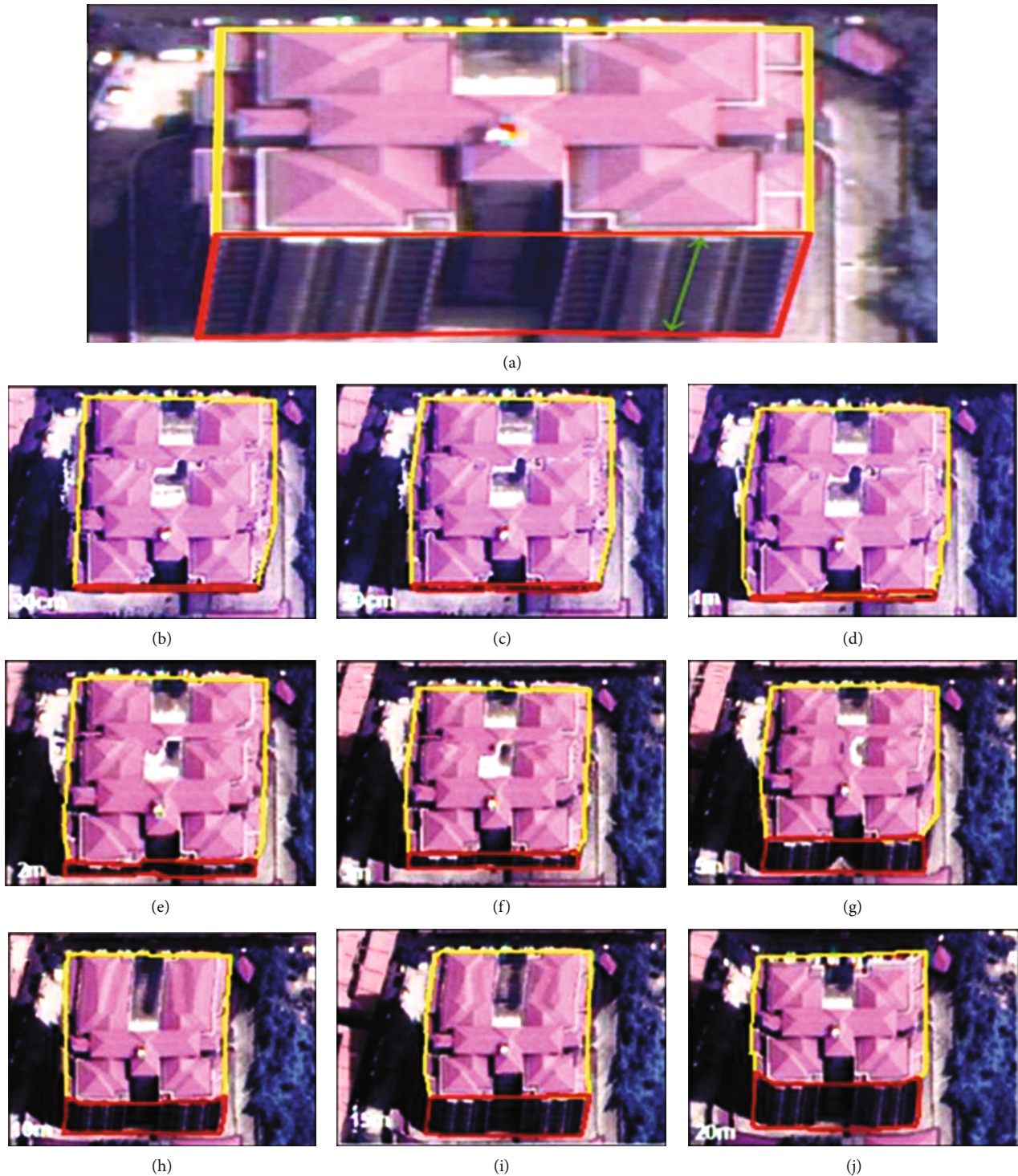


FIGURE 8: (a) Leaning of the building prior to orthorectification; (b–j) image after the orthorectification process and the effects of DSM accuracy on the building lean.

a_2 with DSM 50 cm. The experimental results consistently yielded the most accurate values for validating the GCPs of the orthoimage based on 30 cm DSM in orthoimages. Thus, the accuracy of the orthoimages was improved reasonably based on DSM data.

The RPC orthorectification model was applied to the WorldView-3 image based on the free source DEM of 30 m

(SRTM). The result obtained indicated the highest RMSE value of 7.947 compared with the orthoimage, which was obtained from high-resolution DSM of 31 cm (RMSE = 0.638). The significant difference between the DSM (31 cm) and the DEM (SRTM) (30 m) results indicated a unique relationship between the DEM or DSM accuracy and orthorectification accuracy.

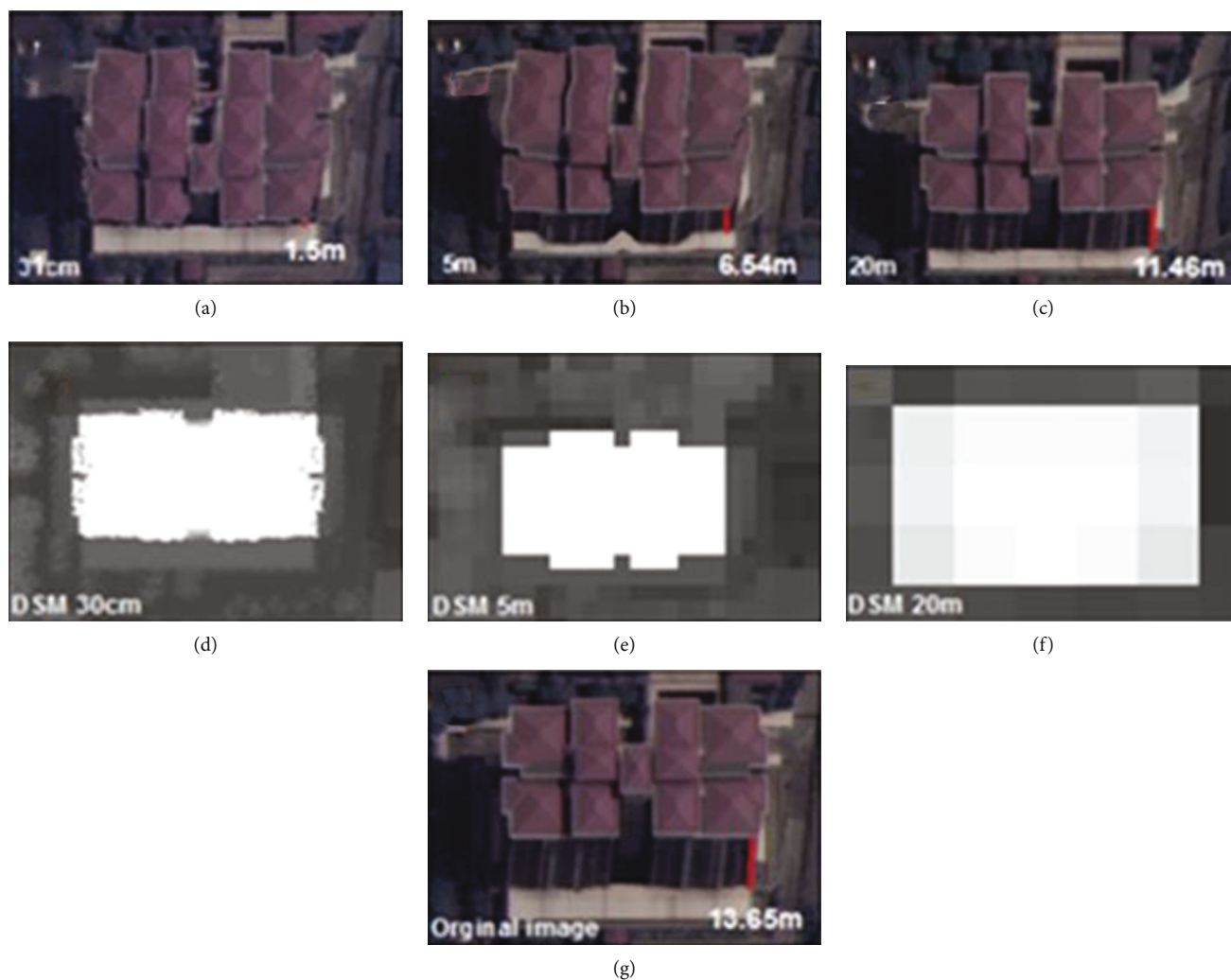


FIGURE 9: (a–f) Relation between DSM resolution and leaning of building; (g) image prior to the orthorectification process.

According to the results obtained, the final optimal DSM of the orthorectification process was 31 cm resolution, which showed the least RMSE value. The high-resolution DSM and GCPs derived from high-resolution DEM combined in the proposed model (RPC orthorectification model) reduced the RMSE of the orthorectification of the final result to 0.638 m compared with the 1.07 m achieved by Zhang et al. [1], who developed a model based on the combination of RPCs and the Spline Function Model and using DEM SRTM at 30 m. The orthorectification model was applied different times to produce various orthoimages. Each orthoimage showed different horizontal distortions and building lean effects. Therefore, increasing the DSM resolution increased the accuracy level of the orthoimages, whereas distortion and building lean effects were decreased, as shown in Figure 8. Additionally, our proposed was also applied for the orthorectification process on the scenario image (Figure 8) based on a varying resolution of DSM from 31 cm to 20 m.

The final results revealed that building lean and DSM accuracy are highly related. The original building lean was 13.65, which decreased to 11.46 after applying orthorectifi-

TABLE 2: Sample of horizontal distortion in buildings with height of 91–120 m.

Type of DSM	Horizontal distortion
Original image prior to orthorectification	13.5–14.5
DSM 30 cm	1.31–1.4
DSM 50 cm	1.41–1.6
DSM 1 m	2.51–3.00
DSM 2 m	3.51–4.00
DSM 3 m	5.01–5.8
DSM 5 m	8.01–10.00
DSM 10 m	9.41–11.30
DSM 15 m	10.61–12.20
DSM 20 m	10.81–12.40

cation to the building at DSM of 20 m. Figure 9 shows the details of the results obtained after orthorectification.

Therefore, developing an approach to present a table-based ranking that compares the accuracy of the same image obtained from orthorectification and GCP with different

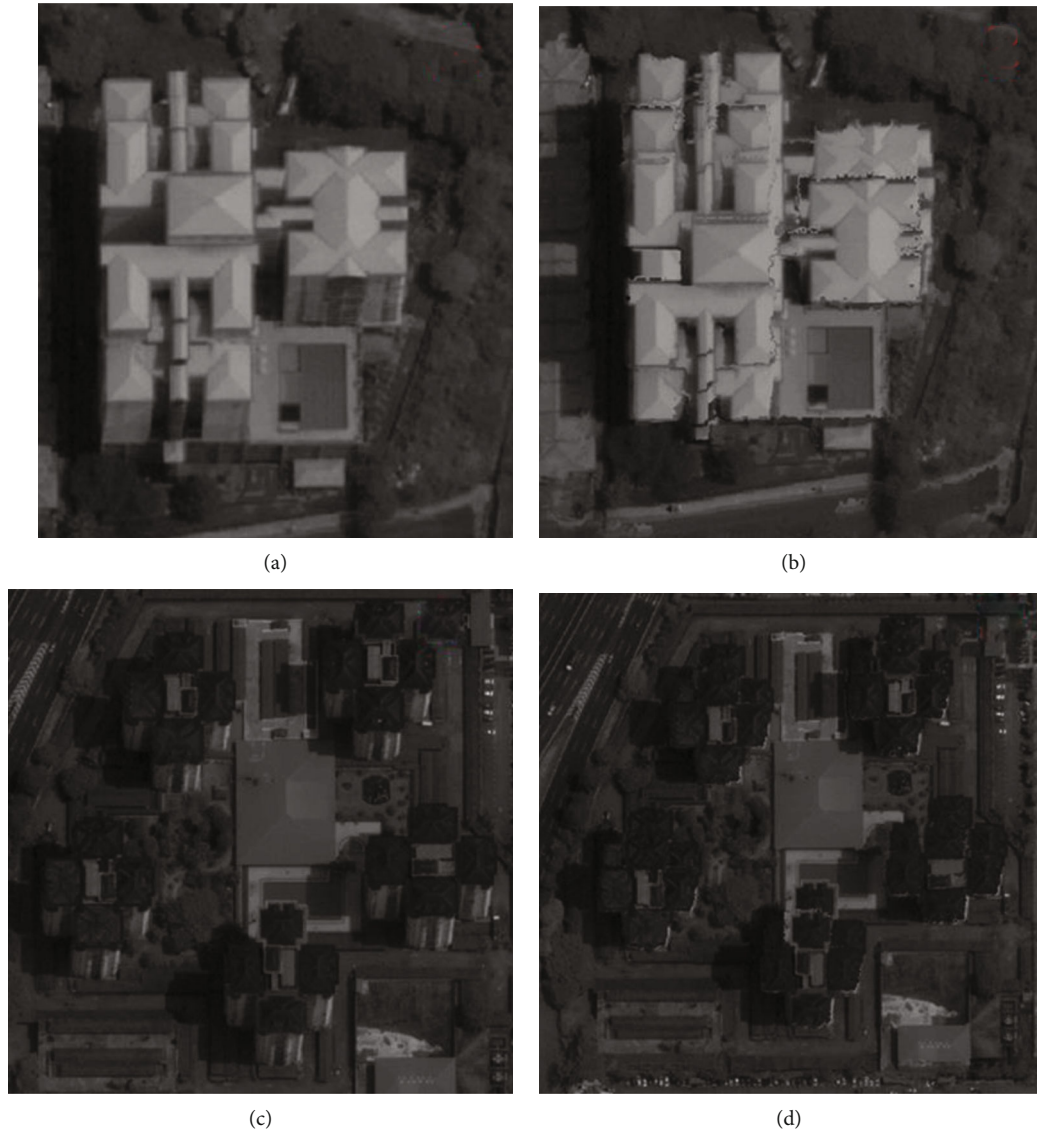


FIGURE 10: Leaning of the building prior to orthorectification based on DSM 0.30 cm whereas (a, c) before orthorectification and (b, d) after orthorectification.

DSM resolutions is necessary. This approach would provide clear information for future analysis and development. LiDAR point clouds with very high spatial resolution were used to produce a very high-resolution DEM. Thus far, no available criterion has been provided regarding the best DEM data. Improved image orthorectification result could be achieved if DEM data with high spatial resolution are available for orthorectifying images. The increased DSM resolution indicated the decreased error in the horizontal distortion of high buildings (>30 m). For instance, for a building height of 91–120 m, the horizontal distortion was measured and is shown in Table 2. Additionally, Figure 10 shows the leaning of the building prior to orthorectification based on DSM 0.30 cm, where it can be observed that the building height at A is 95 m and at C is between 109 and 116 m and the horizontal distortion is between 1.33 and 1.36.

4. Conclusions

LiDAR-derived GCPs and different DSM resolutions (31 and 50 cm and 1, 2, 3, 5, 10, 15, and 20 m) were proposed for image orthorectification. LiDAR data were used to obtain high-ability GCPs and DSM at the increased accuracy required for photogrammetry and orthorectification. The final image demonstrated the advantage of LiDAR-based GCPs with high-resolution DSM in producing high-quality orthoimages with an accuracy of 0.638 m. The accuracy of the orthorectified image was improved by increasing GCPs to more than the usual value. The comparison between final results indicated that the optimal orthoimage was selected based on the best accuracy of the final results, depending on the optimal images. Moreover, the optimal DSM used in orthorectification with the WV-3 image was DSM resolution of 31 cm. The orthorectification applied on WV-3

multispectral image resolution was 1 m, and the optimal DSM was 1 m. Furthermore, the correlation between horizontal distortion and DSM resolution was identified. The increased accuracy led to decreased horizontal distortion. The developed advanced remote sensing data allowed the generation of GCPs and was useful in the event of limited access to field surveys. Therefore, it can be said that a better result for image orthorectification may be expected with higher spatial resolution; especially, DSM was produced from airborne laser-scanning, which provides a very useful source of information for 3D building reconstruction. The orthorectified images increased the quality of land use and land cover used in many fields. Therefore, the proposed methodology will provide a useful tool to aid decision-makers in selecting the best LiDAR for orthorectification. With the wide range of application of high-resolution satellite imagery, using existing commercial image processing packages, the development of operational and efficient satellite image processing procedures such as high accurate image orthorectification will benefit those users who have a limited knowledge of remote sensing image processing. Finally, our method has been proven to be applicable to correct significant geometric distortions present on test image sets.

Data Availability

The data used in this study can be available from the corresponding author.

Conflicts of Interest

The authors declare no conflict of interest.

Acknowledgments

This research was funded by the Centre for Advanced Modelling and Geospatial Information Systems (CAMGIS), Faculty of Engineering and IT, University of Technology Sydney, and supported by Basic Science Research Program through the National Research Foundation of Korea (NRF) funded by the Ministry of Education (No. 2019R1A2C1085686). Also, this research is also supported by Researchers Supporting Project number RSP-2021/14, King Saud University, Riyadh, Saudi Arabia.

References

- [1] H. Zhang, R. Pu, and X. Liu, "A new image processing procedure integrating PCI-RPC and ArcGIS-Spline tools to improve the orthorectification accuracy of high-resolution satellite imagery," *Remote Sensing*, vol. 8, no. 10, p. 827, 2016.
- [2] N. Joshi, M. Baumann, A. Ehammer et al., "A review of the application of optical and radar remote sensing data fusion to land use mapping and monitoring," *Remote Sensing*, vol. 8, no. 1, p. 70, 2016.
- [3] S. Abdullahi and B. Pradhan, "Sustainable brownfields land use change modeling using GIS-based weights-of-evidence approach," *Applied Spatial Analysis and Policy*, vol. 9, no. 1, pp. 21–38, 2016.
- [4] R. Bridgelall, J. B. Rafert, and D. Tolliver, *Remote Sensing of Multimodal Transportation Systems*, Mountain Plains Consortium, Colorado State University, 2016.
- [5] E. Symeonakis, K. Petroulaki, and T. Higginbottom, "Landsat-based woody vegetation cover monitoring in southern African savannahs," *ISPRS - International Archives of the Photogrammetry, Remote Sensing and Spatial Information Sciences*, vol. XLI-B7, pp. 563–567, 2016.
- [6] Y. Peng, R. B. Kheir, K. Adhikari et al., "Digital mapping of toxic metals in Qatari soils using remote sensing and ancillary data," *Remote Sensing*, vol. 8, no. 12, 2016.
- [7] J. Rodriguez, S. Ustin, S. Sandoval-Solis, and A. T. O'Geen, "Food, water, and fault lines: remote sensing opportunities for earthquake-response management of agricultural water," *Science of the Total Environment*, vol. 565, pp. 1020–1027, 2016.
- [8] J.-P. Jhan, J.-Y. Rau, and C.-Y. Huang, "Band-to-band registration and ortho-rectification of multilens/multispectral imagery: a case study of MiniMCA-12 acquired by a fixed-wing UAS," *ISPRS Journal of Photogrammetry and Remote Sensing*, vol. 114, pp. 66–77, 2016.
- [9] E. P. Baltsavias, "Object extraction and revision by image analysis using existing geospatial data and knowledge: state-of-the-art and steps towards operational systems," *ETH Zurich*, vol. XXXIV, Part 2, 2002.
- [10] Y. Hu and C. V. Tao, "Updating solutions of the rational function model using additional control information," *Photogrammetric Engineering and Remote Sensing*, vol. 68, no. 7, pp. 715–724, 2002.
- [11] J. S. Evans and A. T. Hudak, "A multiscale curvature algorithm for classifying discrete return LiDAR in forested environments," *IEEE Transactions on Geoscience and Remote Sensing*, vol. 45, no. 4, pp. 1029–1038, 2007.
- [12] X. Liu, Z. Zhang, J. Peterson, and S. Chandra, "LiDAR-derived high quality ground control information and DEM for image orthorectification," *GeoInformatica*, vol. 11, no. 1, pp. 37–53, 2007.
- [13] O. R. Belfiore and C. Parente, "Comparison of different algorithms to orthorectify WorldView-2 satellite imagery," *Algorithms*, vol. 9, no. 4, p. 67, 2016.
- [14] T. Prakash, B. Comandur, T. Chang, N. Elfiky, and A. Kak, "A generic road-following framework for detecting markings and objects in satellite imagery," *IEEE Journal of Selected Topics in Applied Earth Observations and Remote Sensing*, vol. 8, no. 10, pp. 4729–4741, 2015.
- [15] I. Henrico, L. Combrinck, and C. Eloff, "Accuracy comparison of Pléiades satellite ortho-images using GPS device based GCPs against TerraSAR-X-based GCPs," *South African Journal of Geomatics*, vol. 5, no. 3, pp. 358–372, 2016.
- [16] T. G. Whiteside and R. E. Bartolo, "Mapping aquatic vegetation in a tropical wetland using high spatial resolution multispectral satellite imagery," *Remote Sensing*, vol. 7, no. 9, pp. 11664–11694, 2015.
- [17] D. Chaudhuri, N. K. Kushwaha, A. Samal, and R. Agarwal, "Automatic building detection from high-resolution satellite images based on morphology and internal gray variance," *IEEE Journal of Selected Topics in Applied Earth Observations and Remote Sensing*, vol. 9, no. 5, pp. 1767–1779, 2016.
- [18] J. T. Kerr and M. Ostrovsky, "From space to species: ecological applications for remote sensing," *Trends in Ecology & Evolution*, vol. 18, no. 6, pp. 299–305, 2003.

- [19] D. Vlastic, P. Peers, I. Baran et al., “Dynamic shape capture using multi-view photometric stereo,” in *ACM SIGGRAPH Asia 2009 papers*, pp. 1–11, 2009.
- [20] J. Grodecki and G. Dial, “IKONOS geometric accuracy,” in *Proceedings of joint workshop of ISPRS working groups I/2, I/5 and IV/7 on high resolution mapping from space*, pp. 19–21, 2001.
- [21] J. E. Nichol, A. Shaker, and M.-S. Wong, “Application of high-resolution stereo satellite images to detailed landslide hazard assessment,” *Geomorphology*, vol. 76, no. 1-2, pp. 68–75, 2006.
- [22] E. Widyaningrum, M. Fajari, and J. Octariady, “Accuracy comparison of vhr systematic-ortho satellite *imageries* against vhr orthorectified imageries using GCP,” *International Archives of the Photogrammetry, Remote Sensing & Spatial Information Sciences*, vol. XLI-B1, pp. 305–309, 2016.

Research Article

A State-Domain Robust Chi-Square Test Method for GNSS/INS Integrated Navigation

Zhangjun Yu , Qiuzhao Zhang , Ke Yu , and Nanshan Zheng 

School of Environment Science and Spatial Informatics, China University of Mining and Technology, Xuzhou 221116, China

Correspondence should be addressed to Qiuzhao Zhang; qiuzhao.zhang@cumt.edu.cn

Received 3 June 2021; Revised 27 August 2021; Accepted 11 September 2021; Published 7 October 2021

Academic Editor: Aijun Yin

Copyright © 2021 Zhangjun Yu et al. This is an open access article distributed under the Creative Commons Attribution License, which permits unrestricted use, distribution, and reproduction in any medium, provided the original work is properly cited.

Aiming at abrupt faults in GNSS/INS integrated systems in complex environments, classical fault detection algorithms are mostly developed from the measurement domain. A robust chi-square test method based on the state domain is proposed in this paper. The fault detection statistic is built based on the difference between the prior state estimation and the posterior state estimation in Kalman filtering. To improve the calculation stability, singular value decomposition (SVD) is used to factor the covariance matrix of the difference. The relevant formulas of the proposed method were theoretically derived, and the relationship between the proposed method and the existing innovation chi-square test method was revealed. The proposed method was compared with state-of-the-art chi-square test methods and verified by GNSS/INS integrated navigation experiments using simulation data and real data. The experimental results show that the proposed method (a) directly works in the state domain, (b) does not require the known real system state, (c) has computational efficiency and good robustness, and (d) accurately detects abrupt faults.

1. Introduction

To take full advantage of each individual navigation system and overcome their shortcomings, integrated navigation systems based on Global Navigation Satellite System (GNSS) and Inertial Navigation System (INS) are widely used in positioning and attitude determination applications [1]. Kalman filtering plays an important role in the integration of GNSS and INS data. A basic assumption for applying standard Kalman filtering is that both the dynamic model and the stochastic information provided to the filter are accurate [2]. If this assumption is not valid or there are many outliers, the Kalman filter may result in poor performance such as abrupt faults in the filtering result [3, 4]. Therefore, it is necessary to carry out real-time fault detection to ensure the reliability and precision of the integrated navigation system [5, 6].

In the field of integrated navigation fault detection, chi-square test methods are the classical methods and are widely used because they can detect the faults caused by outliers in

the measurements and inaccurate dynamic models or random information of the Kalman filter. The methods determine the fault detection threshold by the probability of a false alarm (FA) specified in the integrated navigation system, so they do not require any user interaction. The methods can be principally divided into two groups [7–9]:

- (i) *State chi-square test methods*: detect faults through the state estimate error. A state chi-square test method, which directly detects faults based on the difference between the true state and the posterior state estimate, was proposed in [10]; however, it requires knowledge of the true state and is thus suitable for simulation-based fault detection, not for real-time fault detection. The state chi-square test method, which is based on a state propagator and detects faults based on the difference between the estimate of the state propagator and the posterior state estimate, is affected by the initial system value error, the system noise, and the modelling error as

it works, and the state propagator value will deviate increasingly from the true value because there is no measurement update [11]. The double-state chi-square test method uses two state propagators that work alternately and correct each other, which can avoid the problem of no measurement update, but the fault detection rate and calculation efficiency will decrease over time [12–17]

- (ii) *Innovation chi-square test methods*: detect faults through the innovation (i.e., the measurement prediction error). The innovation chi-square test method, which indirectly detects faults based on the difference between the true measurement and the predictive measurement, can detect abrupt faults in time with a small amount of calculation [18–22]. In [23], the Federal Kalman filter based on the innovation chi-square test method is used in suborbital vehicles, and the results show that the proposed method can quickly correct the errors caused by GPS abrupt faults within 1 s. However, this method provides a direct assessment of the measurement prediction error but only an indirect assessment of the filtering state estimate error. In fact, accurate and consistent measurement predictions do not necessarily result in accurate and consistent state estimates [24]

The goal of the paper is to propose a state-domain robust fault detection method addressing the aforementioned limitations of the state-of-the-art tests, i.e., to design a method that (a) directly works in the state domain, (b) does not require the known real system state, (c) has computational efficiency (i.e., detect faults without state propagators) and good robustness, and (d) accurately detects the abrupt fault.

The remainder of this paper is organized as follows. Section 2 lists the formulas of the dynamic and observation equations of the GNSS/INS system. In Section 3, the innovation chi-square test method is reviewed and analysed. The state-domain robust fault detection method is described in Section 4. The experimental description and analysis are given in Section 5. Finally, the paper is concluded in Section 6.

2. The Dynamic and Observation Equations of the GNSS/INS System

A loosely coupled GNSS/INS system is adopted. The state vectors are composed of the position and velocity error in an earth-centered and earth-fixed frame (ECEF frame, e frame), the attitude error is described between the computer e frame and the platform e' frame, and the gyro and accelerometer drift error is in the body frame (b frame), which can be expressed as [25–27]

$$\mathbf{x}_k = \left[\Delta \mathbf{R}^e \Delta \mathbf{V}^e \boldsymbol{\phi}^e \nabla^b \boldsymbol{\varepsilon}^b \right]^T. \quad (1)$$

The nonlinear differential error model of a low-cost INS is as follows:

$$\begin{cases} \Delta \dot{\mathbf{R}}^e = \Delta \mathbf{V}^e, \\ \Delta \dot{\mathbf{V}}^e = (\mathbf{I}_{3 \times 3} - \mathbf{C}_{e'}^e) \mathbf{f}^{e'} + \mathbf{C}_b^{e'} \nabla^b - 2\boldsymbol{\Omega}_{ie}^e \Delta \mathbf{V}^e, \\ \dot{\boldsymbol{\phi}}^e = \left(\mathbf{I}_{3 \times 3} - \mathbf{C}_{e'}^e \right) \boldsymbol{\omega}_{ie}^e - \mathbf{C}_b^{e'} \boldsymbol{\varepsilon}^b, \\ \dot{\nabla}^b = 0, \\ \dot{\boldsymbol{\varepsilon}}^b = 0, \end{cases} \quad (2)$$

where $\Delta \mathbf{R}^e$ and $\Delta \mathbf{V}^e$ are the position and velocity error in the e frame, respectively; $\boldsymbol{\phi}^e$ is the attitude error between the computer e frame and the platform e' frame; $\mathbf{I}_{3 \times 3}$ is a 3×3 unit matrix; $\mathbf{C}_{e'}^e$ is the rotation matrix between the computer e frame and the platform e' frame; $\mathbf{C}_b^{e'}$ is the rotation matrix between the body frame and the platform e' frame; $\boldsymbol{\Omega}_{ie}^e$ is the skew symmetric matrix of the earth rotation rate $\boldsymbol{\omega}_{ie}^e$; and $\boldsymbol{\varepsilon}^b$ and ∇^b are gyro and accelerometer drift errors in the body frame, respectively.

The dynamic model of a loosely coupled GNSS/INS system can be expressed as follows:

$$\mathbf{x}_{k+1} = \mathbf{f}_k(\mathbf{x}_k) + \mathbf{w}_k, \quad (3)$$

where the vector \mathbf{x}_k represents the state of the system, \mathbf{f}_k is the system function, and \mathbf{w}_k is the process noise vector, which is commonly assumed to be zero-mean Gaussian white noise with covariance matrix \mathbf{Q}_k .

Generally, the measurement model can be expressed as

$$\mathbf{z}_k = \begin{bmatrix} \widehat{\mathbf{R}}_{\text{INS}}^e - \widehat{\mathbf{R}}_{\text{GPS}}^e \\ \widehat{\mathbf{V}}_{\text{INS}}^e - \widehat{\mathbf{V}}_{\text{GPS}}^e \end{bmatrix} = \mathbf{h}_k(\mathbf{x}_k) + \mathbf{v}_k, \quad (4)$$

where the vector \mathbf{z}_k represents the measurement, $\widehat{\mathbf{R}}_{\text{INS}}^e$ and $\widehat{\mathbf{V}}_{\text{INS}}^e$ are the INS-computed position and velocity vectors in the e frame, $\widehat{\mathbf{R}}_{\text{GPS}}^e$ and $\widehat{\mathbf{V}}_{\text{GPS}}^e$ are the GNSS vector outputs, \mathbf{h}_k is the measurement function, and \mathbf{v}_k is the measurement noise vector, which is commonly assumed to be zero-mean Gaussian white noise with covariance matrix \mathbf{R}_k .

3. Problem Formulation

Fault detection is a vital and safety-related task for integrated navigation systems. In this section, the Kalman filter for GNSS/INS integrated navigation is formulated and the innovation chi-square test method, which is a popular and widely discussed test used for several decades, is introduced and analysed.

3.1. Kalman Filter for GNSS/INS Integrated Navigation. The methods purposely designed for abrupt fault detection in the integrated navigation system are based on the Gaussian assumption and the statistical hypothesis testing. Therefore,

let a state variable \mathbf{x} with a known prior Gaussian probability density function (PDF)

$$p(\mathbf{x}) = \mathcal{N}\{\mathbf{x}; \hat{\mathbf{x}}', \mathbf{P}'_{xx}\} \quad (5)$$

be considered, where the notation $\mathcal{N}\{\mathbf{x}; \hat{\mathbf{x}}', \mathbf{P}'_{xx}\}$ stands for the normal distribution with the mean $\hat{\mathbf{x}}' = E[\mathbf{x}]$ and the covariance matrix $\mathbf{P}'_{xx} = \text{cov}[\mathbf{x}]$; meanwhile, the time update and measurement update of the Kalman filter for GNSS/INS integrated navigation can be expressed as follows:

$$\hat{\mathbf{x}}_k = \hat{\mathbf{x}}'_k + \mathbf{K}_k(\mathbf{z}_k - \hat{\mathbf{z}}'_k), \quad (6)$$

$$\mathbf{K}_k = \mathbf{P}'_{xz,k}(\mathbf{P}'_{zz,k})^{-1}, \quad (7)$$

$$\mathbf{P}'_{xx,k} = \mathbf{P}'_{xx,k} - \mathbf{K}_k \mathbf{P}'_{zz,k} (\mathbf{K}_k)^T, \quad (8)$$

$$\hat{\mathbf{x}}'_{k+1} \approx \int \mathbf{f}_k(\mathbf{x}_k) \mathcal{N}\{\mathbf{x}_k; \hat{\mathbf{x}}_k, \mathbf{P}'_{xx,k}\} d\mathbf{x}_k, \quad (9)$$

$$\mathbf{P}'_{xx,k+1} \approx \int \left(\mathbf{f}_k(\mathbf{x}_k) - \hat{\mathbf{x}}'_{k+1} \right) \left(\mathbf{f}_k(\mathbf{x}_k) - \hat{\mathbf{x}}'_{k+1} \right)^T \mathcal{N}\{\mathbf{x}_k; \hat{\mathbf{x}}_k, \mathbf{P}'_{xx,k}\} d\mathbf{x}_k + \mathbf{Q}_k, \quad (10)$$

$$\hat{\mathbf{z}}'_k \approx \int \mathbf{h}_k(\mathbf{x}_k) \mathcal{N}\{\mathbf{x}_k; \hat{\mathbf{x}}_k, \mathbf{P}'_{xx,k}\} d\mathbf{x}_k, \quad (11)$$

$$\mathbf{P}'_{zz,k} \approx \int \left(\mathbf{h}_k(\mathbf{x}_k) - \hat{\mathbf{z}}'_k \right) \left(\mathbf{h}_k(\mathbf{x}_k) - \hat{\mathbf{z}}'_k \right)^T \mathcal{N}\{\mathbf{x}_k; \hat{\mathbf{x}}_k, \mathbf{P}'_{xx,k}\} d\mathbf{x}_k + \mathbf{R}_k, \quad (12)$$

$$\mathbf{P}'_{xz,k} \approx \int \left(\mathbf{x}_k - \hat{\mathbf{x}}'_k \right) \left(\mathbf{h}_k(\mathbf{x}_k) - \hat{\mathbf{z}}'_k \right)^T \mathcal{N}\{\mathbf{x}_k; \hat{\mathbf{x}}_k, \mathbf{P}'_{xx,k}\} d\mathbf{x}_k, \quad (13)$$

where $\hat{\mathbf{x}}'_k$ is the prior state estimate, $\mathbf{P}'_{xx,k}$ is the covariance matrix of $\hat{\mathbf{x}}'_k$, \mathbf{K}_k is the gain matrix, $\hat{\mathbf{x}}_k$ is the posterior state estimate, $\mathbf{P}'_{xx,k}$ is the covariance matrix of $\hat{\mathbf{x}}_k$, $\hat{\mathbf{z}}'_k$ is the predictive measurement, $\mathbf{P}'_{zz,k}$ is the covariance matrix of $\hat{\mathbf{z}}'_k$, and $\mathbf{P}'_{xz,k}$ is the ‘‘crosscovariance’’ matrix of joint $\hat{\mathbf{x}}'_k$ and $\hat{\mathbf{z}}'_k$.

3.2. The Innovation Chi-Square Test Method. In principle, the detection of the abrupt faults can be formulated using statistical hypothesis testing. The null hypothesis H_0 : assuming no fault, i.e., assuming $\hat{\mathbf{x}}_k$ and $\mathbf{P}'_{xx,k}$, is accurate enough, which is tested against the alternative hypothesis H_1 : assuming there is a fault.

The innovation chi-square test method that detects abrupt faults by predictive measurement $\hat{\mathbf{z}}'_k$ and measurement \mathbf{z}_k is described as follows:

Step 1. Define a required (or allowed) probability of false alert P_{FA} .

Step 2. Compute statistic

$$\mathcal{Z}_k = (\mathbf{e}_k)^T (\mathbf{P}'_{zz,k})^{-1} \mathbf{e}_k, \quad \mathcal{Z}_k \sim p(\mathcal{Z}_k). \quad (14)$$

If the null hypothesis H_0 is valid, then the PDF $p(\mathcal{Z}_k)$ is (approximately) a chi-squared distribution with n_z degrees of freedom (DOF), where $\mathbf{e}_k = \mathbf{z}_k - \hat{\mathbf{z}}'_k$ and n_z is the dimension of the measurement domain.

Step 3. Compute the corresponding P_{FA} quantile

$$q_{FA,k}^{\mathcal{Z}} = \inf \{ \mathcal{Z}_k \in : (1 - P_{FA}) \leq F(\mathcal{Z}_k) \}, \quad (15)$$

where $F(\mathcal{Z}_k)$ is the cumulative distribution function with respect to $p(\mathcal{Z}_k)$ and the operator \inf stands for the infimum. The quantile $q_{FA,k}^{\mathcal{Z}}$ is further denoted as the fault detection threshold.

Step 4. Compare the statistic \mathcal{Z}_k (14) with the threshold $q_{FA,k}^{\mathcal{Z}}$ (15). If $\mathcal{Z}_k \leq q_{FA,k}^{\mathcal{Z}}$, then it is considered to be no fault. Otherwise, it would be considered to have a fault.

However, this method provides a direct assessment of the measurement prediction error \mathbf{e}_k but just an indirect assessment of the filtering state estimate error. In fact, accurate and consistent measurement predictions do not necessarily result in accurate and consistent state estimates. The measurement domain test assumes the Gaussian of the measurement prediction PDF and therefore cannot consider the error in computation of the ‘‘crosscovariance’’ matrix $\mathbf{P}'_{xz,k}$ [24].

4. The State-Domain Robust Chi-Square Test Method

In this section, the state-domain robust chi-square test method is proposed.

4.1. Derivation. The proposed test is based on a statistical analysis of the difference between prior and posterior state estimates defined as

$$\mathbf{d}_k = \hat{\mathbf{x}}_k - \hat{\mathbf{x}}'_k. \quad (16)$$

Its statistical properties are summarized in the following theorem.

Theorem 1. *Under valid hypothesis H_0 , the difference \mathbf{d}_k is a random variable with*

$$\hat{\mathbf{d}}_k = E[\mathbf{d}_k] = \mathbf{0}_{n_x}, \quad (17)$$

$$\mathbf{P}_{dd,k} = \mathbf{P}'_{xx,k} - \mathbf{P}_{xx,k} = \mathbf{K}_k \mathbf{P}'_{zz,k} (\mathbf{K}_k)^T, \quad (18)$$

where n_x is the dimension of the state domain.

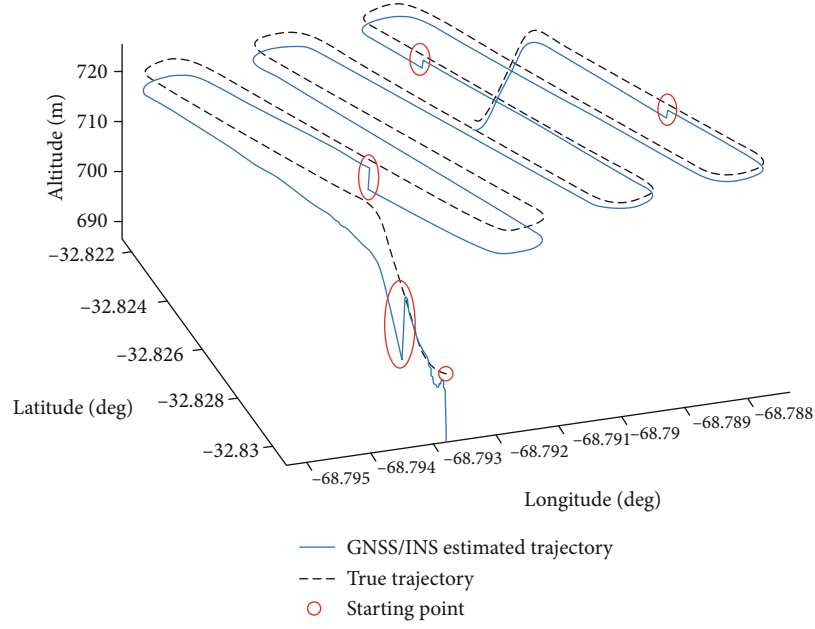


FIGURE 1: The true trajectory and the GNSS/INS estimated trajectory.

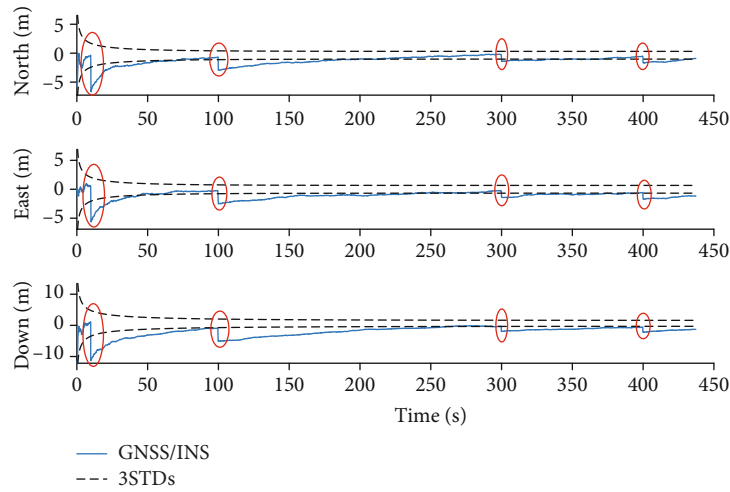


FIGURE 2: The position error using the simulation data and the confidence region defined by $\pm 3\text{STDs}$.

Proof. The proof of (17): both the prior and posterior mean estimates are unbiased, i.e., $\tilde{\mathbf{x}}'_k = \tilde{\mathbf{x}}_k = E[\mathbf{x}_k]$. The proof of (18): the difference \mathbf{d}_k (16) can be written as

$$\mathbf{d}_k = \mathbf{x}_k - \tilde{\mathbf{x}}'_k - (\mathbf{x}_k - \tilde{\mathbf{x}}_k) = \tilde{\mathbf{x}}'_k - \tilde{\mathbf{x}}_k, \quad (19)$$

where $\tilde{\mathbf{x}}'_k$ is the prior state estimate error and $\tilde{\mathbf{x}}_k$ is the posterior state estimate error.

$$\mathbf{P}_{dd,k} = E[\mathbf{d}_k \mathbf{d}_k^T] = \mathbf{P}'_{xx,k} + \mathbf{P}_{xx,k} - \mathbf{M}'_{x',x,k} - \mathbf{M}_{xx',k}, \quad (20)$$

where the (cross-)second-order moment of the posterior and prior state estimate error is defined as $\mathbf{M}'_{x',x,k} = E[\tilde{\mathbf{x}}'_k \tilde{\mathbf{x}}_k^T]$, and $\mathbf{M}_{xx',k} = (\mathbf{M}'_{x',x,k})^T$.

$$\begin{aligned} \mathbf{M}'_{x',x,k} &= E\left[\left(\mathbf{x}_k - \tilde{\mathbf{x}}'_k\right)\left(\mathbf{x}_k - \tilde{\mathbf{x}}'_k - \mathbf{K}_k\left(\mathbf{z}_k - \tilde{\mathbf{z}}'_k\right)\right)^T\right] \\ &= \mathbf{P}'_{xx,k} - \mathbf{P}'_{xz,k}\left(\mathbf{K}_k\right)^T \\ &= \mathbf{P}_{xx,k}. \end{aligned} \quad (21)$$

Then, by substituting (21) into (20), the expression for (18) is obtained. \square

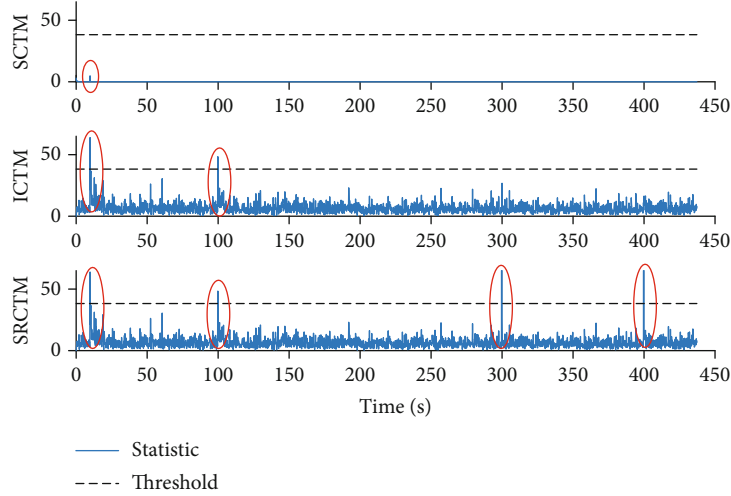


FIGURE 3: Statistics of the different methods using the simulation data.

4.2. *Algorithm.* The state-domain robust chi-square test method that detects abrupt faults by the difference \mathbf{d}_k is described as follows:

Step 1. Define a required (or allowed) probability of false alert P_{FA} .

Step 2. Compute statistic

$$\mathcal{E}_k = (\mathbf{d}_k)^T (\mathbf{P}_{dd,k})^{-1} \mathbf{d}_k, \quad \mathcal{E}_k \sim p(\mathcal{E}_k). \quad (22)$$

If the null hypothesis H_0 is valid, then the PDF $p(\mathcal{E}_k)$ is (approximately) a chi-squared distribution with n_x DOF. To improve the calculation stability, singular value decomposition (SVD) is used to factor $\mathbf{P}_{dd,k}$.

Step 3. Compute the corresponding P_{FA} quantile

$$q_{FA,k}^{\mathcal{E}} = \inf \{ \mathcal{E}_k \in : (1 - P_{FA}) \leq F(\mathcal{E}_k) \}, \quad (23)$$

where $F(\mathcal{E}_k)$ is the cumulative distribution function with respect to $p(\mathcal{E}_k)$.

Step 4. Compare the statistic \mathcal{E}_k (22) with the threshold $q_{FA,k}^{\mathcal{E}}$ (23). If $\mathcal{E}_k \leq q_{FA,k}^{\mathcal{E}}$, then it is considered to be no fault. Otherwise, it would be considered to have a fault.

4.3. *Relationship between the Proposed Method and the Innovation Chi-Square Test Method.* The innovation chi-square test method can be seen as a special case of the proposed method under the consideration of certain simplifications.

With respect to (6) and (8), the difference \mathbf{d}_k and $\mathbf{P}_{dd,k}$ can be written as

$$\begin{aligned} \mathbf{d}_k &= \mathbf{K}_k \mathbf{e}_k, \\ \mathbf{P}_{dd,k} &= \mathbf{K}_k \mathbf{P}'_{zz,k} (\mathbf{K}_k)^T. \end{aligned} \quad (24)$$

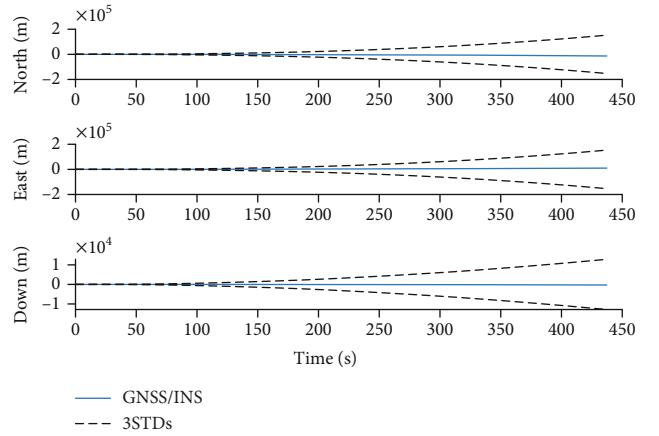


FIGURE 4: The position error using the simulation data and the confidence region of the state propagator defined by 3STDs.

Assuming $n_x = n_z$, \mathbf{K}_k is invertible, and faults caused by the outliers in the measurements and inaccurate dynamic models or random information of the Kalman filter, the statistic \mathcal{E}_k (22) can be further treated as

$$\begin{aligned} \mathcal{E}_k &= (\mathbf{e}_k)^T (\mathbf{K}_k)^T \left(\mathbf{K}_k \mathbf{P}'_{zz,k} (\mathbf{K}_k)^T \right)^{-1} \mathbf{K}_k \mathbf{e}_k \\ &= (\mathbf{e}_k)^T \left(\mathbf{P}'_{zz,k} \right)^{-1} \mathbf{e}_k \\ &= \mathcal{Z}_k. \end{aligned} \quad (25)$$

In this case, the proposed method is equivalent to the innovation chi-square test method.

5. Experiment Description

In this section, the proposed method, called the state-domain robust chi-square test method (SRCTM), is compared with the innovation chi-square test method (ICTM) and the state chi-square test method (SCTM) and verified



FIGURE 5: The University of Nottingham test vehicle.

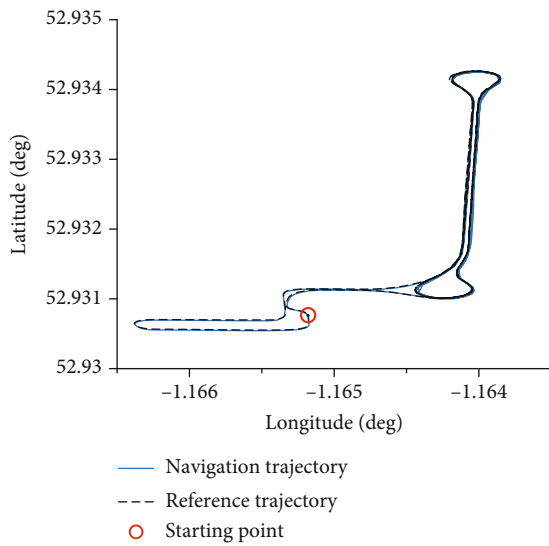


FIGURE 6: The test trajectory.

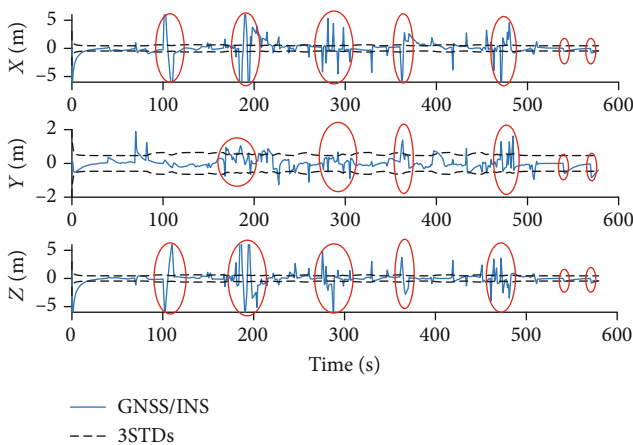


FIGURE 7: The position error using the real data and the confidence region defined by $\pm 3STDs$.

by GNSS/INS integrated navigation experiments using simulation data and real data. To objectively compare the efficiency of the different methods, the probability of false alerts P_{FA} is set as 10^{-6} and $n_x = n_z = 6$. Meanwhile, the same hardware and software are adopted. The hardware is a PC with a Core i5-10500 CPU and 16GB RAM. The R2019b

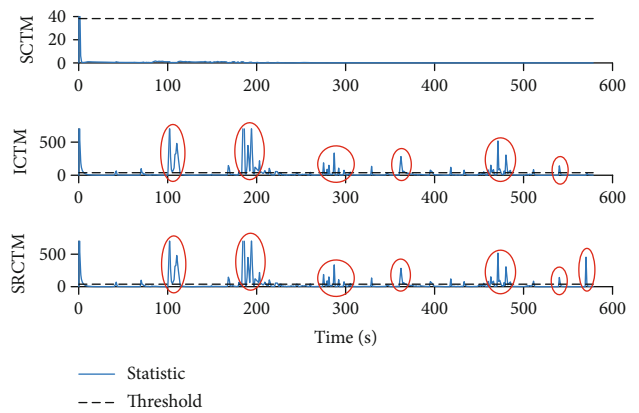


FIGURE 8: Statistics of the different methods using the real data.

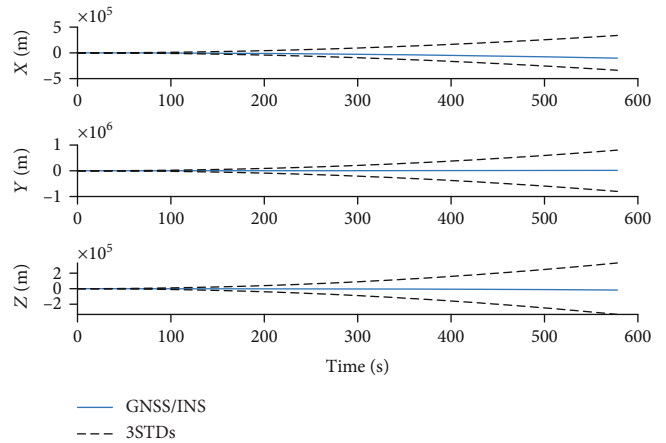


FIGURE 9: The position error using the real data and the confidence region of the state propagator defined by $3STDs$.

version of MATLAB software running on a Windows 10 system is used to design the different algorithms.

5.1. GNSS/INS Integrated Navigation Experiment Using the Simulation Data. The GNSS/INS integrated navigation experiment using simulation data utilized a simulation framework for low-cost integrated navigation systems called NaveGo, which simulates measurements from inertial sensors and a GNSS receiver. It is found that the absolute differences between real and simulated systems are under 23

centimeters for 2D position and under 10 centimeters for vertical position [28].

To verify the effectiveness of the SRCTM and compare it with the ICTM and the RCTM, two abrupt faults based on the standard deviation (STD) as 9STDs were added in the dynamic model (3) artificially at 10 s and 100 s, and two abrupt faults based on the STD as 5STDs were added in the posterior state estimate (6) artificially at 300 s and 400 s. Figure 1 shows the true trajectory and the estimated trajectory, which contains the abrupt faults.

Figure 2 contains the position error of the GNSS/INS and confidence region based on the STD as ± 3 STDs, and the error exceeds 3STDs at the time when the abrupt fault is added.

Figure 3 shows the statistics of the different methods, and both the ICTM and the SRCTM are very sensitive to abrupt faults in the dynamic model. Only the SRCTM can detect faults in the posterior state estimate (because the SRCTM is based on the difference between the prior and posterior state estimates). In addition, the SRTM can hardly detect faults, and the statistics change only in the initial period, because the state propagator value will deviate increasingly from the true value without measurement update. Note that the SRTM is clearly more time-consuming than the ICTM and the SRCTM because of the extra state propagator. In Figure 4, the position error using the simulation data and the confidence region of the state propagator defined by 3STDs are provided.

5.2. GNSS/INS Integrated Navigation Experiment Using the Real Data. The GNSS/INS integrated navigation experiment using real data was carried out at the University of Nottingham, UK, in November 2013. A GNSS antenna, a GNSS receiver, and a SPAN-LCI IMU were mounted in a van, and data were logged from the receiver's serial ports to a laptop for storage and processing. The vector between the IMU center and GNSS antenna was accurately surveyed using a total station and was considered accurate within 1 cm. A base station was set up on the roof of the Nottingham Geospatial Building to provide DGPS and RTK corrections. The update rate of INS is 200 Hz, and that of the GNSS is 1 Hz. The average baseline length was less than 3 km for the test. When driving on the roads of the University of Nottingham, the test vehicle performed accelerations and braking at an average speed of at least 20 km/h. Figure 5 is a photograph of the van, and Figure 6 is the test trajectory. The high accuracy real-time output results of the SPAN system are used as the reference value, and the double-difference code GNSS position and velocity results are used as the input measurements.

To verify the effectiveness of the SRCTM and compare it with the SCTM and the ICTM, an abrupt fault based on the STD as 5STDs was artificially added in the measurement model (4) at 540 s, and an abrupt fault based on the STD as 5STDs was added in the posterior state estimate (6) artificially at 570 s. In addition, the results contain some outliers due to the vehicle passing over a speed bump or the data was lost.

Figure 7 contains the position error of the GNSS/INS using real data and the confidence region given by ± 3 STDs, and the error exceeds 3STDs at the time when the abrupt fault is added or there are many outliers.

Figure 8 shows the statistics of the different methods using the real data, and it can be seen that both the ICTM and the SRCTM are very sensitive to abrupt faults in the measurement model. Only the SRCTM can detect the fault in the posterior state estimate (because the SRCTM is based on the difference between the prior and posterior state estimates). As in Section 5.1, the SRTM can hardly detect the faults, and the statistics change only in the initial period because the state propagator value will deviate increasingly from the true value without measurement update. In Figure 9, the position error using the real data and the confidence region of the state propagator defined by 3STDs are provided.

6. Conclusion

This paper focuses on detecting abrupt faults in integrated navigation systems. A state-domain robust chi-square test method was proposed. Compared to the state-of-the-art method, the proposed method (a) directly works in the state domain, (b) does not require the known real system state, (c) has computational efficiency and good robustness, and (d) can accurately detect abrupt faults. The performance and properties of the proposed method are illustrated in the theoretical derivation and experimental description.

Data Availability

The data that support the findings of this study are available from the corresponding author upon reasonable request.

Conflicts of Interest

The authors declare no conflict of interest.

Acknowledgments

The authors would like to thank Yang Gao and Scott Stephenson from the University of Nottingham for their help in collecting the testing data in Nottingham. This work was supported by the National Key R&D Program of China (2017YFE0119600) and Agentúra na Podporu Výskumu a Vývoja (APVV) (SK-CN-RD-18-0015).



References

- [1] D. A. Grejner-Brzezinska, R. Da, and C. Toth, "GPS error modeling and OTF ambiguity resolution for high-accuracy GPS/INS integrated system," *Journal of Geodesy*, vol. 72, no. 11, pp. 626–638, 1998.
- [2] C. Hide, T. Moore, and M. Smith, "Adaptive Kalman filtering for low-cost INS/GPS," *Journal of Navigation*, vol. 56, no. 1, pp. 143–152, 2003.
- [3] Y. R. Geng and J. L. Wang, "Adaptive estimation of multiple fading factors in Kalman filter for navigation applications," *GPS Solutions*, vol. 12, no. 4, pp. 273–279, 2008.
- [4] J. Wang, C. Liu, J. X. Gao, and C. H. Xu, "GNSS/INS tightly coupled navigation model based on robust EKF," *Geomatics and Information Science of Wuhan University*, vol. 36, no. 5, pp. 596–600, 2011.

- [5] T. S. Bruggemann, D. G. Greer, and R. A. Walker, "GPS fault detection with IMU and aircraft dynamics," *IEEE Transactions on Aerospace and Electronic Systems*, vol. 47, no. 1, pp. 305–316, 2011.
- [6] L. Yi-ting, X. Xiao-su, L. Xi-xiang et al., "A fast gradual fault detection method for underwater integrated navigation systems," *Journal of Navigation*, vol. 69, no. 1, pp. 93–112, 2016.
- [7] M. Joerger and B. Pervan, "Kalman filter-based integrity monitoring against sensor faults," *Journal of Guidance, Control, and Dynamics*, vol. 36, no. 2, pp. 349–361, 2013.
- [8] B. Brumback and M. Srinath, "A chi-square test for fault-detection in Kalman filters," *IEEE Transactions on Automatic Control*, vol. 32, no. 6, pp. 552–554, 1987.
- [9] X. Zhao, S. C. Wang, J. S. Zhang, Z. L. Fan, and H. B. Min, "Real-time fault detection method based on belief rule base for aircraft navigation system," *Chinese Journal of Aeronautics*, vol. 26, no. 3, pp. 717–729, 2013.
- [10] Y. Bar-Shalom, T. Kirubarajan, and X. R. Li, *Estimation with Applications to Tracking and Navigation*, Wiley, 2001.
- [11] R. Da and C.-F. Lin, "Sensitivity Analysis of the State Chi-Square Test," *IFAC Proceedings*, vol. 29, no. 1, pp. 6596–6601, 1996.
- [12] R. Da, "Failure detection of dynamical systems with the state chi-square test," *Journal of Guidance, Control, and Dynamics*, vol. 17, no. 2, pp. 271–277, 1994.
- [13] R. Han, H. L. Qin, C. Li, and J. Tian, "A two-stage fault detection structure for JIDS/SINS/GPS integrated navigation system," *Avionics Technology*, vol. 39, no. 3, pp. 43–49, 2008.
- [14] H. Q. Zhang, L. I. Dong-Xing, and G. Q. Zhang, "Application of hybrid chi-square test method in fault detection of integrated navigation system," *Journal of Chinese Inertial Technology*, vol. 24, pp. 696–700, 2016.
- [15] J. X. Xu, Z. Xiong, J. Y. Liu, and R. Wang, "A dynamic vector-formed information sharing algorithm based on two-state chi square detection in an adaptive federated filter," *Journal of Navigation*, vol. 72, no. 1, pp. 101–120, 2019.
- [16] F. Zhang, Y. Wang, and Y. B. Gao, "A novel method of fault detection and identification in a tightly coupled, INS/GNSS-integrated system," *Sensors*, vol. 21, no. 9, p. 2922, 2021.
- [17] Z. K. Li, Z. Liu, and L. Zhao, "Improved robust Kalman filter for state model errors in GNSS-PPP/MEMS-IMU double state integrated navigation," *Advances in Space Research*, vol. 67, no. 10, pp. 3156–3168, 2021.
- [18] Y. X. Zhu, X. H. Cheng, and L. Wang, "A novel fault detection method for an integrated navigation system using Gaussian process regression," *Journal of Navigation*, vol. 69, no. 4, pp. 905–919, 2016.
- [19] C. Yang, J. Guo, L. Zhang, Q. W. Chen, and S. O. Automation, "Fuzzy adaptive unscented Kalman filter integrated navigation algorithm using chi-square test," *Control and Decision*, vol. 33, no. 1, pp. 81–87, 2018.
- [20] G. L. Gao, S. S. Gao, G. Y. Hong, X. Peng, and T. Yu, "A robust INS/SRS/CNS integrated navigation system with the chi-square test-based robust Kalman filter," *Sensors*, vol. 20, no. 20, p. 5909, 2020.
- [21] Y. T. Gao, Y. Gao, B. Y. Liu, and Y. Jiang, "Enhanced fault detection and exclusion based on Kalman filter with colored measurement noise and application to RTK," *GPS Solutions*, vol. 25, no. 3, p. 82, 2021.
- [22] C. W. Chen and S. S. Kia, "A Renyi divergence based approach to fault detection and exclusion for tightly coupled GNSS/INS system," in *Proceedings of the 2021 International Technical Meeting of the Institute of Navigation*, pp. 674–687, Manassas, VA, 2021.
- [23] J. Liu, D. Li, and Z. Xiong, "Research on an improved residual chi-square fault detection method for federated unscented Kalman filter," *Chinese Journal of Scientific Instrument*, vol. 30, pp. 2568–2573, 2009.
- [24] J. Dunik and O. Straka, "State estimate consistency monitoring in Gaussian filtering framework," *Signal Processing*, vol. 148, pp. 145–156, 2018.
- [25] M. Petovello, *Real-Time Integration of a Tactical-Grade IMU and GPS for High-Accuracy Positioning and Navigation*, University of Calgary (Canada), 2003.
- [26] Q. Z. Zhang, S. B. Zhang, Z. P. Liu, and H. F. Bian, "Robust cubature Kalman filter based on SVD and its application to integrated navigation," *Control and Decision*, vol. 29, no. 2, pp. 341–346, 2014.
- [27] Q. Z. Zhang, X. L. Meng, S. B. Zhang, and Y. J. Wang, "Singular value decomposition-based robust cubature Kalman filtering for an integrated GPS/SINS navigation system," *Journal of Navigation*, vol. 68, no. 3, pp. 549–562, 2015.
- [28] R. Gonzalez, J. Giribet, and H. Patiño, "NaveGo: a simulation framework for low-cost integrated navigation systems," *Control Engineering and Applied Informatics*, vol. 17, pp. 110–120, 2015.

Research Article

Improved Mitigation Method for the Multipath Delays of BDS-3 Code Observations with the Aid of a Sparse Modeling Algorithm

Chao Hu ^{1,2}, Qianxin Wang ², and Alberto Hernandez Moraleda³

¹School of Spatial Informatics and Geomatics Engineering, Anhui University of Science and Technology, Huainan 232001, China

²School of Environment Science and Spatial Informatics, China University of Mining and Technology, Xuzhou 221116, China

³International University of La Rioja, Madrid, Spain

Correspondence should be addressed to Qianxin Wang; wqx@cumt.edu.cn

Received 23 March 2021; Revised 2 August 2021; Accepted 23 August 2021; Published 23 September 2021

Academic Editor: Antonio Martinez-Olmos

Copyright © 2021 Chao Hu et al. This is an open access article distributed under the Creative Commons Attribution License, which permits unrestricted use, distribution, and reproduction in any medium, provided the original work is properly cited.

Global navigation satellite systems are essential for positioning, navigation, and timing services. The quality and reliability of satellite observations determine the system performance, especially in the case of the newly launched global BDS-3 service. However, analyses of multipath delays in BDS-3 satellite observations suggest that there are appreciable errors at different frequencies. Improvement of the accuracy and precision of positioning, navigation, and timing services provided by BDS-3 requires the mitigation of multipath delays of the satellite observations. This paper models the multipath delays of BDS-3 observations using a least-squares combined autoregressive method. Furthermore, a sparse modeling algorithm is proposed to obtain a multipath delay series using total variation and elastic net terms for denoising and eliminating the effect of limited original observations. The estimated coefficients of multipath delays are then set as prior information to correct the next-arc code observations, where the square-root information filter is used in the coefficient estimation. Moreover, four groups of experiments are conducted to analyze the results of modeling the BDS-3 multipath delay using the proposed methods, with single-frequency precise point positioning (PPP) and real-time PPP solutions being selected to test the correction of multipath delays in BDS-3 code observations. The residuals of iGMAS and MGEX station coordinates indicate improvements in eastward, northward, and upward directions of at least 4.1%, 9.6%, and 1.2%, respectively, for the frequency B1I; 6.6%, 5.3%, and 0.2%, respectively, for B3I, 12.5%, 14.3%, and 3.8%, respectively, for B1C; and 5.9%, 7.4%, and 18.1%, respectively, for B2a relative to the use of the traditional method in BDS-3 single-frequency PPP. Furthermore, the real-time double-frequency PPP is optimized by at least 10% for B1I + B3I and B1C + B2a. An improved result was obtained with the proposed strategy in a standard point positioning experiment. The proposed multipath delay mitigation method is therefore effective in improving BDS-3 satellite code observations.

1. Introduction

Global navigation satellite systems (GNSSs) provide all-weather and continuous services to global users in the area of high-precision spatial information. China has developed the BeiDou Navigation Satellite System (BDS) in a three-step strategy involving a verification system (BDS-1), regional system (BDS-2), and global system (BDS-3) [1, 2]. BDS-3 was officially announced to be operational in 2020, representing a shift in the BDS from regional to global services [3]. At present, more than 40 BDS satellites in the orbit provide positioning, navigation, and timing (PNT) services

(<http://www.csno-tarc.cn>). BDS-3 will provide the majority of spatial and temporal references for services in the future. Therefore, the high performance of BDS-3 services, especially in terms of the precision and accuracy of observations, is essential for the development of BDS [4, 5].

The GNSS observation quality relates to the ambiguity resolution [6], bias parameters [7, 8], and correction models [9]. The parameter estimation of the satellite orbit and clock offsets is affected by errors in the satellite-ground observations, such as multipath delays. Meanwhile, the precision of precise point positioning (PPP) is directly limited by the quality of satellite observations [10, 11]. In terms of quality

control, studies on BDS observations have focused on the C/N_0 ratio [12, 13], corrections for noise and multipath delay [14], and precision analyses of the phase and code [15]. Moreover, for BDS-3 multifrequency observations, the characteristics of the observation signals [16], qualities of new observations [17], and biases of data fusion [3] have typically been discussed. In summary, the quality of BDS-3 satellite observations is better than that of traditional BDS-2 satellite observations [16]. However, the results of experiments on BDS-3 code multipath delays suggest that there is a trend term in the code observations [2]. Therefore, to mitigate BDS-3 code multipath delays, methods of modeling BDS-3 multipath delays need to be studied for high-precision applications.

In the processing of GNSS observation multipath delays, there are four aspects to high-precision estimation and modeling methods: (1) time domain filtering algorithms, such as the wavelet algorithm and Vondrak algorithm, (2) modeling using the repeating periods of satellites, such as modeling using the sidereal filtering algorithm [18], (3) compensation algorithms in the spatial domain, which provide a multipath hemispherical map [14] and allow spherical harmonic analysis [19], and (4) machine learning methods, such as Tikhonov regularization and sparse modeling [20, 21]. The literature indicates that all the methods mentioned above are useful for the mitigation of BDS code multipath delays. Notably, new signals and their modulation and multiplexing techniques are used for BDS-3 satellites. However, widely used strategies for BDS code multipath delays focus on BDS-2 observations, for example, a two-step modeling method, which first models the multipath delay and then the code bias [2], cannot be applied to BDS-3. Owing to differences in the signal characteristics, signal numbers, signal quality, and satellite spatial distributions between BDS-2 and BDS-3, BDS-3 observations should be carefully investigated when using multiple frequencies. The present study divides the code multipath delays of BDS-3 observations (at four frequencies) into systematic and random parts for modeling and mitigation, respectively.

It is difficult to directly construct the multipath delay with a theoretical model owing to the effects of the complex environment and receiver front end. Additionally, the estimated multipath delays are mainly contaminated by noise, which cannot be modeled and mitigated for using an empirical algorithm [20]. Additionally, the Tikhonov regularization algorithm has been used to denoise a series of BDS clock offsets [22] and model GNSS multipath errors [20], with the results of experiments suggesting that the regularization algorithm obtains a better PPP solution. Moreover, Kalman filtering [23], spectral analysis [24], and the particle filter [25] have been proposed to denoise a series of GNSS multipath delays. Meanwhile, to improve the accuracy of models, machine learning methods, such as sparse modeling [21] and the kernel trick [26], have been presented recently for processing GNSS observations, where the least absolute shrinkage selection operator (Lasso), elastic net, and fast iterative shrinkage threshold algorithm (FISTA) are used to output the estimated model coefficients. However, two important issues, namely, the length of the multipath delay

series and the condition of noise in the observations, are ignored in widely used sparse modeling strategies [27]. In general, elastic net is an improved version of the Lasso algorithm to conduct the sparse modelling, which is more stable for the extreme correlations among various predictors as the combination of L_1 norm and L_2 norm regularization terms. Thus, elastic net is set in the process of minimizing the loss function, which ensures the sparsity of the model and increases the stability of the model solution. Additionally, total variation uses the nonsmooth norm to replace the traditional L_2 norm regularization, in which the local structure information can be captured to further eliminate the influence of noise on the reconstruction of a complex network structure and to increase the robustness of the model. In consideration of the characteristic of BDS-3 code observations and the limited sample points, sparse modeling combined with the elastic net term EN and the total variation term TV [27] is investigated for improving the robustness of BDS-3 multipath modeling in the present paper.

The aim of this paper is at optimizing the model of BDS-3 code multipath delay and at mitigating the effects of the delay on rapid PPP solutions. A new strategy for modeling the BDS-3 code multipath delay is proposed in Section 2, where sparse modeling combined with EN and TV terms is first presented, an integrated estimation of model coefficients is then derived in detail, and the correction model of next-arc observations is finally designed using prior information. Section 3 tests single-frequency PPP, real-time PPP, and standard point positioning (SPP) using the proposed strategy. Conclusions and perspectives are presented in Section 4.

2. Materials and Methods

The service performance of a satellite system directly reflects observation multipath delays as a main error in GNSS PPP. To reduce the effects of noise and limited observations, this section discusses the high-precision modeling of BDS-3 code multipath delays, for which the systematic and random parts are separately considered. Meanwhile, a strategy of correcting for the code multipath delay of the next-arc observation is also studied.

2.1. Modeling BDS-3 Code Multipath Delays. To overcome the effects of the observation noise and series length in modeling BDS-3 multipath delays, sparse modeling from the field of machine learning [27] is adopted to optimize and process the series of BDS-3 multipath errors (raw code multipath delays for each satellite with continuous ambiguity calculated by equations (1) and (2)). In this research, based on the continuous tracking of satellites, the multipath delays of different BDS-3 code observations are first estimated using a combination of two frequencies as [2].

$$MP_i^s(t_k) = P_i^s(t_k) - m_{ij}^s \cdot \lambda_i \cdot \phi_i^s(t_k) + \left(m_{ij}^s - 1\right) \cdot \lambda_j \cdot \phi_j^s(t_k), \quad (1)$$

$$m_{ij}^s = \frac{f_i^2 + f_j^2}{f_i^2 - f_j^2}, \quad (2)$$

where f and λ are the frequency and wavelength of the signals, respectively, the subscripts i and j indicate different frequencies, s represents the satellite (BDS-3 in this paper), φ and P are the observations of the phase and code, respectively, and t_k is the epoch time.

Using the estimated code multipath delays, a series function is written for the i th BDS-3 satellite as

$$\begin{bmatrix} y_i(t_1) \\ y_i(t_2) \\ \vdots \\ \vdots \\ y_i(t_M) \end{bmatrix} = \begin{bmatrix} \varphi_{i1}(t_1) & \varphi_{i2}(t_1) & \cdots & \varphi_{iN}(t_1) \\ \varphi_{i1}(t_2) & \varphi_{i2}(t_2) & \cdots & \varphi_{iN}(t_2) \\ \vdots & \vdots & \vdots & \vdots \\ \vdots & \vdots & \vdots & \vdots \\ \varphi_{i1}(t_M) & \varphi_{i2}(t_M) & \cdots & \varphi_{iN}(t_M) \end{bmatrix} \begin{bmatrix} x_{i1} \\ x_{i2} \\ \vdots \\ \vdots \\ x_{iN} \end{bmatrix} + \begin{bmatrix} \varsigma_{i1} \\ \varsigma_{i2} \\ \vdots \\ \vdots \\ \varsigma_{iM} \end{bmatrix}, \quad (3)$$

where y denotes the multipath delays of different epochs or elevations (estimated values), ϕ denotes the independent variable of multipath models, which can be constructed using the epoch, elevation, and azimuth, x denotes the model coefficients, ζ denotes the residuals of the models, and M and N are the total number of epochs and the length of the series, respectively.

Equation (3) is rewritten in matrix form as

$$\mathbf{Y}_i = \varphi_i \cdot \mathbf{X}_i + \boldsymbol{\varsigma}_i. \quad (4)$$

Then, to improve the robustness of equation (4) against observation noise, EN of the sparse structure and the TV term are introduced into the objective function [28]:

$$F(\mathbf{M}_i) = \|\mathbf{Y}_i - \varphi_i \mathbf{X}_i\|_2^2 + \frac{\beta}{2} \|\varphi_i \mathbf{X}_i\|_2^2 + \lambda \|\varphi_i \mathbf{X}_i\|_1 + \gamma \text{TV}(\varphi_i \mathbf{X}_i) = \min, \quad (5)$$

where $(\beta/2)\|\varphi_i \mathbf{X}_i\|_2^2 + \lambda \|\varphi_i \mathbf{X}_i\|_1$ denotes the regularization term of EN, $\text{TV}(\varphi_i \mathbf{X}_i)$ is the regularization term of TV, and β , λ , and γ are coefficients of the objective function, which can be set as prior values or selected using the Thomas algorithm [20]. The smoothness strategy of TV regularization is adopted to obtain solutions to equation (5) [29] as follows:

$$\text{TV}(\varphi_i \mathbf{X}_i) = \sum \|\mathbf{A} \cdot \varphi_i \mathbf{X}_i\|, \quad \mathbf{A} = \begin{bmatrix} -1 & 1 & & & & \\ & -1 & 1 & & & \\ & & & \cdots & \cdots & \\ & & & & -1 & 1 \\ & & & & & -1 & 1 \end{bmatrix}. \quad (6)$$

We adopt the concept of FISTA to iterate the results of model coefficients using the inequality approximation algorithm and the corresponding interval threshold of convergence (ε) [30]. The final solutions of equation (5) are thus obtained using the iteration condition

$$\left| F(\mathbf{M}_i^{k+1}) - F(\mathbf{M}_i^k) \right| \leq \varepsilon, \quad (7)$$

where k is the number of iterations.

2.2. Integrated Modeling of BDS-3 Code Multipath Delays.

On the basis of the sparse modeling of BDS-3 code observation multipath delays, the PPP service can be improved theoretically through the precise correction of multipath errors. However, the short-term prediction of multipath delays should be obtained for next-arc or real-time PPP uses, where a more precise model coefficient is needed to construct the BDS-3 code multipath delay. Adopting the integrated estimation strategy, the systematic and random parts of the multipath series are separated and modeled in one solution. Taking the k th BDS-3 satellite as an example, the code multipath delays are expressed as a function of the satellite elevation:

$$Y_k(e_i) = B_k(e_i) + R_k(e_i) + \varepsilon_k(e_i), \quad (8)$$

where e_i is the i th elevation of the satellite, Y_k denotes the code multipath delays after processing with equations (1)–(7), and $B(e_i)$ and $R(e_i)$ are functions of systematic and random parts, respectively. Traditionally, the systematic part is modeled with a polynomial function, where a second-order function is used to process the BDS code multipath delays [2]. The random part can be expressed as an autoregressive (AR) model. ε represents the model residuals.

As mentioned above, the AR model is used to describe the random terms of multipath errors, where the relationship among variables of a random series is expressed as

$$R_k(e_i) = \kappa_k^1 R_k(e_i - 1) + \cdots + \kappa_k^d R_k(e_i - d) + \mu_k(e_i). \quad (9)$$

Here, κ is the coefficient of the AR model estimated by the least-squares (LS) algorithm, d is the order of the model, and μ is the white noise. In equation (9), the order of the AR model is selected using the Akaike information criterion [22, 29]. To estimate the model coefficients properly and rapidly, we take all coefficients into one solution as

$$Y_k(e_{i+1}) = \mathbf{K}_k(e_{i+1}) \cdot \mathbf{b}_k + R_k(e_{i+1}) + v_k(e_i), \quad (10)$$

where v is the model error, $\mathbf{K}(e_i) = [1 \ e_i \ e_i^2]$, and $\mathbf{b}_k = [b_0^k \ b_1^k \ b_2^k]^T$. Equation (10) can be rewritten as

$$\begin{aligned} R_k(e_{i+1}) &= Y_k(e_{i+1}) - \mathbf{K}_k(e_{i+1}) \cdot \mathbf{b}_k + v_k(e_i) \\ &= \kappa_k^1 \cdot [Y_k(e_i) - \mathbf{K}_k(e_i) \cdot \mathbf{b}_k] + \cdots + \kappa_k^d \\ &\quad \cdot [Y_k(e_{i+1-d}) - \mathbf{K}_k(e_{i+1-d}) \cdot \mathbf{b}_k] + v_k(e_i). \end{aligned} \quad (11)$$

Furthermore, inserting equation (10) into equation (11) yields

$$\begin{aligned} Y_k(e_{i+1}) - \left[\kappa_k^1 \cdot Y_k(e_i) + \dots + \kappa_k^d \cdot Y_k(e_{i+1-d}) \right] + v'_k(e_i) \\ = \mathbf{K}_k(e_{i+1}) \cdot \mathbf{b}_k - \sum_{h=1}^d \kappa_k^h \cdot \mathbf{K}_k(e_{i+1-h}) \cdot \mathbf{b}_k + v'_k(e_i). \end{aligned} \quad (12)$$

Stacking all equations for satellite elevations from $e_{(f)}$ to $e_{(t)}$, the model coefficients for the k th satellite are obtained from the integrated estimation as

$$\begin{bmatrix} \mathbf{c}_{d+1}^T \\ \mathbf{c}_{d+2}^T \\ \vdots \\ \mathbf{c}_t^T \end{bmatrix} - \mathbf{F} \cdot \begin{bmatrix} \mathbf{N}_{d+1} \\ \mathbf{N}_{d+2} \\ \vdots \\ \mathbf{N}_t \end{bmatrix} \cdot \mathbf{Y}_k = \begin{bmatrix} \mathbf{A}_k(e_{d+1}) \\ \mathbf{A}_k(e_{d+2}) \\ \vdots \\ \mathbf{A}_k(e_t) \end{bmatrix} - \mathbf{F} \cdot \begin{bmatrix} \mathbf{M}_{d+1} \\ \mathbf{M}_{d+2} \\ \vdots \\ \mathbf{M}_t \end{bmatrix} \cdot \mathbf{b}_k, \quad (13)$$

where \otimes denotes the Kronecker product, $\mathbf{F} = \mathbf{I}_{t-d} \otimes \kappa_k^T$, $\kappa_k = [\kappa_k^1 \ \kappa_k^2 \ \dots \ \kappa_k^d]^T$, \mathbf{I}_{t-d} is an identity matrix with order $t-d$, \mathbf{c}_j is the j th column of the $t \times t$ identity matrix, $\mathbf{N}_j = [\mathbf{c}_{j-1}^T \ \mathbf{c}_{j-2}^T \ \dots \ \mathbf{c}_{j-d}^T]^T$, and $\mathbf{M}_j = [\mathbf{A}_k(e_{j-1}) \ \mathbf{A}_k(e_{j-2}) \ \dots \ \mathbf{A}_k(e_{j-d})]^T$.

The model coefficients are obtained from the estimation of equation (13). Using equation (11), all satellites (e.g., satellite l) are processed in one solution:

$$\mathbf{C} \cdot \mathbf{Y}' = \mathbf{T} \cdot \mathbf{b}, \quad (14)$$

$$\begin{cases} \mathbf{Y}' = [\mathbf{Y}_1 \ \mathbf{Y}_2 \ \dots \ \mathbf{Y}_k \ \dots \ \mathbf{Y}_l]^T \\ \mathbf{b} = [\mathbf{b}_1 \ \mathbf{b}_2 \ \dots \ \mathbf{b}_k \ \dots \ \mathbf{b}_l] \\ \mathbf{C} = [\mathbf{C}_1 \ \mathbf{C}_2 \ \dots \ \mathbf{C}_k \ \dots \ \mathbf{C}_l] \\ \mathbf{T} = [\mathbf{T}_1 \ \mathbf{T}_2 \ \dots \ \mathbf{T}_k \ \dots \ \mathbf{T}_l] \\ \mathbf{C}_k = \left[[\mathbf{c}_{d+1}^T \ \mathbf{c}_{d+2}^T \ \dots \ \mathbf{c}_t^T]^T - \mathbf{F} \cdot [\mathbf{N}_{d+1} \ \mathbf{N}_{d+2} \ \dots \ \mathbf{N}_t]^T \right] \\ \mathbf{T}_k = \left[[\mathbf{A}_k(e_{d+1}) \ \mathbf{A}_k(e_{d+2}) \ \dots \ \mathbf{A}_k(e_t)]^T - \mathbf{F} \cdot [\mathbf{M}_{d+1} \ \mathbf{M}_{d+2} \ \dots \ \mathbf{M}_t]^T \right] \end{cases} \quad (15)$$

2.3. Multipath Delay Correction of Next-Arc Observations. The estimated coefficients are traditionally introduced into next-arc observations to mitigate the multipath delays [2]. However, considering the orbital period and the surrounding environments of the receivers, it is difficult to obtain a perfect PPP solution under the effect of code multipath delays. For correction of the multipath delays of the next-arc BDS-3 code observations using the estimated coefficients, a new strategy is proposed to further improve the accuracy of multipath mitigation. The estimation of the next-arc multipath delays using the LS algorithm is expressed as

$$\mathbf{r} = \mathbf{B}\mathbf{x} + \boldsymbol{\eta}\mathbf{P}, \quad (16)$$

where \mathbf{x} denotes the true values of the model coefficients for the next-arc multipath delay and \mathbf{P} is the weight matrix. In addition, to improve the accuracy of the model coefficients, a constraint function based on the prior information \mathbf{x}_0 , $\tilde{\mathbf{x}}_0 = \mathbf{x} + \tilde{\boldsymbol{\varepsilon}}_0$, is used. Here, a weight matrix $\tilde{\mathbf{P}}_0$ is set. $\boldsymbol{\varepsilon}$ and $\boldsymbol{\eta}$ are the model residuals. During the estimation of equation (16), the weight matrix is decomposed as $\tilde{\mathbf{P}}_0 = \tilde{\mathbf{R}}_0^{-1} \tilde{\boldsymbol{\varepsilon}}_0^{-T}$ and $\mathbf{P} = \mathbf{R}^{-1} \mathbf{R}^{-T}$.

Equation (16) and its constraint function are then rewritten as

$$\begin{aligned} \tilde{\mathbf{z}}_0 &= \tilde{\mathbf{R}}_0 \cdot \mathbf{x} + \tilde{\mathbf{v}}_0, \\ \mathbf{z} &= \mathbf{A}\mathbf{x} + \mathbf{v}, \end{aligned} \quad (17)$$

where $\tilde{\mathbf{z}}_0 = \tilde{\mathbf{R}}_0 \cdot \tilde{\mathbf{x}}_0$, $\mathbf{z} = \mathbf{R} \cdot \mathbf{v}$, $\mathbf{A} = \mathbf{R} \cdot \mathbf{B}$, $\tilde{\mathbf{v}}_0 = \tilde{\mathbf{R}}_0 \cdot \tilde{\boldsymbol{\varepsilon}}_0$, and $\mathbf{v} = \mathbf{R} \cdot \boldsymbol{\eta}$.

Meanwhile, the Householder conversion for equation (17) is further expressed as

$$\mathbf{S} \cdot \begin{bmatrix} \tilde{\mathbf{R}}_0 \\ \mathbf{A} \end{bmatrix} \mathbf{x} = \mathbf{S} \cdot \begin{bmatrix} \tilde{\mathbf{z}}_0 \\ \mathbf{z} \end{bmatrix} + \mathbf{S} \cdot \begin{bmatrix} \tilde{\mathbf{v}}_0 \\ \mathbf{v} \end{bmatrix} \Rightarrow \begin{bmatrix} \tilde{\mathbf{R}}_0 \\ 0 \end{bmatrix} \mathbf{x} = \begin{bmatrix} \tilde{\mathbf{z}}_0 \\ \mathbf{e} \end{bmatrix} + \begin{bmatrix} \tilde{\mathbf{v}}_0 \\ \mathbf{v}_e \end{bmatrix}, \quad (18)$$

where \mathbf{e} and \mathbf{v}_e are the model errors and the corresponding noise, respectively.

An objective function is defined as

$$J(x) = \left\| \begin{bmatrix} \tilde{\mathbf{R}}_0 \\ \mathbf{A} \end{bmatrix} x - \begin{bmatrix} \tilde{\mathbf{z}}_0 \\ \mathbf{z} \end{bmatrix} \right\|^2 = \|\mathbf{R} \wedge_0 x - \mathbf{z} \wedge_0\|^2 + \|\mathbf{e}\|^2 \geq \|\mathbf{e}\|^2. \quad (19)$$

In obtaining the minimum $J(x)$, the parameter solution reads as

$$\hat{\mathbf{R}}_0 x = \hat{\mathbf{z}}_0. \quad (20)$$

Finally, the solution to equation (20) is

$$\mathbf{x} = \hat{\mathbf{R}}_0^{-1} \cdot \hat{\mathbf{z}}_0, \quad (21)$$

where the covariance matrix of the estimated \mathbf{x} is $\hat{\mathbf{P}}_0 = \hat{\mathbf{R}}_0^{-1} \cdot \hat{\mathbf{R}}_0^{-T}$.

According to equations (16)–(21), the code multipath delay of BDS-3 can be further mitigated, especially in rapid applications, with the aid of prior information. Figure 1 is a flowchart of the integrated method of processing BDS-3 code observations proposed in this research.

3. Experiments and Results

To verify the proposed strategy of correcting for BDS-3 observation multipath delays, BDS-3 observations of the Multi-GNSS Experiment (MGEX) and International GNSS Monitoring and Assessment System (iGMAS) are used in positioning experiments. The distribution of MGEX and

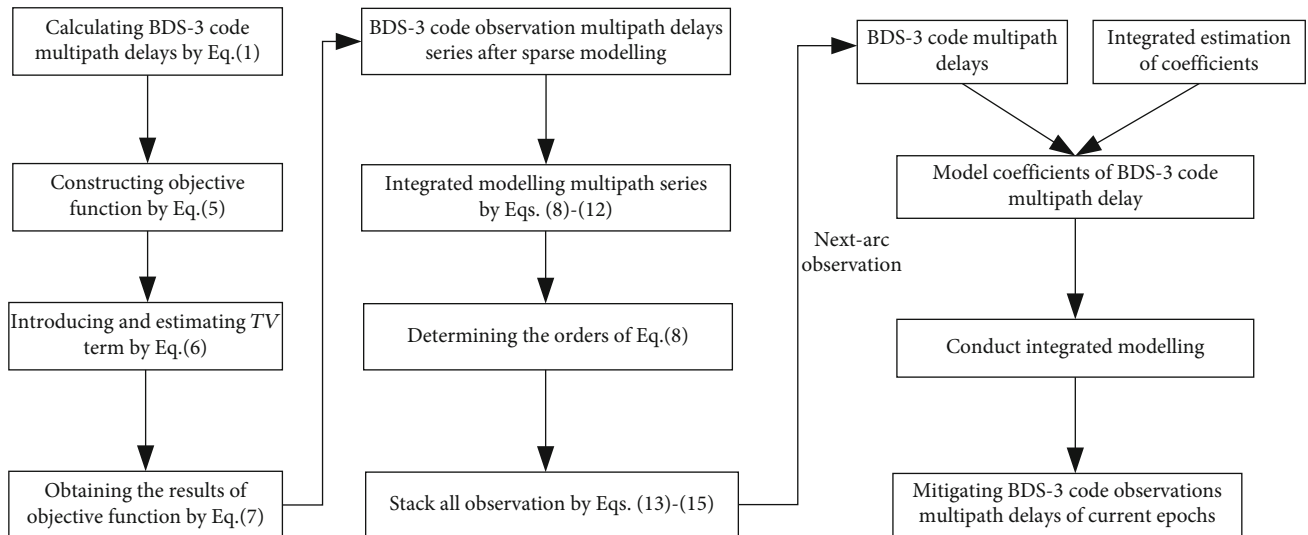


FIGURE 1: Flowchart of mitigating BDS-3 code observation multipath delays.

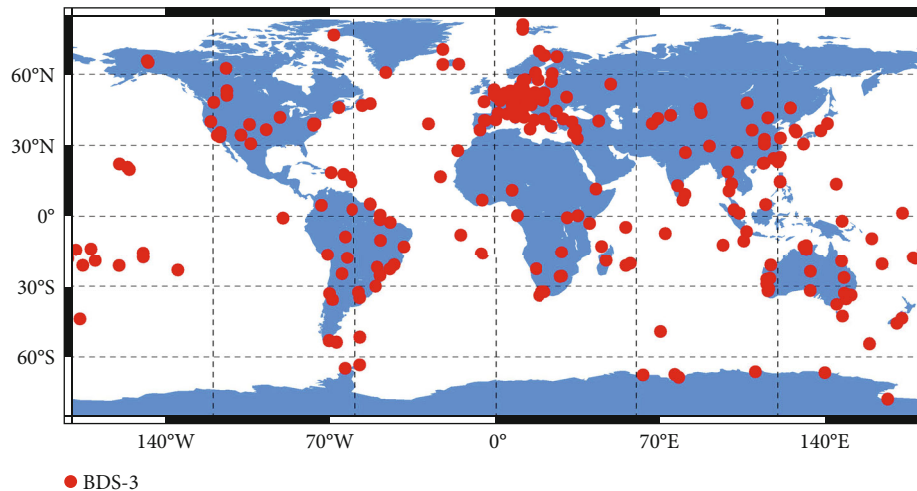


FIGURE 2: Distribution of BDS-3 satellite tracking stations.

iGMAS stations relating to the BDS-3 observations is presented in Figure 2.

3.1. Analysis of BDS-3 Code Multipath Delays. Four groups of experiments are conducted with different schemes to analyze the proposed method. In the experiments, one-month observations (day of year (DOY) 214–244, 2020) made by BDS-3 stations are selected. The characteristics of the multipath delays of BDS-3 satellite code observations at different frequencies (i.e., B1I, B3I, B1C, and B2a) are first analyzed. Results for two iGMAS stations calculated using equations (1)–(7) are shown in Figure 3, where the series of multipath delays of station-WUH1 code observations of three satellites (i.e., C34, C38, and C59) and the corresponding satellite elevations are plotted for DOY 228 as examples. Figure 3 suggests that BDS-3 observations contain appreciable code multipath delays. Meanwhile, a trend term is seen along the satellite elevation, with the observations corresponding to lower elevations having more obvious multipath errors.

Therefore, the trend term (systematic part) and the residual term (random part) should be modeled separately in the mitigation of BDS-3 multipath errors.

The first group of experiments are conducted to test the algorithm of sparse modeling in processing the BDS-3 code multipath series. In the experiments, three comparison schemes are designed to fully analyze the performance of the sparse modeling of the multipath delays of BDS-3 code observations.

Scheme 1: A series of estimated BDS-3 multipath delays at different frequencies is first modeled using a regularization algorithm [20]. Typical distributions for MP1 (station MP at the B1I frequency) after regularization are plotted in Figure 4(b), where all medium Earth orbit (MEO) satellite observations of WUH1 on DOY 228 are input in the analysis.

Scheme 2: Similarly, the series of multipath delays are optimized using EN of the sparse structure. The processed series are presented in Figure 4(c).

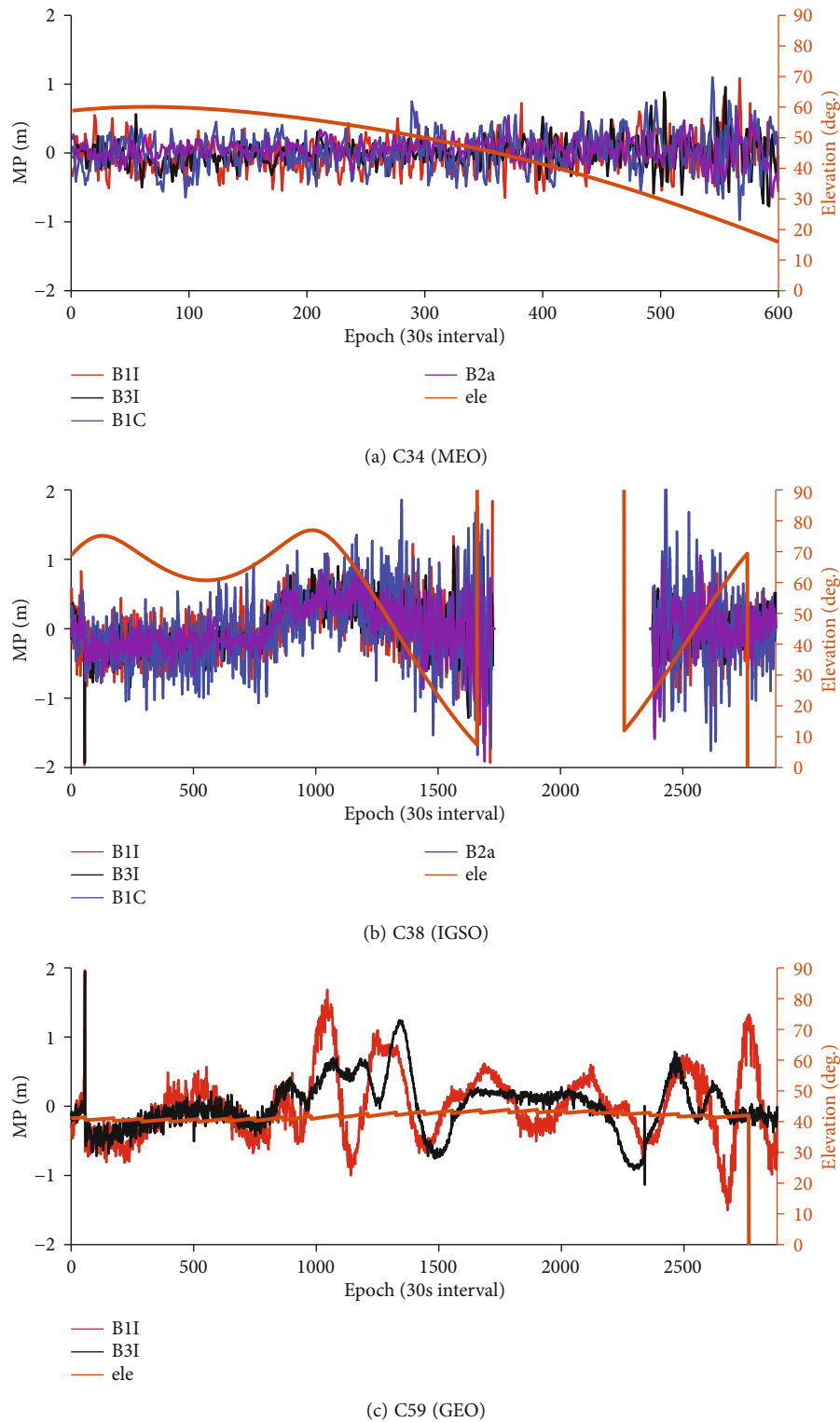


FIGURE 3: Series of BDS-3 multipath delays for the iGMAS (WUH1) station (DOY 228).

The objective function of Scheme 2 is further improved by introducing the TV term. The corresponding typical distributions of the MP1 series are shown in Figure 4(d).

Owing to the large volume of experimental observations, the MEO satellites of BDS-3 observations are taken as exam-

ples to show the performances of the sparse modeling algorithm in Figure 4. Furthermore, the results for frequencies B3I, B1C, and B2a are analyzed using the one-month observations for all BDS-3 MEO satellites, where the standard deviations of the series are given in Table 1. The table shows

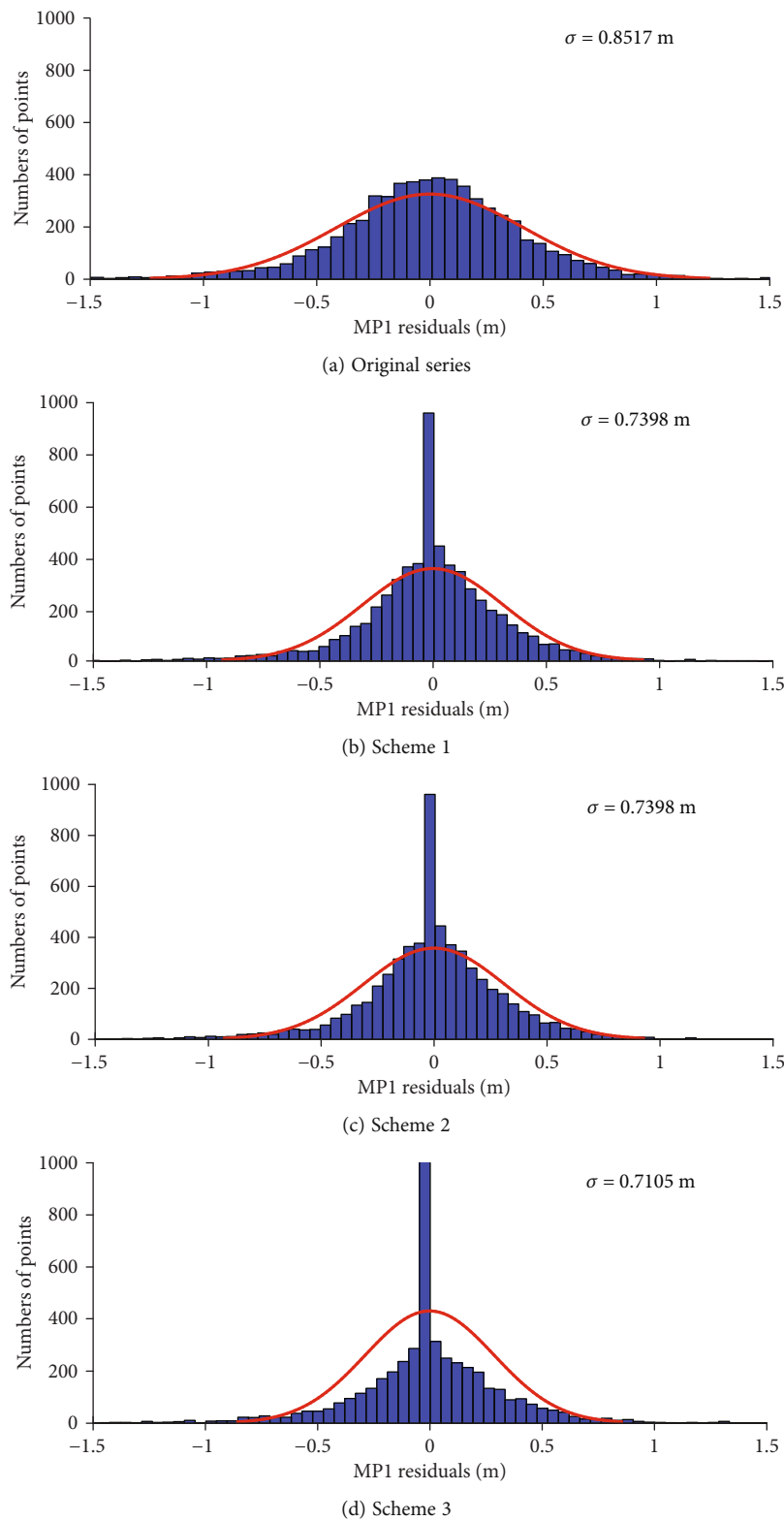


FIGURE 4: Typical distributions of the BDS-3 MP1 series obtained using the sparse modeling algorithm.

that different values of the standard deviation are output for different schemes, where the adoption of regularization, EN, and TV denoises the MP series, realizes sparse modeling, and overcomes the restriction of limited series, respectively.

The results of multipath delays obtained using the different processing strategies indicate that sparse modeling with the aid of the TV term provides a more stable series. Because the series of observations selected in constructing the

TABLE 1: Standard deviations (m) of multipath series at frequencies B1I, B3I, B1C, and B2a for BDS-3 satellite observations.

		B1I		B3I		B1C		B2a	
		MEO	IGSO	MEO	IGSO	MEO	IGSO	MEO	IGSO
MGEX	Original series	0.300	0.295	0.209	0.287	0.228	0.225	0.240	0.194
	Scheme 1	0.286	0.281	0.199	0.273	0.216	0.214	0.228	0.185
	Scheme 2	0.194	0.193	0.105	0.191	0.126	0.133	0.138	0.102
	Scheme 3	0.169	0.172	0.097	0.188	0.114	0.119	0.129	0.098
iGMAS	Original series	0.311	0.407	0.266	0.368	0.316	0.495	0.259	0.347
	Scheme 1	0.296	0.388	0.254	0.350	0.301	0.472	0.247	0.331
	Scheme 2	0.214	0.333	0.186	0.303	0.208	0.367	0.175	0.226
	Scheme 3	0.209	0.285	0.180	0.242	0.196	0.355	0.171	0.224

mitigation model of multipath delays are usually within a period of 1 day, the TV term added to the sparse modeling function theoretically reduces the effects of noise and limited epochs. An integrated modeling strategy of the BDS-3 multipath series is investigated in the second group of experiments. Three modeling scenarios of multipath delays are considered for four iGMAS and four MGEX stations. The details of integrated modeling were presented in Figure 1. The experiments on multipath modeling using the proposed methods are described as follows.

3.1.1. Scenario 1. On the basis of the results of Scheme 3, the series of BDS-3 multipath delays is firstly modeled using the AR algorithm. Model residuals are output and analyzed.

3.1.2. Scenario 2. In mitigating the trend terms of the residuals of Scenario 1, a polynomial function is used to reduce the multipath errors. Meanwhile, the strategy of Scenario 1 is adopted to model residuals after the processing of trend terms.

3.1.3. Scenario 3. With the consideration of the two-step strategy adopted in Scenario 2, the integrated estimation of model coefficients is tested using the integrated LS-combined AR method.

The model residuals of the three scenarios are shown in Figure 5 for the analysis of the results of the integrated method in modeling the BDS-3 multipath series. The figure shows that the integrated method, especially in one-step estimation, is more stable than the traditional AR-only method. Therefore, the integrated estimation strategy of modeling multipath delays using the LS-combined AR method is recommended for the processing of BDS-3 code observations.

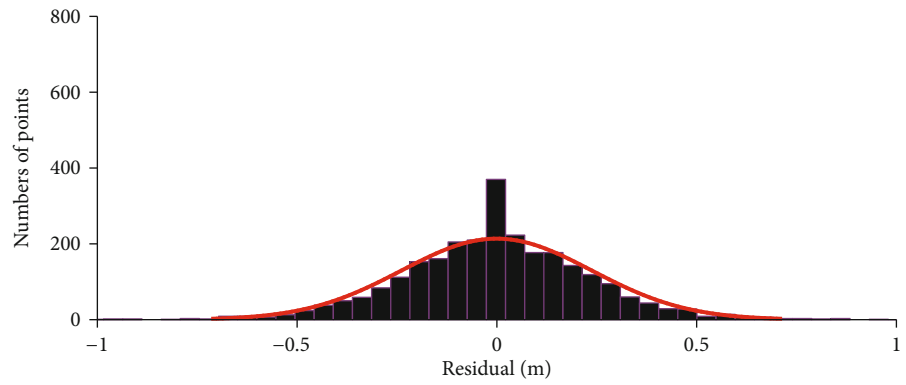
Figure 5 shows that the LS-combined AR-integrated strategy well models and mitigates the BDS-3 code multipath errors and can be induced to improve the quality of BDS-3 satellite observations. However, the real-time applications of BDS-3 services cannot estimate model parameters with long-term observations. As an example, widely adopted sidereal filtering is conducted on the basis of the satellite orbit period. Therefore, in correcting for the multipath delays of next-arc observations in real-time or near real-time applications, it is necessary to further improve the model coefficients of multipath errors. According to

Figure 1, the multipath delays are output and modeled by LS-combined AR method based on equations (1)–(15) for BDS-3 satellites' multifrequency observations. As mentioned above, we take the estimated model coefficients as prior information into the solution of multipath errors of the next-arc observations for real-time or rapid applications. In experiments, the tracking station of iGMAS (WUH1, DOY 228, 2020) is taken into modelling and correcting BDS-3 (MEO satellites) multipath delays. It should be noted that the proposed method takes the correlation between multipath delays and satellites' elevations into consideration, which is different from the traditional sidereal filtering based on the repeat time of satellites' orbit. Therefore, only one-day (DOY 228, 2020) observations are selected into experiments to model multipath delay and real-time correction with its prior information. In verifying the availability of the improved multipath model with the prior constraints, two experiments are conducted to analyze the multipath residuals. Additionally, the observations are preprocessed to detect and repair the cycle slips and delete satellites without observations during modeling multipath delays.

3.1.4. Experiment 1. On the basis of the estimated model coefficients of a multipath series, the next-arc observations are corrected using the predicted values. The residuals between the predicted and real multipath series are plotted in Figure 6(b) (AR method only) and Figure 6(c) (integrated-LS combined AR method).

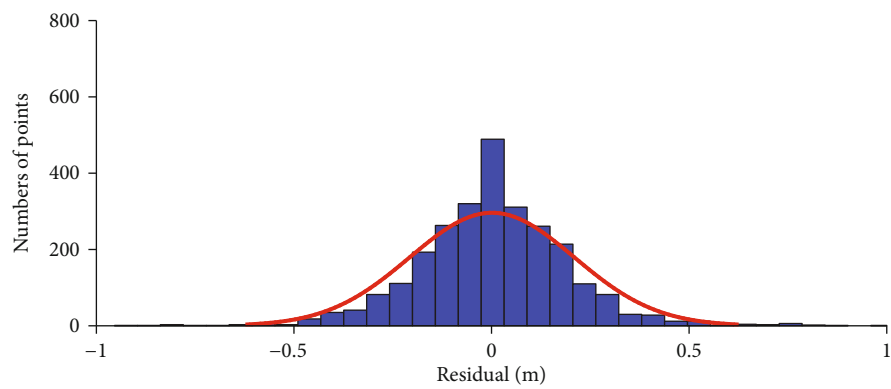
3.1.5. Experiment 2. In the correction of next-arc BDS-3 multipath errors, the estimated model coefficients are set as prior information to obtain the new model. The next-arc residuals between the real and calculated values are shown in Figure 6(d).

The residuals of the multipath series in the third group of experiments show that the next-arc BDS-3 observations can be optimized with the prior information in the estimation of multipath models. Table 2 gives the average daily root-mean-square (RMS) values of multipath residuals for different frequencies (MGEX stations) to show the performance of the proposed strategy in Experiments 1 and 2. Figure 6 and Table 2 show that the improved strategy of modeling BDS-3 multipath delays indeed improves the accuracy of BDS-3 observations for rapid and real-time



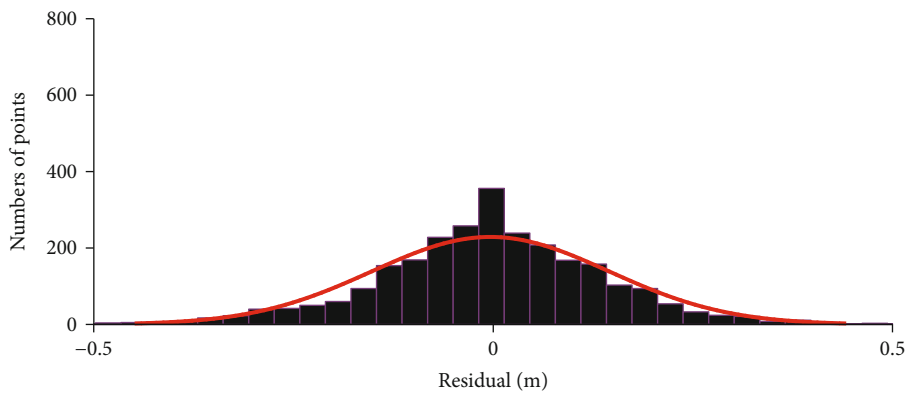
■ B1C MP series

(a) AR method only (B1C)



■ B2a MP series

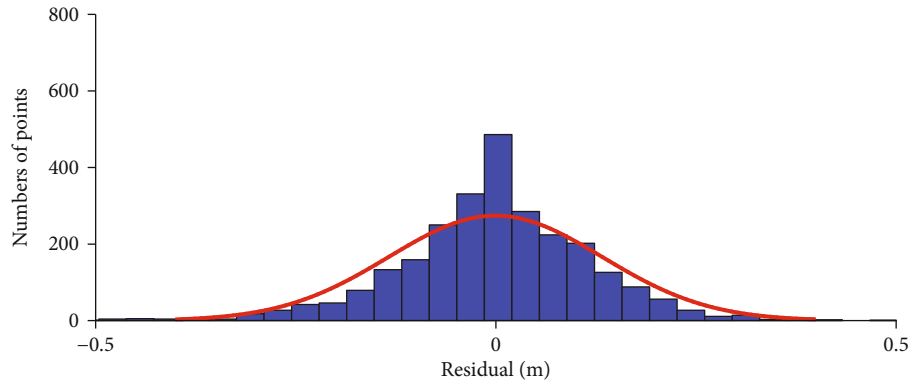
(b) AR method only (B2a)



■ B1C MP series

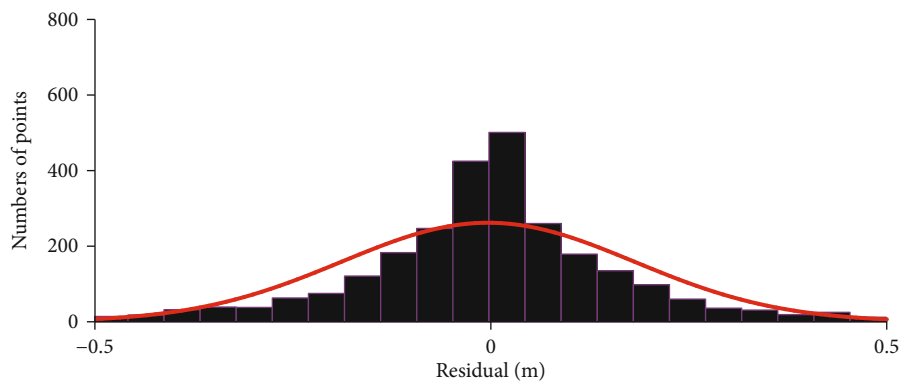
(c) Two-step strategy (B1C)

FIGURE 5: Continued.



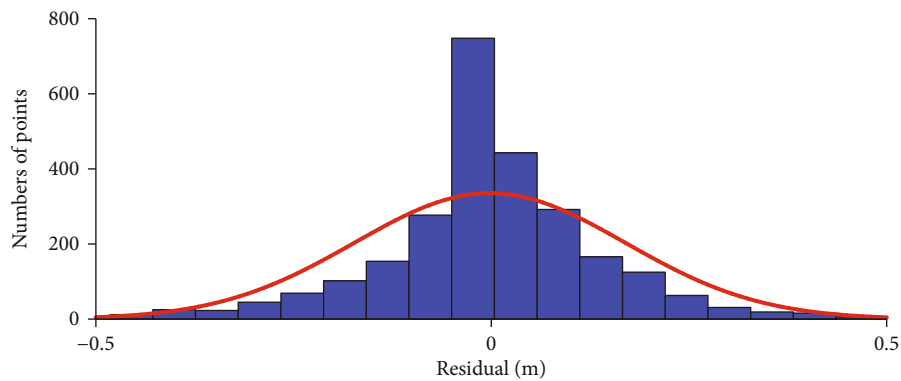
■ B2a MP series

(d) Two-step strategy (B2a)



■ B1C MP series

(e) Integrated LS-combined AR method (B1C)



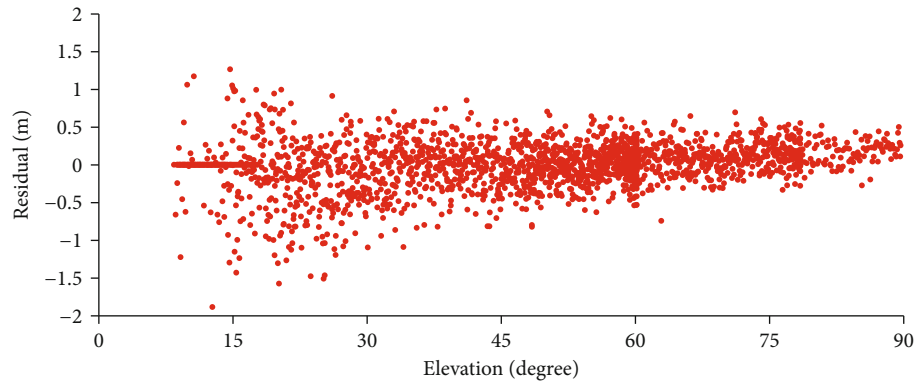
■ B2a MP series

(f) Integrated LS-combined AR method (B2a)

FIGURE 5: Model residuals of BDS-3 B1I and B3I code observations (original series and post modeling) for Scenarios 1, 2, and 3 (C33, C34, and C35).

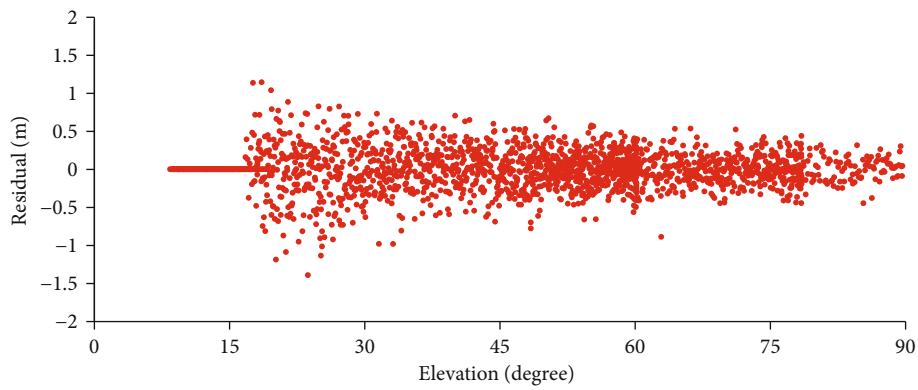
applications. In previous researches [2], the BDS-2 satellites' code biases are discussed and corrected by a proposed method called the one-step method, in which the high-correction factor between multipath delays and code biases are considered. In this research, the multipath delays of BDS-3 multifrequency observations are analyzed, in which a systematic term and a random term divided from BDS-3 satellites' code observations can be found from the first

group of experiments. It should be noted that the BDS-2 code biases are different from BDS-3 systematic multipath delays based on mechanism, characteristic, and order of magnitude. Although the code bias related to the BDS-2 internal multipath vanished for BDS-3 code observations, the multipath of BDS-3 multifrequency observations should be paid more attention and be improved to optimize the positioning services. Due to the differences between BDS-2



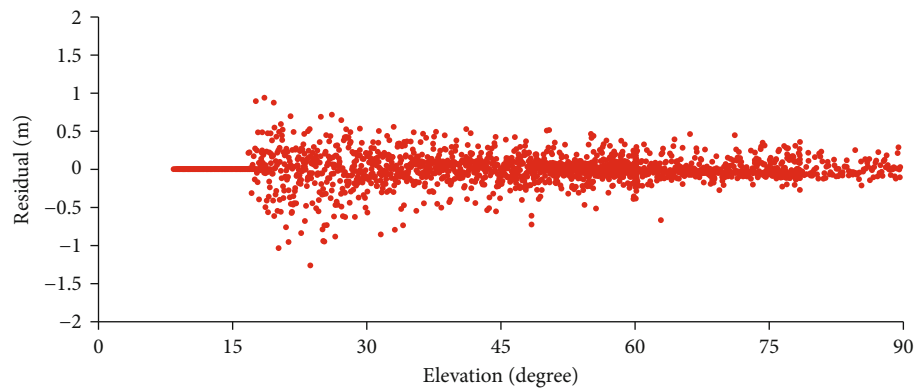
• B1I

(a) Original multipath series



• B1I

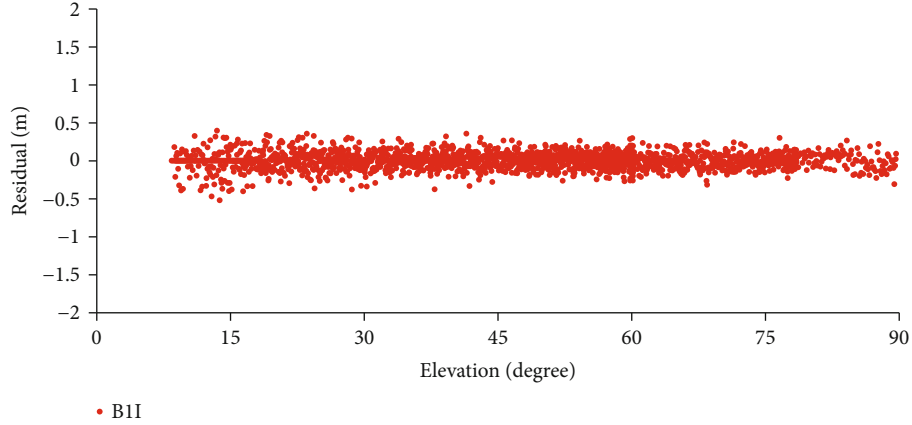
(b) Multipath residuals for the AR method only



• B1I

(c) Multipath residuals of the LS-combined AR

FIGURE 6: Continued.



(d) Multipath residuals with prior information

FIGURE 6: Residuals between predicted and estimated delays of Experiments 1 and 2 in the third group of experiments (WUH1, DOY 228, 2020).

TABLE 2: Average daily RMS values (m) of multipath residuals in the third group of experiments.

	B1I	B3I	B1C	B2a
Experiment 1 (LS combined AR)	0.261	0.144	0.172	0.154
Experiment 2 (prior information)	0.135	0.102	0.092	0.089

and BDS-3 satellites, we usually take additional parameters, such ISB and DCB, to accurately estimate BDS-2- and BDS-3-related results [3]. In this research, it is difficult to mitigate the multipath delays of BDS-2 and BDS-3 within one solution, which reasons can be summarized as two points: firstly, differences of the coefficient of systematic terms for the BDS-2 and BDS-3 multipath delays are more than an order of magnitude [16]. So, we cannot together estimate the coefficients with a unified model; secondly, the code bias of BDS-2 observations should be firstly corrected. And the residuals of multipath of BDS-2 can be modeled with a same strategy of BDS-3. In the next step, we will take the proposed model into the positioning services of combined BDS-2 and BDS-3 satellites after the model and elimination of BDS-2 code biases.

3.2. Results for BDS-3 PPP Solutions. The aim of this study is at improving the performance of BDS-3 PPP services. It is concluded from the above three groups of experiments that the proposed integrated method with the aid of sparse modeling provides a more stable series of the BDS-3 multipath delay. Meanwhile, a fourth group of experiments on BDS-3 single-frequency PPP and double-frequency real-time PPP is conducted using the proposed strategy for the BDS-3 multipath delay. Further details of configurations for single-frequency PPP and real-time PPP have been published [2]. We set the cutoff angle at 5° in estimating the positioning parameters. The antenna types are described in the literature [3]. Because of the lack of accurate BDS-3 satellite phase center variation (PCV) parameters, we simply ignore the effects of PCV on the PPP solution. All position-

ing experiments are conducted using the orbit determination and positioning software package of CUM (an iGMAS analysis center), where the reference frame is ITRF 2014.

3.2.1. Single-Frequency PPP Experiments. Three iGMAS stations and one MGEX station making BDS-3 observations are selected in the experiments for the analysis of BDS-3 single-frequency PPP. The configuration of single-frequency PPP is listed in Table 3. The double-frequency combination is adopted to model multipath delays. The experimental session is set as DOY 221–228, 2020, for which observations made at four frequencies (i.e., B1I, B3I, B1C, and B2a) are analyzed. Precise satellite products, such as orbit and clock offsets, are downloaded from the GFZ analysis center (GBM products). Moreover, four schemes using different strategies to mitigate BDS-3 multipath delays, namely, the original series (none), AR model (AR), LS + AR (two-step), and integrated correction (one step), are analyzed. Residuals of station coordinates are plotted in Figure 7 (B1I) and Figure 8 (B1C), where the results for DOY 226–228 are presented with 2880 epochs per day. Moreover, to present all results of the four stations and four frequencies, the average RMS values of eight-day single-frequency PPP and the corresponding improvements are given in Table 4 (B1I and B3I) and Table 5 (B1C and B2a). In particular, the processing of different strategies for the single-frequency PPP solution is analyzed after the sparse modeling of BDS-3 multipath delays with the aid of the EN structure and TV term.

In the experiments, to avoid errors common to the different PPP solutions, positions of the double-frequency BDS/global positioning system (GPS) solution (i.e., the millimeter difference with the SINEX file) are taken as references to calculate the accuracy of single-frequency PPP. Figures 7 and 8 show that the quality is obviously better for B1C than for B1I, which is consistent with the results of previous research [16]. Additionally, the integrated LS-combined AR strategy obtains position solutions more accurately. Specifically, the results of single-frequency PPP

TABLE 3: Strategy for the single-frequency PPP solution [2].

Parameters	Main configurations
Observations	Four frequencies of phase and pseudorange (B1I, B3I, B1C, and B2a)
Cutoff elevation angle	5°
Weigh assignment	Elevation-dependent (below 30° by 1/2sin (elevation))
Epoch interval	30 seconds per epoch
Ionospheric parameters	Prior products + random walk
Tropospheric parameters	Saastamonien + estimated wet components
Satellites PCO	http://www.igmas.org
Tide models	International earth rotation and reference systems (IERS) 2010
Relativity	IERS 2010
Gravity model	EGM 08 model with 12 × 12 orders
Satellites PCV	Ignored
Station positions	Estimated and output
Receivers clock errors	Estimated and output
Ambiguity parameters	Float solutions

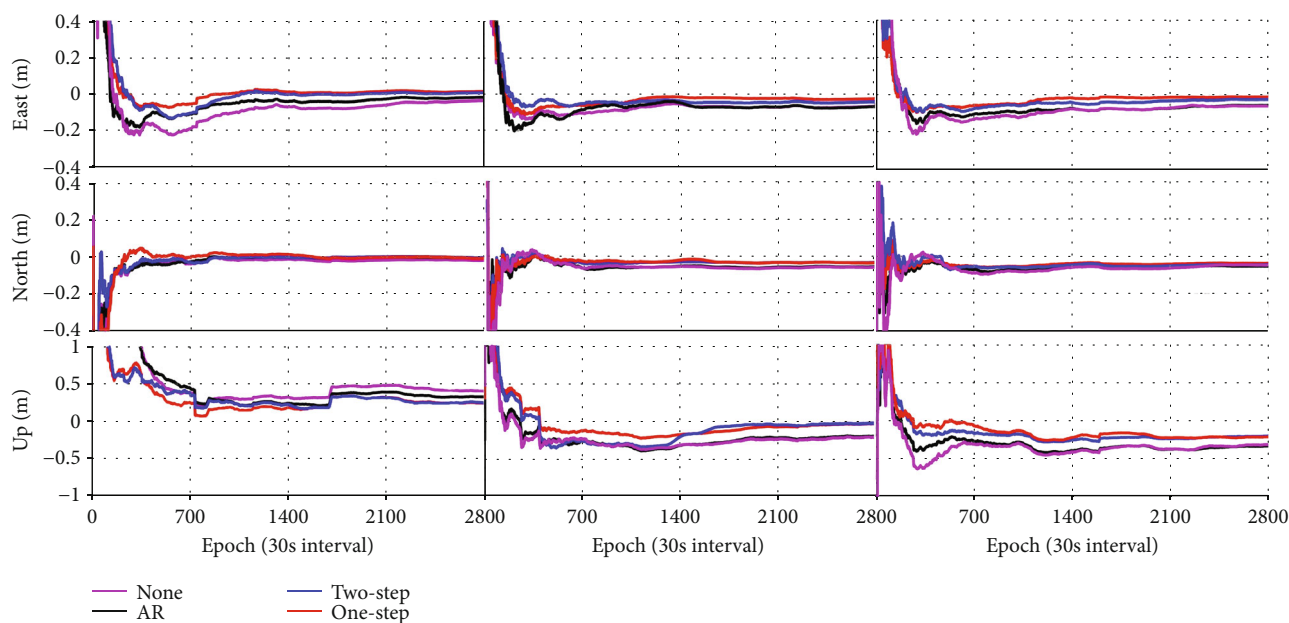


FIGURE 7: Results of BDS-3 single-frequency PPP obtained for B1I observations (DOY 226-228).

obtained for the four frequencies reveal that the accuracy in eastward (E), northward (N), and upward (U) directions is improved by at least 4.1%, 9.6%, and 1.2%, respectively, for B1I; 6.6%, 5.3%, and 0.2%, respectively, for B3I, 12.5%, 14.3%, and 3.8%, respectively, for B1C; and 5.9%, 7.4%, and 18.1%, respectively, for B2a, relative to the results obtained using the traditional method (none). However, because of the high-quality observation of BDS-3, the integrated strategy is slightly more optimized than the two-step method. The ultimate goal of the present study is the development of rapid and high-accuracy positioning services of BDS-3. Therefore, real-time double-frequency BDS-3 PPP is tested with different strategies for multipath errors in the following experiments.

The real-time PPP solution is obtained according to the stage of CUM. A flowchart of real-time BDS-3 double-frequency PPP has been published in the literature [2]. Before obtaining the solution of real-time PPP, the satellite ultrarapid orbit and clock offsets are first estimated [2], which is not the focus of the present study. Additionally, the experimental session of real-time PPP is set as DOY 221–228, 2020, where the combinations of B1I + B3I and B1C + B2a are tested for four iGMAS and four MGEX stations. To avoid the restrictions of the real-time stream in the experiments, the RINEX files of observations are input into real-time PPP solutions. Similarly, four schemes of comparative experiments on BDS-3 multipath delays are designed, namely, no correction (none), correction with

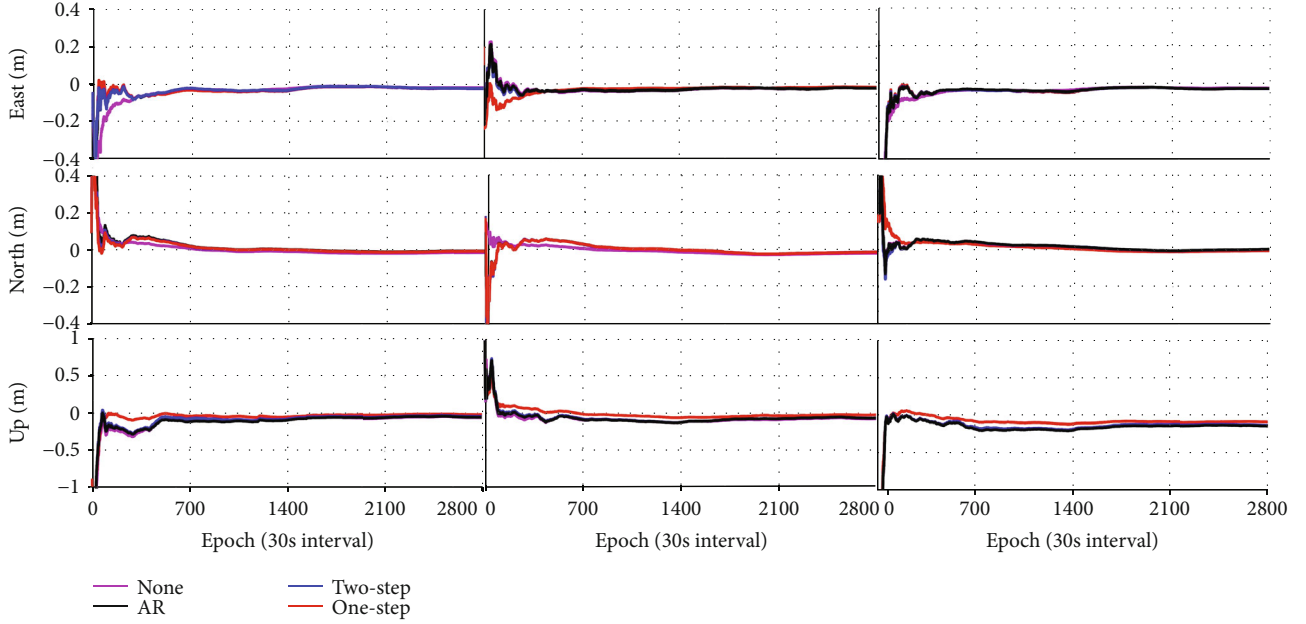


FIGURE 8: Results of BDS-3 single-frequency PPP for B1C observations (DOY 226-228).

TABLE 4: Average daily RMS values (m) of position residuals (B1I, B3I) for four stations obtained using three BDS-3 observation multipath delay processing strategies and the corresponding improvements.

Stations	Directions	B1I					B3I				
		None	Two-step	Imp. (%)	One-step	Imp. (%)	None	Two-step	Imp. (%)	One-step	Imp. (%)
WUH2	E	-0.085	-0.037	56.5	-0.032	62.4	-0.253	-0.249	1.6	-0.132	47.8
	N	-0.044	-0.041	6.8	-0.033	25.0	-0.091	-0.084	7.6	-0.056	38.5
	U	-0.089	-0.084	5.6	-0.059	33.7	-0.239	-0.205	14.2	-0.150	37.2
KNDY	E	-0.024	-0.019	20.8	-0.018	25.0	-0.042	-0.037	11.9	-0.034	19.0
	N	-0.022	-0.013	40.9	-0.012	45.4	-0.042	-0.036	14.3	-0.028	33.3
	U	0.259	0.225	13.1	0.222	14.3	0.178	0.175	1.6	0.171	3.9
BJF1	E	-0.049	-0.048	2.0	-0.047	4.1	-0.045	-0.045	0.0	-0.042	6.6
	N	-0.031	-0.029	6.5	-0.028	9.6	-0.038	-0.036	5.2	-0.036	5.3
	U	0.058	0.051	12.1	0.043	25.9	0.033	-0.033	0.0	0.032	3.0
XIA1	E	-0.043	-0.039	9.3	-0.036	16.3	-0.041	-0.039	4.9	-0.038	7.3
	N	-0.029	-0.026	10.3	-0.024	17.2	-0.045	-0.044	2.2	-0.042	6.6
	U	0.580	0.577	0.5	0.573	1.2	0.886	0.885	0.1	0.884	0.2

the AR model (AR), correction with the two-step LS + AR model (LS + AR), and the integrated estimation of the LS + AR model (one step). However, in comparison with BDS-3 single-frequency PPP, the AR strategy is adopted for the estimated coefficients of the previous day and the multipath delays are mitigated by the predicted values. In contrast, the one-step and two-step strategies are based on the prior information of previous model coefficients. Furthermore, the updated model coefficients are estimated with short-term observations (of an hour or so).

The position residuals (BJF1) for three continuous days (DOY 226–228, 2020) are plotted in Figure 9 (B1I + B3I) and Figure 10 (B1C + B2a) to show the results of BDS-3

real-time PPP. Moreover, the average daily RMS residuals for eight days, four stations, and three strategies (none, two-step, and one-step) and the corresponding improvements are listed in Table 6. Figures 9 and 10 show that there are no appreciable differences in the final precision among the four strategies, although the one-step correction performs slightly better than the two-step strategy. Furthermore, there is a bias in the direction of U, which might be due to the uncalibrated PCV and phase center offset of the satellites.

There are no obvious differences in the simulated final position residuals between single-frequency PPP and real-time PPP. Table 6 shows that the improvements in E, N,

TABLE 5: Average daily RMS values (m) of position residuals (B1C, B2a) for four stations obtained using three BDS-3 observation multipath delay processing strategies and the corresponding improvements.

Stations	Directions	B1C					B2a				
		None	Two-step	Imp. (%)	One-step	Imp. (%)	None	Two-step	Imp. (%)	One-step	Imp. (%)
WUH2	E	-0.058	-0.050	13.8	-0.045	22.4	-0.029	-0.025	13.8	-0.025	13.8
	N	-0.038	-0.034	10.5	0.032	15.8	0.082	0.052	36.6	0.050	39.0
	U	-0.249	-0.228	8.4	-0.222	10.8	-0.271	-0.240	11.4	-0.222	18.1
KNDY	E	-0.050	0.018	64.0	0.009	82.0	-0.115	-0.080	30.4	-0.035	69.6
	N	-0.030	-0.029	3.3	-0.017	43.3	-0.054	-0.052	3.7	-0.050	7.4
	U	-0.105	-0.105	0.0	-0.101	3.8	-0.240	-0.076	68.3	-0.059	75.4
BJF1	E	-0.022	-0.022	0.0	-0.013	40.9	-0.055	-0.028	49.1	-0.027	50.9
	N	-0.028	-0.028	0.0	-0.024	14.3	-0.017	-0.0150	11.8	-0.050	70.6
	U	-0.320	-0.314	1.9	-0.282	11.9	-0.608	-0.592	2.6	-0.073	87.9
XIA1	E	-0.032	-0.029	9.4	-0.028	12.5	-0.017	-0.016	5.9	-0.016	5.9
	N	-0.020	-0.016	20.0	-0.015	25.0	-0.024	-0.023	4.2	-0.022	8.3
	U	-0.075	-0.071	5.3	-0.069	8.0	-0.033	-0.021	36.4	-0.014	57.6

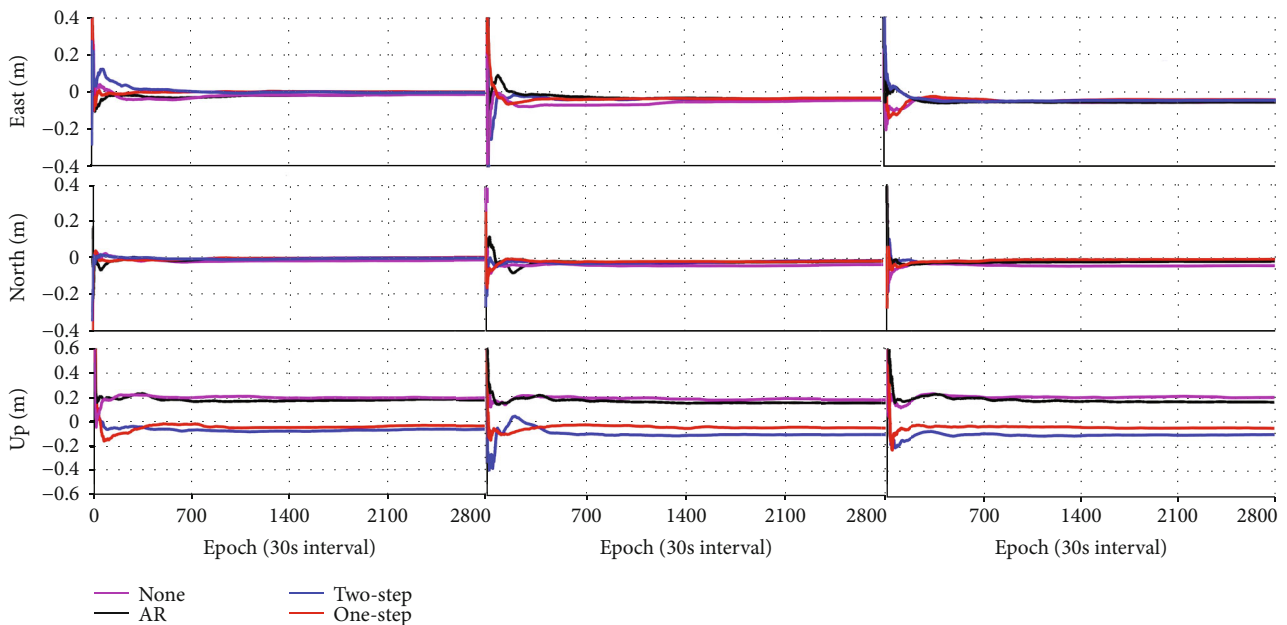


FIGURE 9: Position residuals of BDS-3 double-frequency real-time PPP for B1I + B3I (BJF1).

and U directions are at least 13.9%, 60.0%, and 45.9%, respectively, and 19.1%, 46.5%, and 23.9%, respectively, for B1I + B3I and B1C + B2a, respectively. It is suggested that the one-step strategy with the prior information for modeling the BDS-3 multipath has better real-time application than the traditional method (none). It should be noted that the convergence time is also an important indicator for the PPP performances. In experiments, the convergence time and position residuals are simultaneously considered. However, it is suggested that there is an average improvement within 2% for E and N directions based on the proposed method, which cannot be as a significant improvement in experiments. However, it is difficult to count the convergence time of the U direction as a systematic error found.

Therefore, the convergence time of the PPP solution is ignored in experiments.

More BDS-3 observations collected by GNSS receivers are used to test the proposed strategy of mitigating the BDS-3 multipath delay. Furthermore, the results of the SPP experiment are verified using a set of real observations, the trajectory of which is shown in Figure 11. In consideration of the decoding ability of GNSS receivers, the code observations of B1C are analyzed with an interval of 0.2 s, where B1I and B3I are used to model the code multipath delays. In experiments, three test scenarios are conducted with the same observations, strategies, and parameter estimations. However, the BDS-3 code multipath delays are modeled and corrected with the proposed method (one-step),

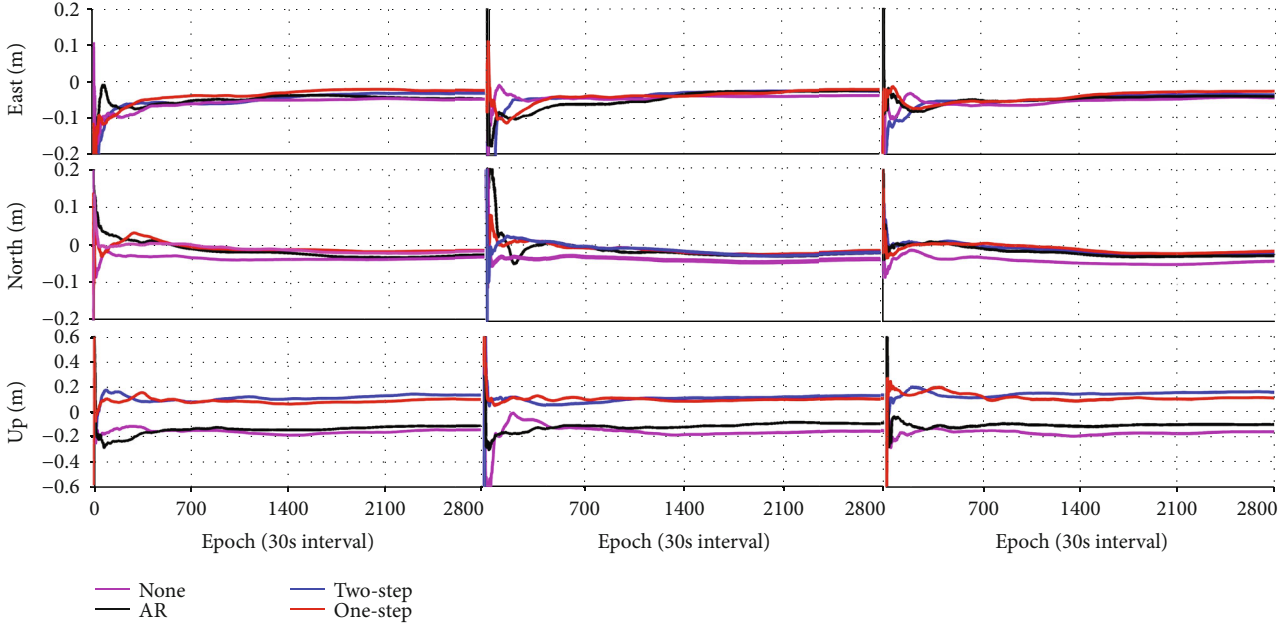


FIGURE 10: Position residuals of BDS-3 double-frequency real-time PPP for B1C + B2a (BJF1).

TABLE 6: Average daily RMS values (m) of position residuals for four stations and three multipath error modeling strategies and corresponding improvements.

Stations	Directions	B1I + B3I						B1C + B2a				
		None	Two-step	Imp. (%)	One-step	Imp. (%)	None	Two-step	Imp. (%)	One-step	Imp. (%)	
BJF1	E	-0.054	-0.040	25.9	-0.039	27.8	-0.056	-0.048	14.3	-0.041	26.8	
	N	-0.040	-0.023	42.5	-0.016	60.0	-0.043	-0.032	25.6	-0.023	46.5	
	U	-0.174	-0.157	9.8	-0.094	45.9	-0.156	-0.127	18.6	-0.092	41.0	
KNDY	E	-0.055	-0.055	0.0	-0.043	21.8	-0.047	-0.043	8.5	-0.038	19.1	
	N	-0.040	-0.016	60.0	-0.013	67.5	-0.040	-0.025	37.5	-0.021	47.5	
	U	-0.204	-0.093	54.4	-0.043	78.9	-0.161	-0.149	7.5	-0.103	36.0	
WUH1	E	-0.043	-0.043	0.0	-0.037	13.9	-0.039	-0.026	33.3	-0.026	33.3	
	N	-0.035	-0.016	54.3	-0.013	62.9	-0.039	-0.022	43.6	-0.017	56.4	
	U	-0.183	-0.100	45.4	-0.046	74.9	-0.154	-0.131	14.9	-0.092	40.3	
XIA1	E	-0.052	-0.014	73.1	-0.013	75.0	-0.051	-0.050	1.9	-0.034	33.3	
	N	-0.054	-0.015	72.2	-0.013	75.9	-0.033	-0.028	15.2	-0.016	51.5	
	U	-0.108	-0.058	46.3	-0.028	74.1	-0.142	-0.134	5.6	-0.108	23.9	

traditional method (two-step), and none considerations (none) in the preprocessing of BDS-3 observations. In a word, the changes of position residuals are caused by the different multipath mitigation method. The single-epoch solution of SPP in E and N directions is shown for three strategies (none, one-step, and two-step) in Figure 12. In analyzing the accuracy of SPP, the station positions of GPS double-frequency kinematic PPP are taken as a reference. SPP does not provide the desired result owing to the complex kinematic environments around the stations. However, the precision and stability can be improved easily by adopting the one-step and two-step strategies. Moreover, there are no appreciable differences in results between the one-step and two-step strategies as no prior information is used in modeling BDS-3 multipath errors. Therefore, a more precise



FIGURE 11: Trajectory of the SPP experiment.

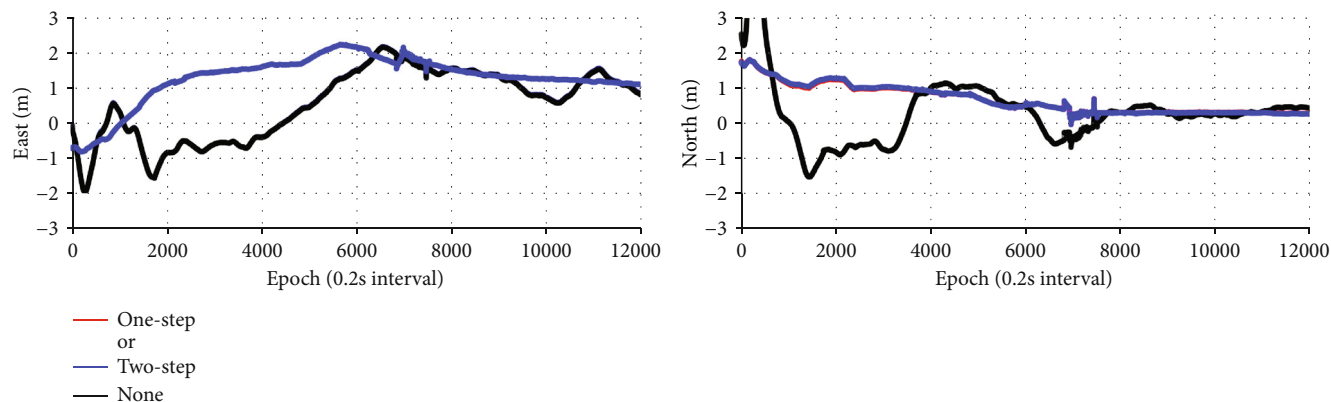


FIGURE 12: Position residuals obtained in SPP experiments with different strategies.

and accurate strategy should be developed to outperform the proposed one-step correction for multipath delays in real-time applications. Figure 6 shows that the multiple paths resulting from the kinematic environment cannot be precisely corrected for, whereas the systematic and trend terms along the elevation angle can be reduced using our method. Because of the complex environments, the improvements of dynamic multipath mitigation for position residuals cannot totally be ascribed to the proposed method as the significant errors in different directions. In the next step, the dynamic multipath mitigation will be paid more attention to improve the applications of BDS-3 real-time services.

4. Discussion

The present study modeled and mitigated the multipath delays of BDS-3 code observations adopting a new strategy, namely, the one-step mitigation strategy, where three points are optimized in contrast with the algorithm traditionally used. First, to avoid the effects of noise and limited observations in modeling the multipath series, sparse modeling is adopted using a combination of TV and EN terms. Second, the multipath series of BDS-3 observations can be divided into two parts, namely, random and systematic components. Therefore, a one-step estimation strategy based on the LS + AR model was proposed. Third, in consideration of real-time and near real-time high-precision applications, the model coefficients of multipath series are estimated and improved with the aid of a prior information.

To verify the proposed strategy, four groups of experiments were conducted with one-month iGMAS and MGEX observations. The model residuals suggest that sparse modeling by adding TV and EN terms improves the accuracy of multipath series. Meanwhile, single-frequency PPP and double-frequency PPP were tested for the proposed one-step mitigation method. The accuracy in E, N, and U directions was improved by at least 4.1%, 9.6%, and 1.2%, respectively, for B1I; 6.6%, 5.3%, and 0.2%, respectively, for B3I; 12.5%, 14.3%, and 3.8%, respectively, for B1C; and 5.9%, 7.4%, and 18.1%, respectively, for B2a relative to the use of the traditional (AR) method in BDS-3 single-frequency PPP. Moreover, there were improvements in E, N, and U directions of at least 13.9%, 60.0%, 45.9%, respec-

tively, for B1I + B3I and 19.1%, 46.5% and 23.9%, respectively, for B1C + B2a. Furthermore, the solution of SPP can be optimized using the proposed method. The use of the proposed method thus improves the accuracy of BDS-3 multipath mitigation and real-time application.

As discussed above, the multipath delays of BDS-3 code observations affect the PPP solution, especially in single-frequency applications. In general, continuously operating reference stations and base stations can ignore the effects of multipath delays by adopting a suitable cutoff elevation angle. However, three problems relating to the raw observations remain: (1) iGMAS and MGEX code observations suggest that there are multipath delays in different observations, with which values are lower than that of actual situations [20], (2) the multipath delays have systematic and random components, which can be explained by code bias [2] and the complex environments around stations [20], and (3) the most destructive near-field multipath has a frequency exceeding 1 Hz, as verified by real-time SPP solutions. In fact, widely used 30 s observations cannot avoid the effects of the environment and the characteristics of signals. In improving the performance of BDS-3, we need to analyze and mitigate the effects of multiple paths of code observations, which are the result of complex factors, especially for the newly deployed BDS-3 satellites. Furthermore, the method can be used in the application of low-cost receivers [31].

Researches about mitigating GPS multipath delays from day-to-day range measurements [32] involved the pseudo-observation with an empirical sample variance, in which systems of errors are divided into two subsystems. Compared with this research, improved algorithms and more analyses are included in our study, in which differences can be summarized as three points: (1) the new-generation BDS-3 satellites and its multifrequency observations are fully discussed. In fact, there are a lot of methods, strategies and algorithms about the mitigation of GPS multipath delays, while the BDS-3 should be carefully studied as its new services, especially for new observations, (2) the purpose of this research mainly focuses on the real-time or near real-time applications, in which the sample mean and variance cannot be used in estimation of multipath parameters. In addition, the BDS-3 code multipath delays are divided into two parts,

namely, systematic and random components, to model and reduce the next-arc multipath delays, respectively, and (3) the improved method is more easier to conduct and insert into the preprocessing of PPP software. Moreover, the prior information of unknown coefficients can optimize the estimation models. In general, the new method is further improved and simplified than that of traditional algorithms.

In summary, the main goal of the present study was the mitigation of the multipath delay of BDS-3 code observations with the aid of sparse modeling and integrated estimation. We first analyzed the characteristics of BDS-3 multipath delays, which were then modeled using regularization, EN, and TV terms and an integrated LS-combined AR algorithm based on static station observations. Multipath delay coefficients cannot be used for accurate corrections in the real-time and near near-time applications of BDS-3. We therefore proposed an improved method that takes the estimated coefficients as prior information and feeds the coefficients into the real-time correction of BDS-3 raw observations. Because of the function between the multipath delay and elevation, the next-arc raw observations can be further improved with the real-time estimated coefficients through the accumulation of short-arc observations. Similarly, in dynamic observations, we can accumulate static observations over a short period (of an hour or so) to calculate multipath coefficients, while the prior values are set at zero.

5. Conclusions

The BDS-3 system adopts new frequencies, new observations, and new technologies in providing global services, and these need to be further discussed for high-precision applications. The performance of the BDS-3 system is important in the research field of GNSS navigation and positioning while innovations and developments of the BDS-3 system are important in further expanding high-quality PNT services. In this paper, the mitigation model of the BDS-3 multipath error was optimized for rapid high-accuracy applications. The PPP solution cannot be improved appreciably because the processing of the multiple frequencies and errors of observations still refers to BDS-2 [2]. In future work, we will consider ultrarapid BDS-3 satellite products and bias parameters in optimizing rapid BDS-3 services.

Data Availability

The data used to support the findings of this study are available from the corresponding author upon request.

Conflicts of Interest

The authors declare no conflict of interest.

Acknowledgments

The authors appreciate the International GNSS Monitoring and Assessment Service (iGMAS) for the provision of rele-

vant data and products. This work was supported by the Natural Science Foundation of Anhui Colleges (Grant no. KJ2020A0310), the National Key Research and Development Program of China (Grant no. 2020YFA0713502), the National Natural Science Foundation of China (Grant no. 41874039), Anhui Natural Science Foundation (Grant no. 2108085QD173), and the Jiangsu Natural Science Foundation (Grant no. BK20181361).

References

- [1] Y. Yang, Y. Mao, and B. Sun, "Basic performance and future developments of BeiDou global navigation satellite system," *Satellite Navigation*, vol. 1, no. 1, 2020.
- [2] C. Hu, Z. Wang, P. Rao, and T. Cheng, "One-step correction strategy for BDS-2/BDS-3 satellite observation code bias and multipath delay," *Acta Geodaetica et Geophysica*, vol. 56, no. 1, pp. 29–59, 2021.
- [3] C. Hu, *An Investigation of Key Technologies Related to Combining BDS-2 and BDS-3 Observations in Data Processing*, China University of Mining and Technology, Xuzhou, China, 2020.
- [4] C. Tang, C. Su, X. Hu et al., "Characterization of pseudorange bias and its effect on positioning for BDS satellites," *Acta Geodaetica et Cartographica Sinica*, vol. 49, pp. 1131–1138, 2020.
- [5] W. Liu, J. Hao, Z. Lv, J. Xie, J. Liu, and B. Jiao, "Evaluation and comparative analysis of BDS-3 signal-in-space range error," *Acta Geodaetica et Cartographica Sinica*, vol. 49, no. 9, pp. 1213–1221, 2020.
- [6] Y. Yifei, G. Jing-xiang, L. Zeng-ke, X. Chang-hui, and C. Xinyun, "A new robust Kalman filtering algorithm of unequal precision observations based on residual vectors in static precise point positioning," *Acta Geodynamica et Geomaterialia*, vol. 13, no. 4, pp. 397–408, 2016.
- [7] C. Hu, Z. Wang, Q. Wang, and P. Rao, "An improved model for inter-system bias estimation based on BDS-2/BDS-3 combined precise orbit determination," *Geomatics Information Science of Wuhan University*, vol. 46, no. 3, pp. 360–370, 2021.
- [8] A. Zeng, Y. Yang, F. Ming, and Y. Jing, "BDS-GPS inter-system bias of code observation and its preliminary analysis," *GPS Solutions*, vol. 21, no. 4, pp. 1573–1581, 2017.
- [9] C. Shi, F. Zheng, Y. Lou et al., "National BDS augmentation service system (NBASS) of China: progress and assessment," *Remote Sensing*, vol. 9, no. 8, 2017.
- [10] J. Wang, M. Stewart, and M. Tsakiri, "Stochastic modeling for static GPS baseline data processing," *Journal of Survey Engineering*, vol. 124, no. 4, pp. 171–181, 1998.
- [11] L. Fangchao, G. Jingxiang, L. Zengke, Q. Nijia, Y. Liu, and Y. Yifei, "A step cycle slip detection and repair method based on double-constraint of ephemeris and smoothed pseudorange," *Acta Geodynamica et Geomaterialia*, vol. 16, no. 4, pp. 337–348, 2019.
- [12] Z. Zhang, B. Li, Y. Gao, and Y. Shen, "Real-time carrier phase multipath detection based on dual-frequency C/N₀ data," *GPS Solutions*, vol. 23, no. 1, p. 7, 2019.
- [13] O. Montenbruck, A. Hauschild, P. Steigenberger, U. Hugentobler, P. Teunissen, and S. Nakamura, "Initial assessment of the COMPASS/BeiDou-2 regional navigation satellite system," *GPS Solutions*, vol. 17, no. 2, pp. 211–222, 2013.

- [14] L. Wanninger and S. Beer, "BeiDou satellite-induced code pseudorange variations diagnosis and therapy," *GPS Solutions*, vol. 19, no. 4, pp. 639–648, 2015.
- [15] C. Cai, C. He, R. Santerre, L. Pan, X. Cui, and J. Zhu, "A comparative analysis of measurement noise and multipath for four constellations: GPS, BeiDou, GLONASS and Galileo," *Survey Review*, vol. 48, no. 349, pp. 287–295, 2016.
- [16] X. Zhang, M. Wu, W. Liu et al., "Initial assessment of the COMPASS/BeiDou-3: new-generation navigation signals," *Journal of Geodesy*, vol. 91, no. 10, pp. 1225–1240, 2017.
- [17] C. Hu, Q. Wang, Z. Wang, and A. Hernández Moraleda, "New-generation BeiDou (BDS-3) experimental satellite precise orbit determination with an improved cycle-slip detection and repair algorithm," *Sensors*, vol. 18, no. 5, p. 1402, 2018.
- [18] K. Park, R. Nerem, M. Schenewerk, and J. L. Davis, "Site-specific multipath characteristics of global IGS and CORS GPS sites," *Journal of Geodesy*, vol. 77, no. 12, pp. 799–803, 2004.
- [19] J. Y. Guo, G. W. Li, Q. L. Kong, and S. Y. Wang, "Modeling GPS multipath effect based on spherical cap harmonic analysis," *Transactions of Nonferrous Metals Society of China*, vol. 24, no. 6, pp. 1874–1879, 2014.
- [20] G. Chang, C. Chen, Y. Yang, and T. Xu, "Tikhonov regularization based modeling and sidereal filtering mitigation of GNSS multipath errors," *Remote Sensing*, vol. 10, no. 11, p. 1801, 2018.
- [21] C. Chen, G. Chang, N. Zheng, and T. Xu, "GNSS multipath error modeling and mitigation by using sparsity-promoting regularization," *IEEE Access*, vol. 7, pp. 24096–24108, 2019.
- [22] C. Hu, Q. Wang, Y. Min, Y. Mao, and Y. Gong, "An improved model for BDS satellite ultra-rapid clock offset prediction based on BDS-2 and BDS-3 combined estimation," *Acta Geodaetica et Geophysica*, vol. 54, no. 4, pp. 513–543, 2019.
- [23] Q. Zhang, W. Yang, S. Zhang, and X. Liu, "Characteristics of BeiDou navigation satellite system multipath and its mitigation method based on Kalman filter and Rauch-Tung-Striebel smoother," *Sensors*, vol. 18, no. 2, p. 198, 2018.
- [24] C. Ogaja and C. Satirapod, "Analysis of high-frequency multipath in 1-Hz GPS kinematic solutions," *GPS Solutions*, vol. 11, no. 4, pp. 269–280, 2007.
- [25] T. Yi, H. Li, and M. Gu, "Characterization and extraction of global positioning system multipath signals using an improved particle-filtering algorithm," *Measurement Science and Technology*, vol. 22, no. 7, article 075101, 2011.
- [26] G. Chang, N. Qian, C. Chen, and J. Gao, "Precise instantaneous velocimetry and accelerometry with a stand-alone GNSS receiver based on sparse kernel learning," *Measurement*, vol. 159, article 107803, 2020.
- [27] T. Luo, *Research on Learning Models Based on Sparse Optimization and Their Applications*, National University of Defense Technology, Changsha, China, 2018.
- [28] J. Bonnans, J. Gilbert, C. Lemaréchal, and C. Sagastizabal, *Numerical Optimization: Theoretical and Practical Aspects*, Springer Science and Business Media, 2006.
- [29] C. Hu, Z. Wang, W. Lv, and Z. Yu, *A One-Step Modelling for BeiDou Satellite Observations Multipath Delay Based on Prior Constraints*, Geomatics and Information Science of Wuhan University, 2021.
- [30] A. Beck and M. Teboulle, "A fast iterative shrinkage-thresholding algorithm for linear inverse problems," *SIAM Journal on Imaging Sciences*, vol. 2, no. 1, pp. 183–202, 2009.
- [31] Z. Zhang, H. Yuan, B. Li, X. He, and S. Gao, "Feasibility of easy-to-implement methods to analyze systematic errors of multipath, differential code bias, and inter-system bias for low-cost receivers," *GPS Solutions*, vol. 25, no. 3, p. 116, 2021.
- [32] J. Wu and C. Hsieh, "Statistical modeling for the mitigation of GPS multipath delays from day-to-day range measurements," *Journal of Geodesy*, vol. 84, no. 4, pp. 223–232, 2010.

Research Article

A New GPT2w Model Improved by PSO-LSSVM for GNSS High-Precision Positioning

Xuanxuan Zhang, Yamin Dang, and Changhui Xu 

Chinese Academy of Surveying & Mapping, Beijing 100036, China

Correspondence should be addressed to Changhui Xu; chxucasm@yeah.net

Received 18 March 2021; Revised 7 April 2021; Accepted 23 April 2021; Published 24 May 2021

Academic Editor: Qiu-Zhao Zhang

Copyright © 2021 Xuanxuan Zhang et al. This is an open access article distributed under the Creative Commons Attribution License, which permits unrestricted use, distribution, and reproduction in any medium, provided the original work is properly cited.

Tropospheric delay is an important error affecting GNSS high-precision navigation and positioning, which will decrease the precision of navigation and positioning if it is not well corrected. Actually, tropospheric delay, especially in the zenith direction, is related to a series of meteorological parameters, such as temperature and pressure. To estimate the zenith tropospheric delay (ZTD) as accurately as possible, the paper proposes a new fused model using the least squares support vector machines (LSSVM) and the particle swarm optimization (PSO) to improve the precision and temporal resolution of meteorological parameters in global pressure and temperature 2 wet (GPT2w). The proposed model uses the time series of meteorological parameters from the GPT2w model as the initial value, and thus, the time series of the residuals can be obtained between the meteorological parameters from meteorological sensors (MS) and the GPT2w model. The long time series of meteorological parameters is the evident periodic signal. The GPT2w model describes its dominant frequency (harmonics), and the residuals thus can be seen as the short-period signal (nonharmonics). The combined PSO and LSSVM model (PSO-LSSVM) is used to predict the specific value of the short-period signal. The new GPT2w model, in which the meteorological parameter value is obtained by combining the estimated meteorological parameters residuals and the GPT2w-derived meteorological parameters, can be acquired. The GNSS network stations in Hong Kong throughout 2017-2018 are processed by the GNSS Processing and Analysis Software (GPAS), which is developed by the Chinese Academy of Surveying & Mapping, to estimate the zenith tropospheric delay and station coordinates using the new GPT2w model. Statistical results reveal that the accuracy of the new GPT2w model-derived ZTD was improved by 60% or more compared with that of the GPT2w-derived ZTD. In addition, the positioning accuracy of the GNSS station has been effectively improved up to 44.89%. Such results reveal that the new GPT2w model can greatly reduce the influence of nonharmonic components (short-period terms) of the meteorological parameter time series and achieve better accuracy than the GPT2w model.

1. Introduction

Tropospheric delay is an important error that affects the positioning accuracy of the global navigation satellite system (GNSS). However, it is also an important parameter to calculate tropospheric delay for GNSS meteorology. Usually, the value can reach tens of meters [1] for satellites with low altitude so that this error should be carefully considered in the GNSS positioning. Establishing an accurate and reliable ZTD model becomes crucial and critical for GNSS research.

According to the relationships between ZTD and meteorological parameters obtained from the ground, the com-

monly ZTD models are established including Hopfield model [2], Saastamoinen model [3], Black model [4], and Ifadis model [5]. The accuracy of these models is limited by the input meteorological parameters and environments. When meteorological parameters cannot be acquired accurately, the accuracy of GNSS high-precision positioning will be decreased. Additionally, when GNSS stations are not equipped with the meteorological sensors, ZTD is not able to be obtained by these models.

Thus, the ZTD empirical models are proposed that only rely on the location and observation time without the need of any auxiliary information. For example, the UNB3 model

[6] stores the meteorological parameters in the form of a table from the equator to poles at the intervals of 15 degrees. IGGtrop model [7] is established by using four years of National Centers for Environment Prediction (NCEP) data. Yao used the Global Geodetic Observing System (GGOS) Atmosphere data to establish the GZTD model [8] and improved the GZTD2 model [9] by introducing diurnal variations. Some other ZTD empirical models are also established by considering other factors, such as IGGtrop_SH and IGGtrop_RH models [10], the GZTDS model [11], the SHAtropE model [12], the RGZTD model [13], and the global pressure and temperature 2 wet (GPT2w) model [14]. The GPT2w model that is the paper concerned can offer precise ZTD products.

However, the ZTD empirical models are not applicable to some regions limited by the spatiotemporal resolution. Fortunately, the Continuously Operating Reference Station (CORS), whose ZTD products have high accuracy and high temporal resolution, provides an opportunity for establishing new ZTD models with higher accuracy. This paper proposes a new model combining the particle swarm optimization algorithm with the least squares support vector machine (PSO-LSSVM) model to improve the GPT2w model. First, the GPT2w is used to calculate meteorological parameters that as the initial value. Second, the time series of meteorological parameters residuals can be obtained as the difference between meteorological parameters from meteorological sensors (MS-derived) and GPT2w-derived meteorological parameters over GNSS stations. Third, the PSO-LSSVM model is used to predict meteorological parameters residuals. So the meteorological parameter value can be acquired by combining the estimated meteorological parameters and GNSS-derived meteorological parameters. Finally, the zenith tropospheric delay (ZTD), zenith hydrostatic delay (ZHD), and station coordinates can be obtained by GNSS Processing and Analysis Software (GPAS) using the meteorological parameters, which is developed by the Chinese Academy of Surveying & Mapping.

2. Methodology

2.1. The GPT2w Model. The Global Pressure and Temperature (GPT) series model is an empirical model to provide the global temperature and pressure at any GNSS station in the world. These models include GPT [15], GPT2 [16], and GPT2w [14]. GPT2w, a very comprehensive tropospheric model, can be used for a range of geodetic, meteorological, and climatic purpose without auxiliary information. It provides the annual and semiannual amplitudes of a set of meteorological parameters that include pressure (P) in hpa, weighted mean temperature (T_m) in K, water vapor pressure (e) in hpa, and water vapor lapse rate (λ). These parameters are originated from the European Center for Medium-Range Weather For Medium-Range Weather Forecasts (ECMWF ERA-Interim) reanalysis data with a global horizontal resolution of $1^\circ \times 1^\circ$ geographical grid from 2001 to 2010. The GPT2w model, as an empirical model, only needs to input the ellipsoidal coordinates (latitude, longitude, and height) of GNSS stations and the consistent modified

Julian date. The meteorological parameters are calculated by equation (1).

$$r(t) = A_0 + A_1 \cos\left(\frac{\text{doy}}{365.25} 2\pi\right) + B_1 \sin\left(\frac{\text{doy}}{365.25} 2\pi\right) + A_2 \cos\left(\frac{\text{doy}}{365.25} 4\pi\right) + B_2 \sin\left(\frac{\text{doy}}{365.25} 4\pi\right) \quad (1)$$

In equation (1), $r(t)$ is the estimated meteorological parameters. A_0 denotes the mean value as well as A_1, B_1 and A_2, B_2 are annual and semiannual amplitudes, which can be downloaded from https://vmf.geo.tuwien.ac.at/codes/gpt2_1w.grd. doy denotes the day of the year. So the needed meteorological quantities at the four nearest grid points can be acquired. Then, the estimated meteorological parameters of a site can be calculated by the bilinear interpolation algorithm. The ZTD values are calculated [17] as equations (2)–(4).

$$\text{ZHD} = \frac{0.0022768 \times P}{1 - 0.00266 \times \cos(2\varphi) - 0.00028 \times H}, \quad (2)$$

$$\text{ZWD} = 10^{-6} \left(k_2' + \frac{k_3}{T_m} \right) \frac{R_d}{(\lambda + 1) g_m} e, \quad (3)$$

$$\text{ZTD} = \text{ZHD} + \text{ZWD}. \quad (4)$$

In equations (2)–(4), ZHD and ZWD denote, respectively, the zenith hypostatic delay and zenith wet delay, φ is the latitude of station, H is the geoid height of the station, and P is the surface pressure. R_d is the dry air ratio gas constant with a value of $287.0464 \text{ JK}^{-1} \text{ kg}^{-1}$, k_2' and k_3 are the atmospheric refractive index formula constants with values of 16.52 K/hpa and $3.776 \times 10^5 \text{ K}^2/\text{hpa}$, respectively; g_m is the mean gravity acceleration with a value of 9.80665 m/s^2 at the mass center of the vertical column of the atmosphere.

2.2. The Least Squares Support Vector Machine. Support vector machine (SVM) is a machine learning method with a perfect theoretical system, which is different from general statistical methods. It avoids the process from induction to deduction and thus realizes the inference and estimation from training samples to forecast samples and obtains the simplification of regression analysis and other problems [18]. The Least Squares Support Vector Machine (LSSVM) inherits the basic idea of SVM and uses the quadratic square loss function instead of the classical SVM quadratic programming method. The LSSVM model converts the optimization problem to the linear equation problem, reducing the complexity of the algorithm [19]. Therefore, the LSSVM model can solve the problem of inequality constraints and improve the speed and accuracy in solving the linear equation problem simultaneously [20]. Additionally, the random error and overtraining can be avoided in this model [21].

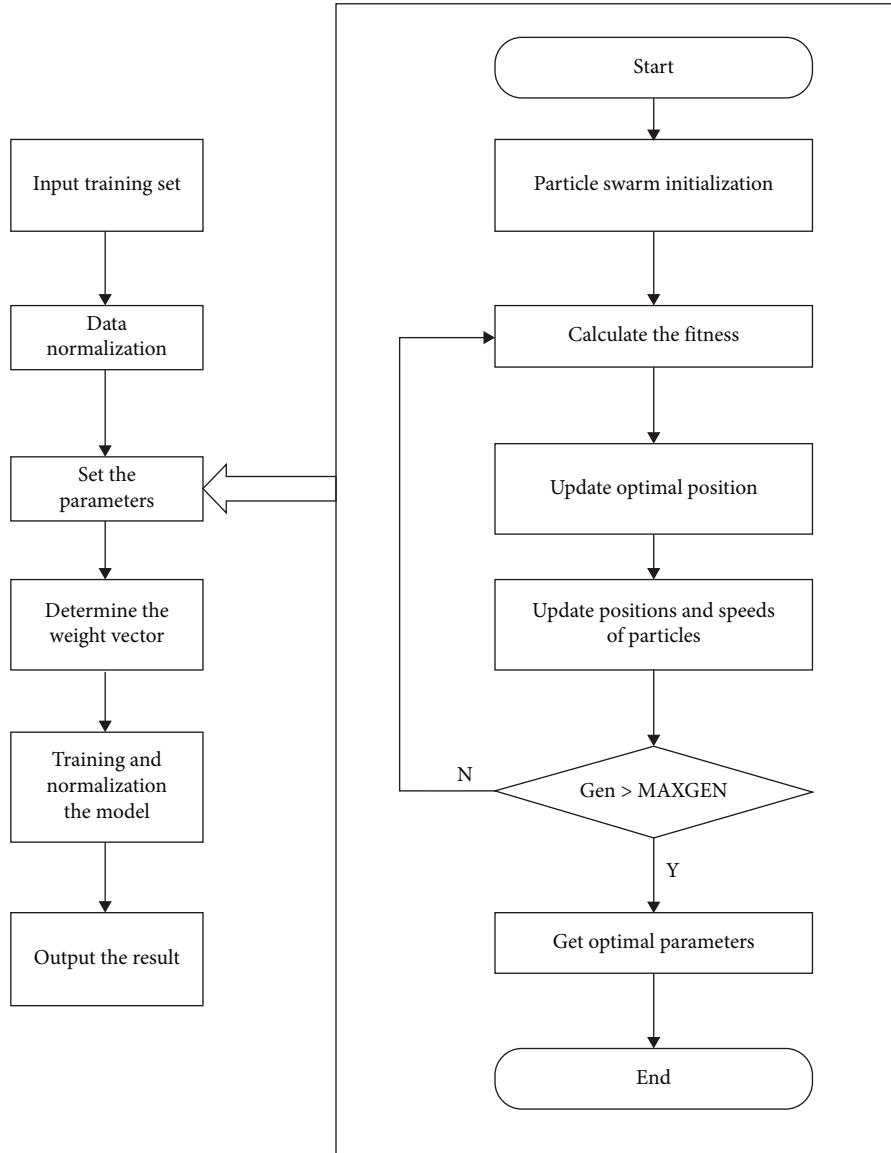


FIGURE 1: The parametrization workflow of PSO-LSSVM.

The LSSVM can be explained as follows: for the training sample $D = \{(x_k, y_k) \mid k = 1, 2, \dots, N\}$, where $x_k \in R^m$ is the input data and $y_k \in R$ is the output data. The linear regression function can be introduced to establish relationship between x_k and y_k as equation (5).

$$f(x) = w^T \varphi(x) + b \quad (5)$$

In equation (5), w is the weight vector of the hyperplane, b is the bias constant, and $\varphi(x)$ is the linear mapping function which can make the input vector be mapped to a high-dimensional feature space so that the original linearly inseparable samples can be separated in the kernel space. Then, the regression problem is converted into a quadratic optimization problem whose objective function and constraints are as equations (6) and (7).

$$\min_{w,b,e} J(w, e) = \frac{1}{2} w^T w + \frac{1}{2} \gamma \sum_{k=1}^N e_k^2 \quad (6)$$

$$y_k = w^T \varphi(x) + b + e_k, k = 1, \dots, N \quad (7)$$

In equations (6) and (7), J is loss function, γ is the regularization parameter, and e is slack variable.

The equation (6) is convex function which belongs to the quadratic programming problems. To solve the optimization problem, the equation (8) is introduced.

$$L(w, b, e, a) = J(w, e) - \sum_{k=1}^N a_k \{w^T \varphi(x_k) + b + e_k - y_k\} \quad (8)$$

In equation (8), the a_k is the Lagrange multiplier of the model.

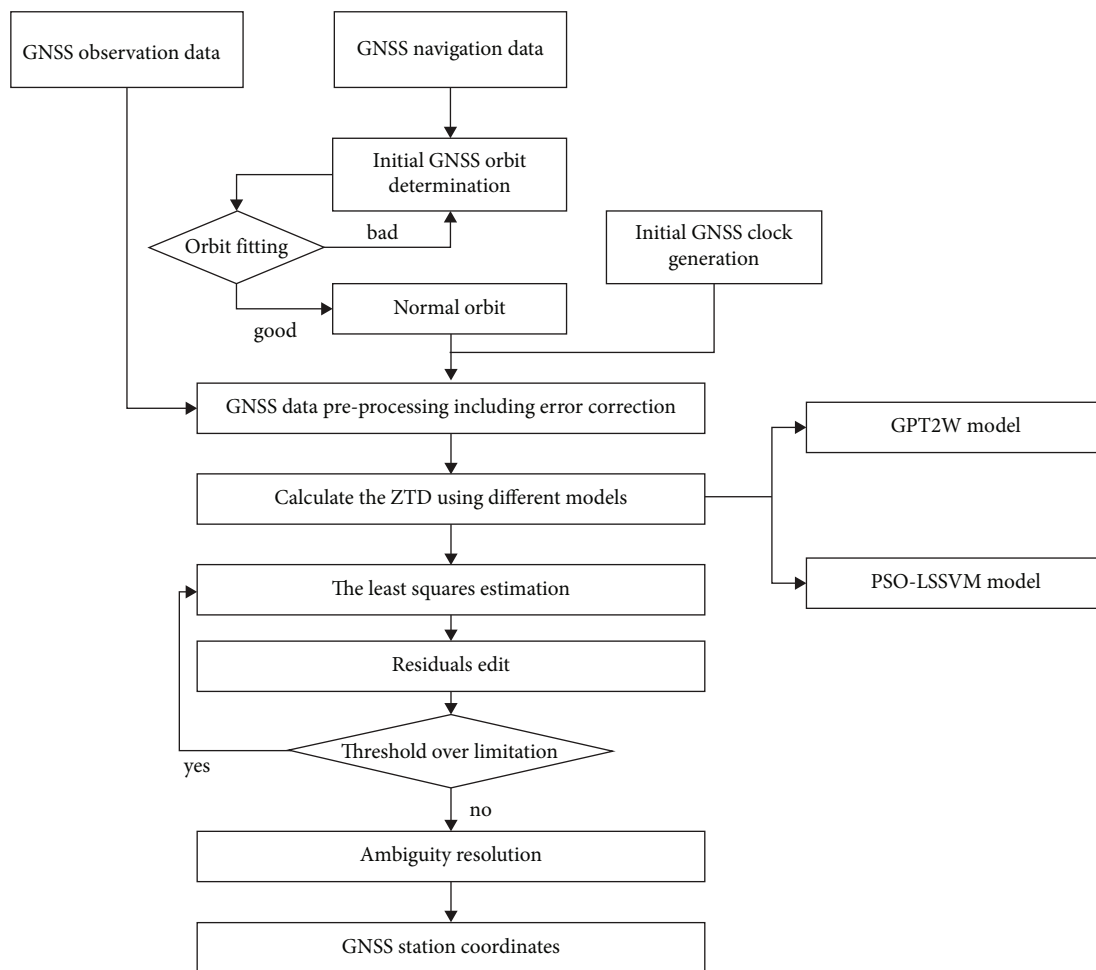


FIGURE 2: GNSS processing of GPAS software.

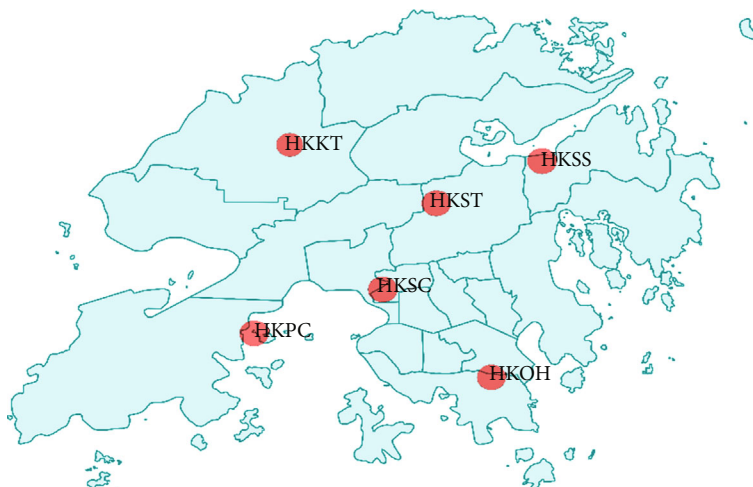


FIGURE 3: The distribution of selected (GNSS) stations in Hong Kong SatRef.

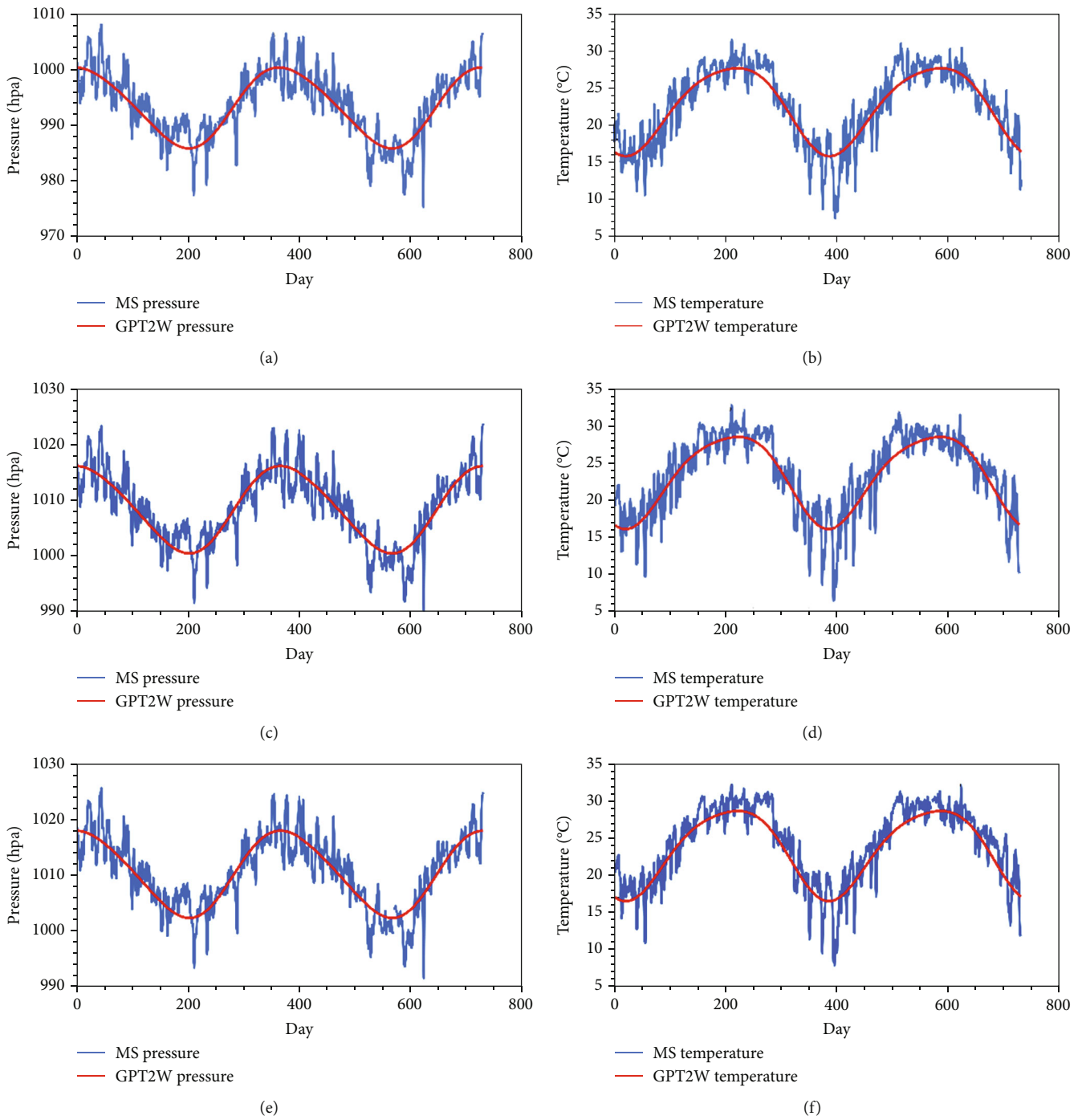


FIGURE 4: Continued.

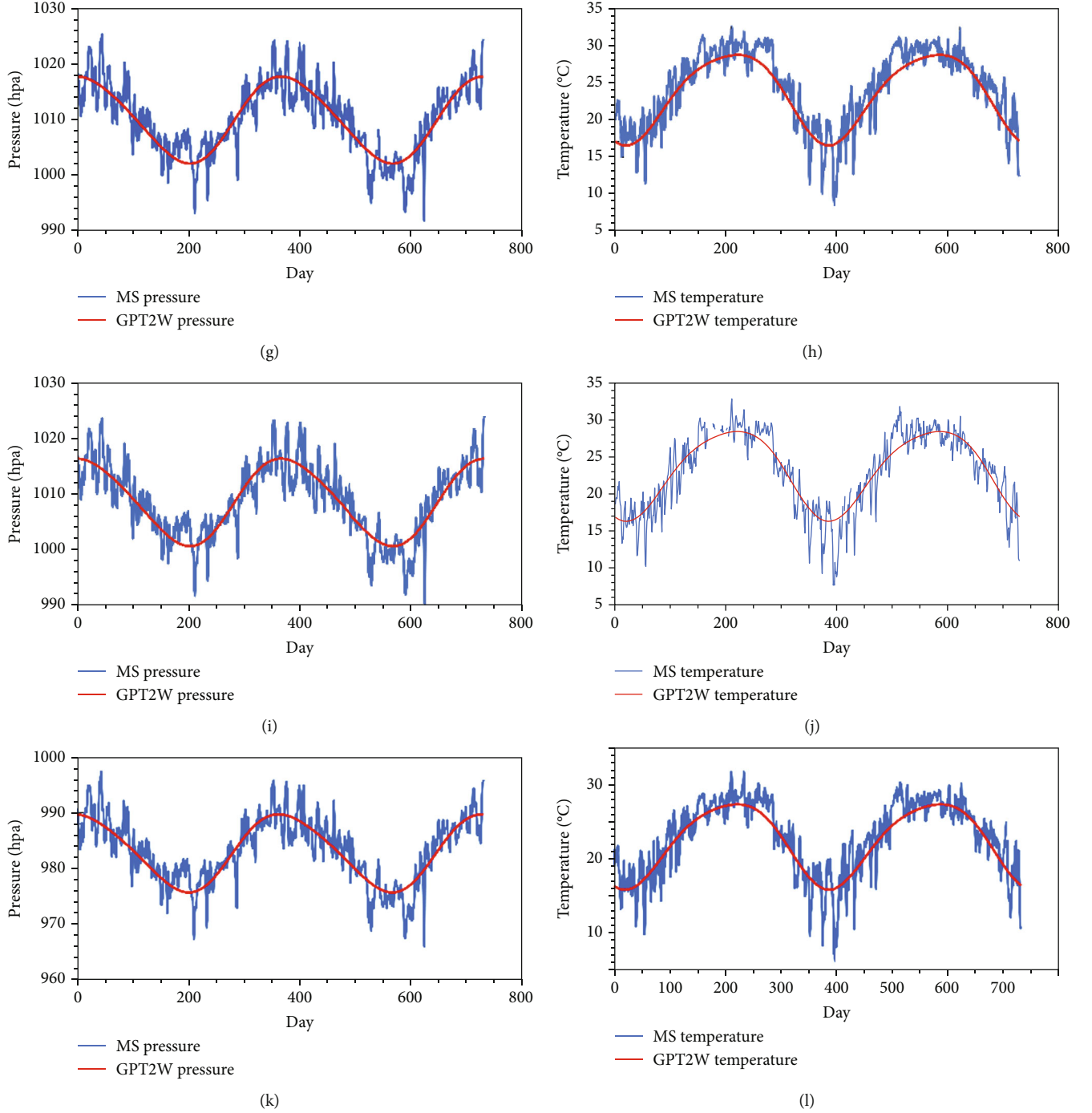


FIGURE 4: Time series of pressure from MS and GPT2w at stations. (a) HKOH. (c) HKKT. (e) HKPC. (g) HKSC. (i) HKSS. (k) HKST. Time series of temperature from MS and GPT2w at stations. (b) HKOH. (d) HKKT. (f) HKPC. (h) HKSC. (j) HKSS. (l) HKST. Throughout 2017-2018.

Let $\partial L/\partial w = 0, \partial L/\partial b = 0, \partial L/\partial e_k = 0, \partial L/\partial a_k = 0$, then the equations (9)–(13) can be acquired.

$$\begin{bmatrix} 0 & \mathbf{E}_v^T \\ \mathbf{E}_v^T & \mathbf{\Omega} + \frac{1}{\gamma} \mathbf{I} \end{bmatrix} \begin{bmatrix} b \\ \mathbf{a} \end{bmatrix} = \begin{bmatrix} 0 \\ \mathbf{y} \end{bmatrix}, \quad (9)$$

$$\mathbf{E}_v = [1 \ \cdots \ 1]^T, \quad (10)$$

$$\mathbf{a} = [a_1 \ \cdots \ a_N]^T, \quad (11)$$

$$\mathbf{\Omega} = \varphi(x_k)^T \varphi(x_l), \quad k, l = 1, \dots, N, \quad (12)$$

$$\mathbf{y} = [y_1 \ \cdots \ y_N]^T. \quad (13)$$

In equation (9), \mathbf{I} is the identity matrix and the kernel function is $\mathbf{\Omega} \cdot \mathbf{a}$ and b can be calculated by the least square

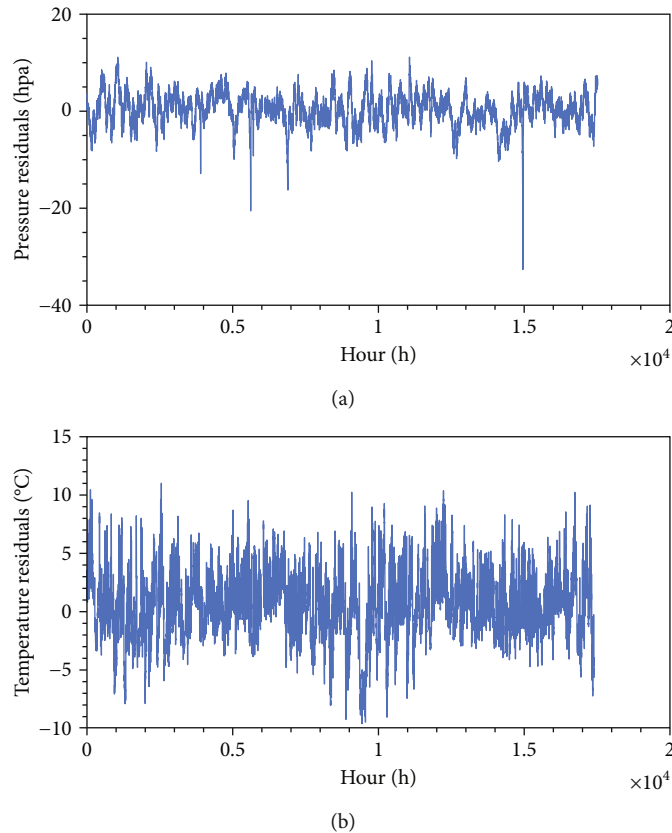


FIGURE 5: Time series of (a) pressure and (b) temperature residuals between MS and GPT2w at HKOH.

model. Thus, the regression estimation function of the LSSVM is equation (14).

$$y(x) = \sum_{k=1}^N a_k k(x, x_k) + b. \quad (14)$$

In equation (14), the constructed support vector machine varies with the kernel function. Since the radial basis kernel function (RBF) corresponds to an infinite dimensional feature space, the limited samples are linearly separable in the feature space, and it has better computational performance. Therefore, the RBF kernel function is chosen as equation (15).

$$k(x_k, x_l) = \exp\left(\frac{-\|x_k - x_l\|}{2\sigma^2}\right). \quad (15)$$

In equation (15), x_k and x_l are the input data and σ is the shape parameter of the RBF kernel function.

2.3. Fusion of Particle Swarm Optimization and LSSVM. There are two important parameters (σ and γ) determined difficultly for the LSSVM model, which decrease the accuracy of the LSSVM model if they are not well treated. Actually, it is usually tried or determined by experience, which may not be effective. The Particle Swarm Optimization (PSO) originally originated from the foraging behavior of bird flocks [22]. It simulates the mutual learning behavior between individuals

through the shared information in the biological group and finds the optimal solution in its solution space [23]. The PSO can determine the optimal parameters through individual and global particle optimization, which is practicable for the LSSVM parameter determination.

For the optimization problem of the PSO, the solution can be regarded as a bird in the search space, which has its own initial velocity, position, and fitness to a certain position. Finding the optimal solution is to find the position where the particle has the best fitness value from the starting position to the current position. The update formulas for the velocity and position of each particle in the particle swarm are as equations (16) and (17).

$$v_i(t+1) = \omega v_i(t) + c_1 R_1 [R_i^b(t) - x_i(t)] + c_2 R_2 [R_g^b(t) - x_i(t)], \quad (16)$$

$$x_i(t+1) = x_i(t) + \varphi v_i(t+1). \quad (17)$$

In equations (16) and (17), t is the defined number of iterations, and $v_i(t)$ is the speed of the i th particle in the particle swarm at the t th iteration; $x_i(t)$ is the location of the i th particle in the particle swarm at the t th iteration; c_1 and c_2 are the positive learning coefficients and influence partial search capability and global search capability, respectively; R_1 and R_2 are two uniformly distributed random numbers that ensure the particles move to their optimal position and the optimal position of the group in the form of equational probability; ω is the

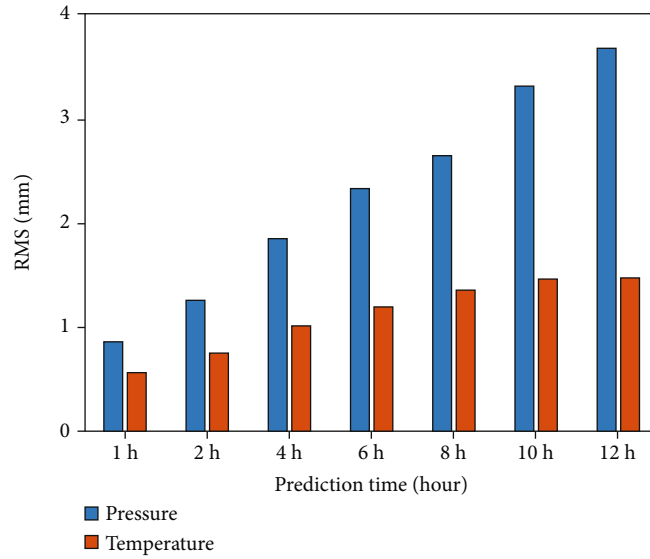


FIGURE 6: RMS of meteorological parameters under different forecasting modes at HKOH.

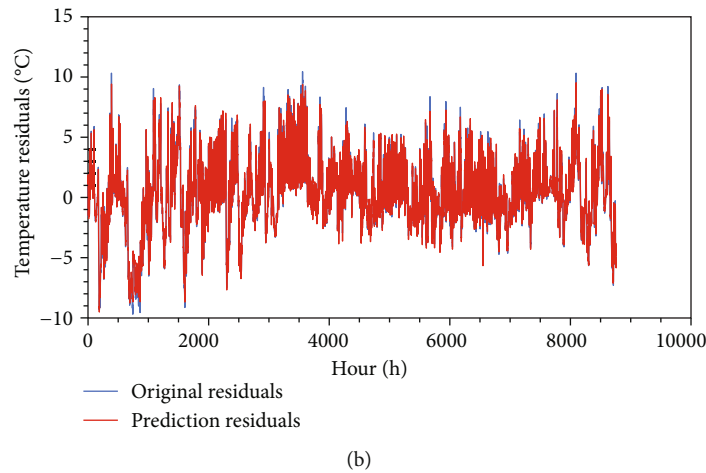
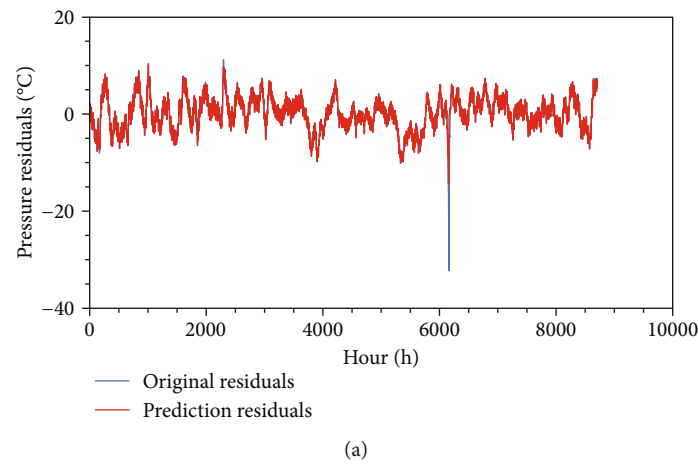


FIGURE 7: Time series of (a) pressure and (b) temperature residuals of the observed and proposed model prediction at HKOH.

ability of a particle to maintain the state of motion at the previous moment that can achieve a balance between global search and partial search of particles. $R_i^b(t)$ is the optimal loca-

tion of the individuals; $R_g^b(t)$ is the global optimal location of the community. φ is the shrink silver that keeps the particle speed in a certain range to ensure convergence.

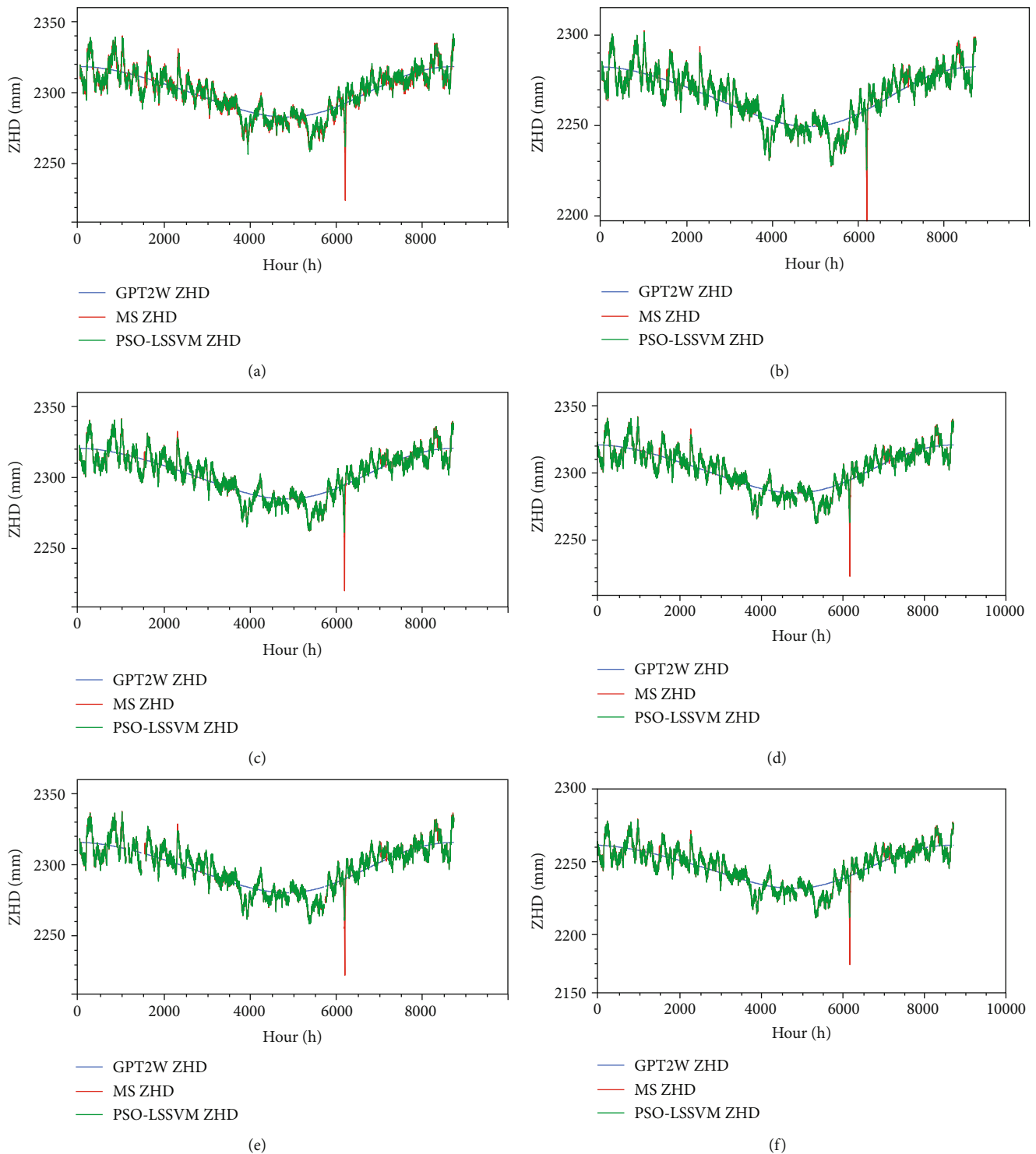


FIGURE 8: Time series of ZHD of the GPT2w, MS and PSO-LSSVM at stations. (a) HKKT. (b) HKOH. (c) HKPC. (d) HKSC. (e) HKSS. (f) HKST.

To demonstrate the advantage of the LSSVM and the PSO clearly, the optimization process is shown in Figure 1. The steps are as follows:

Step 1. Initialize the particle swarm and the parameters of the LSSVM.

Step 2. Calculate the fitness of each particle. The fitness of the current particle is compared with the fitness of the individual's optimal position and the historical optimal position. If the fitness of the current particle is optimal, the position is replaced; otherwise, the original optimal position is maintained.

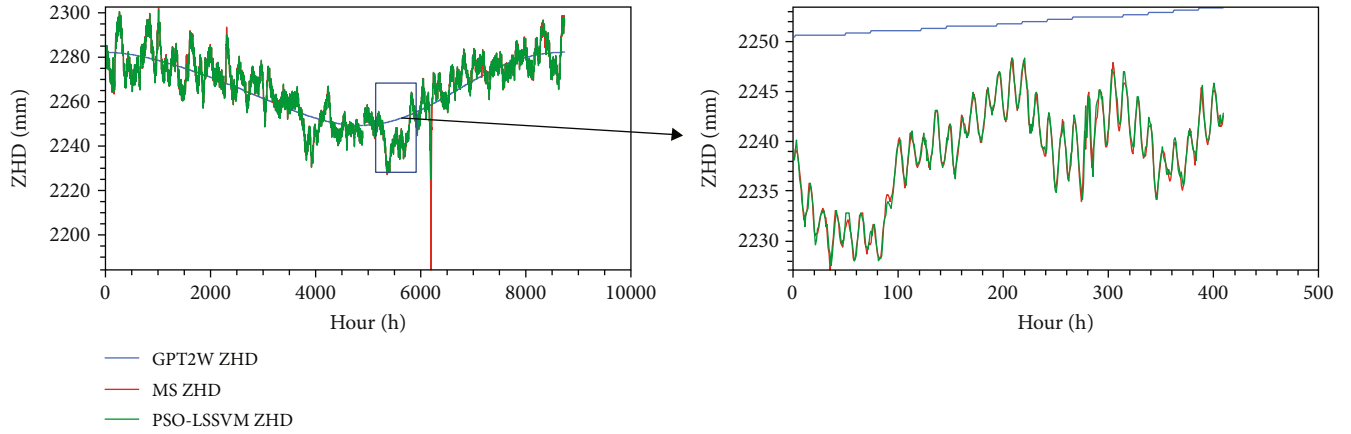


FIGURE 9: Time series of ZHD of the GPT2w, MS, and PSO-LSSVM at station HKOH in 2018 (left) and Time series of ZHD of the GPT2w, MS, and PSO-LSSVM at station HKOH throughout August 10, 2018-August 27, 2018 (right).

Step 3. Update the position and velocity of the particles by the maximum number of evolutions.

Step 4. Judgment of termination conditions. When the error requirements or the maximum number of evolutions are met, the process will end. Otherwise, the process will repeat Step 2 to continue until reach the requirements.

2.4. GNSS Station Solution Based on PSO-LSSVM Model. The GNSS Processing and Analysis Software (GPAS) is developed by Chinese Academy of Surveying & Mapping to obtain the zenith tropospheric delay (ZTD), zenith hydrostatic delay (ZHD), and station coordinates. The process of GPAS is shown in Figure 2. To clarify the tropospheric delay with the proposed PSO-LSSVM method, tropospheric delay is given before the least squares. Firstly, it is necessary to initialize GNSS orbit and determine GNSS clock including preparation of earth rotation parameters and ephemeris, calculating GNSS clock by broadcast ephemeris and checking the ephemeris. Secondly, GNSS observation data is preprocessed including conversion of data format, detecting cycle slip and marking resolution. At the same time, some errors are corrected including tropospheric delay, where GPT2w model and PSO-LSSVM model are contrastively analyzed. Then, the traditional GNSS data processing is implemented to get the station coordinates, such as the least squares estimation, residual edit, and ambiguity resolution.

3. Experiment Description

The Hong Kong Survey and Mapping Office (SMO) of the Lands Department builds a local satellite positioning reference station network (SatRef). It consists eighteen CORSs and six of them are chosen considering the continuity and completeness of observation data, which is shown in Figure 3. The paper adopts the meteorological observations from January 1, 2017, to December 31, 2018, with a temporal resolution of 1 hour and the GNSS observations' sampling rate is 30 s.

The ground weather stations obtain the temperature, air pressure, relative humidity, and other meteorological parameters at the site through meteorological sensors (MS). The air

pressure detection accuracy can reach 0.5 hpa, and the air temperature detection accuracy is high. Therefore, the meteorological sensors are regarded as a criterion for selected GNSS stations. Since the temporal resolution of the GPT2w model is one day, the GPT2w-derived meteorological parameter for each hour is replaced the calculation value of GPT2w model. Then long-term meteorological parameters residuals between GPT2w-derived and MS-derived can be obtained. The residual data from January 1, 2017, to November 30, 2017, is used to train the PSO-LSSVM model; the residual data from December 2017 is used to test whether the model has overfitting Phenomenon; the residual data for the whole year of 2018 is used as the validation set. Then, the paper adds the fitted residual data and the GPT2w model value of the corresponding time period to obtain the improved meteorological parameters, and analyzes the root mean square error (RMS) as the evaluation index as equation (18).

$$\text{RMS} = \sqrt{\frac{\sum_{i=1}^n (Y_i - Y_i^i)^2}{n}}. \quad (18)$$

In equation (18), Y_i is the improved meteorological parameters; Y_i^i is the MS-derived parameters; n is the time of prediction.

4. Analysis and Discussion of Experiment

The time series of pressure and temperature residuals between GPT2w and MS at stations (HKOH, HKKT, HKPC, HKSC, HKSS, and HKST) are given in Figure 4. The MS-derived meteorological parameters in the unit of day are obtained by taking the average of meteorological parameters a day. It can be seen from Figure 4 that the time series of meteorological parameters such as atmospheric pressure and temperature consists two parts: harmonic and nonharmonic. The harmonic part reflects its long-period characteristics, and the nonharmonic part reflects its short-period characteristics. The GPT2w model fits the harmonic part of the meteorological parameter time series well and reflects its long-period characteristics. However, for its nonharmonic

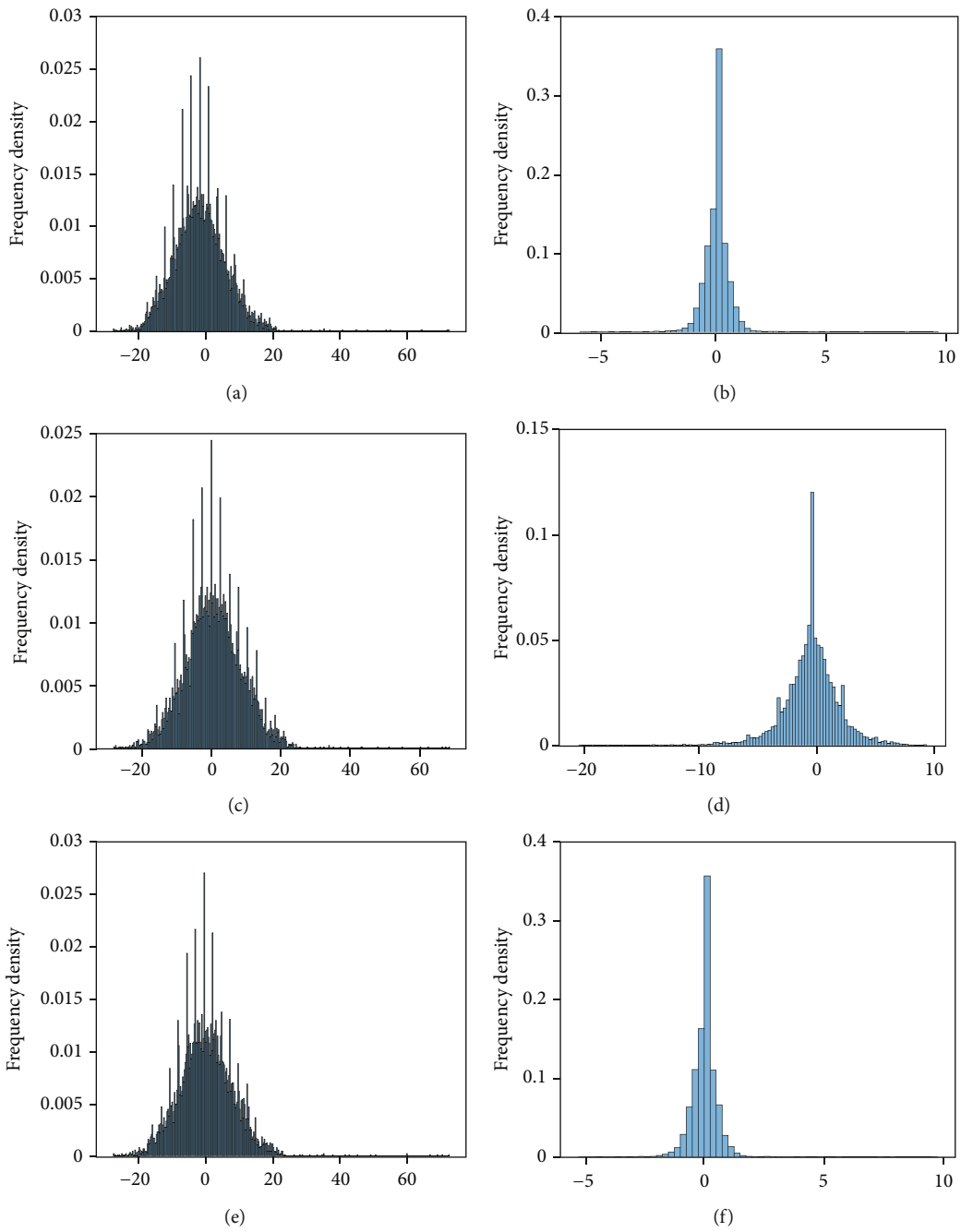


FIGURE 10: Continued.

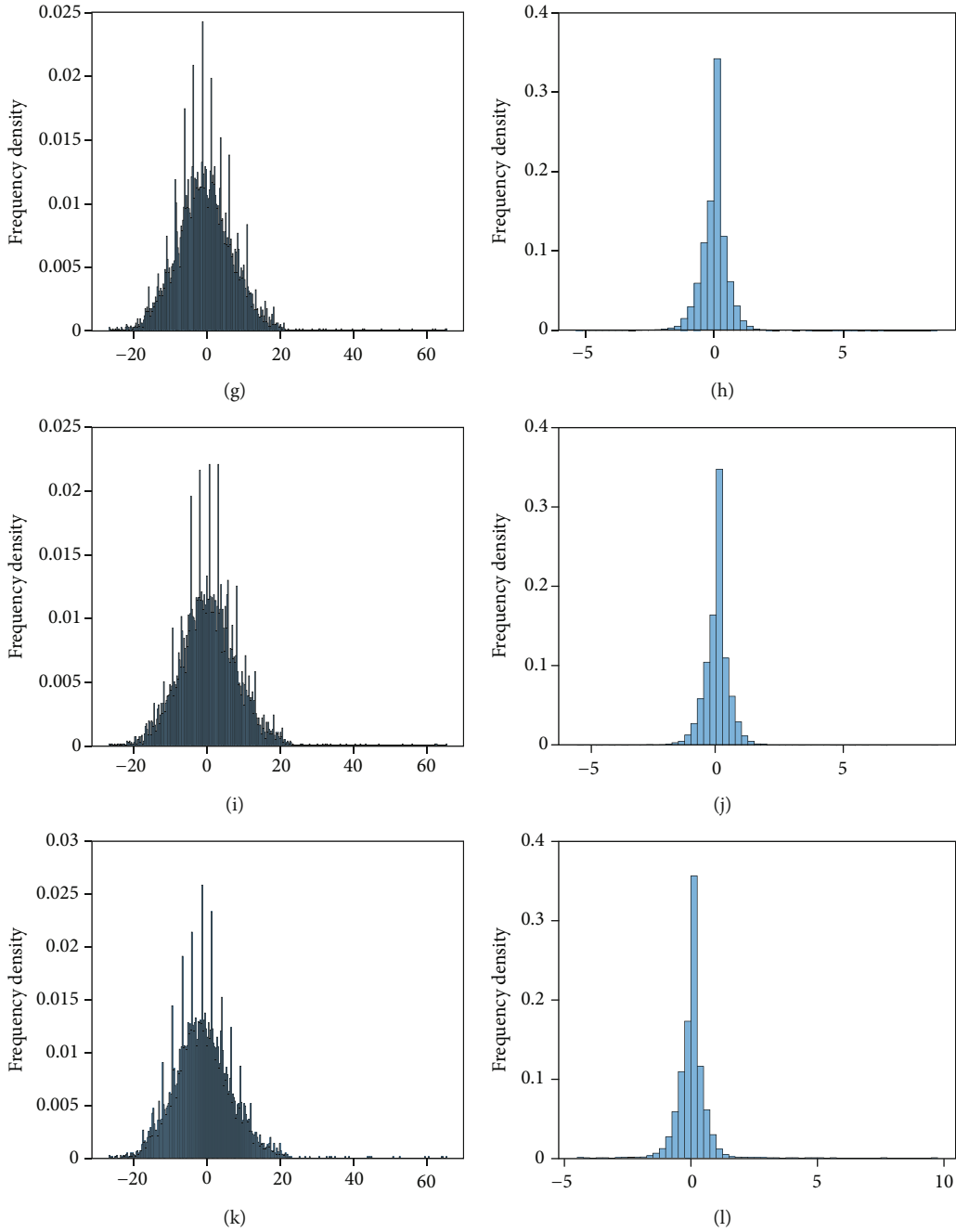


FIGURE 10: Frequency histogram of the ZTD difference using the GPT2w model at selected stations. (a) HKKT. (c) HKOH. (e) HKPC. (g) HKSC. (i) HKSS. (k) HKST. Frequency histogram of the ZTD difference using the PSO-LSSVM model at selected stations. (b) HKKT. (d) HKOH. (f) HKPC. (h) HKSC. (j) HKSS. (l) HKST.

part, there is still some residual errors affecting the accuracy to a certain extent. If those errors can be reduced, it will be meaningful for the improvement of accuracy.

Taking the HKOH as example, Figure 5 presents the short-period (nonharmonic) part of the meteorological parameters. The results of other stations are similar.

In Figure 5, there is the phenomena of nonlinearity, non-stationarity, and noise in the time series of residuals. This means that it is difficult to establish the relationship between the time series in the past and in the future. The PSO-LSSVM model is used to solve this problem.

TABLE 1: Comparison of ZTD between GPT2w and PSO-LSSVM at selected stations.

GNSS stations	GPT2w-ZTD RMS (mm)	PSO-LSSVM-ZTD RMS (mm)	Percentage of improvement
HKKT	1.4514	0.4989	65.62%
HKOH	1.3078	0.3231	75.29%
HKPC	1.4006	0.3320	76.29%
HKSC	1.3983	0.3141	77.54%
HKSS	1.3845	0.3014	78.23%
HKST	1.3074	0.3036	76.78%

TABLE 2: Comparison of coordinate accuracy between GPT2w and PSO-LSSVM at selected stations.

GNSS stations	GPT2w-coordinate RMS (mm)			PSO-LSSVM-coordinate RMS (mm)			Percentage of improvement		
	X	Y	Z	X	Y	Z	X	Y	Z
HKKT	0.4366	0.7504	0.3188	0.2936	0.4117	0.1757	32.75%	45.14%	44.89%
HKOH	0.3499	0.5935	0.2735	0.2324	0.3495	0.1483	33.58%	41.11%	45.78%
HKPC	0.2678	0.5316	0.2585	0.2216	0.3654	0.1555	17.25%	31.26%	39.85%
HKSC	0.4832	0.5391	0.2514	0.2975	0.3768	0.1425	38.43%	30.11%	43.32%
HKSS	0.2610	0.5217	0.2543	0.2439	0.3792	0.1917	6.55%	27.31%	24.62%
HKST	0.2766	0.5170	0.2462	0.2569	0.4627	0.2189	7.12%	10.50%	11.09%

The LSSVM is a nonparametric model, which means that it does not require any prior information about the underlying data. Thus, this paper uses the past 24 hours of historical meteorological parameters residuals (nonharmonic part) to train the model. To determine the appropriate forecast range, the meteorological parameters residuals of the next 1 h, 2 h, 4 h, 6 h, 8 h, 10 h, and 12 h are, respectively, predicted. The RMS values of the model meteorological parameters and the measured meteorological parameters are calculated to evaluate the performance of different prediction models. It can also be seen from Figure 6 that with the increase of the prediction range, the RMS value also increases. So the prediction range is 1 h.

Figure 7 is the time series of the model prediction and the observed value (nonharmonic component). The RMS of the pressure residuals and temperature residuals are, respectively, 0.8536 hpa and 0.5609°C, which have high accuracy.

Thus, the predicted meteorological parameters are obtained by adding the predicted nonharmonic components and the harmonic components estimated by the GPT2w model and then the GPAS software is used to output ZHD and ZTD.

It can be seen from Figure 8 that the predicted results of the PSO-LSSVM model are usually consistent with the MS. The ZHD output by the meteorological parameters from the PSO-LSSVM are in good agreement with the MS. This is because the good performance of the GPT2w empirical model itself, which better fits the harmonic components of the meteorological parameter time series, provides a solid foundation for further prediction of nonharmonic components. At the same time, the nonlinear factors of the time series are not ignored, and the nonlinear relationship can be found by the RBF kernel function of the LSSVM.

The paper selects the data from August 10th, 2018, to August 27th, 2018, when the weather of Hong Kong was rainy continuously to validate the proposed model. The right picture in Figure 9 is the time series of ZHD from the GPT2w, MS, and PSO-LSSVM model from August 10th, 2018, to August 27th, 2018, at station HKOH. It can be seen from the right picture that the PSO-LSSVM ZHD are in good agreement with the MS ZHD. However, the GPT2w ZHD has a large bias with the MS ZHD. This verifies the new proposed model has a better performance than GPT2w model. The results of other stations are similar.

The left pictures of Figure 10 are the frequency histograms of the difference between the GPT2w-derived ZTD

and the MS-derived ZTD, and the right are the difference between the ZTD output by the PSO-LSSVM model and MS-derived ZTD. In Figure 10, the frequency histograms of the right pictures are thinner than the left pictures which demonstrate the standard deviations of the right pictures are smaller. According to the properties of Gaussian function, the smaller the standard deviation is, the more stable the distribution will be. Thus, the LSSVM has a certain learning ability for Gaussian white noise in the time series of ZTD.

It can be seen from Table 1 that the improved meteorological parameter model proposed in this paper shows better performance than the GPT2w model. The accuracy of the ZTD value has been effectively improved. Especially, the proposed model achieves RMS of 0.4989 mm, 0.3231 mm, 0.3320 mm, 0.3141 mm, 0.3014 mm, and 0.3036 mm at stations of HKKT, HKOH, HKPC, HKSC, HKSS, and HKST, respectively, which has approximately 65.62%, 75.29%, 76.29%, 77.54%, 78.23%, and 76.78% improvements over them, respectively.

Finally, the proposed model is applied to the GPAS and compared with the GPT2w model. From Table 2, it is obvious that the proposed model also reaches improvements of more than 30% over stations of HKKT, HKOH, HKPC, and HKSC though the improvements are not evident over HKSS and HKST. Above all, for each station, the positioning accuracy has also been improved. The improvement verifies the universality and effectiveness of the model proposed in this paper for the research GNSS stations.

5. Conclusions

To improve the accuracy of estimating ZTD, the new meteorological parameters model based on GPT2w model and PSO-LSSVM model is proposed. Based on the advantages of MS-derived meteorological parameters and GPT2w model, the time series of meteorological parameters is divided into two categories: harmonic and nonharmonic. Then, the PSO-LSSVM model is used to estimate the nonharmonic and GPT2w is applied to fit the harmonic. Then, the improved meteorological parameters are obtained. Finally, these parameters are input into GPAS which can process GNSS data; the ZTD and coordinates of stations are obtained accordingly. The results show that the proposed model has higher temporal resolution and higher accuracy than GPT2w model. Also, the proposed model is robust even though the weather is rainy.

The future work will focus on the following aspects. First, the past 24 h of historical meteorological parameter residuals (nonharmonic part) are used to train the PSO-LSSVM model. A shorter time should also be considered, such as 12 h. Second, the estimation and forecasting of meteorological parameters are a complicated process. This paper only considers the correlation of its one-dimensional time series. In the following work, more relevant variables can be considered to improve the accuracy of model.

Data Availability

The codes of GPT2w model can be downloaded at <https://vmf.geo.tuwien.ac.at/codes/>. The GNSS observation and meteorological data of Hong Kong can be obtained from <https://www.geodetic.gov.hk/en/satref/satref.htm>.

Conflicts of Interest

The authors declare no conflict of interest.

Acknowledgments

At the end of the paper, I would like to extend my sincere gratitude to those who have provided help in my process of writing this paper. First, I would like to appreciate Xu who has given me guidance and has helped me to improve this paper many times patiently. Second, I would like to thank Dang who has provided favorable environments and working conditions. Last but not least, Chinese Academy of Surveying & Mapping is acknowledged for providing GPAS software and I would like to thank the research group of Advanced Geodesy of TU Vienna and the Hong Kong Geodetic Survey Services for providing the GPT2w model and meteorological data, respectively. This research is funded by the Fundamental Research Funds for the Central Public Research Institutes (AR2004, AR2005) and Research on Regional Ground Surface Dynamic Environmental Impact Model and the Overall Refinement Method of Reference Frame (No.41974010).

References

- [1] Q. M. Chen, S. L. Song, and W. Y. Zhu, "An analysis for the accuracy of tropospheric zenith delay calculated from ECMWF/NCEP data over Asia," *Chinese Journal of Geophysics*, vol. 55, no. 3, pp. 275–283, 2012.
- [2] H. S. Hopfield, "Two-quartic tropospheric refractivity profile for correcting satellite data," *Journal of Geophysical Research Atmospheres*, vol. 74, no. 18, pp. 4487–4499, 1969.
- [3] J. Saastamoinen, "Atmospheric correction for the troposphere and stratosphere in radio ranging satellites," *The use of artificial satellites for geodesy*, vol. 15, pp. 247–251, 2013.
- [4] H. D. Black and A. Eisner, "Correcting satellite Doppler data for tropospheric effects," *Journal of Geophysical Research: Atmospheres*, vol. 89, no. D2, pp. 2616–2626, 1984.
- [5] I. Ifadis, "The atmospheric delay of radio waves: modelling the elevation dependence on a global scale," *Licentiate Thesis, Technical Report*, vol. 38, 1986.
- [6] J. P. Collins and R. B. Langley, *A Tropospheric Delay Model for the User of the Wide Area Augmentation System*, Fredericton: Department of Geodesy and Geomatics Engineering, University of New Brunswick, 1997.
- [7] W. Li, Y. B. Yuan, J. K. Ou, H. Li, and Z. S. Li, "A new global zenith tropospheric delay model IGGtrop for GNSS applications," *Chinese Science Bulletin*, vol. 57, no. 17, pp. 2132–2139, 2012.
- [8] Y. Yi-Bin, H. Chang-Yong, Z. Bao, and X. Chao-Qian, "A new global zenith tropospheric delay model GZTD," *Chinese Journal of Geophysics-Chinese Edition*, vol. 56, no. 7, pp. 2218–2227, 2013.
- [9] Y. Yao, Y. Hu, C. Yu, B. Zhang, and J. Guo, "An improved global zenith tropospheric delay model GZTD2 considering diurnal variations," *Nonlinear Processes in Geophysics*, vol. 23, no. 3, pp. 127–136, 2016.
- [10] W. Li, Y. Yuan, J. Ou, and Y. He, "IGGtrop_SH and IGGtrop_rH: two improved empirical tropospheric delay models based on vertical reduction functions," *IEEE Transactions on Geoscience and Remote Sensing*, vol. 56, no. 9, pp. 5276–5288, 2018.
- [11] J. Sun, Z. Wu, Z. Yin, and B. Ma, "A simplified GNSS tropospheric delay model based on the nonlinear hypothesis," *GPS Solutions*, vol. 21, no. 4, pp. 1735–1745, 2017.
- [12] J. Chen, J. Wang, A. Wang, J. Ding, and Y. Zhang, "SHAtropE—a regional gridded ZTD model for China and the surrounding areas," *Remote Sensing*, vol. 12, no. 1, p. 165, 2020.
- [13] L. Yang, J. Gao, D. Zhu, N. Zheng, and Z. Li, "Improved zenith tropospheric delay modeling using the piecewise model of atmospheric refractivity," *Remote Sensing*, vol. 12, no. 23, p. 3876, 2020.
- [14] J. Böhm, G. Möller, M. Schindelegger, G. Pain, and R. Weber, "Development of an improved empirical model for slant delays in the troposphere (GPT2w)," *GPS Solutions*, vol. 19, no. 3, pp. 433–441, 2015.
- [15] J. Boehm, R. Heinkelmann, and H. Schuh, "Short note: a global model of pressure and temperature for geodetic applications," *Journal of Geodesy*, vol. 81, no. 10, pp. 679–683, 2007.
- [16] K. Lagler, M. Schindelegger, J. Böhm, H. Krásná, and T. Nilsson, "GPT2: empirical slant delay model for radio space geodetic techniques," *Geophysical Research Letters*, vol. 40, no. 6, pp. 1069–1073, 2013.
- [17] J. Askne and H. Nordius, "Estimation of tropospheric delay for microwaves from surface weather data," *Radio Science*, vol. 22, no. 3, pp. 379–386, 1987.
- [18] M. A. Ahmadi and A. Bahadori, "A LSSVM approach for determining well placement and conning phenomena in horizontal wells," *Fuel*, vol. 153, pp. 276–283, 2015.
- [19] B. A. Forman and R. H. Reichle, "Using a support vector machine and a land surface model to estimate large-scale passive microwave brightness temperatures over snow-covered land in North America," *IEEE Journal of Selected Topics in Applied Earth Observations and Remote Sensing*, vol. 8, no. 9, pp. 4431–4441, 2015.
- [20] M. Schwieder, P. Leitão, S. Suess, C. Senf, and P. Hostert, "Estimating fractional shrub cover using simulated EnMAP data: a comparison of three machine learning regression techniques," *Remote Sensing*, vol. 6, no. 4, pp. 3427–3445, 2014.
- [21] L. Wang, D. Liu, Q. Wang, and Y. Wang, "Spectral unmixing model based on least squares support vector machine with unmixing residue constraints," *IEEE Geoscience and Remote Sensing Letters*, vol. 10, no. 6, pp. 1592–1596, 2013.

- [22] B. Roshanravan, H. Aghajani, M. Yousefi, and O. Kreuzer, "Particle swarm optimization algorithm for neuro-fuzzy prospectivity analysis using continuously weighted spatial exploration data," *Natural Resources Research*, vol. 28, no. 2, pp. 309–325, 2019.
- [23] L. Huijun, S. Hongjun, and Z. Bo, "Hyperspectral multiple features optimization using improved firefly algorithm," *Remote Sensing Technology and Application*, vol. 33, no. 1, pp. 110–118, 2018.